University of Padua

Department of Industrial Engineering – DII

Master Degree in Mechanical Engineering

In cooperation with

České Vysoké Učení Technické v Praze, ČVUT

A COMPARISON OF DIFFERENT LOCAL ANALYSIS METHODOLOGIES FOR FATIGUE STRENGTH ASSESSMENT

Advisor: Eng. Jan Papuga, PhD

Co-advisor: Prof. Giovanni Meneghetti, PhD

Candidate: Zanatta Manuele

Badge Number: 1241858

Academic year 2021/2022

To my parents
and my sister

Contents

List of Figures

List of Tables

Acknowledgements

Italian version

Al professor J. Papuga, che mi ha accolto all'università tecnica Ceca di Praga, voglio dire un enorme Grazie. Non solo per la sua professionalità, ma anche per avermi seguito, con pazienza, in questa esperienza di ricerca. Con la speranza di risentirLo in futuro, grazie per tutto.

Al professor G. Meneghetti, che mi ha dato l'opportunità di partecipare a questa straordinaria avventura in un paese fuori dall'Italia, in un laboratorio fuori dall'Italia. Porterò, assieme al mio bagaglio culturale acquisito durante i suoi corsi, anche i suoi consigli per diventare un buon ingegnere.

Ai due dottorandi M. Martin e M. Matej, grazie per avermi aiutato e seguito durante la fase sperimentale del mio lavoro di tesi. Spero di rivedervi presto in futuro.

A mio padre Mauro, mia madre Marisa e mia sorella Valentina, che mi hanno sopportato durante tutti questi anni di ingegneria e tanto altro.

Ai miei compagni di corso, a tutti i bei momenti passati insieme tra i banchi, tra mille corsi ed esami. Con voi ho potuto vivere un'esperienza incredibile: l'università.

Agli amici di vecchia data, che hanno cercato di capire il mio percorso e non mi hanno abbandonato.

Ai miei nuovi amici sparsi in giro per il mondo: Fofo, Vicky, Adka, Megy, Lukas, Deniz, Ebrar, Beatrice, Aggelos, George, e tanti altri. Grazie a tutti voi, Grazie Praga.

English version

To Professor J. Papuga, who welcomed me to the Czech Technical University in Prague, I want to say a huge thank you. Not only for his professionalism, but also for patiently following me through this research experience. With the hope of hearing from him again in the future, thank you for everything.

To Professor G. Meneghetti, who gave me the opportunity to participate in this extraordinary adventure in a country outside Italy, in a laboratory outside Italy. I will bring, along with my cultural background acquired during his courses, his advice on how to become a good engineer.

To the two PhD students M. Martin and M. Matej, thank you for helping and following me during the experimental phase of my thesis work. I hope to see you again soon in the future.

To my father Mauro, my mother Marisa and my sister Valentina, who have put up with me during all these years of engineering and more.

To my fellow students, to all the good times we spent together between the desks, between a thousand courses and exams. With you I was able to live an incredible experience: university.

To my long-standing friends, who tried to understand my path and did not abandon me.

To my new friends scattered around the world: Fofo, Vicky, Adka, Megy, Lukas, Deniz, Ebrar, Beatrice, Aggelos, George, and many others. Thank you all, Thank you Prague.

Abstract

This thesis work, developed in cooperation with the Czech Technical University in Prague, systematically analyses and compares different approaches for the local fatigue strength assessment of notched specimens. The paper collects experimental data from the FABEST analysis campaign. After the experimental tests using the Amsler testing machine were performed, the data were efficiently collected and processed using statistical techniques to determine the classical S-N curves, i.e. stress versus number of cycles to failure. Subsequently, the theory of critical distances, the relative stress gradient method and the strain energy density were applied through finite element analysis and other computer tools in order to compare the theoretical approaches with experiment. To achieve this goal, the thesis has been divided into eight chapters:

- In the first chapter, the classical fatigue strength analysis, i.e. the one that takes a nominal stress as a reference, was introduced by means of some historical references. In the final paragraphs, a particular criticality in the use of this approach was highlighted.
- The second chapter is based on Neuber's innovative idea from which multiple approaches for the evaluation of fatigue strength will arise. In particular, the theory of critical distances - TCD - is described and it brings together two methods: the first is based on an integral average determined up to a certain length ϵ and the second is based on the extraction of a certain stress at a distance x_c. Both of them use the material curve to determine an effective stress.
- The third chapter presented the theory of the relative stress gradient - RSG - which defines a local component S-N curve to determine fatigue strength. Various techniques from different authors and also from the FKM guidelines were studied.
- In the fourth chapter, the point of view was changed, i.e. a new physical quantity was considered: the strain energy density - SED. Again, this approach rests its foundation on Neuber's idea of structural volume.
- In the fifth chapter, the experimental apparatus adopted to obtain the necessary data was described. Furthermore, not only the statistical methods for the determination of fatigue curves were described, but further results of fatigue tests performed on other types of material and geometries were added.
- In Chapter Six, the fatigue crack initiation points and the fatigue failure surface of the specimens under analysis were described by means of microscopic analysis.
- In the seventh chapter, FEM analyses were conducted to determine the physical quantities required to apply the theoretical approaches described in the first chapters of the thesis. In the second part, all useful parameters were determined using the Matlab programming language in order to establish a comparison between TCD, RSG and SED with the experimental tests in order to determine the deviations between experimental reality and the analytical approach.
- In the eighth and final chapter, an accuracy analysis between the different approaches was performed with the aim of finding the best method to predict the fatigue strength.

Finally, the various appendices describe the static tensile tests for determining certain parameters useful for the analyses and the programming codes used.

Chapter 1

FATIGUE OF METALLIC MATERIALS: NOMINAL APPROACH

1.1 Brief historical description of fatigue

The first studies on fatigue of metallic materials date back to 1829 when the German engineer W. A. J. Albert, Fig. 1.1, director of the mining industry in Clausthal in the Harz region, observed and studied the failure of chains of iron mining conveyors. After many experimental observations, carried out thanks to a testing machine built by himself, published in 1837 the studies related to the phenomenon. His finding was that fatigue was not associated with an accidental overload, but was dependent on load and the number of repetitions of load cycles [46]. As early as the first half of the 1800s, the first concepts of the phenomenon of fatigue, as it is known today, were introduced. In particular, the idea of "repetitions" associated with "number of cycles" hinted that the fatigue must be protracted over time.

Figure 1.1: *Engineer Wilhelm August Julius Albert*

Because of the excessive cost of replacing chains, Albert invented the wire rope, which was certainly more important than the early fatigue studies.
With the development of metallic materials and their use in applications such as bridges and railroads, sudden breaks began to become more frequent. Due to the railway accident at Versailles, France, fatigue research was performed in 1842. In particular, W. J. M. Rankine (Fig. 1.2a), commonly known for his studies in the field of thermodynamics, discussed the railway axles failure and he said that areas of concentrated stress could initiate failures. This was an early example of defining the notch effect [46].
In 1853 the french physicist Arthur-Jules Morin, Fig. 1.2b, discussed axles failure of horse-drawn mail coaches and he asserted that the replacement of the axles should be made approximately at 60000 *km*. This was a first example of the safe life design approach. In addition, he noticed that cracks mainly occurred at section changes [46].
The term *fatigue* was mentioned for the first time by the Englishman and engineer Braithwaite in 1854, Fig. 1.3a. Braithwaite, however, says that Mr. Field coined the term. In his paper, Braithwaite,

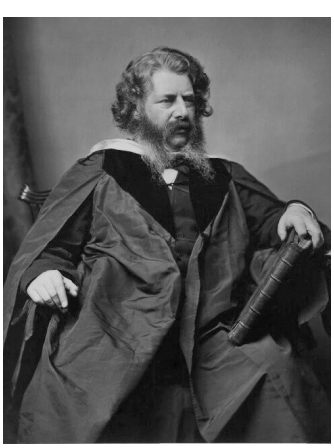

(a)

(b)

Figure 1.2: (a) *Engineer William John Macquorn Rankine,* (b) *Physicist Arthur-Jules Morin*

describes many service fatigue failures of brewery equipment, water pumps, propeller shafts, crankshafts railway axles, levers, cranes, etc. Allowable stresses for fatigue-loaded components are also discussed [46].

(a)

(b)

Figure 1.3: (a) *Engineer John Braithwaite,* (b) *Mathematician and Engineer Jean-Victor Poncelet*

The mathematician and engineer Jean-Victor Poncelet, Fig. 1.3a, professor of mechanics at the *école d'application* in 1825 [46], in his lectures he coined the term *fatigue* to describe the state of materials subjected to stress. He is particularly interested in the design of turbines and water wheels.
Between 1850 and 1860, the german engineer August Wöhler, Fig. 1.4, royal *Obermaschinenmeister* of the *Niederschlesische-Märkische Bahn* Railways in Frankfurt an der Oder, conducted a series of experiments on railway axles with self-developed deflection gauges. The tests were performed in fatigue laboratory under repeated stresses subjected to bending, torsion and axial loads. These studies showed that the fatigue life increased with decreasing applied stress so that below a certain amount of tension componer seemed to have infinite life. Even Wöhler, in those years, noted that the fatigue life of the component decreased drastically in the presence of notching effects [46].
Wöhler represented his test results in the form of tables. Spangenberg, his successor, as director of the *Mechanisch-Technische-Versuchsanstalt* in Berlin [43], plotted the results of Wöhler as curves forms, although in the unusual form of linear abscissa and ordinate, obtaining S-N curves, where *S* stands for *Stress* and *N* stands for *Number of cycles*. The S-N curves were called *Wöhler curves* since 1936 [46][52].

1.2 Introduction to fatigue phenomenon

Nowadays, mechanical structures have to meet a number of design requirements such as static strength fatigue strength and stiffness. However, fatigue tends to be the most common reason for the limited

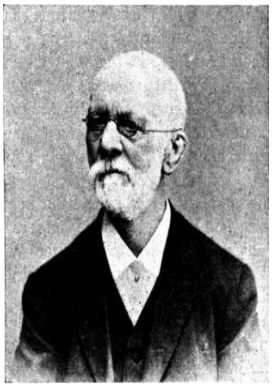

Figure 1.4: *Engineer August Wöhler*

lifetime of a mechanical component. Fatigue is a progressive damage mechanism of material that can lead to failure of a mechanical component subjected to repeated stresses even if the external load cause stresses well below the ultimate tensile strength (σ_{UTS}) of material. These stresses, in order to cause fatigue fracture, are not only well below σ_{UTS}, but also the yield stress σ_y. In other words, stresses that would be absolutely safe from a static point of view can cause fatigue failure.

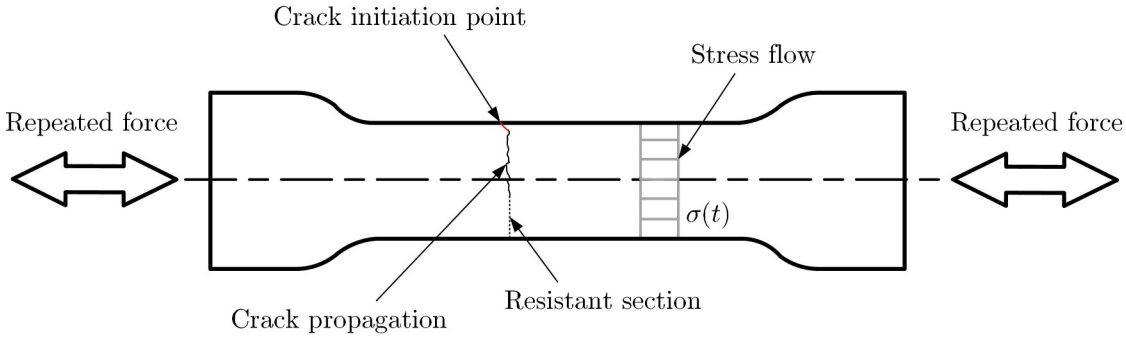

Figure 1.5: *Phenomenon of crack propagation on a specimen subjected to a tension-compression load*

To describe the fatigue phenomenon a metallic material specimen is considered (for example steel), as depicted in Fig. 1.5, repeatedly subjected to tension–compression load. After a certain number of cycles N, a first sign of damage occurs when a crack is initiated from the surface. After this initial phase has developed, as the tensile and compressive load cycles continue, the crack propagates in the orthogonal direction to the stress flow. The repeated action of the stresses causes a propagation until the resistant section is reduced to such an extent that it can no longer bear the maximum load of the stress, at which point a failure occurs. Fatigue phenomenon described above is very dangerous, in fact:

- Fracture occurs without any obvious warning signs, i.e. it is manifested in a brittle manner even in materials that prove to be ductile in a tensile test, such as steel.
- Fatigue failure occurs over time (just when the structure is considered tested).

80-90% of mechanical failures in operation occur through fatigue, hence the importance of these studies. Static failures are very rare and occur if the designer did something wrong during verification or the structure was subjected to excessive load.
As will be better seen in Ch. 6, in the following Fig. 1.6 it is possible to identify the three main phases involved in fatigue damage.
As can be seen, the first phase of fatigue damage is characterized by a smooth surface, i.e. there are no traces of plastic deformation that have altered the initial section of the specimen. The final resistance section presents a rough surface as can be easily verified in the static tensile test.

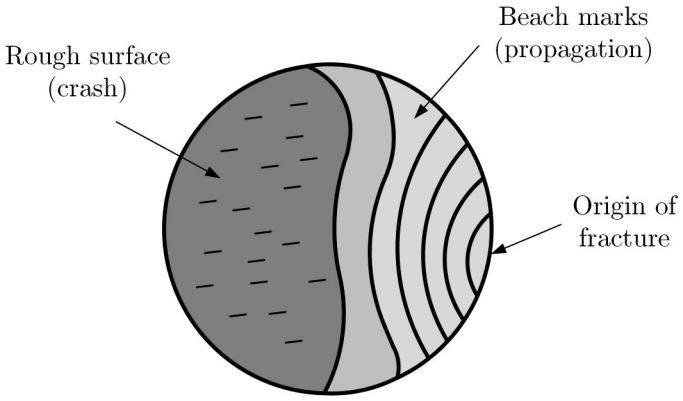

Figure 1.6: *The 3 phases of fatigue damage:initiation, propagation and failure*

1.3 Armonic load description

At the beginning a simple case of repeated stress over time is considered, ideal spectrum stress as shown in Fig. 1.7:

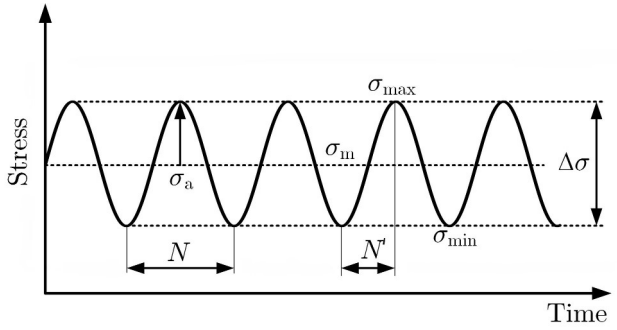

Figure 1.7: $\sigma = \sigma(t)$ *function [1]*

The meaning of the symbols are as follows [4]:

σ_a = Amplitude of stress
$\Delta\sigma$ = Range of stress
σ_{max} = Maximum stress
σ_{min} = Minimum stress
σ_m = Mean stress
N = Number of cycles
N' = Alternation

Another parameter of the stress sine wave is defined, that is stress ratio R:

$$R = \frac{\sigma_{min}}{\sigma_{max}} \tag{1.1}$$

The parameters mentioned above are linked to each other. In particular, for the stress range:

$$\Delta\sigma = \sigma_{max} - \sigma_{min} \tag{1.2}$$

and for the stress amplitude:

$$\sigma_a = \frac{\Delta\sigma}{2} = \frac{\sigma_{max} - \sigma_{min}}{2} \tag{1.3}$$

Knowing the mean stress σ_m and the stress amplitude σ_a it is possible to determine the maximum stress σ_{max} as:

$$\sigma_{max} = \sigma_m + \sigma_a \tag{1.4}$$

and the minimum stress σ_{min} as follow:

$$\sigma_{min} = \sigma_m - \sigma_a \tag{1.5}$$

Eq. 1.1 can be written as:

$$R = \frac{\sigma_m - \sigma_a}{\sigma_m + \sigma_a} \tag{1.6}$$

Referring to Fig. 1.8, the most commonly applied stress ratios in fatigue tests are $R = -1$ (fully reversed loading).

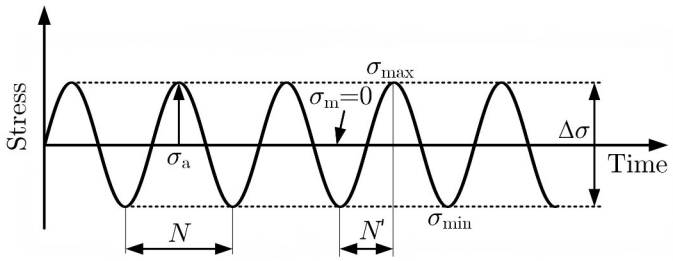

Figure 1.8: *Fully reversed loading with $R = -1$ [1]*

In this case $\sigma_m = 0$ and $\sigma_{min} = -\sigma_{max}$.

1.4 Characterisation of metallic materials at fatigue

As said before, in order to have fatigue phenomenon, time-varying stresses must be induced. To carry out fatigue tests on specimens, the stress cycle of Fig. 1.8 is initially applied, i.e. with a mean stress equal to zero in this case. A certain stress amplitude σ_a is set and, in the meantime, is necessary to count the number of cycles N_f that induce fracture. In this way on (σ_a, N_f) plane it is possible to individuate points. What is obtained, with a fit of the experimental points, is the Wöhler curve in Fig. 1.9.

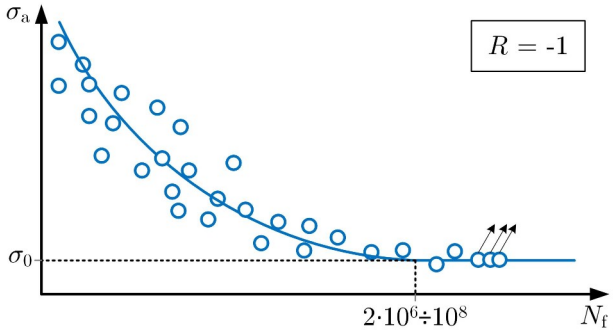

Figure 1.9: *Wöhler curve in linear scale*

In order to understand which stress has been applied, it is necessary to define a second parameter, called stress ratio R, shown at the top right of the graph in Fig. 1.9 ($\sigma_a = f(N_f)$). It can be seen that as the stress amplitude σ_a increases, the number of cycles to failure N_f decreases, i.e., the fatigue life decreases. Conversely, if the applied stress decreases, the fatigue life increases. By applying a certain stress level, a limit is reached beyond which the specimen does not break even after many millions of cycles, conventionally set at $2 \times 10^6 \div 10^8$ for steel, according to UNI 7670. These points are represented with an arrow. The trend obtained from the fit of the experimental data suggests a particular stress amplitude beyond which, theoretically, the life of the fatigue specimen is infinite. This stress level is so important for design that it is called the *fatigue limit* and is denoted by $\sigma_{a,\infty,-1}$, where a denotes the stress amplitude, ∞ denotes that the fatigue life is theoretically infinite and −1 is the stress ratio. To lighten this notation $\sigma_{a,\infty,-1}$

is equal to σ_0. It should be noted that there is some statistical scatter in the experimental results, so fatigue is a statistical phenomenon and this adds an additional danger factor.
Plotting the experimental points on a graph having linear scales, for a low number of cycles, the data cloud would be very compressed towards the *y*-axis equals to the stress amplitude σ_a. For this reason, the graph was reconstructed using logarithmic scales in base 10 of both axes. A set of points with an S-shaped trend and a mean fit curve interpolating the experimental data were obtained in Fig. 1.10.

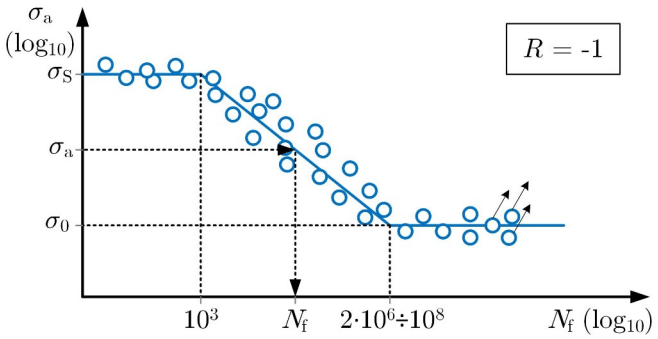

Figure 1.10: *Wöhler curve in log − log scale*

Considering a certain value of stress amplitude σ_a, it is possible to determine a number of cycles N_f that on average the specimens showed at failure. This means that in 50% of cases the specimens broke before crossing the mean curve and in 50% of cases other specimens broke after crossing the mean curve. This means that the curve plotted on the graph is a curve with 50% probability of survival. In this graph in logarithmic scales, it is possible to identify the fatigue limit σ_0 and the stress amplitude σ_S that leads to failure of the specimen at the first load cycle, i.e., for a stress ratio $R = -1$, equal precisely to the ultimate tensile strength σ_{UTS} of the material. To plot the curve in Fig. 1.10 typically a cylindrical specimen having a constant diameter of 10 mm, with a lapped surface and subjected to rotating bending tests was adopted, as shown in the scheme in Fig. 1.11.

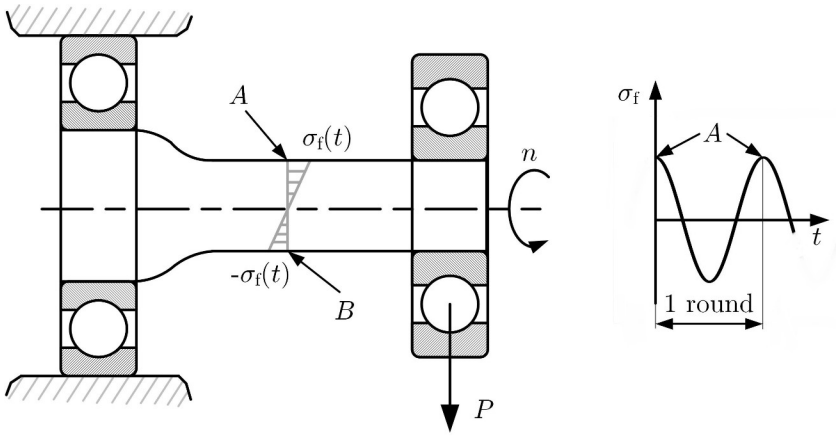

Figure 1.11: *Alternating bending test machine*

The specimen is supported by a left-hand bearing anchored to the frame of the testing machine. A weight P is applied to the right end through a second bearing, precisely on the outer ring. The specimen is driven with a number of revolution n. The weight results in a Navier's stress trend, where it is easily identified a point A subject to a bending stress σ_f and a point B subject to a bending stress equal to $-\sigma_f$. In the graph $\sigma = \sigma_f(t)$, starting from point A, integral to the test specimen, the stress goes from a positive value to a negative value and after one revolution it returns positive. In this case 1 cycle is equal to one revolution of the sample.

1.5 Effect of shape variation on fatigue

1.5.1 Static stress analysis and stress concentration factors

In Sec. 1.4 it was determined the fatigue curve of smooth specimens; in this way it was possible to obtain the fatigue limit σ_0 which is a property of the material. A generic mechanical component, however, has geometric variations and is used in different environments compared to a testing laboratory. To make the transition from a laboratory specimen to the real component, a number of parameters must be taken into account. Performing this step allows to translate the Wöhler curve of the base specimen (smooth) to the Wöhler curve of a generic mechanical component under real operating conditions. An important internal parameter that affects fatigue life takes into account changes in the shape of a component. As an example, a plate subjected to a fatigue load is taken as reference in Fig. 1.12a. It is smooth because its rectangular cross section is constant along the entire length of the specimen. To introduce a shape variation, its section can be perturbed by introducing a hole, Fig. 1.12b. The hole alters the smooth shape of the plate, i.e. the rectangular cross section is no longer constant with a certain width W and thickness t.

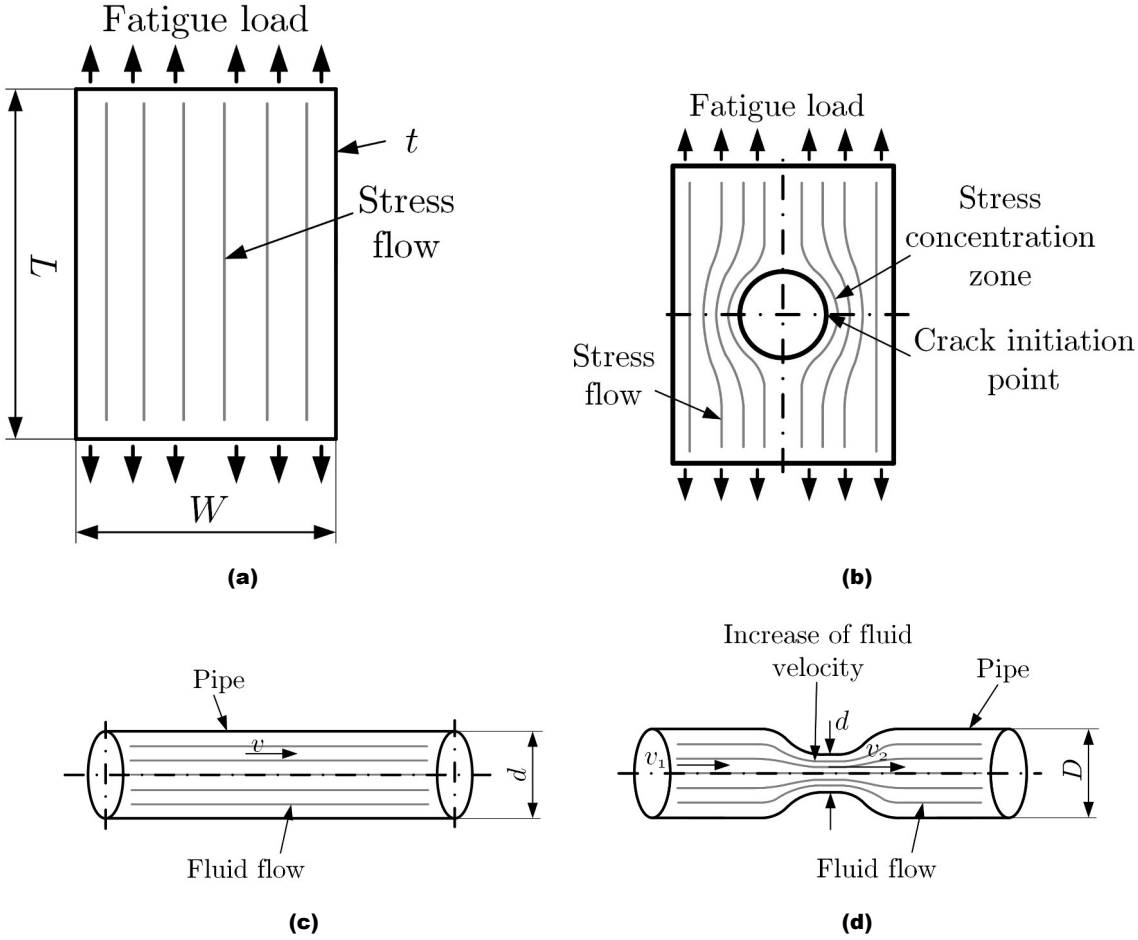

Figure 1.12: *Effect of shape variation and hydrodynamic analogy*

In the smooth plate, the stress σ flow lines run parallel, like the fluid flow lines of a fluid inside a pipe in Fig. 1.12c. Following the hydrodynamic analogy, the fluid flow lines inside a pipe in Fig. 1.12d are forced to deflect. From the fluid dynamic point of view a shrinkage of the section from a diameter equal to D to a diameter equal to d causes an increase in fluid velocity from v_1 to v_2. A completely equivalent situation also occurs in the drilled plate where, in the vicinity of the hole, the stress flow lines are forced to bypass the obstacle and this, from a tensional point of view, alters the path of the stress flow lines. Locally there is a stress increase and this has an effect on fatigue strength.
Initially, to better understand the effect that a change in shape has on the fatigue life of a component, the stress field near the hole was analyzed from a static point of view. The plate with hole in Fig. 1.13 has width W and hole diameter equal to ϕ.

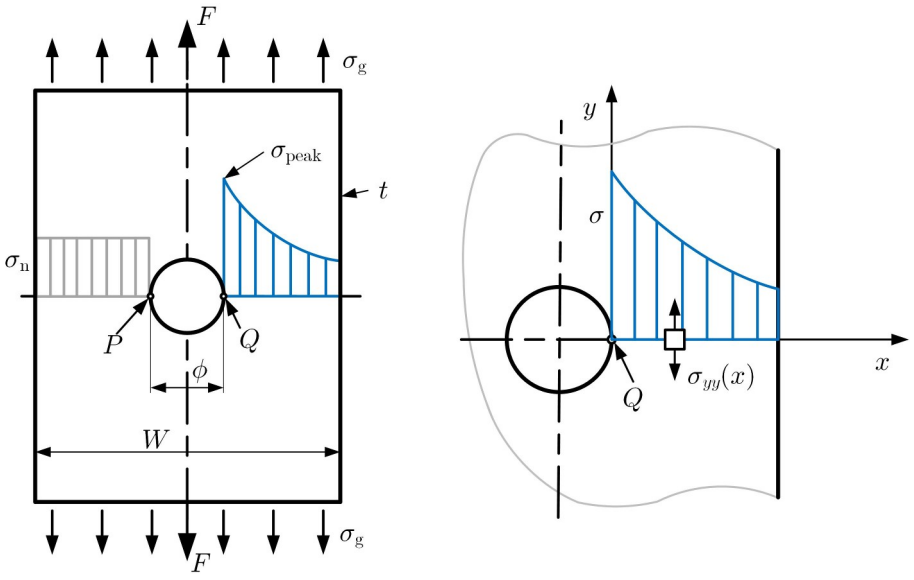

Figure 1.13: *Stress concentration effect on a flat-bar with a hole*

The hole causes increased stress in the vicinity of points *P* and *Q*. Any alteration in shape, which causes a concentration of stress, is called *notch*. The effect of stress concentration is called the *notch effect*, and the point at which the maximum stress occurs is called the *notch tip*. Stress far from the hole is defined as the gross nominal stress σ_g

$$\sigma_g = \frac{F}{A_g} = \frac{F}{W t} \tag{1.7}$$

where F is the force acting on the rectangular section of the plate and A_g is the gross area of the section and it is equal to $A_g = W t$. Along the horizontal axis of the hole, another reference tension is defined called net nominal tension σ_n

$$\sigma_n = \frac{F}{A_n} = \frac{F}{(W - \phi)t} \tag{1.8}$$

where A_n is the net area and it is equal to $A_n = (W - \phi)t$. σ_n is greater than σ_g because A_n is lower than A_g. In reality, the stress at the net section is not uniform at all, but increases progressively towards the tip of the notch. The stress field has a peak at the apex of the notch and then, with some gradient, decreases. Under the assumption of linear elastic material behavior, the stress peak is denoted as σ_{peak}. The blue area must be equal to the gray area, in fact, considering a reference system that originates at the tip of the notch:

$$F = \int_0^{\frac{W}{2} - \frac{\phi}{2}} \sigma_n t dx = \int_0^{\frac{W}{2} - \frac{\phi}{2}} \sigma_{yy}(x) t dx \tag{1.9}$$

To quantitatively describe the stress concentration effect, theoretical stress concentration factors were defined as follows:

$$K_{t,n} = \frac{\sigma_{peak}}{\sigma_n} \tag{1.10}$$

if it is referred to the nominal net stress σ_n, and:

$$K_{t,g} = \frac{\sigma_{peak}}{\sigma_g} \tag{1.11}$$

if it is referred to the nominal gross stress σ_g. There is a link between the two factors, in fact:

$$\sigma_{peak} = K_{t,n} \cdot \sigma_n = K_{t,g} \cdot \sigma_g \tag{1.12}$$

and then

$$\frac{K_{t,g}}{K_{t,n}} = \frac{\sigma_n}{\sigma_g} = \frac{A_n}{A_g} \tag{1.13}$$

It can be guessed from these relationships that the stress concentration factors K_t depend on the geometry of the component and the loading mode. The stress concentration factors for various structural details are collected in handbooks, e.g. Peterson's [41], in the form of diagrams. An example of a diagram is depicted in Fig. 1.14

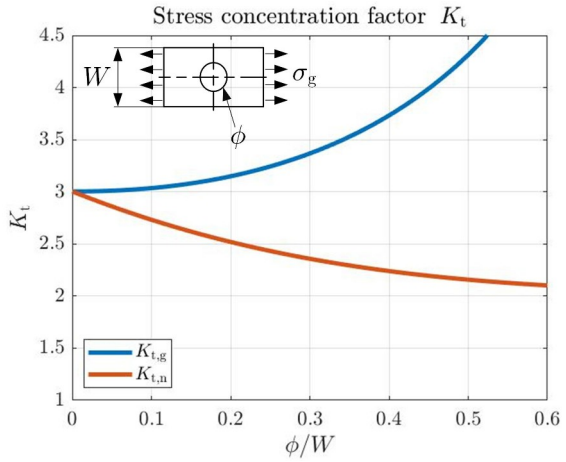

Figure 1.14: *Peterson's diagram of $K_t = f(\phi/W)$ [41]*

If the structure or the structural detail are more complex, a finite element analysis is used.

1.5.2 Example of stress concentration factor determination

In this subsection, a simple finite element analysis is presented to determine the stress concentration factor. As has been seen, K_t can be determined through graphs provided by Peterson or [41], or through numerical methods, as in this case. The following flat-bar with a hole in Fig. 1.15 is subjected to a fatigue load fluctuating between $+F$ and $-F$.

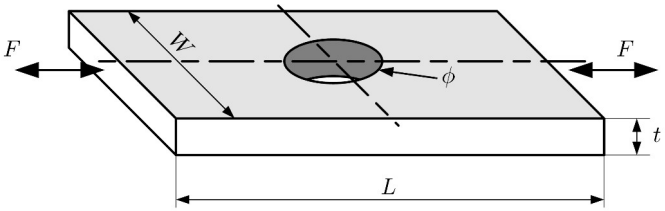

Figure 1.15: *Analyzed flat-bar with hole*

In this case $F = 100\ N$, $W = 45\ mm$, $L = 150\ mm$ $t = 10\ mm$ and $\phi = 15\ mm$. This exercise has been carried out by means of the ansys® calculation code. Since the thickness $t << \overline{W\,L}$ a 2D analysis was performed to simplify the problem. The analysis started from the Pre-Processor environment. The element type has been defined with the following commands: Element type - Add/Edit/Delet - Solid - Quad 4 Node 182. Through the Option has been set a K1 on simple enhanced strn and a K3 on plane stress with thickness. The material was set up using the commands: Material Props - Material Models - Structural - Linear - Elastic - Isotropic and the Young's modulus $E = 206000\ MPa$ and Poisson's coefficient $\upsilon = 0.3$ have been inserted. The thickness was set using the following commands: Real constants - Add/Edit/Delet - Add - Ok. These three screens are shown in Fig. 1.16.
Later, geometry was created using the following commands: Modeling - Create - Areas - Rectangle - By dimensions. In the window the coordinates of the points have been inserted, following the scheme in Fig. 1.17. The following commands were used to create the hole: Circle - By dimensions to create the circle and Booleans - Substract - Areas to subtract the excess area from the flat-bar. As can be seen, only 1/4 plate was modeled to take advantage of the symmetry conditions and not to engage the software with unnecessary computational operations.

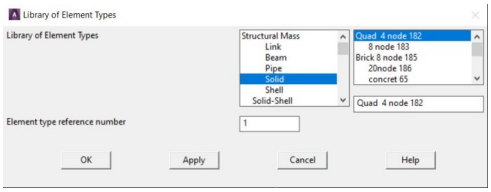

(a) *Element type*

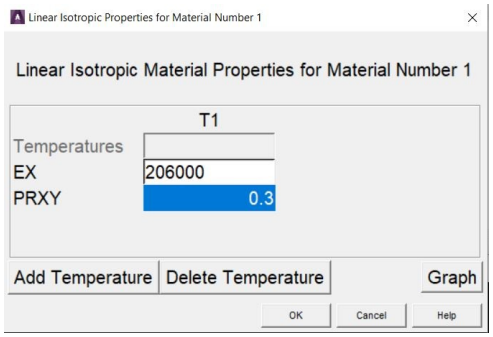

(b) *Material properties*

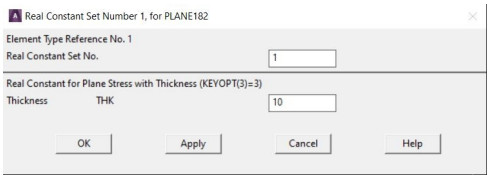

(c) *Thickness t equal to 10 mm*

Figure 1.16: *Element type and material definition*

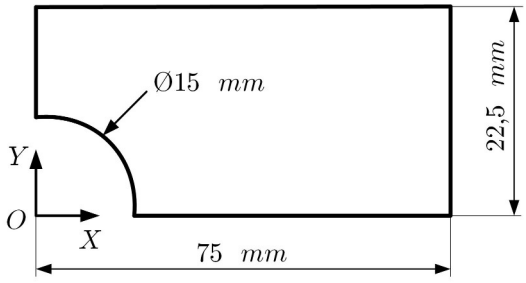

Figure 1.17: *Modeled geometry in* ansys®

In the next step, the mesh was created through the following operations: Mesh - Size cntrls - Manualsize - Lines - Picked lines to set the number of subdivisions or the size of the elements (with also the Spacing Ratio command to thicken the hot zone) and Flip bias to reverse the thickening zone, if necessary. On Mesh - Areas - Free a free mesh was created. Fig. 1.18 shows the mesh.

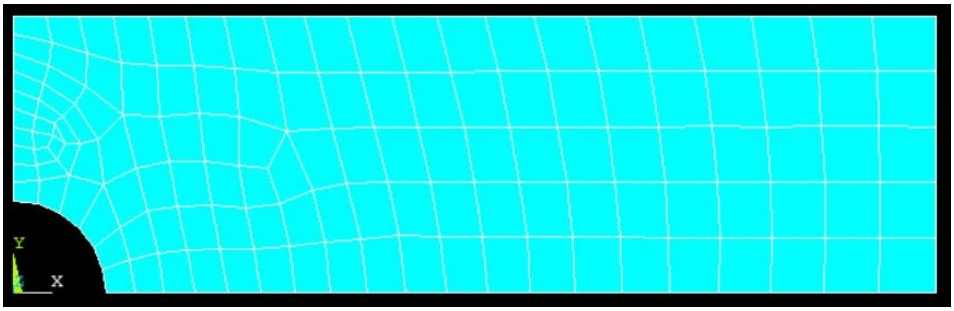

Figure 1.18: *Free mesh of flat-bar*

The boundary conditions were applied with the commands: Loads - Define loads - Apply - Structural - Displacement - Symmetry B.C. and the load with the following commands Pressure - On lines. Symmetry conditions impose carriage constraints along X that block U_Y displacements and along Y that lock U_X displacements, as shown in Fig. 1.19

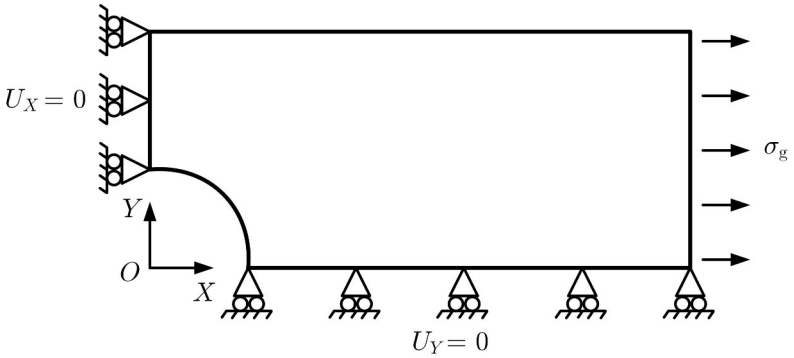

Figure 1.19: *BCs and load*

a gross stress σ_g was applied equal to:

$$\sigma_g = \frac{F}{2 \cdot \frac{W}{2} \cdot t} = \frac{F}{W t} = \frac{100}{45 \cdot 10} = 0.222 \text{ MPa} \tag{1.14}$$

The nominal stress σ_n on the net section is:

$$\sigma_n = \frac{(F)}{2 \cdot \left(\frac{W}{2} - \frac{\phi}{2}\right) \cdot t} = \frac{(F)}{2 \cdot \frac{W-\phi}{2} \cdot t} = \frac{F}{(W-\phi)t} = \frac{100}{(45-15) \cdot 10} = 0.333 \text{ MPa} \tag{1.15}$$

To apply the definitions from Eq. (1.10) and Eq. (1.11), $\sigma_{peak} = ?$, if necessary. Through the Post-Processor environment it was possible to determine the peak stress with Plot results - Contour plot - Nodal solution - 1st Principal Stress commands.
It was possible to derive the stress plot in Fig. 20 and the diagram representing the stress field along the net section as in Fig. 1.21 with the following commands: Paths - Operations - Define Path - By Nodes and Map Onto Path - S1.
The peak stress is determined by reading the value at $x = 0$, $\sigma_{peak} = 0,7676\ MPa$. The following analytical expressions of K_t for a flat-bar with a hole, have been derived from the Peterson handbook [41]:

$$K_{t,g} = 0,284 + \frac{2}{1 - \frac{\phi}{W}} - 0,600 \cdot \left(1 - \frac{\phi}{W}\right) + 1,32 \cdot \left(1 - \frac{\phi}{W}\right)^2 \tag{1.16}$$

$$K_{t,n} = 2 + 0,284 \left(1 - \frac{\phi}{W}\right) - 0,600 \cdot \left(1 - \frac{\phi}{W}\right)^2 + 1,32 \cdot \left(1 - \frac{\phi}{W}\right)^3 \tag{1.17}$$

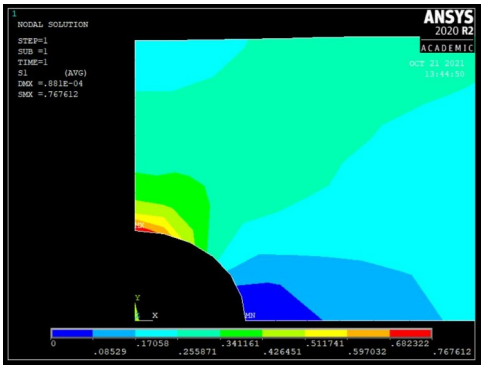

Figure 1.20: *1st principal stress plot*

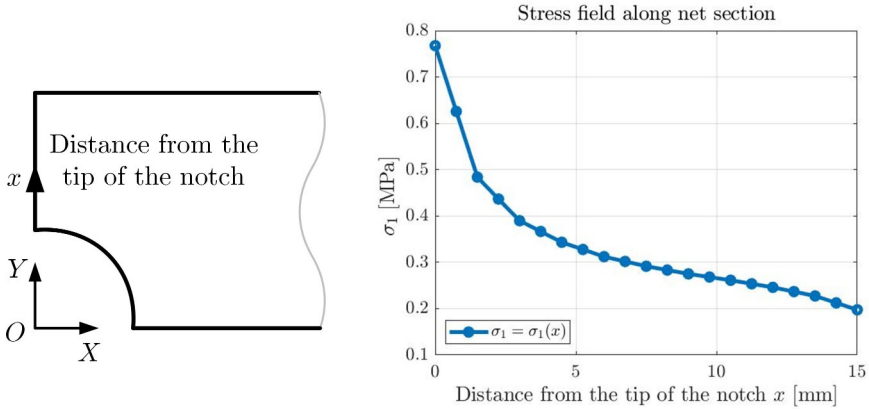

Figure 1.21: *1st principal stress field as a function of distance x*

In this case $K_{t,g} = 3,47$ and $K_{t,n} = 2,31$. Instead, below, the definitions from Eq. 1.10 and Eq. 1.11 were applied:

$$K_{t,g,FEM} = \frac{\sigma_{peak}}{\sigma_g} = \frac{0,767}{0,222} = 3,45 \tag{1.18}$$

$$K_{t,n,FEM} = \frac{\sigma_{peak}}{\sigma_n} = \frac{0,767}{0,333} = 2,30 \tag{1.19}$$

Between finite element method and Peterson's diagram were obtained errors equal to:

$$\Delta_{g,\%} = \frac{K_{t,g} - K_{t,g,FEM}}{K_{t,g}} \cdot 100 = \frac{3,47 - 3,45}{3,47} \cdot 100 = 0,57\% \tag{1.20}$$

$$\Delta_{n,\%} = \frac{K_{t,n} - K_{t,n,FEM}}{K_{t,n}} \cdot 100 = \frac{2,31 - 2,30}{2,31} \cdot 100 = 0,43\% \tag{1.21}$$

results, from an engineering point of view, more than acceptable.

1.5.3 Fatigue strength behavior

In the previous section, the theoretical stress concentration factor K_t was obtained using two methods: through the Peterson's diagrams and through a finite element analysis. At this point, the effect of shape variation on fatigue strength was considered by taking the flat-bar in Fig. 1.12a and Fig. 1.12b. The Wöhler curve was derived for both the smooth (or material) and notched specimen, as shown in Fig. 1.22 below.

At the fatigue limit, the K_f factor was introduced as:

$$K_f = \frac{\sigma_0}{\sigma_{0,n}} \tag{1.22}$$

where $\sigma_{0,n}$ is the fatigue limit of the notched component referred to the net section. Since the stress field near the notch is not uniform, an elastic peak stress was identified. In this case, when the

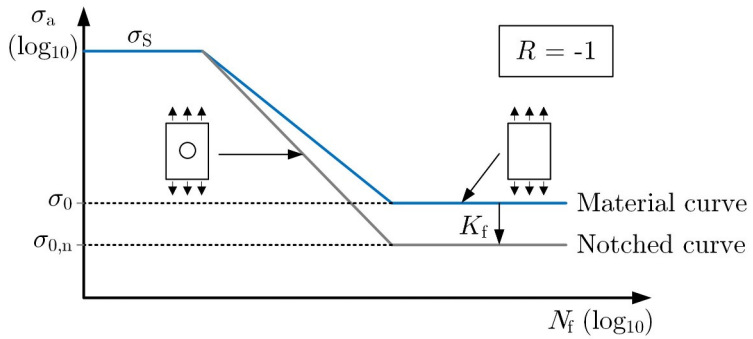

Figure 1.22: *Wöhler curve of material and notched specimen [4]*

point most stressed by fatigue comes to undergo a stress amplitude equal to the material property, here is where the crack begins to propagate. This condition occurs when:

$$\sigma_{0,peak} = \sigma_0 \tag{1.23}$$

where $\sigma_{0,peak}$ is the peak stress amplitude at the fatigue limit. From equation 1.10 it is possible to write:

$$K_{t,n}\sigma_{0,n} = \sigma_0 \tag{1.24}$$

whence:

$$\sigma_{0,n} = \frac{\sigma_0}{K_{t,n}} \tag{1.25}$$

Comparing Eq. 1.25 with Eq. 1.22 it is possible to state that $K_f = K_{t,n}$. Experimental results have shown that in fact $K_f \leq K_{t,n}$. In design, Peterson's expression is often used:

$$K_f - 1 = q \cdot (K_{t,n} - 1) \tag{1.26}$$

where q is the notch sensitivity factor modulating the relationship between K_f and $K_{t,n}$. According to Eq. 1.26, q is defined as:

$$q = q(\rho) = \frac{1}{1 + \frac{a^*}{\rho}} \tag{1.27}$$

The following three cases can be distinguished:

- $q = 0$: zero notch sensitivity, i.e. for each value of $K_{t,n}$ the fatigue factor is $K_f = 1$. Even in the presence of a stress-concentrator, this has no effect from the fatigue point of view.
- $0 < q < 1$: partial notch sensitivity, it can be observed that $1 < K_f < K_{t,n}$.
- $q = 1$: full notch sensitivity, i.e. $K_f = K_{t,n}$.

The index q varies in a range between 0÷1 and thus it weights the stress concentration effect described by $K_{t,n}$, which only highlights the static stress reality, to assess what is the true effect of stress concentration on fatigue strength. To solve a mechanical design problem, a^* is a function of the ultimate tensile stress of the material, i.e. $a^* = f(\sigma_{UTS})$ and can be found in the literature. It is possible to see the function $q = q(\rho)$ in Fig. 1.23.

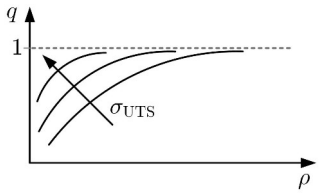

Figure 1.23: *Notch sensitivity factor as a function of radius*

Chapter 2

CRITICAL DISTANCES APPROACH

In this chapter the theory of critical distances will be described. This approach is based on the foundations built by Neuber arounf 1950 and its aim is to evaluate fatigue strength in a simple way, by means of a linear elastic stress distribution near the apex of the notch in any mechanical component [38].

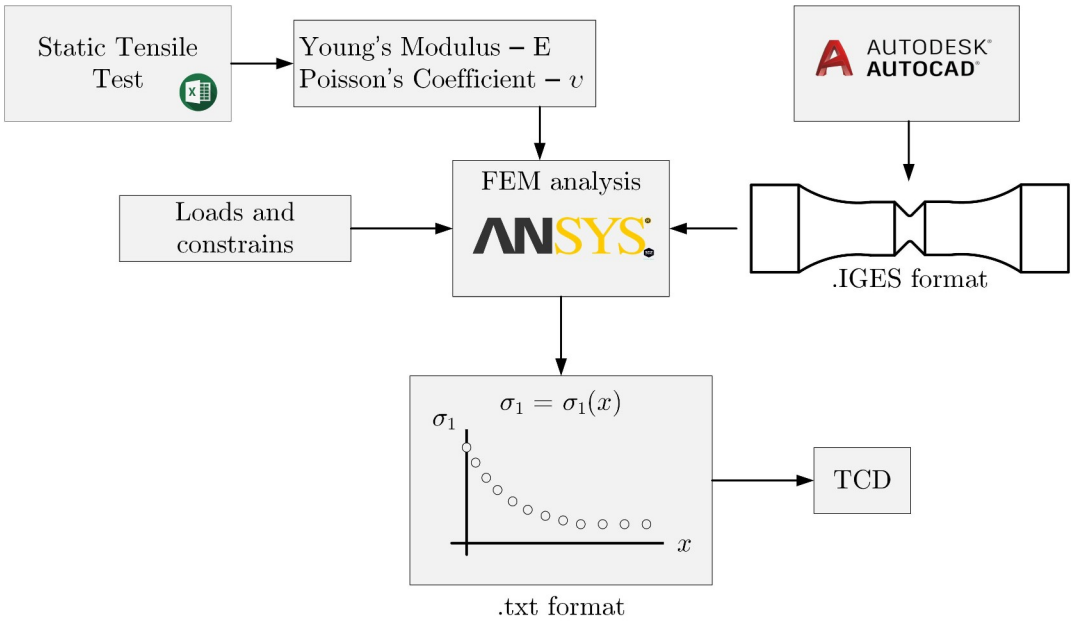

Figure 2.1: *Sketch of input parameters for the TCD method*

From the static tensile test (see Ch. 5) the material properties were determined as input parameters for the FE analysis. With the help of autocad ®, the geometry was imported into the structural analysis software and the load and constraint conditions were entered. The output is the maximum principal stress which was used to apply the method (Fig. 2.1).

2.1 Neuber's consideration on the shape variation effect

As said in the previous chapter, experimental reality highlights the fact that $K_f \leq K_t$. To explain why the experiment deviates from theory, in the 1950s, German professor H. Neuber, introduced the concept of structural volume to interpret fatigue strength in the presence of notch effects [38]. He asserted that fatigue failure is determined not so much by the maximum point stress that occurs at the surface of the component, but by the local stress σ^- averaged in some structural volume δ whose size is a property of the material. Taking as reference a notch (Fig. 2.2) on a mechanical component subject to an external load that produces fatigue, to see if the crack propagates it is necessary to study the stress level averaged in δ.

At the fatigue limit of the notched component, the following condition must occur:

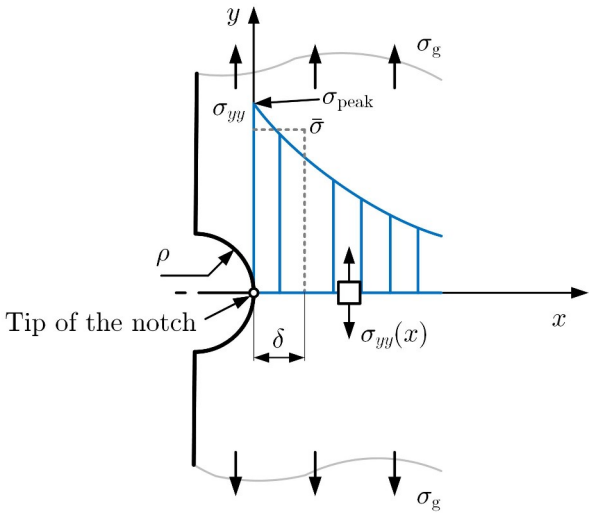

Figure 2.2: *Neuber's considerations [38]*

$$\bar{\sigma_0} = \sigma_0 \tag{2.1}$$

i.e. the stress amplitude averaged in the structural volume, at fatigue limit, must be equal to σ_0. At this point, when the notch is blunt, it can be inferred, from the numerous graphs provided by Peterson, that the theoretical stress concentration factor $K_{t,n}$ is quite low and therefore the stress field gradient is modest (Fig. 2.3). It can be concluded that the peak stress σ_{peak} obtained at the tip of the notch is not that different from the stress averaged in the structural volume $\bar{\sigma}$, viz:

$$\bar{\sigma} \approx \sigma_{peak} \tag{2.2}$$

At fatigue limit, from equation 2.1, and considering 2.2:

$$\sigma_{peak,0} = \sigma_0 \tag{2.3}$$

where $\sigma_{peak,0}$ is the peak stress at fatigue limit. From definition 1.10:

$$K_{t,n}\,\sigma_{n,0} = \sigma_0 \tag{2.4}$$

With a smaller fillet radius ρ the equation 2.4 is too conservative, in fact, in this situation $K_{t,n}$ is higher than the previous case and this causes a high stress gradient. In this case, it is necessary to state that the stress averaged in the structural volume is less than the peak stress, as shown in Fig. 2.4. This Fig. 2.4. the transition from nominal net stress to $\bar{\sigma}$, must occur with a coefficient K_f that is damped relative to $K_{t,n}$. The reason for this consideration can be easily seen in the Fig. 2.4 where it can be noticed that $K_{t,n}$ allows the transition from the nominal net stress to the peak stress, a passage that is far too pronounced since the goal is to arrive at the stress averaged in the structural volume which is less than the peak stress. Through these considerations it is possible to develop the first member of equation 2.4 by writing K_f instead of $K_{t,n}$, as follows:

$$K_f\,\sigma_{n,0} = \sigma_0 \tag{2.5}$$

From Neuber's idea, a series of more advanced theories for evaluating the fatigue strength of notched mechanical elements were developed.

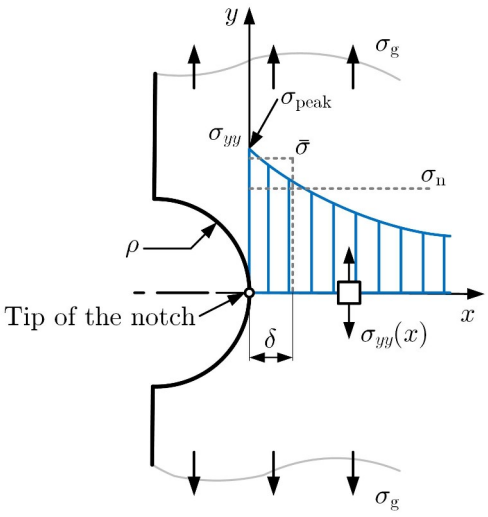

Figure 2.3: *Blunt notch [38]*

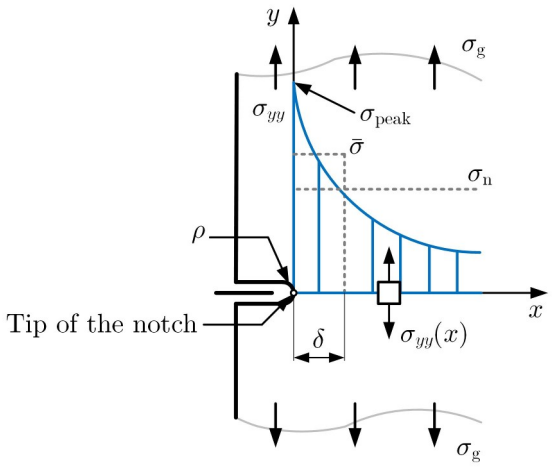

Figure 2.4: *Notch with small radius [38]*

2.2 The theory of critical distances

As Taylor maintains [51][50], critical distance theory (TCD) is the name given to a group of theories used to predict the notching effects [31][29][51][47]. The first attempt to use TCD in fatigue strength determination was made by Neuber in Germany, in the 1950s. Based on the considerations made in Section 2.1, Neuber proposed that the fatigue limit of a component containing a notch can be predicted using the average stress calculated along a line drawn from the tip of the notch to a length that is a property of the material. His approach was expressed as follows:

$$\frac{1}{\epsilon}\int_0^{\epsilon} \Delta\sigma(x)\mathrm{d}x = \Delta\sigma_0 \tag{2.6}$$

Where ϵ is the distance up to which the integral calculation is performed, $\Delta\sigma(x)$ is the stress field as a function of distance from the apex of the notch and $\Delta\sigma_0$ is the fatigue limit range of unnotched specimen. This method has been formalized as the *Line Method* (LM) and states that a real notched component is in its fatigue limit when the mean integral of the stress field from the tip of the notch to a length ϵ is equal to the range of the fatigue limit of the material. Later, Peterson proposed a simplified approach formalized as the *Point Method* (PM) expressed as:

$$\Delta\sigma(x_c) = \Delta\sigma_0 \tag{2.7}$$

where x_c is the distance at the apex notch from which the stress is taken. PM states that a component with a notch is in its fatigue limit when the stress taken at a certain distance equals the fatigue limit of the material [10][3].
These two formulations at the time presented a not insignificant problem: the determination of the notch-tip stress distribution $\Delta\sigma(x)$. Therefore, through the fit of numerous experimental data, Neuber proposed the following empirical expression:

$$K_f = 1 + \frac{K_{t,n} - 1}{1 + \sqrt{\frac{a^*}{\rho}}} \tag{2.8}$$

and Peterson the following one:

$$K_f = 1 + \frac{K_{t,n} - 1}{1 + \frac{a'}{\rho}} \tag{2.9}$$

Moreover, in the above relationships, ρ is the notch root radius, a^* and a' are two critical distance constants [48].

2.3 Critical distances theory applied to high-cycle fatigue

The critical distance theory assumes that the stress distribution near stress concentrator is necessary to correctly assess fatigue damage. With the advent of the finite element method today it is possible to develop more refined calculations and use the original expressions. According to the TCD, notched components are in their fatigue limit condition when the effective stress, $\Delta\sigma_{\text{eff}}$, which depends on the maximum principal stress distribution ahead of the tip of the notch, equals the reference material streng $\Delta\sigma_{\text{ref}}$ [18][8]:

$$\Delta\sigma_{\text{eff}} = \Delta\sigma_{\text{ref}} \tag{2.10}$$

Initially, the critical distance is defined by El-Haddad from LEFM [12]. In particular, according to the linear-elastic TCD, the material characteristic length, L, can be calculated as follows:

$$L = \frac{1}{\pi}\left(\frac{\Delta K_{\text{th}}}{\Delta\sigma_0}\right)^2 \tag{2.11}$$

where ΔK_{th} is the range of the threshold value of the stress intensity factor and $\Delta\sigma_0$ is the range of the fatigue limit (both determined under the same load ratio, R). L is, therefore, also a property of the material. A component, according to TCD-LM, is in the fatigue limit condition when the following condition is assured:

$$\Delta\sigma_{\text{eff}} = \frac{1}{2L}\int_0^{2L} \Delta\sigma_1(\theta = 0, r)\mathrm{d}r = \Delta\sigma_0 \tag{2.12}$$

i.e. when the range of the maximum principal stress, averaged over a distance from the apex of the notch of $2L$, equals the range of the reference stress of the material. With high-cycles fatigue problem the reference material strength is equal to the plain fatigue limit, i.e. $\Delta\sigma_{\text{ref}} = \Delta\sigma_0$. Fig. 2.5 is taken as a reference for the symbology used in the Eq. 2.12 and Eq. 2.13.

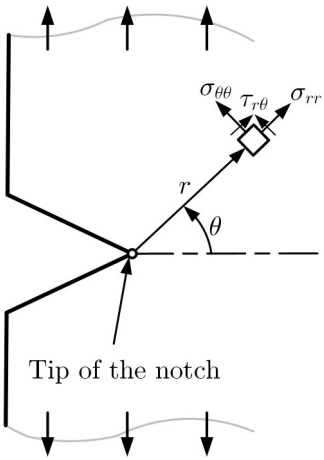

Figure 2.5: *Adopted sumbology for the TCD application [49]*

The formalisation of the TCD-PM, on the other hand, is written as follows:

$$\Delta\sigma_{\text{eff}} = \Delta\sigma_1\left(\theta = 0, r = \frac{L}{2}\right) = \Delta\sigma_0 \tag{2.13}$$

and states that a notched component reaches its fatigue limit when a certain stress, taken at a distance $L/2$, equals the fatigue limit of the material. Fig. 2.6 graphically shows how the line method and the point method work.

For information purposes, there are additional formulations of TCD. Taylor revived an idea suggested by Sheppard, namely that the effective stress can be calculated by averaging the range of the maximum principal stress over a semicircular area. This method has been formalised as the *Area Method* (AM), Fig. 2.7 and is defined as follows:

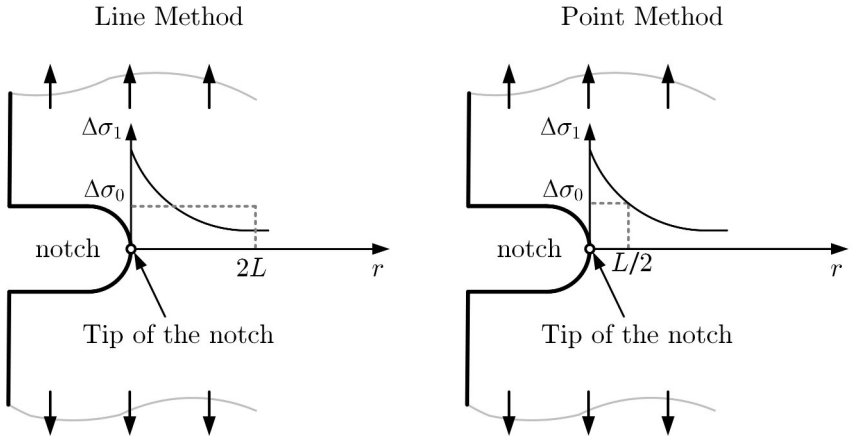

Figure 2.6: *Line Method and Point Method formalisation [48]*

$$\Delta\sigma_{\text{eff}} = \frac{4}{\pi L} \cdot \int_{-\pi/2}^{\pi/2} \int_{0}^{L} \Delta\sigma_1(\theta, r) \cdot \mathrm{d}r \cdot \mathrm{d}\theta \approx \Delta\sigma_0 \tag{2.14}$$

Finally, it is worth recalling here that, according to Bellett et al., the range of the effective stress can alternatively be calculated by averaging the range of the first principal stress, $\Delta\sigma_1$, in a hemisphere centred at the apex of the stress raiser and having radius equal to $1.54L$: this is known as the *Volume Method* (VM).

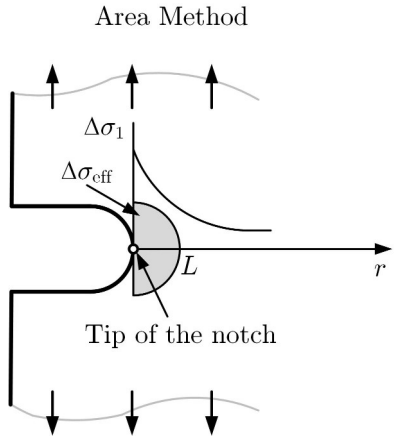

Figure 2.7: *Area method formalisation [29]*

2.4 Critical distances theory applied to medium-cycle fatigue

Given the remarkable accuracy achieved by the theory of critical distances in predicting fatigue failure at high cycle regime [49], its version for medium cycle fatigue was also implemented. The results achieved with the application of TCD in static, medium and high cycle fatigue are really interesting considering the fact that only a linear stress distribution, obtained through a simple FEM analysis, is required in the vicinity of the notch. In the previous paragraph, it was mentioned that the most successful formulation of TCD postulates that an effective stress, calculated in various ways, must equal a stress taken as a reference. If TCD is used to predict static failure then the characteristic length of material to be used is as follows [49]:

$$L_S = \frac{1}{\pi}\left(\frac{K_{Ic}}{\sigma_{ref}}\right)^2 \tag{2.15}$$

where K_{Ic} is the plane strain fracture toughness and σ_{ref} is a reference stress which in many cases is equal to ultimate tensile strenght of the material σ_{UTS}. The formalisation of the line method, in statics, takes the following form:

$$\Delta\sigma_{eff} = \frac{1}{2L_S}\int_0^{2L_S} \Delta\sigma_1(\theta = 0, r)\mathrm{d}r = \Delta\sigma_{ref} \tag{2.16}$$

while for the point method:

$$\Delta\sigma_{eff} = \Delta\sigma_1\left(\theta = 0, r = \frac{L_S}{2}\right) = \Delta\sigma_{ref} \tag{2.17}$$

In general, the characteristic lengths of the material, respectively L_S for static problems and L for high-cycle fatigue, have different values. For finite-life applications, this length will vary as the number of cycles to failure varies and therefore L, renamed L_M in this field, will be a function of N_f. There are two approaches to determining this function:

- A classical approach using material properties in static and high-cycle fatigue.
- Reversed point method with two calibration curves, the first one from smooth specimen and the second one from notched specimen.

Before going into more detail, it is necessary to understand what kind of function was used to achieve the aim. Knowing that, in accordance with the schematisation of the Wöhler curve, the relationship between the stress amplitude and the number of cycles to failure is a power function, a similar relationship was also determined between L_M and N_f, viz:

$$L_M(N_f) = AN_f^B \tag{2.18}$$

The following sub-sections describe the two methods for determining the function written above.

2.4.1 Determination of the functional relationship between L and N_f using the classical approach

The first method that has been developed to determine the constants A and B of function $L_M = L_M(N_f)$ is based on the use of material properties given by static and dynamic loading. The Wöhler curve of a smooth specimen, generated with a cycle ratio R of and with reference to the nominal stress amplitude (Fig. 2.8), is considered to derive the fatigue limit of the material σ_0 and the stress that leads to static failure of the specimen related to the UTS by the following relation:

$$\sigma_S = \frac{(1 - R)}{2} \cdot \sigma_{UTS} \tag{2.19}$$

Specific to the case in this thesis work $\sigma_S = \sigma_{UTS}$.

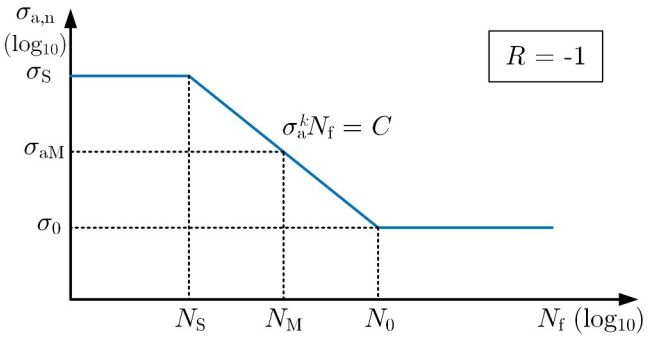

Figure 2.8: *Application of TCD in its classical formulation in MCF [49]*

The following system of two equations in two unknowns can be written:

$$\begin{cases} L_S = AN_S^B \\ L = AN_0^B \end{cases} \tag{2.20}$$

which provides the following solutions:

$$B = -\frac{\log\left(\frac{L_S}{L}\right)}{\log\left(\frac{N_0}{N_S}\right)} \tag{2.21}$$

$$A = L N_0^{-B} \tag{2.22}$$

From a theoretical point of view, this procedure is correct if N_0 and N_S have been precisely determined. In practice, due to statistical scatter, the calibration of the equation Eq. 2.18 is, most of the time, not adequate enough to predict notch effects in the finite-life range. In addition, many different tests are required to derive the necessary material properties and this may lead to increased costs within a production process [49].

2.4.2 Determination of the functional relationship between L and N_f using calibration curves

Two curves were considered for the application of this second approach: the smooth and the notched specimens curve (Fig. 2.9). The two curves shown were determined using statistical techniques described in Ch. 5. The point method can be used to derive the critical distance following an inverse path, at any given number of cycles to failure. Referring to Fig. 2.9, the stress profile acting in the vicinity of the notch due to an external load, $\sigma_{a,g}$, at a number of cycles equal to N_f was determined. The stress applied to the smooth specimen, at the same number of cycles as previously assumed, was used as input data to determine the corresponding critical distance, $L(N_f)/2$, by crossing the diagram $\sigma_1 = \sigma_1(r)$.

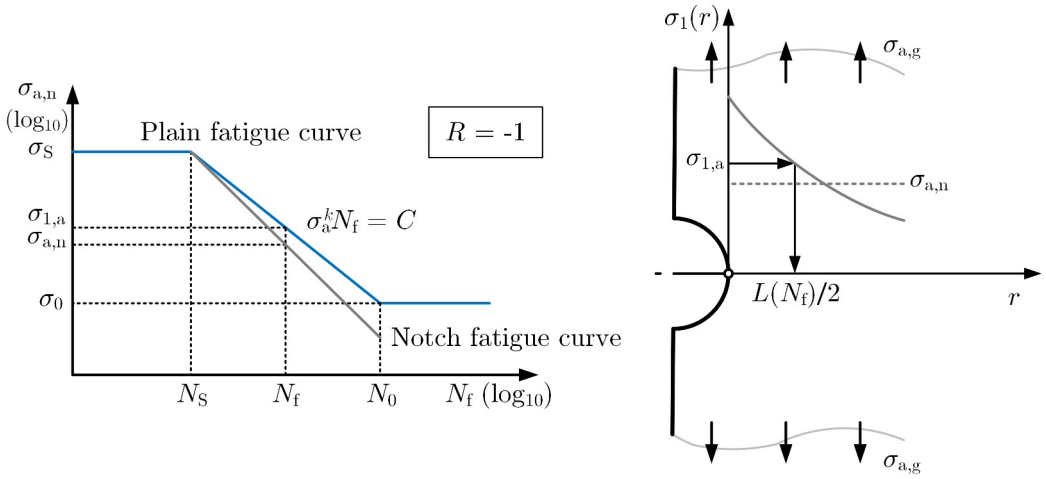

Figure 2.9: *Application of TCD with two calibration curves in MCF [49]*

If this is done for any two or more values of N_f, the constants in Eq. 2.18 can be found. This method is statistically consistent and this is advantageous compared to the approach defined in Sec. 2.4.1 [49].

Chapter 3

RELATIVE STRESS GRADIENT APPROACH

In this chapter, the stress gradient method will be addressed from the perspective of the femfat® software and the FKM guidelines. Given the simplicity of linear analysis using the FE method, the starting point is always the same: the determination of the stress field near the tip of the notch. The approach according to femfat® requires the determination of the equivalent Von Mises stress distribution [13], whereas the approach followed by FKM requires the maximum principal stress distribution [15].

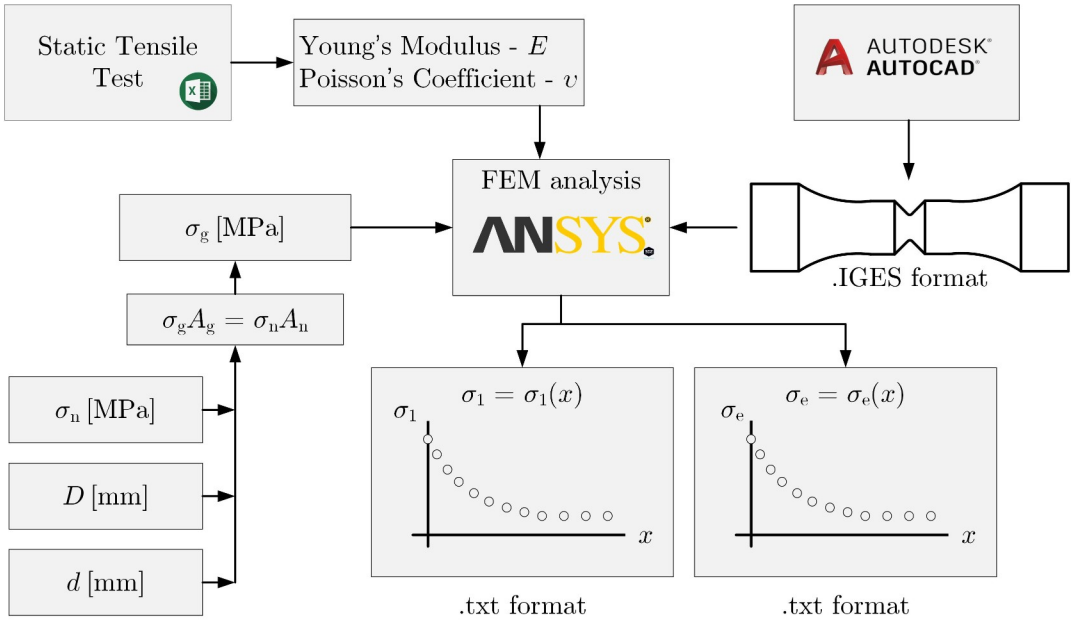

Figure 3.1: *Example of sketch input parameters for the RSG method*

After setting the appropriate load and constraint conditions, Von Mises $\sigma_e = \sigma_e(x)$ and first principal stress $\sigma_1 = \sigma_1(x)$ were obtained using a .txt file. These two curves, derived by points, are the input for the two methods described in this thesis work.

3.1 Theory implemented on FEMFAT

Fatigue life estimation of notched components in femfat® , is based on the use of influence factors. They take into account effects related to stress gradient, mean stress, surface condition, and other effects that have not been mentioned. In this work, only the effect due to the stress gradient will be analyzed. The focus on notching effects has been, over the years, to the mathematical formalisation of the thought that fatigue strength depends not only on the maximum stress acting on the tip of the stress concentrator but also on the relative stress gradient [36]. A local approach has been defined because it is based

on the analysis of the stress state in the vicinity of the notch. In this region, which is of most interest, the corresponding local S-N curve was output, which is described, using a log-log graph, by the following three parameters (Fig. 3.2):

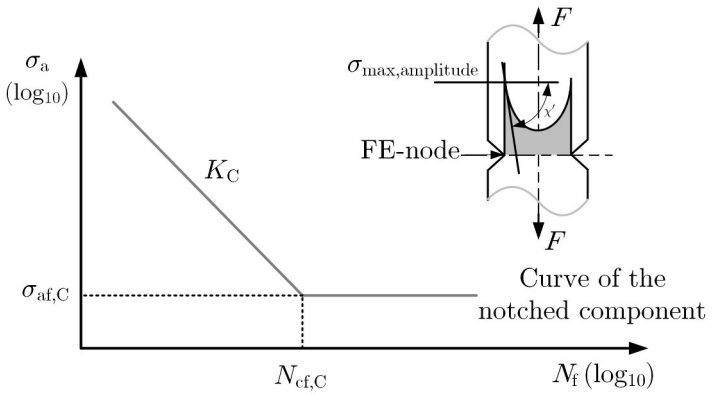

Figure 3.2: *Diagram of component S-N curve [13]*

$\sigma_{af,C}$ = Endurance stress limit
$N_{cf,C}$ = Endurance cycle number
K_C = inclination

The main purpose of the method is to determine these three parameters with a functional relation with influence factors, as described below [40]:

$\sigma_{af,C} = f_1$(influence factors)
$N_{cf,C} = f_2$(influence factors)
$K_C = f_3$(influence factors)

Influence factors related to the effect of the stress gradient are:

- $f_{GR,af}$: has an effect on the fatigue limit
- $f_{GR,cf}$: has an effect on the number of cycles to failure
- $f_{GR,sf}$: has an effect on the inclination

The factors described above modify the three parameters of the material curve: tension-compression fatigue limit $\sigma_{A,t-c}$, number of cycles at knee point $N_{cf,M}$ and the slope k_M through the functions f_1, f_2 and f_3. As described in Ch. 1, the nominal strength of a smooth specimen should, for the same imposed external stress, be greater than that of a notched component by a factor of K_t. However, as shown in Ch. 2, by experimental evidence, the presence of a stress concentrator reduces fatigue strength by a coefficient smaller than K_t, exactly by K_f [42]. The approach refers to the classical viewpoint where S-N curves are compared under the same nominal stress. This method results in a reduction in the fatigue limit of the notched component. From the local point of view, however, the comparison is made in terms of peak stress. The fatigue limit of a smooth specimen is increased by the presence of a notch or, more generally, by a stress gradient. This support effect is proportional to K_t, which includes geometric and type of load factors, damped by K_f, dependent on the material [42]. This explains, for example, why the fatigue limit of a specimen subjected to rotating bending is always greater than one subjected to pure tension-compression. On this basis, the central idea of the support effect as the beneficial consequence of a stress gradient on the fatigue life was introduced by Stieler [42]. From the original definition of K_f, here re-interpreted with different symbols, it was obtained:

$$K_f = \frac{\sigma_{D(\chi=0)}}{\sigma_{D(\chi'=0)}} \qquad (3.1)$$

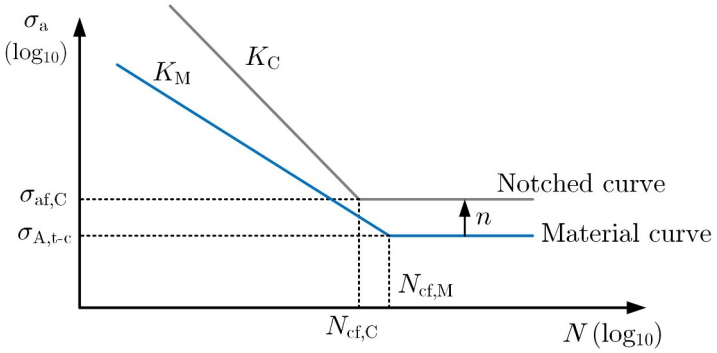

Figure 3.3: *Support effect*

where $\sigma_{D(\chi=0)}$ is practically the fatigue limit of a specimen subjected to tension-compression load, $\sigma_{A,t-c}$ and $\sigma_{D(\chi=0)}$ is the nominal fatigue limit of a notched specimen. Multiplying both members by $\sigma_{D(\chi=0)}$ and dividing by K_f it was obtained:

$$\sigma_{D(\chi=0)} = \frac{\sigma_{D(\chi=0)}}{K_f} \tag{3.2}$$

To switch to the local viewpoint, it was multiplied by the theoretical stress concentration factor:

$$\sigma_{D(\chi=0)} \cdot K_t = \sigma_{D(\chi=0)} \cdot \frac{K_t}{K_f} \tag{3.3}$$

on the left the local peak stress was obtained, indicated as $\sigma_{D,local(\chi=0)}$, while on the right the fatigue factor n was recognised:

$$n = \frac{K_t}{K_f} \tag{3.4}$$

As can be seen from the Fig. 3.3, $n \geq 1$. femfat® the support effect is determined by means of the relative stress gradient χ' [13]. First of all, the stress gradient is defined as:

$$\chi(x) = \frac{d\sigma_e}{dx} \tag{3.5}$$

where σ_e is the Von Mises' equivalent stress, while the relative stress gradient:

$$\chi'(x) = \frac{1}{\sigma_{e,max}} \cdot \frac{d\sigma_e}{dx} \tag{3.6}$$

To record the support effect, the following approaches were analyzed in the software: the Siebel method, the IABG method and the femfat® method [13]. In the first case, the support effect depends on the relative stress gradient and the yield stress of the material:

$$n = 1 + \sqrt{\chi'} \cdot 10^{\left(0{,}33+\frac{\sigma_y}{712}\right)} \tag{3.7}$$

The following expressions were derived for different classes of materials using the IABG method:

$$n = 1 + 0{,}45 \cdot \chi'^{0{,}30} \quad \text{for steel} \tag{3.8}$$

$$n = 1 + 0{,}33 \cdot \chi'^{0{,}65} \quad \text{for cast-steel} \tag{3.9}$$

$$n = 1 + 0{,}43 \cdot \chi'^{0{,}68} \quad \text{for cast-iron} \tag{3.10}$$

while in femfat® the following equation was developed [13]:

$$n = \left[1 + \left(\frac{\sigma_{A,b}}{\sigma_{A,t-c}} - 1\right) \cdot \left(\frac{\chi'}{(2/b)}\right)^{K_D}\right] \tag{3.11}$$

where $\sigma_{A,b}$ is the fatigue limit for a smooth specimen subjected to rotating bending, $\sigma_{A,t-c}$ is the fatigue limit of the material subjected to tension-compression load and K_D is the damping coefficient of the support effect for the calculation of the fatigue limit and b is the specimen thickness [11][37].

Kind of material	Stainless steel	Other kind of steel
a_G	0.40	0.50
b_G	2400	2700

Table 3.1: *Constants a_G and b_G [15]*

In this thesis, the Stieler and IABG methods were developed while the femat® method, described in the Eq. 3.11, was unusable because of the lack of tests under bending load on the analyzed specimens [13].

3.1.1 Determination of local Wöhler curve parameters

To determine the fatigue strength of the notched component it is necessary to multiply the fatigue limit of the smooth specimen subjected to tension-compression with the fatigue factor:

$$\sigma_{af,C} = f_{GR,af} \cdot \sigma_{A,t-c} = n \cdot \sigma_{A,t-c} \tag{3.12}$$

The factor that takes into account the effect of the stress gradient and influences the slope of the local S-N curve, k_C, is $f_{GR,sf}$ and it was determined in this way [13]:

$$f_{GR,sf} = 1 + \frac{1,8 \cdot \chi'^{1,2}}{f_{GR,af}} \tag{3.13}$$

The slope, at this point, was determined as follows [13]:

$$k_C = \frac{k_M - IFK2}{f_{GR,sf}^{IFK3}} + IFK2 \tag{3.14}$$

where k_M is the slope of the curve of the base material, IFK2 is the exponent of inclination of the incipient fracture S-N curve and and IFK3 is the material group dependent exponent. For steel and alluminium alloys IFK2 = 3 and IFK3 = 2. The factor that influence the number of cycles to failure is $f_{GR,cf}$ and it is defined as [13]:

$$f_{GR,cf} = \frac{10^{\left(6,8 - \frac{3,6}{k_C}\right)}}{10^{\left(6,8 - \frac{3,6}{k_M}\right)}} \tag{3.15}$$

The number of cycles to failure for the notched component is obtained from that of the base material by simply multiplying by the influence factor as shown below [13]:

$$N_{cf,C} = N_{cf,M} \cdot f_{GR,cf} \tag{3.16}$$

3.2 FKM Guideline

The guide drawn up by FKM proposes the following approach [15]. Three expressions have been derived for the fatigue factor depending on the value obtained for the relative stress gradient:

$$n = \begin{cases} 1 + \chi' \cdot 10^{-\left(a_G - 0,5 + \frac{\sigma_{UTS}}{b_G}\right)} & \chi' \leq 0,1\ mm^{-1} \\ 1 + \sqrt{\chi'} \cdot 10^{-\left(a_G + \frac{\sigma_{UTS}}{b_G}\right)} & 0,1\ mm^{-1} < \chi' \leq 1\ mm^{-1} \\ 1 + \sqrt[4]{\chi'} \cdot 10^{-\left(a_G + \frac{\sigma_{UTS}}{b_G}\right)} & 1\ mm^{-1} < \chi' \leq 100\ mm^{-1} \end{cases} \tag{3.17}$$

where a_G and b_G are two constants tabulated in Tab. 3.1.
In accordance with Fig. 3.4, the guide proposes to calculate the relative stress gradient in this way:

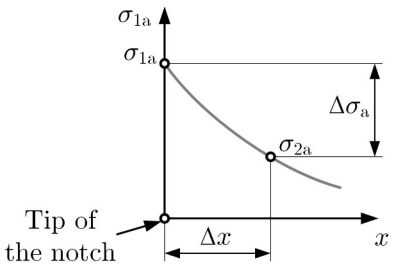

Figure 3.4: *calculation of the relative stress gradient [15]*

$$\chi' = \frac{1}{\sigma_{1,a}} \cdot \frac{\Delta\sigma_a}{\Delta x} = \frac{1}{\Delta x} \cdot \left(1 - \frac{\sigma_{2,a}}{\sigma_{1,a}}\right) \tag{3.18}$$

Given *n* the local fatigue limit of the notched specimen is determined as in Eq. 3.12. The slope of the inclined section was assumed to be $k_C = k$, while the number of cycles to failure of the notched specimen is equal to the number of cycles to failure of the smooth specimen.

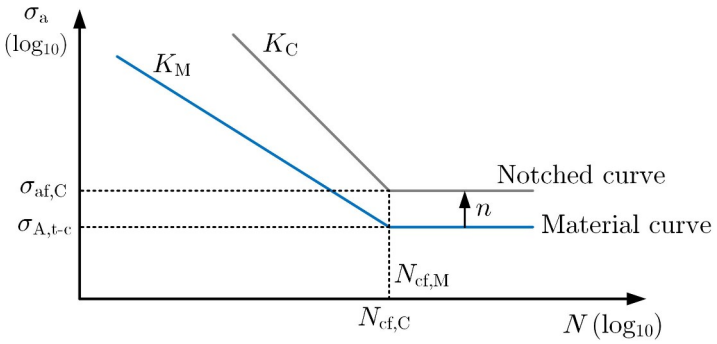

Figure 3.5: *local S-N curve by FKM approach*

The FKM guide greatly simplifies the steps to be followed to derive the S-N curve compared to the approach followed by Fe-Safe®. In Fig. 3.5 a typical output curve from the FKM method can be observed qualitatively [15].

Chapter 4

STRAIN ENERGY DENSITY APPROACH

This chapter will describe an approach that differs slightly from the previous ones. The classical approach, TCD and RSG deal with fatigue in different ways of, course, but they always refer to the stress state present in the vicinity of the notch by means of a peak stress, for the nominal approach, or a stress distribution for TCD or RSG. Strain energy density approach, abbreviated to SED, changes point of view and lays its foundation by considering the strain energy density. The idea proposed by Neuber still applies: the material is sensitive to an average stress within a structural volume whose size is a property of the material. First of all, the linear elastic fracture mechanics is introduced in order to define the correct terminology and the parameters required for subsequent development. In a second step, V-notch will be treated, the environment in which SED was born, with a practical application. Next, the SED applied to fillet-notches, the aim of the thesis work, will be described.

4.1 Hints of linear elastic fracture mechanics

Many mechanical components, as well as being characterised by variations in shape, can have microstructural defects within them which can alter the distribution of the stress field. These defects can be, for example, cracks, fissures or ineliminable microstructural characteristics of the material. Taking the plate with a hole of Ch. 1 as a reference, it can be seen that (Fig. 4.1), as the radius ρ decreases, the stress field along the net section, at least theoretically, tends to infinity.

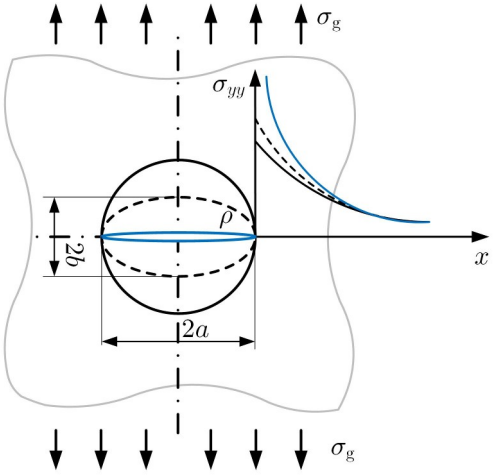

Figure 4.1: *Variation of the stress field as the geometric configuration changes*

Inglis, in 1913 [19], proposed an analytical expression for the determination of K_g in an intermediate case:

$$K_{t,g} = 1 + 2 \cdot \sqrt{\frac{a}{\rho}} \tag{4.1}$$

where a is practically the major half-axis of the elliptical hole and ρ is the radius of curvature at the ends of the major axis. ρ is related to the size of the minor half-axis:

$$\rho = \frac{b^2}{a} \tag{4.2}$$

Through these expressions it is easy to realise that if $\rho \to 0$, then $K_{t,g} \to \infty$.
In order to understand the effect that a crack has on a component, Fig. 4.2 has been considered, which represents a plate subjected to a gross nominal tensile stress σ_g.

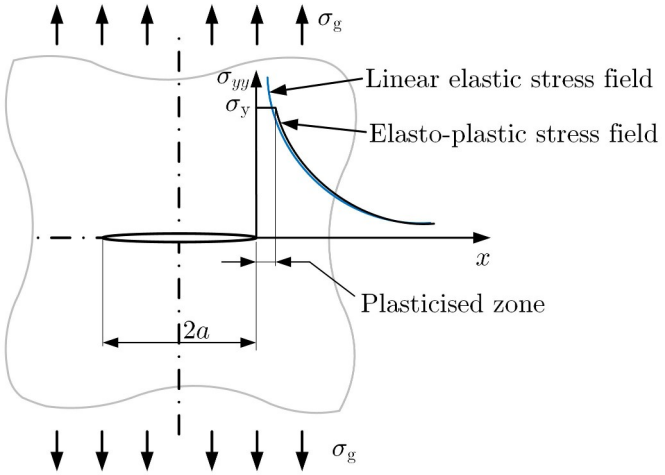

Figure 4.2: *Comparison of the linear elastic stress field with the real elasto-plastic stress field [4]*

Under the assumption that the plasticised zone at the apex of the crack is small, the linear elastic stress field is representative of the real elastic-plastic stress field and linear elastic fracture mechanics, abbreviated LEFM, was considered. As the external load σ_g increases, the distribution of the stress field increases homothetically. This propoportional growth is described by the stress intensity factor K.

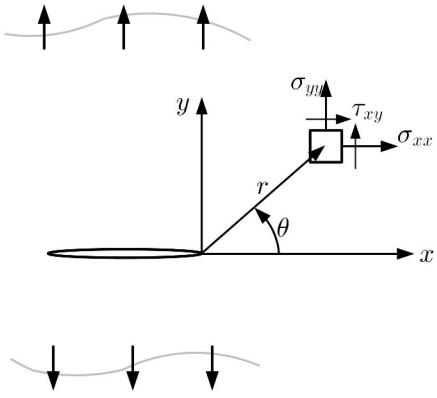

Figure 4.3: *Irwin stress field [20]*

Taking Fig. 4.3 as a reference, in 1957 Irwin [20] determined the analytical expressions of the stress field near the crack tip:

$$\begin{aligned}
\sigma_{xx}(r,\theta) &= \sqrt{\frac{K_I}{2\pi r}} \cdot \cos\frac{\theta}{2} \cdot \left(1 - \sin\frac{\theta}{2} \cdot \sin\frac{3\theta}{2}\right) \\
\sigma_{yy}(r,\theta) &= \sqrt{\frac{K_I}{2\pi r}} \cdot \cos\frac{\theta}{2} \cdot \left(1 + \sin\frac{\theta}{2} \cdot \sin\frac{3\theta}{2}\right) \\
\tau_{xy}(r,\theta) &= \sqrt{\frac{K_I}{2\pi r}} \cdot \sin\frac{\theta}{2} \cdot \left(\cos\frac{\theta}{2} \cdot \cos\frac{3\theta}{2}\right)
\end{aligned} \tag{4.3}$$

K_I is the stress intensity factor and is determined, analytically, as:

$$K_I = \sqrt{2\pi} \cdot \lim_{r \to 0^+} \sigma_{yy}(r, \theta = 0) \cdot r^{1/2} \tag{4.4}$$

The limit above exists and is finite. The expressions described in Eq. 4.3 are applied for: plane stress or plane strain, the latter condition with $\varepsilon_{zz} = 0$ and a stress in direction z equal to:

$$\sigma_{zz}(r, \theta) = \upsilon \cdot (\sigma_{xx} + \sigma_{yy}), \tag{4.5}$$

near the crack tip, for mode I stress and an external applied stress σ_g which must not exceed a value conventionally set at $0,5\sigma_y$ in order not to make the plasticised zone excessively large. There are also stress modes II and III, represented in Fig. 4.4.

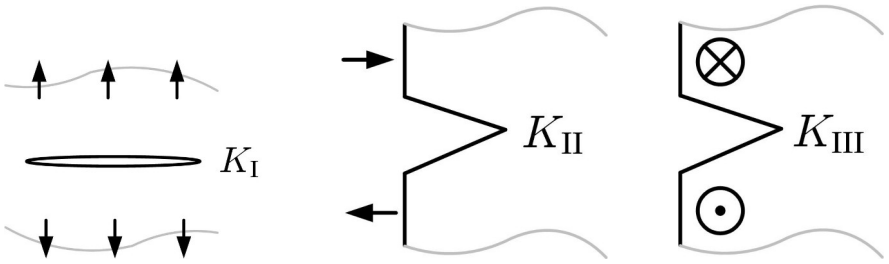

(a) *Mode I: opening* **(b)** *Mode II: in-plane shear* **(c)** *Mode III: out-of-plane shear*

Figure 4.4: *Description of load modes [6]*

Sometimes, to get a first estimate, it is useful to have an engineering expression given by K_I:

$$K_I = \alpha \sigma_g \sqrt{\pi a} \tag{4.6}$$

where σ_g is a nominal stress calculated in a simple way, such as F/A or M_f/W_f, a is a reference crack lenght and α is a dimensionless correction factor which depends on the type of load and the shape of the component and can be found in the literature. A typical diagram, for a crack on a plate subject to traction, is depicted in Fig. 4.5

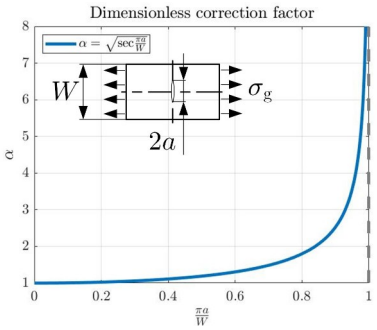

Figure 4.5: *dimensionless correction factor as a function of 2a/W*

up to a value of $2a/W = 0.3$, α remains unitary.

4.1.1 Fatigue fracture mechanics

In the case of fatigue, the crack propagation phenomenon is controlled by the range of the stress intensity factor, ΔK_I. In LEFM, fatigue tests are performed by stressing the component with a nominal stress range equal to $\Delta\sigma_g$ and cycle ratio $R = 0$, as depicted in Fig. 4.6.
A stress cycle with $R = -1$ has not been considered in this discussion because it would result in a crack closure at each cycle. The diagram of K_I as a function of time was obtained using Eq. 4.6, updated to the fatigue problem:

$$\Delta K_I = \alpha \Delta\sigma_g \sqrt{\pi a} \tag{4.7}$$

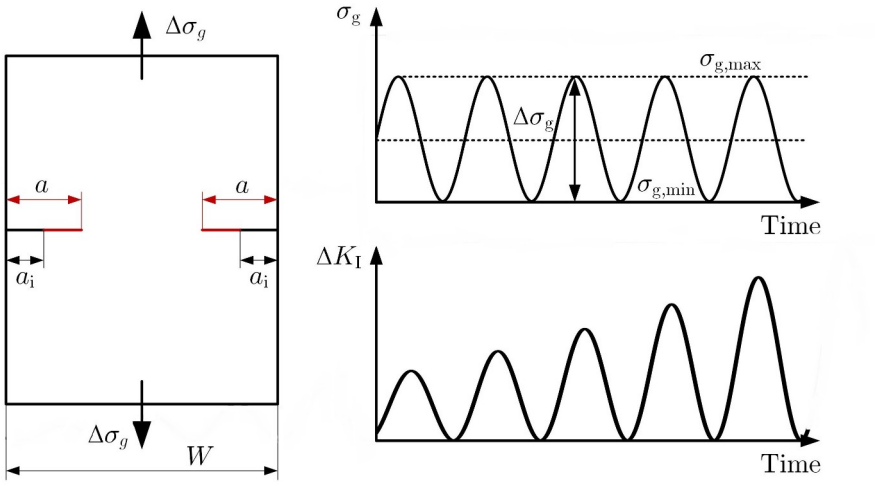

Figure 4.6: *Load applied to specimen for fracture mechanics tests [4]*

Cycle after cycle $\Delta\sigma_g$ remains constant, but the crack length goes from an initial value a_i to the current value a, so α increases and the ΔK increases. The experimental results, collected with the use of a microscope, were plotted in a graph crack length a versus number of cycles to failure N_f (Figure 4.7).

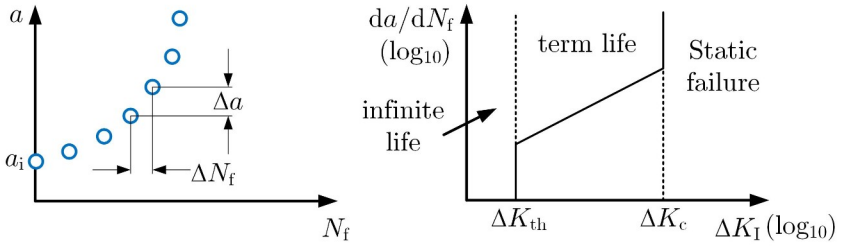

Figure 4.7: *a vs. N_f and crack propagation rate vs. range of stress intensity factor [4]*

In the 1960s, Paul Paris derived a further graph expressing the speed of crack propagation as a function of the range of the stress intensity factor. As can be seen, two limits have been derived: the threshold ΔK_{th} below which there is no propagation and the value which leads to immediate fracture of the component. The equation of the inclined line is:

$$\frac{da}{dN} = C\Delta K_I^m \tag{4.8}$$

where C and m are two material constants. This differential equation can be integrated to derive the number of cycles to failure that a mechanical component with an initial crack size a_i can sustain, up to a crack length a_f

$$dN = \frac{da}{C\Delta K_I^m} \rightarrow \int_0^{N_f} dN = \int_{a_i}^{a_f} \frac{da}{C\Delta K_I^m} \tag{4.9}$$

under the assumption of constant α:

$$N_f = \frac{\left(a_f^{1-\frac{m}{2}} - a_i^{1-\frac{m}{2}}\right)}{\left(1-\frac{m}{2}\right) \cdot C \cdot \alpha^m \cdot \Delta\sigma_g^m \cdot \pi^{m/2}} \tag{4.10}$$

Since in many practical cases, α varies, numerical techniques will be needed to determine a good approximation of the number of cycles to failure.

4.2 Non-conventional extensions of LEFM

In the last 30-40 years, fracture mechanics has been successfully applied to U-notches with a sufficiently small radius. This extension is based on the fact that, at the fatigue limit, the notches have at their tip material that is not healthy, but damaged, precisely with a non-propagating crack. In more modern developments, the sides of the notch have been opened at a certain angle to explain this issue from a theoretical point of view, welded structures have been considered but it can easily be extended to other cases.
In order to understand the application of the SED method, the mechanical components weakened by V-notches was considered in this thesis, applying the method to a welded joint with an opening angle of 2α [32].

4.2.1 Description of the stress state from a static point of view

Is considered a notch with generic opening angle 2α subject to a mode I and mode II loading. In this case the focus is on plane stress condition and therefore mode III loading is not considered. Applied stresses produce a plastic zone that necessarily exist near the V-notch, but of such limited size that the linear elastic fields remain representative of the stress state in the immediate vicinity of the notch tip.

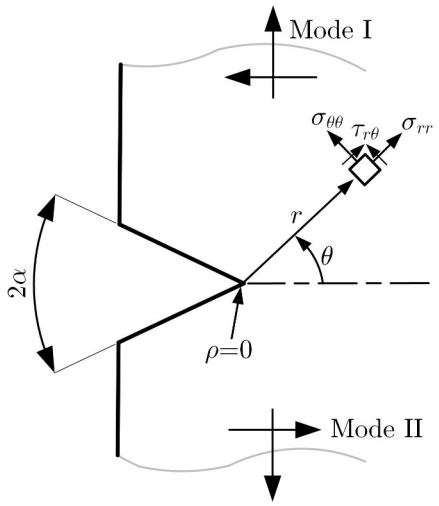

Figure 4.8: *Symbology adopted [32]*

Tip radius represented in Fig. 4.8 is equal to zero, but from the point of view of fatigue behavior, a notch with a non-zero and small radius also behaves like a V-notch as shown by Smith and Miller in 1978, Fig. 4.9.

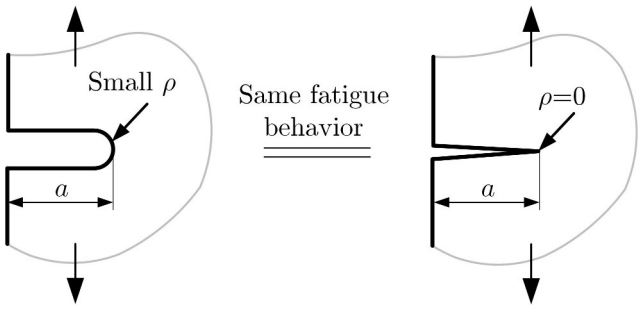

Figure 4.9: *Frost hypothesis [32]*

This statement is considered true if the radius $\rho_0 \geq$ with a_0 length constant defined by El Haddad. Examples of mechanical components weakened by V-notches are described below:

- Power – transmission – shaft (Fig. 4.10): slots for snap rings. Values of the radius in the order of hundredths or tenths of mm can be found in the literature, i.e. values that fall within the

assumptions made above. The opening angle is equal to 90°. Possible fatigue crack initiation from the apex of these notches, dependent on external loading conditions, can be treated with the recently developed theory. Using Peterson manuals may not be a good solution because it would be difficult to derive the notch sensitivity factor q to calculate the notch factor K_f.

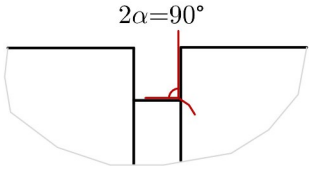

Figure 4.10: *keyway for retaining rings [32]*

- Power – transmission – shaft (Fig. 4.11), keyway. There are notches with a small radius, stress concentration sites that can induce fatigue cracks.

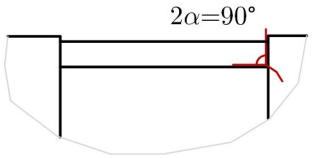

Figure 4.11: *keyway for tab [32]*

- Shaft-hub forced coupling (Fig. 4.12). A gear wheel, flywheel or other mechanical component is mounted on the shaft. Sharp edges are formed between the clamped object and the shaft. These are notches with a small radius, stress concentration sites that can induce fatigue cracks.

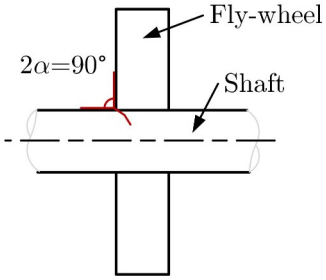

Figure 4.12: *V-notch in forced shaft-hub shrinkage [32]*

- Welded joints such as the typical T-joint. The notch, depicted in Fig. 4.13, has an opening angle equal to $2\alpha = 135°$. In literature values of the fillet radius limited to a few tenths of a mm. In this case the crack initiation point is situated at weld toe.

The idea of fracture mechanics is to analyse the stress field in the immediate vicinity of the crack tip so as to carry out checks at the initiation point and not through a notch sensitivity factor to find the notch factor. For this purpose, the preliminary hypotheses are:

- Plane stress case. Mode I and II loading on the notch plane
- Reduced plastic zone (linear elastic equations)
- Notches with zero or very small radius

External loads induce only mode I and mode II stresses. It was also considered a polar reference system at the tip of the notch and therefore the focus is on an infinitesimal volume of material located at a distance r from the tip and with θ anomaly. Fig. 4.8. The stress components in the plane are: radial stress σ_r, hoop stress σ_θ and shear stress $\tau_{r\theta}$ in polar coordinates. The stress field takes the following form, for mode I:

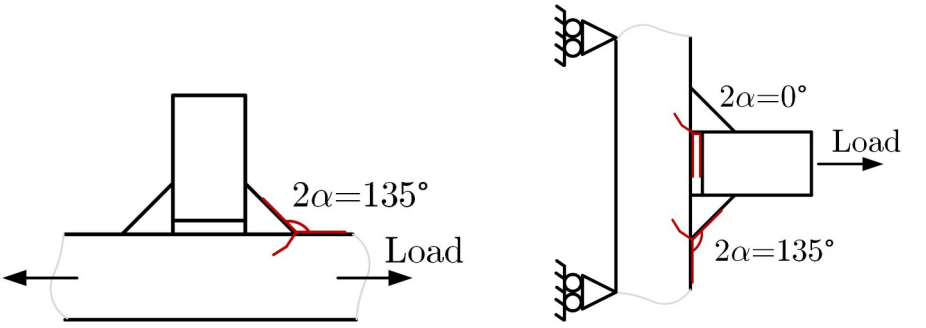

(a) *T-joint with* $2\alpha = 135^\circ$ **(b)** *T-joint with* $2\alpha = 135^\circ$ *and* $2\alpha = 0^\circ$

Figure 4.13: *Welded joints with different load conditions and different V-notches [32]*

$$\begin{Bmatrix} \sigma_{\theta\theta} \\ \sigma_{rr} \\ \tau_{r\theta} \end{Bmatrix} = \frac{1}{\sqrt{2\pi}} \cdot \frac{r^{\lambda_1 - 1} K_1}{(1+\lambda_1) + \chi_1(1-\lambda_1)} \left[\begin{Bmatrix} (1+\lambda_1)\cos(1-\lambda_1)\theta \\ (3-\lambda_1)\cos(1-\lambda_1)\theta \\ (1-\lambda_1)\sin(1-\lambda_1)\theta \end{Bmatrix} + \chi_1(1-\lambda_1) \begin{Bmatrix} \cos(1+\lambda_1)\theta \\ -\cos(1+\lambda_1)\theta \\ \sin(1+\lambda_1)\theta \end{Bmatrix} \right] \tag{4.11}$$

for mode I and II, stress distributions become:

$$\begin{Bmatrix} \sigma_{\theta\theta} \\ \sigma_{rr} \\ \tau_{r\theta} \end{Bmatrix} = r^{\lambda_1 - 1} K_1 \begin{Bmatrix} \tilde{\sigma_{\theta\theta}}(\theta) \\ \tilde{\sigma_{rr}}(\theta) \\ \tilde{\tau_{r\theta}}(\theta) \end{Bmatrix}_{\mathrm{I}} + r^{\lambda_2 - 1} K_2 \begin{Bmatrix} \tilde{\sigma_{\theta\theta}}(\theta) \\ \tilde{\sigma_{rr}}(\theta) \\ \tilde{\tau_{r\theta}}(\theta) \end{Bmatrix}_{\mathrm{II}} \tag{4.12}$$

the functions in the single variable θ can be found in the literature. Subscripts 1 and 2 indicate mode I and mode II stress contributions. The exponents $1-\lambda_1$ and $1-\lambda_2$ describe the singularity degree of the local stress field, are functions of the opening angle 2α and were described by American mathematician Williams in 1972. Through the graph of Fig. 4.14, it is possible to see the trend of these exponents in function of the opening angle.

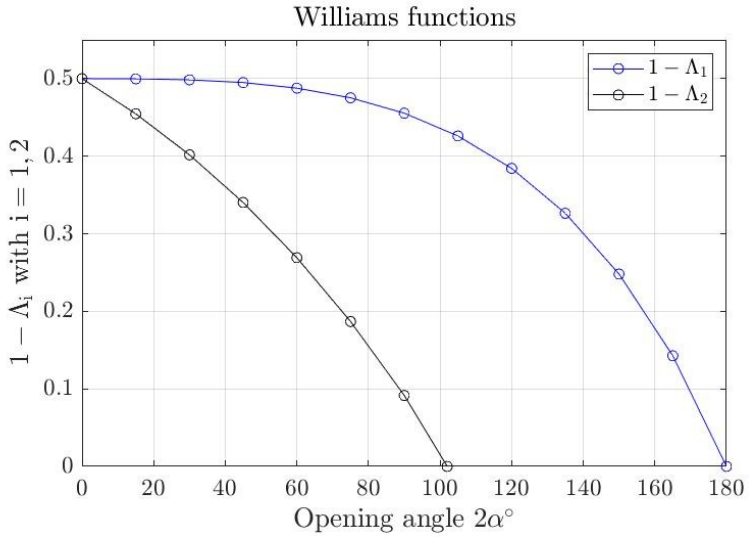

Figure 4.14: *Singularity of stress distributions for V-notches [32]*

For mode II load, the stress field is singular only for $0 < 2\alpha < 102^\circ$, while for Mode I load the range of singularity is $0 < 2\alpha < 180^\circ$. K_1^V and K_2^V describe the intensity of the local singular stress field and have the same meaning as the stress intensity factor in Irwin's crack equations. These are called

notch stress intensity factor (N-SIFs) to distinguish them from stress intensity factors. The definition was given in 1972 by Gross and Mandelson:

$$K_1^V = \sqrt{2\pi} \cdot \lim_{r \to 0^+} \sigma_{\theta\theta}(r, \theta = 0) \cdot r^{1-\lambda_1}$$
$$K_2^V = \sqrt{2\pi} \cdot \lim_{r \to 0^+} \tau_{r\theta}(r, \theta = 0) \cdot r^{1-\lambda_1} \quad (4.13)$$

In summary, simply considering mode I loading, as the opening angle 2α increases, the local stress field remains singular but the power of the singularity decreases, as depicted in Fig. 4.15.

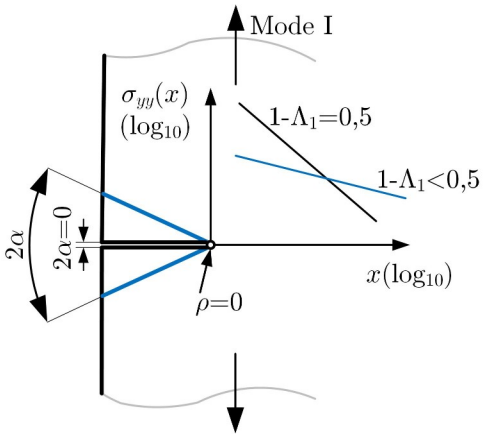

Figure 4.15: *Different singularity of V-notches [32]*

4.2.2 Fatigue application: fixed opening angle and mode I loading

In the case of cracks, the stress intensity factor due to mode I loading is the parameter that governs the fatigue strength of cracked components, i.e. it determines the instantaneous propagation speed. Once the ΔK_I range and the Paris law are known, the crack propagation rate is known and the fatigue life is determined by integrating Eq. 4.8. The extension of fracture mechanics applied to V-notches takes the same point of view: N-SIFs governs fatigue life. Two notched components with the same opening angle 2α and mode I loading have been considered in Fig. 4.16. If the two notches are subject to the same ΔK_1^V value, then they will also be characterised by the same fatigue life and vice versa.

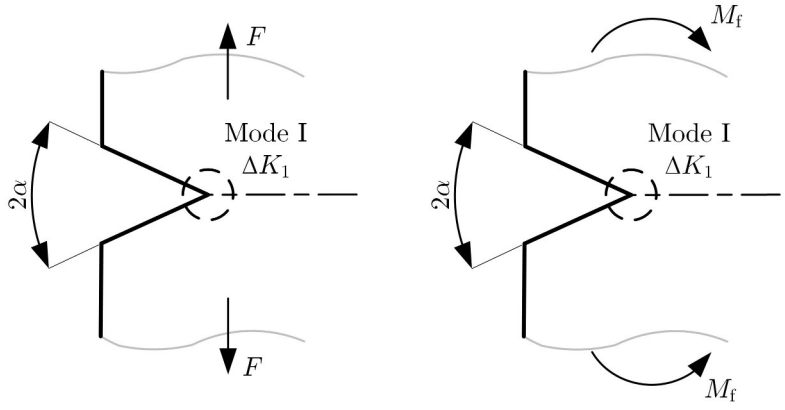

Figure 4.16: *Two V-notches characterised by the same value of the Mode I NSIF range, ΔK_1^V [32]*

The approach described above has an important application in welded joints with weld-toe failure. Two welded joints with two different geometries but with the same 2α opening angle equal to 135° can be considered (see Fig. 4.17).
Expressing the fatigue strength in terms of the nominal stress applied to the main plate falls within the scope of Eurocode 3. For the two joint configurations, assuming experimental testing in the laboratory, the trends shown in Fig. 4.18 would be obtained.

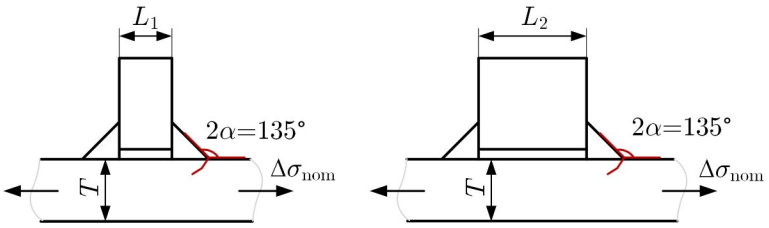

Figure 4.17: *Two welded joints with different dimensions [32]*

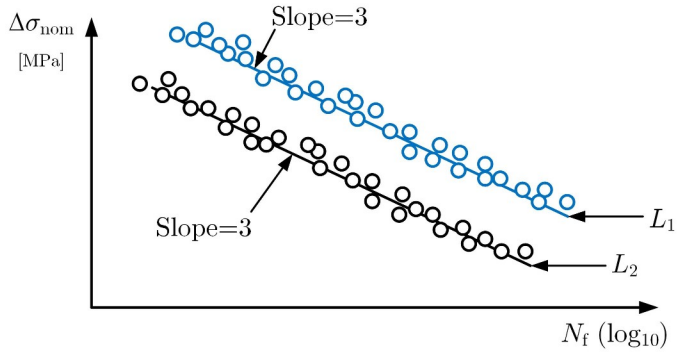

Figure 4.18: *Design curve diagram according to the nominal approach [32]*

The curve describing the joint with a stiffener thickness of L_2 is lower due to pronounced geometric variation. Locally, at the crack initiation point, the stress concentration is higher than in the case with L_1 stiffener thickness. The idea of non-conventional fracture mechanics is to link fatigue strength to the intensity of the local stress state at the crack initiation point. Therefore, ΔK_1^V is used because it describes the intensity of the local stress field that causes the crack initiation at the weld toe. In the literature [25], there was therefore a shift from $\Delta\sigma_{nom}$ to ΔK_1^V. the experimental data collected in the graph in Fig. 4.18 now collapse into a single design curve, as depicted in Fig. 4.19.

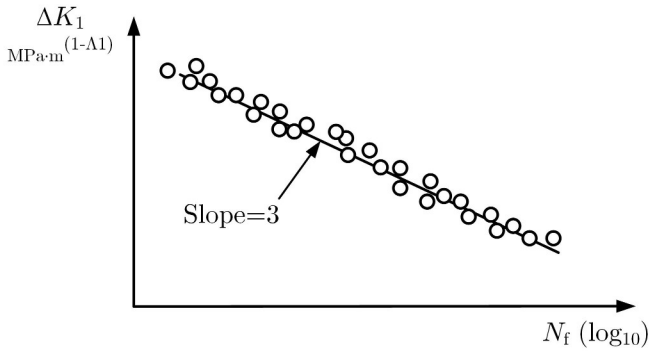

Figure 4.19: *Fatigue curve diagram in terms of ΔK_1^V [32]*

In 1998, Lazzarin and Tovo [25] showed that joints belonging to different classes, if the experimental results are expressed in terms of nominal stress, are part of the same strength class if described in terms of ΔK_1^V. Lazzarin and Tovo summarised 180 experimental results with the following characteristics:

- steel joints
- As-welded joints
- Break only at welding foot (2α = 135)

The advantages are obvious:

- Only one design curve is used

- NSIFs approach oriented to FEM analysis

Using the nominal stress method becomes difficult when analysing complex structures because the stress range varies from point to point and therefore defining a nominal stress as $\Delta\sigma_{nom} = P/A_f$ becomes too complicated. Thanks to the advent of calculation codes that exploit the theory of the finite element method, local analyses can be carried out and this inevitably leads to an enormous advantage.

4.2.3 Fatigue application: different opening angle and mode I and II loadings

In this sub-section, a cross joint has been considered, consisting of a vertical plate to which two horizontal plates are joined, Fig. 4.20. A tensile fatigue load producing a certain nominal stress range must be transmitted.

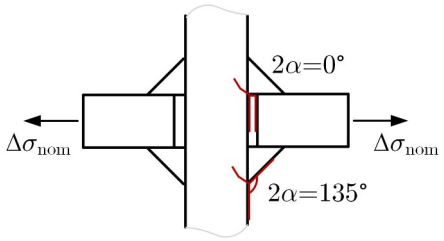

Figure 4.20: *Cross joint [32]*

The nominal approach is to use the appropriate fatigue curve provided by the standard. According to the fracture mechanics approach, the analysis must be conducted locally and here two V-notches were recognised: one at the weld toe with $2\alpha = 135°$ and one at the weld root with $2\alpha = 0°$. These two V-notches can be the site of fatigue fracture initiation. In particular, at the weld toe mode I is singular and mode II is non-singular (being $2\alpha = 135° > 102°$), while at the root side both modes I and II are singular, but in the present case mode II is negligible. Considering the stress distributions on the critical points, Fig. 4.21 was obtained.

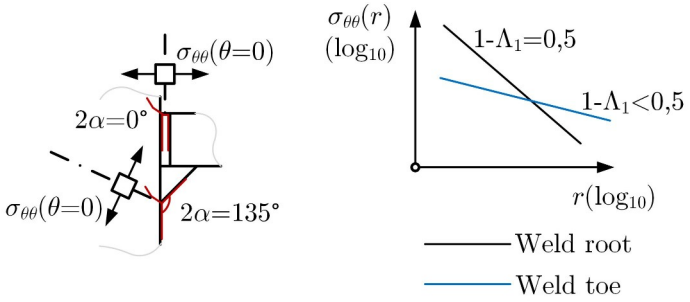

Figure 4.21: *Stress distributions on different critical points [32]*

Although this method brings considerable advantages and improvements over the nominal stress approach, it is not without its drawbacks. Recalling the equations of the notch stress intensity factors (Eq. 4.1), it can be seen that the unit of measurement of each factor is closely related to the eigenvalues λ_i, in fact $MPa \cdot m^{\lambda_i - 1}$, which in turn depend on the angle 2α and the stress mode. As the units of measurement are different, it is not possible to compare ΔK_i. This proves to be a very limiting problem in practical cases since very often the designer wants to know which part of a particular weld is most critical for fatigue strength. This kind of drawback can be solved by the SED (Strain Energy Density) approach, which will be discussed in the next section.

4.3 SED applied to V-notches

The strain energy density (SED) approach was introduced to address the issue of comparing N-SIFs in components with different notch openings and load application modes. The energy criterion proposed by Lazzarin and Zambardi [28] considers as a critical parameter for structural strength the strain energy density averaged over a circular sector of radius R_c, which is considered a material property. As mentioned

in the preamble, the approach is based on the idea of elementary structural volume proposed by Neuber according to which materials are sensitive to the mean stress state in a structural volume whose size is a property of the material. Although the stresses and energy density tend towards infinity at the point of singularity, the energy in a small structural volume surrounding the notch tip has a finite value and this value controls failure. The energy, averaged in a volume of radius R_c (which depends on the material properties), is a precise function of the Notch Stress Intensity Factors and is given in closed form for plane stress and plane strain conditions, the material being thought of as isotropic and linear elastic. The general expression for energy density, according to Beltrami, is:

$$\begin{aligned} W(r,\theta) &= \frac{1}{2}\sigma_{\theta\theta}\varepsilon_{\theta\theta} + \frac{1}{2}\sigma_{rr}\,\varepsilon_{rr} + \frac{1}{2}\sigma_{zz}\varepsilon_{zz} + \frac{\tau_{r\theta}^2}{2G} \\ &= \frac{1}{2E}\left(\sigma_{rr}^2 + \sigma_{\theta\theta}^2 + \sigma_{zz}^2 - 2\upsilon(\sigma_{rr}\,\sigma_{\theta\theta} + \sigma_{rr}\,\sigma_{zz} + \sigma_{\theta\theta}\sigma_{zz}) + 2(1+\upsilon)\tau_{r\theta}^2\right) \end{aligned} \tag{4.14}$$

Where the stress components refer to the polar coordinate reference system shown in Fig. 4.8, G is the shear modulus, E is the Young's modulus and υ is the Poisson's coefficient. Substituting Eq. 4.12 into Eq. 4.14 it was obtained:

$$W(r,\theta) = W_1(r,\theta) + W_2(r,\theta) + W_{12}(r,\theta) \tag{4.15}$$

where subscripts 1 and 2 refer to the loading mode, in particular 1 refers to Mode I, 2 refers to Mode II and 12 refers to a mixed Mode. Written separately, the terms of Eq. 4.15 are:

$$\begin{aligned} W_1(r,\theta) &= \frac{1}{2E}\cdot K_1^{V\,2}\cdot r^{2(\Lambda_1-1)}\cdot \tilde{f}_1(\theta) \\ W_2(r,\theta) &= \frac{1}{2E}\cdot K_2^{V\,2}\cdot r^{2(\Lambda_2-1)}\cdot \tilde{f}_2(\theta) \\ W_{12}(r,\theta) &= \frac{1}{E}\cdot K_1^{V} K_2^{V}\cdot r^{\Lambda_1+\Lambda_2-2}\cdot \tilde{f}_{12}(\theta) \end{aligned} \tag{4.16}$$

Where parameters K_1 and K_2 are the Notch Stress Intensity Factors (N-SIFs) related to Mode I and Mode II stress distributions, respectively. Λ_1 and Λ_2 are Williams' eigenvalues and $\tilde{f}_1(\theta)$, $\tilde{f}_2(\theta)$, $\tilde{f}_{12}(\theta)$ are functions that depend only on the angle θ. The strain energy in a region of radius R_c around the notch tip is:

$$\begin{aligned} E(R_c) &= \int_A W\cdot \mathrm{d}A = \int_0^{R_c}\int_{-\gamma}^{+\gamma}[W_1(r,\theta) + W_2(r,\theta) + W_{12}(r,\theta)]\,r\,\mathrm{d}r\mathrm{d}\theta = \\ &= \frac{1}{E}\left(\frac{I_1(\gamma)}{4\Lambda_1}\cdot K_1^{V\,2}\cdot R_c^{2\Lambda_1} + \frac{I_2(\gamma)}{4\Lambda_2}\cdot K_2^{V\,2}\cdot R_c^{2\Lambda_2}\right) \end{aligned} \tag{4.17}$$

where I_1 and I_2, depending on the angle γ and the Poisson's coefficient υ, are the integrals of the angular functions $\tilde{f}_1(\theta)$ and $\tilde{f}_2(\theta)$. Since the integration field is symmetric with respect to the notch bisector, the contribution of $W_{12}(r,\theta)$ vanishes.
Bearing in mind the Fig. 4.22, the area of the circular sector of radius R_c on which the integration is carried out, is:

$$A(R_c) = \int_0^{R_c}\int_{-\gamma}^{+\gamma} r\,\mathrm{d}\theta = R_c^2\gamma \tag{4.18}$$

Therefore, the elastic deformation energy averaged over area A is equal to:

$$\overline{W} = \frac{E(R_c)}{A(R_c)} = \frac{e_1}{E}\cdot\left(\frac{K_1^V}{R_c^{1-\Lambda_1}}\right)^2 + \frac{e_2}{E}\cdot\left(\frac{K_2^V}{R_c^{1-\Lambda_2}}\right)^2 \tag{4.19}$$

being:

$$e_1(2\alpha) = \frac{I_1(\gamma)}{4\Lambda_1\gamma} \quad \text{and} \quad e_2(2\alpha) = \frac{I_2(\gamma)}{4\Lambda_2\gamma} \tag{4.20}$$

Parameters e_1 and e_2 are the shape functions enclose the angle dependence 2α, as shown in the following Tab. 4.1 and Fig. 4.23.

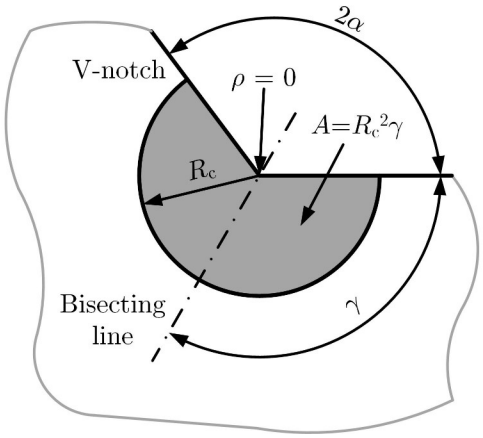

Figure 4.22: *Region of radius R_c around the notch tip [28]*

				Plane stress		Plane strain			
2α	γ/π	Λ_1	Λ_2	I_1	I_2	I_1	e_1	I_2	e_2
0°	1	0.5000	0.5000	1.0250	2.3250	0.8450	0.133	2.1450	0.341
15°	23/24	0.5002	0.5453	1.0216	2.1608	0.8431	0.140	2.0087	0.306
30°	11/12	0.5014	0.5982	1.0108	2.0091	0.8366	0.145	1.8810	0.273
45°	7/8	0.5050	0.6597	0.9918	1.8688	0.8247	0.149	1.7610	0.243
60°	5/6	0.5122	0.7309	0.9642	1.7385	0.8066	0.150	1.6479	0.215
90°	3/4	0.5445	0.9085	0.8826	1.5018	0.7504	0.146	1.4379	0.168
120°	2/3	0.6157	1.1489	0.7701	1.2887	0.6687	0.129	1.2437	-
135°	5/8	0.6736	1.3021	0.7058	1.1883	0.6201	0.118	1.1505	-
150°	7/12	0.7520	1.4858	0.6386	1.0908	0.5678	0.103	1.0590	-
160°	5/9	0.8187	1.6305	0.5930	1.0269	0.5315	0.093	0.9986	-

Table 4.1: *Values of the integrals I_1, I_2 and e_1, e_2*

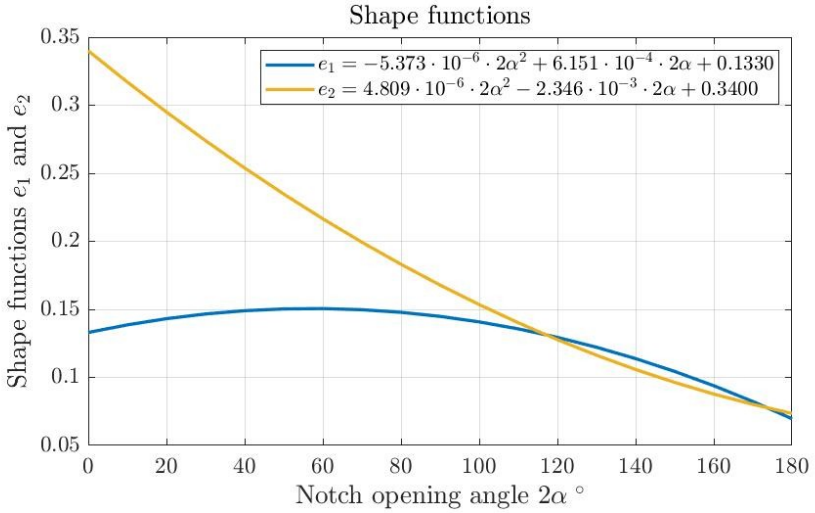

Figure 4.23: *Shape functions e_1, $e_2 = f(2\alpha)$*

In this way, if two V-notches with different opening angles 2α and subjected to different nominal loading conditions (always Mode I and/or Mode II stresses) have the same range of averaged strain energy densit $\Delta\overline{W}$ then they will also have the same fatigue life N_f. At this point, knowing the analytical formula for calculating the averaged SED, the need arises to estimate the value of the control radius R_c. Since this R_c is a function of the material, Lazzarin and Livieri [30] estimated R_c by simply imposing equality between the respective values of the strain energy density for the smooth material and for the notched material, both referring to the same number of fatigue cycles to failure.
Since the welding process locally alters the material properties, Lazzarin and Livieri carried out a series of experimental tests to calculate the critical radius directly on welded steel and aluminium joints with V-notches and welded joints with shaved weld beads, i.e. with an opening angle of $2\alpha = \pi$ (Fig. 4.24).

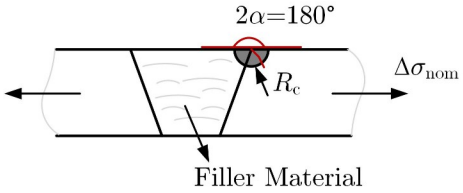

Figure 4.24: *Head-to-head joint without weld caps [32]*

Using a smooth specimen without a weld would give a different estimate of R_c as the base material has different strength characteristics to that inside a weld. The fatigue strength for a number of cycles to failure equal to $N_f = 5 \cdot 10^6$ is σ_D = 155 MPa with *P.S.* 50%. The structural volume of radius R_c can be plotted at the point of crack initiation, which typically occurs at the boundary between the zone of filler material and the thermally altered zone. Within this volume there is an averaged energy corresponding to a load that results in $5 \cdot 10^6$ number of cycles. In the world of welded joints, this type of joint expresses the smooth specimen. The averaged SED is expressed as:

$$\Delta\overline{W}_D^{\mathrm{unnotched}} = \frac{1}{V}\int_V \Delta W_D \, dV = \frac{1}{V}\int_V \frac{\Delta\sigma_D^2}{2E} dV = \frac{\Delta\sigma_D^2}{2E} \tag{4.21}$$

Therefore, taking as reference the weld toe of a welded joint (Fig. 4.22, 4.13a), known the value of ΔK_1 it is possible to determine the range of the averaged strain energy density of the joint under examination:

$$\Delta\overline{W}_{\mathrm{D}}^{\mathrm{notched}} \approx \frac{e_1}{E} \cdot \frac{\Delta K_1^{V\,2}}{R_c^{2(1-\lambda_1)}} \tag{4.22}$$

For this type of joint $\Delta K_{1,\mathrm{D}}^{V} = 211 \text{ MPa} \cdot \text{mm}^{0.326}$ (the subscript D indicates that the value was found at the same number of cycles to failure) with *P.S.* 50%. Through the above considerations:

$$\begin{aligned} \Delta\overline{W}_D^{\mathrm{unnotched}} &= \Delta\overline{W}_{\mathrm{D}}^{\mathrm{notched}} \\ \frac{\Delta\sigma_D^2}{2E} &= \frac{e_1}{E} \cdot \frac{\Delta K_{1,\mathrm{D}}^{V\,2}}{R_c^{2(1-\lambda_1)}} \end{aligned} \tag{4.23}$$

i.e.:

$$R_c = \left(\sqrt{2e_1} \cdot \frac{\Delta K_{1,\mathrm{D}}^{V}}{\Delta\sigma_D} \right)^{\frac{1}{0.326}} = 0.28 \text{ mm} \tag{4.24}$$

For light alloys it was obtained R_c = 0.12 mm. At this point, given any welded joint, it is possible to determine $\Delta\overline{W}$ at each possible crack initiation point. Fatigue failure occurs at the point where $\Delta\overline{W}$ is greatest. By way of Fig. 4.25 shows the graph of fatigue failure of about 900 specimens according to the SED approach carried out by Berto and Lazzarin [27]. In this way it is possible to include in a single curve the welded joints considered which, in nominal approach, present several curves for each strength class.

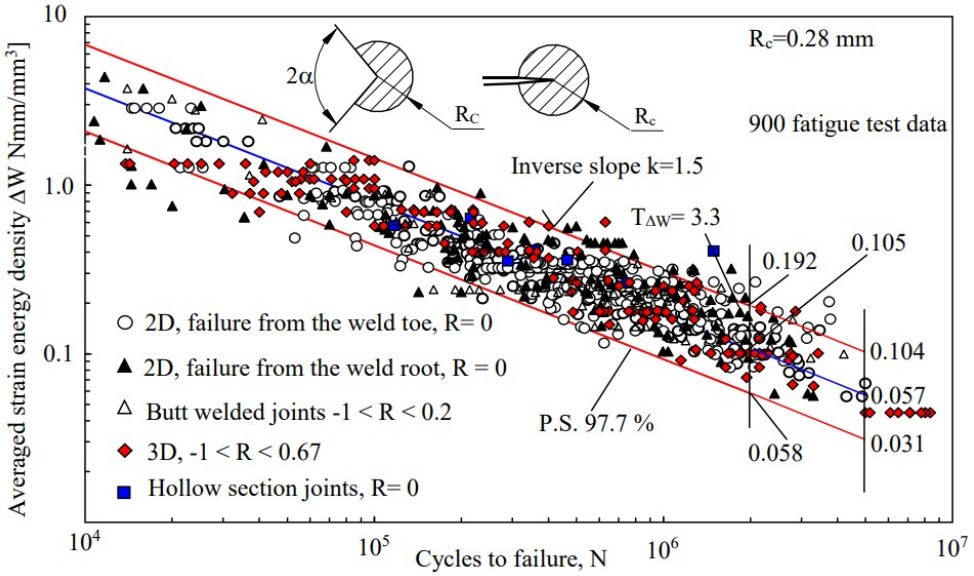

Figure 4.25: *Summary of data on fatigue failure of welded steeljoints during Mode I and II stresses expressed by the design band obtained from the SED method [27]*

X-joint values							
B [mm]	H [mm]	t [mm]	h [mm]	a [mm]	R_c [mm]	$\Delta\sigma_{nom}$ [MPa]	2α [°]
50	25	8	8	5	0.28	1	135

Table 4.2: *Dimensional and load values*

4.3.1 Application of the SED method to a V-notch

In this sub-section a cross-joint has been considered as an application example for the SED approach (Fig. 4.26) through finite element analysis. As can be seen, the problem has symmetries and therefore only 1/4 joint could be analysed (Fig. 4.26 shows the main dimensions). Along the y-axis, the symmetry constraint blocks the displacements along x ($U_X = 0$), while along x-axis it blocks displacements along the y, i.e. $U_Y = 0$.

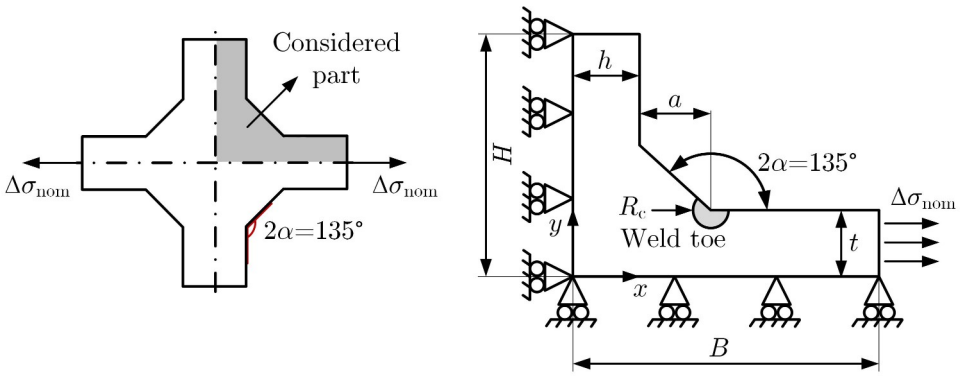

Figure 4.26: *Cross joint and symmetry condition. Main dimensions. [32]*

The joint has been modelled using autocad® software with the dimensions described in Tab. 4.2. It was then exported via an .IGES file and imported into ansys® for structural analysis. The material was defined as steel with E = 206000 MPa and υ = 0.3. quad 8 node 183 was chosen as the element type, with the following second K-option: plane strain. The plane strain state best represents the stress-strain state that results at the apex of a V-notch (since in-plane stresses tend to infinity in theory, out-of-plane stress is also non-zero). The imported geometry consists only of lines, so

it was necessary to create the area entity.

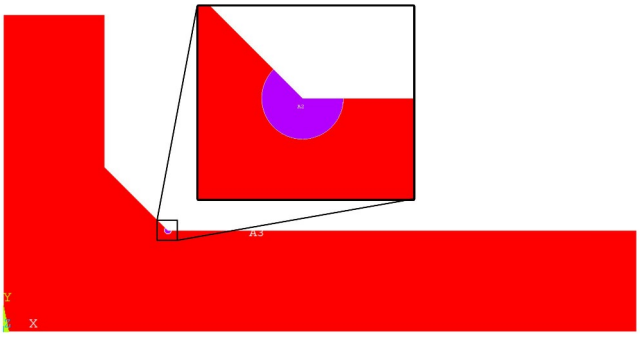

Figure 4.27: *Divide area by lines tool and the control volume with R_c = 0.28 mm*

In the control volume of radius R_c a global element size of 0.05 mm was used. A mesh with a global element size of 1 mm was used outside the control volume. Load and constraint conditions were applied as described in Fig. 4.25. Since the analysis is linear elastic, it is possible to obtain the value of the SED for any external load condition by means of a simple proportion.

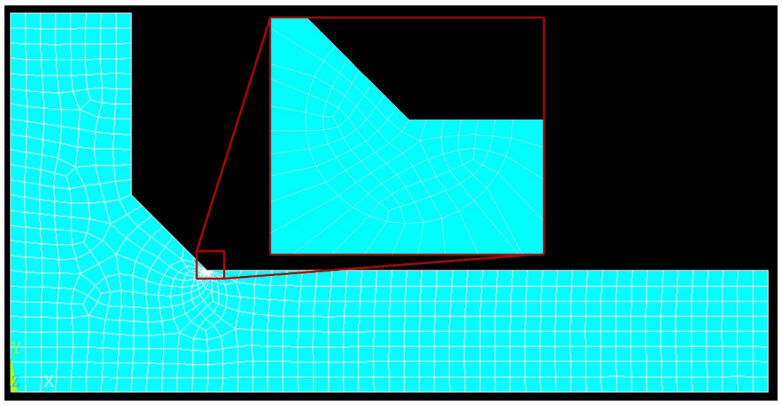

Figure 4.28: *Type of mesh adopted and zoom of the controlvolume for the calculation of the averaged SED*

in order to determine the averaged SED to be used to find the number of cycles to failure, first of all the elements enclosed within the control volume of radius R_c were isolated. Once this is done, with the following commands:

general postprod → element table → define table → add

the strain energy represented by the word sene was chosen. With the same command the geometry volu property was added. The values were then added together to obtain the total energy in the control volume:

$$E = \sum_i E_i \tag{4.25}$$

where E_i is the strain energy of each element and E is the total strain energy. an energy of $E = 0.154054 \cdot 10^{-5}$ mJ was obtained. To find the averaged SED (Eq. 4.19), the area must be determined as the sum of the areas of the individual elements enclosed in the circular sector:

$$A = \sum_i A_i \tag{4.26}$$

and it was obtained $A = 0.153938$ mm^2. With the help of the sum of each element function the total energy and area value were obtained. The averaged SED is therefore determined as:

$$\Delta\overline{W} = \frac{E}{A} = \frac{0.154054 \cdot 10^{-5}}{0.153938} = 1.0007536 \cdot 10^{-5} \frac{MJ}{m^3} \tag{4.27}$$

At this point it is possible to scale the value just found for any stress level, bearing in mind that the proportion must be made with the stresses with exponent 2, i.e:

$$\left(\frac{\Delta\overline{W}}{\Delta\sigma_{nom}^2}\right)_{(load=1\ MPa)} = \left(\frac{\Delta\overline{W}}{\Delta\sigma_{nom}^2}\right)_{(any\ load\ MPa)} \tag{4.28}$$

knowning the averaged SED it is possible to enter in a design curve (in terms of $\Delta\overline{W} = f(N)$) and estimate the number of cycles to failure. In conclusion, the SED approach proves to be an effective and versatile method for any kind of analysis, both static and fatigue, thanks to the solid control volume theory on which it is based. Regardless of the opening angle of the notch 2α or the mode of load stress, any component using the SED approach will be compared to a single design curve with a single unit of comparison, expressed in terms of linear elastic strain energy density.

4.4 SED applied to blunt V-notches

In the case of blunt V-notch, taking as reference the coordinate system in Fig. 4.29, the stress distribution under a mode I load is [26] [24]:

$$\sigma_{ij} = a_1 r^{\lambda_1 - 1}\left[f_{ij}(\theta,\alpha) + \left(\frac{r}{r_0}\right)^{\mu_1 - \lambda_1} g_{ij}(\theta,\alpha)\right] \tag{4.29}$$

where a_1 can be expressed by the notch stress intensity factor in the case of a sharp, zero notch radius, V-notch or by the elastic maximum notch stress in the case of blunt V-notch. r_0 is the distance from the origin of the reference system and the tip of the notch and depends on the opening angle and the notch root radius [14]:

$$r_0 = \frac{q-1}{q}\rho \tag{4.30}$$

and

$$q = \frac{2\pi - 2\alpha}{\pi} \tag{4.31}$$

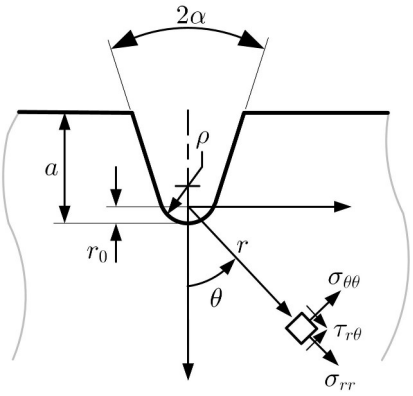

Figure 4.29: *Reference system in the case of blunt V-notch [26]*

The angular functions f_{ij} and g_{ij} are given by:

$$\begin{Bmatrix} f_{\theta\theta} \\ f_{rr} \\ f_{r\theta} \end{Bmatrix} = \frac{1}{1+\lambda_1+\chi_{b_1}(1-\lambda_1)}\left[\begin{Bmatrix} (1+\lambda_1)\cos(1-\lambda_1)\theta \\ (3-\lambda_1)\cos(1-\lambda_1)\theta \\ (1-\lambda_1)\sin(1-\lambda_1)\theta \end{Bmatrix} + \chi_{b_1}(1-\lambda_1)\begin{Bmatrix} \cos(1+\lambda_1)\theta \\ -\cos(1+\lambda_1)\theta \\ \sin(1+\lambda_1)\theta \end{Bmatrix}\right] \tag{4.32}$$

2α (rad)	q	Λ_1	μ_1	χ_{b_1}	χ_{c_1}	χ_{d_1}	$\tilde{\omega_1}$	$F(2\alpha)$
0	2	0.5	−0.5	1	4	0	1	0.785
$\pi\backslash 6$	1.8333	0.5014	−0.4561	1.0707	3.7907	0.0632	1.034	0.6917
$\pi\backslash 4$	1.75	0.505	−0.4319	1.1656	3.5721	0.0828	1.014	0.6692
$\pi\backslash 3$	1.6667	0.5122	−0.4057	1.3123	3.2832	0.096	0.97	0.662
$\pi\backslash 2$	1.5	0.5448	−0.3449	1.8414	2.5057	0.1046	0.81	0.7049
$2\pi\backslash 3$	1.3334	0.6157	−0.2678	3.0027	1.515	0.0871	0.57	0.8779
$3\pi\backslash 4$	1.25	0.6736	−0.2198	4.153	0.9933	0.0673	0.432	1.0717
$5\pi\backslash 6$	1.1667	0.752	−0.1624	6.3617	0.5137	0.0413	0.288	1.4417

Table 4.3: *Parameters for stress distributions, Eq. 4.29 and 4.37, and local strain energy, Eq.* **??**

$$\begin{Bmatrix} g_{\theta\theta} \\ g_{rr} \\ g_{r\theta} \end{Bmatrix} = \frac{q}{4(q-1)[1+\Lambda_1+\chi_{b_1}(1-\Lambda_1)]} \chi_{d_1} \begin{Bmatrix} (1+\mu_1)\cos(1-\mu_1)\theta \\ (3-\mu_1)\cos(1-\mu_1)\theta \\ (1-\mu_1)\sin(1-\mu_1)\theta \end{Bmatrix} + \left[+ \chi_{c_1} \begin{Bmatrix} \cos(1+\mu_1)\theta \\ -\cos(1+\mu_1)\theta \\ \sin(1+\mu_1)\theta \end{Bmatrix} \right] \tag{4.33}$$

considering only a mode I load under the plane strain condition. The eigenfunctions f_{ij} and G_{ij} satisfy the following expressions:

$$f_{zz}(\theta) = \upsilon(f_{\theta\theta}(\theta) + f_{rr}(\theta)) \tag{4.34}$$

$$g_{zz}(\theta) = \upsilon(g_{\theta\theta}(\theta) + g_{rr}(\theta)) \tag{4.35}$$

The table shows the parameters present in the Eq. 4.31, 4.32, 4.33 for some opening angles. In the case of a V-notch the parameter a_1 become:

$$a_1 = \frac{K_1^V}{\sqrt{2\pi}} \tag{4.36}$$

where K_1^V is calculated according to Eq. 4.13. In the presence of blunt V-notch it is possible to link the parameter a_1 to the maximum principal stress present at the notch tip:

$$a_1 = \frac{\sigma_{max}}{r_0^{\Lambda_1-1}\left\{1+\frac{(1+\mu_1)\chi_{d_1}+\chi_{c_1}}{1+\Lambda_1+\chi_{b_1}(1-\Lambda_1)}\frac{q}{4(q-1)}\right\}} = \frac{\sigma_{max} r_0^{1-\Lambda_1}}{1+\tilde{\omega_1}} \tag{4.37}$$

where $\tilde{\omega_1}$ can be found in Tab. 4.3. The stress field with respect to a reference system in polar coordinates becomes:

$$\begin{aligned} \sigma_{\theta\theta}(r,\theta) &= \frac{\sigma_{max}}{1+\tilde{\omega_1}}\left(\frac{r_0}{r}\right)^{1-\Lambda_1}\left[f_{\theta\theta}+\left(\frac{r}{r_0}\right)^{\mu_1-\Lambda_1} g_{\theta\theta}\right] \\ \sigma_{rr}(r,\theta) &= \frac{\sigma_{max}}{1+\tilde{\omega_1}}\left(\frac{r_0}{r}\right)^{1-\Lambda_1}\left[f_{rr}+\left(\frac{r}{r_0}\right)^{\mu_1-\Lambda_1} g_{rr}\right] \\ \tau_{r,\theta}(r,\theta) &= \frac{\sigma_{max}}{1+\tilde{\omega_1}}\left(\frac{r_0}{r}\right)^{1-\Lambda_1}\left[f_{r\theta}+\left(\frac{r}{r_0}\right)^{\mu_1-\Lambda_1} g_{r\theta}\right] \end{aligned} \tag{4.38}$$

Strain energy density is then:

$$W_1(r,\theta) = \frac{1}{2E}\left(\frac{\sigma_{max}}{1+\tilde{\omega_1}}\right)^2\left\{\left(\frac{r}{r_0}\right)^{2(\Lambda_1-1)}\tilde{F}_\Lambda + \left(\frac{r}{r_0}\right)^{2(\mu_1-1)}\tilde{G}_\mu + 2\left(\frac{r}{r_0}\right)^{\Lambda_1+\mu_1-2}+\tilde{M}_{\Lambda\mu}\right\} \tag{4.39}$$

where $\tilde{F_\Lambda}$, $\tilde{G}_\mu$ and $\tilde{M}_{\Lambda\mu}$ depend on the Poisson's modulus and the eigenfunctions described by Eq. 4.32 and 4.33. Considering the structural volume in Fig. 4.30 the strain energy can be expressed as:

$$E_1 = \int_{\Omega} W_1 d\Omega = \int_{-\bar{\theta}}^{+\bar{\theta}} d\theta \int_{R_1(\theta)}^{R_2} W_1(r, \theta) r dr \tag{4.40}$$

by solving the integral:

$$E_1 = \frac{1}{2E} \left[\frac{\sqrt{2\pi}\sigma_{max}}{1 + \omega_1} \right]^2 r_0^{2(1-\lambda_1)} \left(I_\lambda + I_\mu + I_{\lambda\mu} \right) \tag{4.41}$$

where I_λ, I_μ and $I_{\lambda\mu}$ are integral expressions that can be found in [26]. In general, it is possible to write:

$$I_1 = \frac{1}{2\pi} \left(I_\lambda + I_\mu + I_{\lambda\mu} \right) \tag{4.42}$$

where $I_1 = I_1(2\alpha, \rho, R_c)$. The mean value of the strain energy density is then given by:

$$\overline{W}_1 = \frac{1}{E} \left(\frac{I_1}{2\Omega} \right) \sigma_{max}^2 r_0^{2(1-\lambda_1)} \left[\frac{\sqrt{2\pi}}{1 + \omega_1} \right]^2 \tag{4.43}$$

Area Ω is defined as:

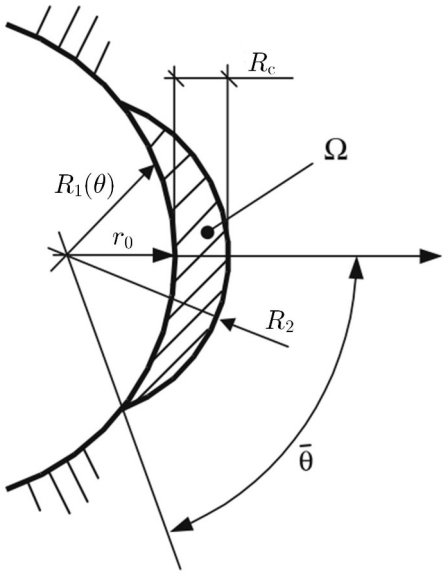

Figure 4.30: *Control volume for averaged SED assessment [26]*

$$\Omega = \int_{R_1(\theta)}^{R_2} \int_{-\bar{\theta}}^{+\bar{\theta}} r dr d\theta \tag{4.44}$$

With mathematical considerations that can be found in [26], the following equation was obtained:

$$\frac{I_1}{2\Omega}\left(2\alpha, \rho, R_c\right) = \frac{1}{\rho^{2(1-\lambda_1)}} \cdot H\left(2\alpha, \frac{R_c}{\rho}\right) \tag{4.45}$$

Eq. 4.43 becomes:

$$\overline{W}_1 = \frac{E_1}{\Omega} = F(2\alpha) \cdot H\left(2\alpha, \frac{R_c}{\rho}\right) \cdot \frac{\sigma_{max}^2}{E} \tag{4.46}$$

where:

$$F(2\alpha) = \left(\frac{q-1}{q} \right)^{2(1-\lambda_1)} \left[\frac{\sqrt{2\pi}}{1 + \omega_1} \right]^2 \tag{4.47}$$

and some notable values are shown in Tab. 4.3.

Chapter 5

EXPERIMENTAL TESTS: THE AMSLER MACHINE

This chapter will describe the static tensile test, which is necessary to obtain the material parameters to be used as input in FE analyses (ch. 7). A description of the reference materials, i.e. 42CrMo4 + QT, S275 and AlMgSi1 will also be given. As far as fatigue curves are concerned, special emphasis will be given to the experimental data obtained, the data fitting techniques and the extrapolation of information needed to develop the theoretical approaches addressed in the next chapters. In order not to cause confusion, and, as will be seen more clearly in Ch. 7 the following nomenclature has been adopted for FABEST specimens:

- FABEST014 - Unnotched specimen
- FABEST050 - Solid bar of circular cross-section, straight-through hole (sometimes also called Fabest_h20 or Fabest_12_h20)
- FABEST051 - Solid bar of circular cross-section, circumferential V-groove, with ρ = 0.5 mm (sometimes also called Fabest_v05)
- FABEST052 - Solid bar of circular cross-section, circumferential V-groove, with ρ = 2 mm (sometimes also called Fabest_v20)

5.1 The static tensile test for 42CrMo4 and material properties

The tensile test is the simplest and quickest test for the characterisation of a material and consists of applying a displacement at constant speed to the end of a sample, taking care to measure the elongation of the sample using a strain gauge and the tensile force applied using a load cell. The tensile test ends with breakage, i.e. the physical separation of the two ends of the specimen. The fracture occurs under quasi-static conditions, as the load is applied slowly. The test also makes it possible to determine the constitutive law of the material in the *stress-strain* plane.
Fig. 5.1 represents a typical scheme of a tensile test machine with the physical quantities it is involved. It is possible to note the tensile force, F_x, in the x-direction and the uniaxial stress, σ_x, that develops along the section of the specimen. Young's modulus can be obtained from the test as:

$$E = \frac{\sigma_x}{\varepsilon_x} \tag{5.1}$$

As mentioned in the preamble, in this section the material properties of 42CrMo4 + QT were determined, namely: the Young's modulus E and the Poisson's coefficient. The tests were performed in Poland at UTP Bydgoszcz by Lukasz Pejkowski and Jan Seyda according to ISO 6892-1:2016 standard, under strain control ε, with an imposed strain rate equal to:

$$\dot{\varepsilon} = \frac{\mathrm{d}\varepsilon}{\mathrm{d}t} = 0.00025\ \mathrm{s}^{-1} \tag{5.2}$$

The Poisson's modulus was determined in accordance with ASTM E132-04 standard. On the certificate provided by the university, it was possible to identify the temperature at which the test was performed,

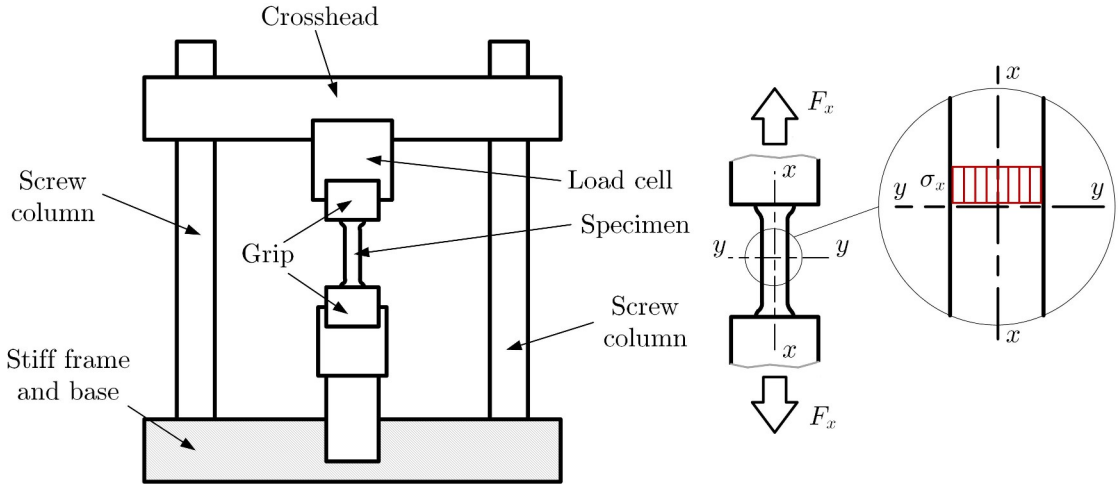

Figure 5.1: *Scheme of static tensile test machine*

Chemical composition [%]							
C	Mn	Si	P	S	Cu	Cr	Ni
0.42	0.64	0.21	0.013	0.009	0.02	1.04	0.06
Al	H	N	Mo	V	Ti	Sn	
0.026	1.30 ppm	0.0086	0.185	0.006	0.0013	0.003	

Table 5.1: *Chemical composition of* 42CrMo4 + QT *steel*

i.e. $T = 20^{\circ}$C and the chemical composition of the material in Tab. 5.1. The specimens for the tensile test were obtained from a rounded bars with a diameter of 35 mm with a tolerance of ±0.600 mm. Four specimens identified as MON were used and their characteristics are described in Tab. 5.2. Five diameter readings were taken and an average value was derived for each specimen. The cross-sectional area was then calculated using the following formula:

$$A_{\text{MON,i}} = \frac{\pi \cdot \phi^2_{\text{mean,i}}}{4} \qquad i = 1, \ldots, 4 \tag{5.3}$$

For each specimen, the stress-strain curve represented in Fig. 5.2 was determined. In order to determine Young's modulus deformations between 0.05% and 0.2% were considered. The data within this range have been fitted with a straight line equation $y = mx + q$, where y is equal to the stress value σ_x, x corresponds to the strain value ε_x, the angular coefficient m is Young's modulus E and q is the intercept on the y-axis. This procedure was done for the four specimens and then the values obtained were averaged.

Specimen no.	**MON 01**	**MON 02**	**MON 03**	**MON 04**
ϕ_1 in (mm)	5.010	5.010	5.020	5.020
ϕ_2 in (mm)	5.010	5.010	5.010	5.010
ϕ_3 in (mm)	5.000	5.010	5.020	5.010
ϕ_4 in (mm)	5.010	5.010	5.010	5.020
ϕ_5 in (mm)	5.000	5.010	5.010	5.010
ϕ_{mean} in (mm)	5.006	5.010	5.014	5.014
St.Dev.	0.005	0	0.005	0.005
Cross section area (mm^2)	19.68	19.71	19.75	19.75
Gripping pressure (bar)	120	120	120	120

Table 5.2: *Specimen diameters, normalcross-section and gripping pressure*

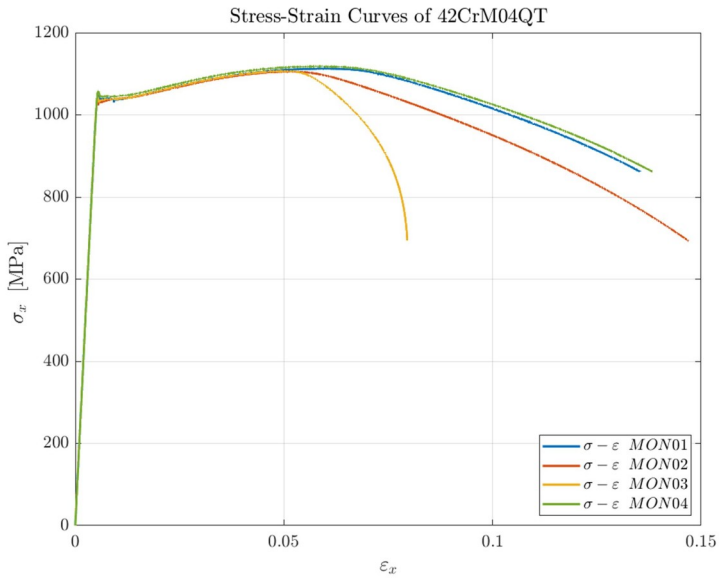

Figure 5.2: *σ − ε curves of MON specimens*

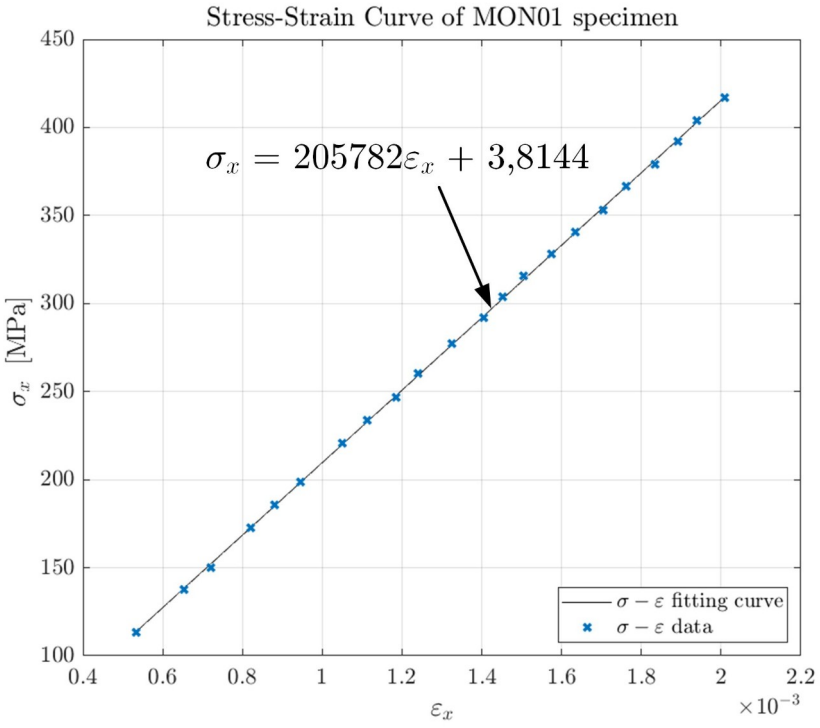

Figure 5.3: *σ − ε curves with small deformation of MON01 specimen*

Material properties				
E [MPa]	υ	R_{eH} [MPa]	R_{eL} [MPa]	σ_{UTS} [MPa]
206362	0.296	1047.6	1034.7	1110.9

Table 5.3: *Material properties of* 42CrMo4 + QT *steel*

Material properties				
Material	E [MPa]	υ	R_{eH} [MPa]	σ_{UTS} [MPa]
S275	206000	0.3	340	475
AlMgSi1	70000	0.33	302	315

Table 5.4: *Material properties of* S275 *structural steel and* AlMgSi1 *alloy*

A fit straight-line for specimen MON01 with an R-square of 0.9999 is shown in Fig. 5.3. Stress curves were also derived as a function of transverse strain ε_y by means of a linear equation $y_1 x + p_2$, where y takes the meaning of σ_x and x becomes ε_y (an example in Fig. 5.4 with an R-square of 0.9955). The other curves have been collected in the App. A.

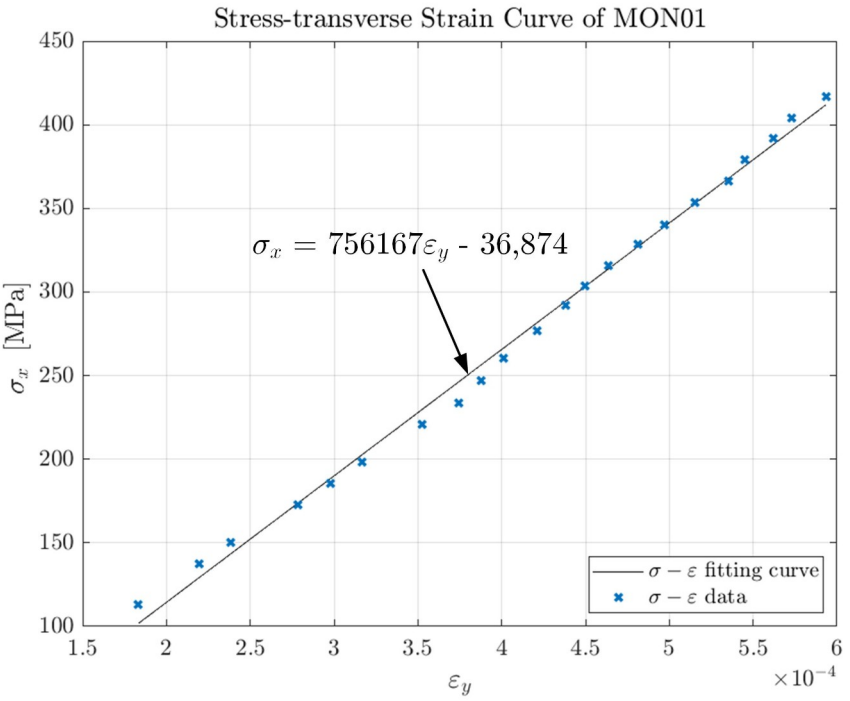

Figure 5.4: $\sigma - \varepsilon_y$ *curve of MON01 specimen*

To determine the Poisson's ratio υ it is necessary to consider its definition:

$$\upsilon = -\frac{\varepsilon_y}{\varepsilon_x} = \frac{p_1}{E} \tag{5.4}$$

After deriving υ for each specimen, the values was averaged to obtain the final coefficient. The material properties are described in the Tab. 5.3.
where R_{eH} is the upper yield strength and R_{eL} is the lower yield strength. The most interesting material properties for unalloyed structural steel S275 and the aluminium-manganese-silica alloy AlMgSi1 have been collected [39]. The mechanical properties have been compiled in Tab. 5.4. In the absence of tensile test certificates, common values [9] for the modulus of elasticity and Poisson's ratio were adopted.

Test frequencies			
Specimen	**Material**	**Frequence** [Hz]	**Stress ratio** R
FAB014	42CrMo4 + QT	125	−1
FAB050	42CrMo4 + QT	167	−1
FAB051	42CrMo4 + QT	184	−1
FAB052	42CrMo4 + QT	184	−1
Blunt	42CrMo4 + QT	150	−1
Sharp	42CrMo4 + QT	150	−1
F2	S275	15-30	−1
F3	S275	15-30	−1
F2	AlMgSi1	15-30	−1
F3	AlMgSi1	15-30	−1

Table 5.5: *Frequencies and stress cycles adopted in fatigue tests*

5.2 Fatigue tests: Amsler machine

The tensile fatigue testing machine is located at the Czech Technical University in Prague (CTU). The machine operates on a frequency between 50-300 Hz according to the manufacturer. The machine plus the specimen create a joint system which gets close to the resonance. This means that the stiffness of the specimen plus the weight of the machine define the operating frequency (set by the test). For less stiff specimens the frequency will get lower and vice versa. A load application frequency of 125 Hz was reached for the unnotched specimen (FAB014), while frequencies of 167 Hz and 184 Hz were reached for the notched FABEST specimens. The experimental tests carried out on the 42CrMo4 + QT specimens were all conducted with a stress ratio of $R = -1$. Data on the test frequency and load ratio adopted were collected in Tab. 5.5.

5.2.1 Set-up Amsler machine at CTU

Before setting up the Amsler test machine, the test specimens were cleaned and painted black (Fig. 5.5) with a high emissivity spray for thermal measurements with infrared cameras. In this way, reflections due to foreign bodies were reduced.

(a) **(b)**

Figure 5.5: (a) *Fabest specimen,* (b) *Painted specimen*

Manual set-up was then performed on the Amsler machine shown in Fig. 5.6
Initially the specimen was screwed to the base and, thanks to the threaded fixture, tightened with knobs shown in Fig. 5.7 (the grease applied to the thread facilitates the whole procedure). The unnotched specimen is shown as an example. A further threaded fixture was placed on top of its lower twin (Fig. 5.8).
A small threaded component required to connect the top of the machine, Fig. 5.8, was inserted through the bore of this device in order to apply the cyclic fatigue load with great precision. This part was then also screwed on at the top and tightened with the knobs (Fig. 5.9- 5.10).
In Fig. 5.10 The complete set-up is illustrated with a notched FABEST specimen as an example. After the 'practical' part had been completed, some settings had to be made from the machine's software. In Fig. 5.11 it is possible to observe the amount of force on the Amsler machine. In Fig. 5.12:(a) is a pre-load value and it is set for the section concerning machine start-up, the transient. In the image (b), on the other hand, it was applied the load at steady state with the stress cycle $R = -1$.

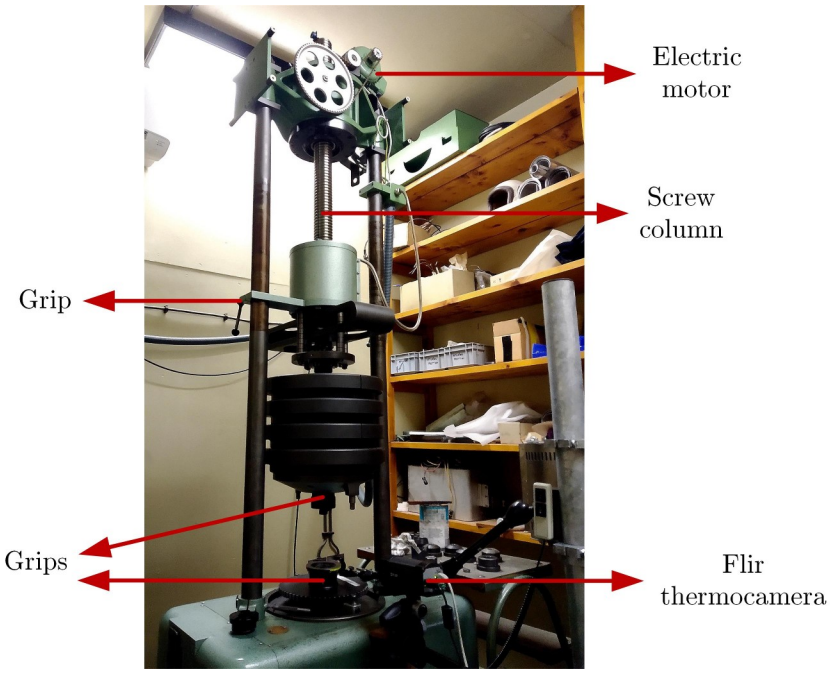

Figure 5.6: *Amsler machine at CTU in Prague*

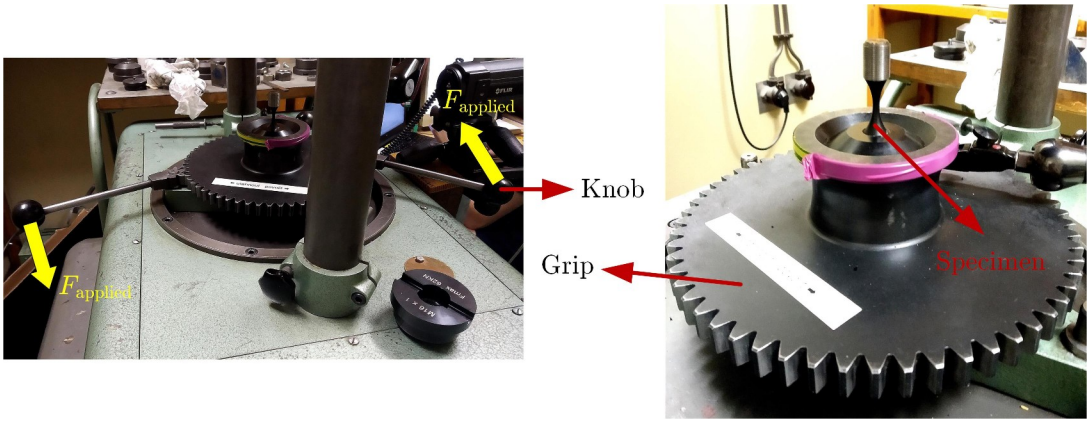

Figure 5.7: *Bottom fixing levers*

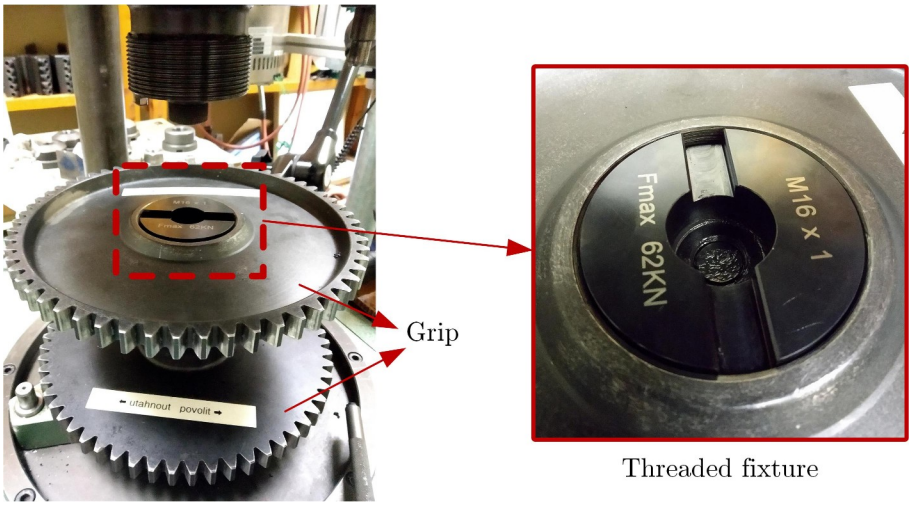

Figure 5.8: *Threaded connection element*

Figure 5.9: *Tightening operation*

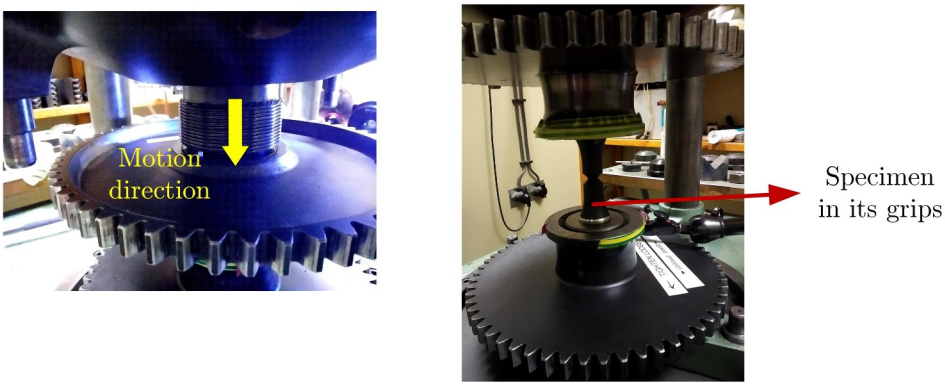

Figure 5.10: *Left: connection between upper and lower part.Right: Specimen fixed*

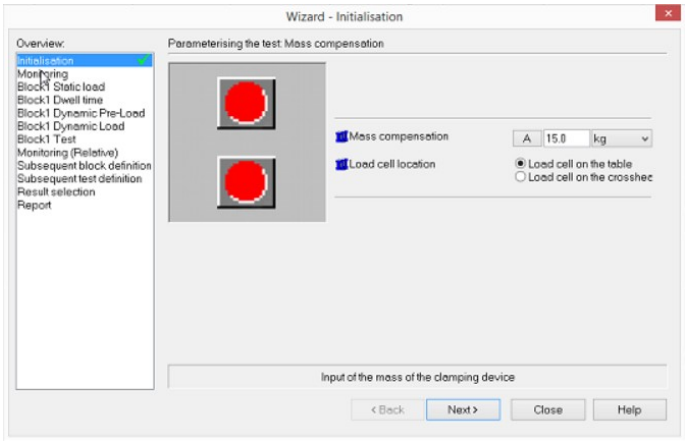

Figure 5.11: *Initialisation*

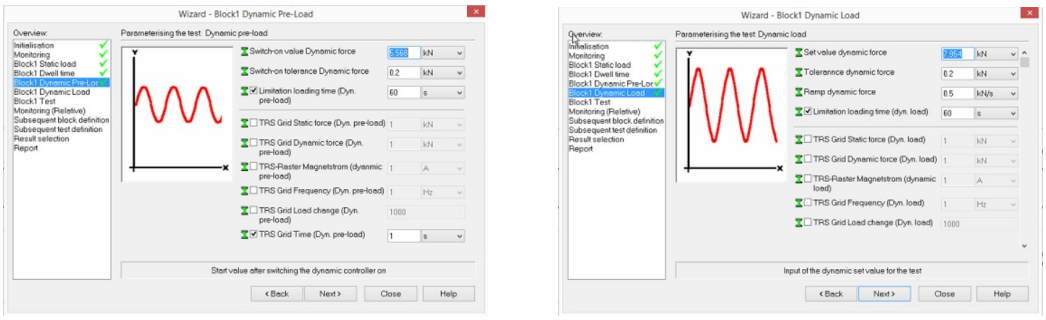

Figure 5.12: (a) *Dynamic pre-load settings,* (b) *Dynamic load settings*

The final screen allows notes to be entered (Fig. 5.13) on the type of material, the tester, the start time and date of the test, etc.

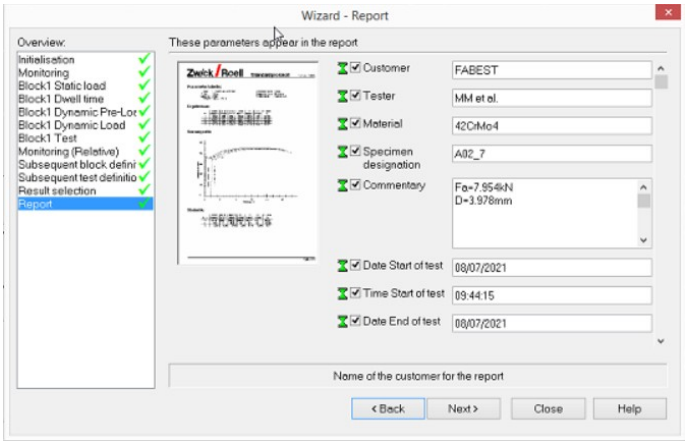

Figure 5.13: *Final options*

5.2.2 Experimental tests

Using the software incorporated in the PCs in the laboratory, the various tests were monitored using: static force diagrams, $F = F_s(t)$ in kN as a function of time, dynamic force diagrams, $F = F_d(t)$ in kN as a function of time and frequency diagrams $f = f(t)$ in Hz as a function of time. In Fig. 5.14 are represented some time instants of a test taken as an example, with the moment of the fatigue crack initiation, where the frequency decreases rapidly. In Ch. 6, together with the fracture sections, graphs such as those represented in Fig. 5.14 will be shown together with the experimental results to relate the fracture cross sections to the parameters of the S-N curve. The graphs of static force, dynamic force and frequency as a function of time will be plotted and it will be possible to note the rapid decrease in frequency as a direct consequence of fatigue crack initiation.

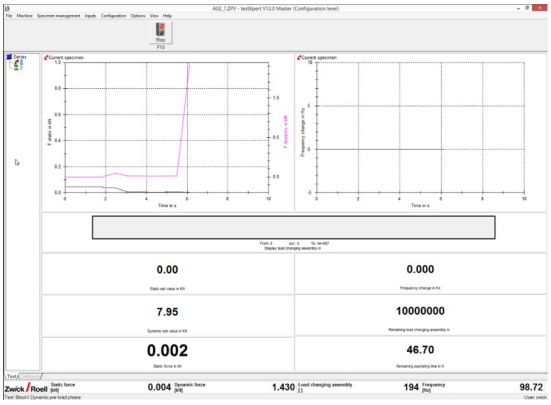

(a) *start of test*

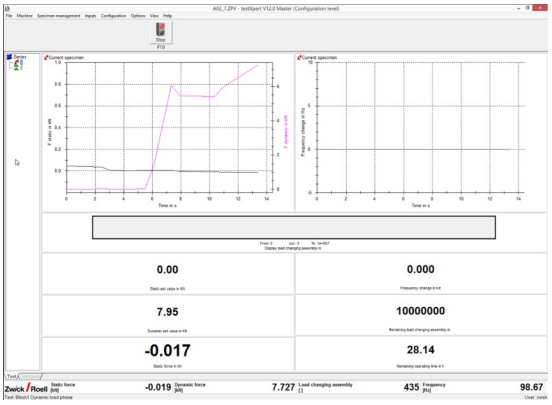

(b) *test in progress at a certain time t*

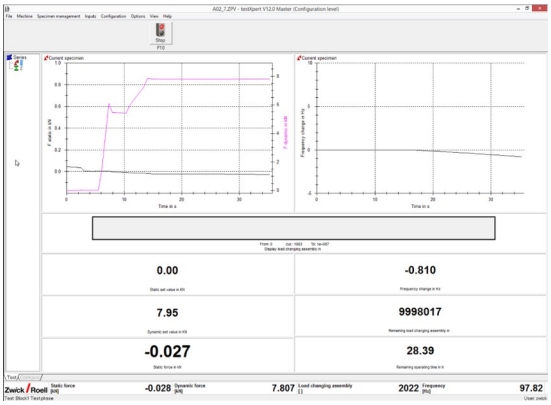

(c) *test in progress at a certain time t + t'*

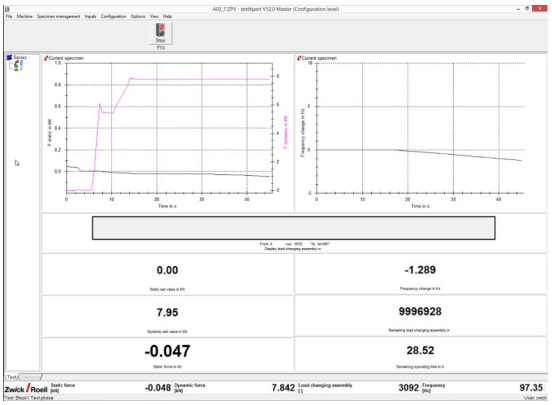

(d) *test in progress at a certain time t + t' + t"*

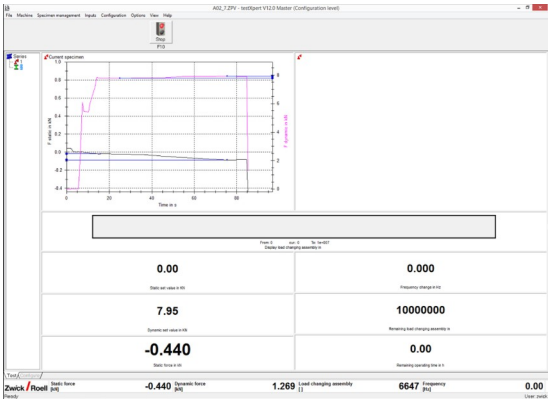

(e) *test in progress at a certain time t + t' + t" + t'"*

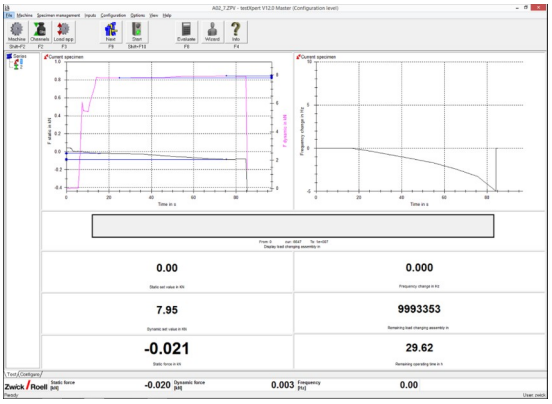

(f) *crack initiation*

Figure 5.14: *Diagrams recorded by the software*

5.2.3 Experimental results Amsler machine

The data collected by the Amsler machine were organised in an excel® file. Using the VBA programming language in Excel®, fit curves were obtained from the experimental data [21] [22]. Several mathematical models were used to fit the experimental results. The first one that was taken into consideration is the following:

$$\log N_f = a + b \cdot \sigma_a \tag{5.5}$$

which can be rewritten if using the notation used in matlab® or excel® to:

$$\log N_f = L1CON + L1LIN \cdot \sigma_a \tag{5.6}$$

this equation has been used for log N_f - σ_a axes and is called logN-linS regression. In $\log N_f - \log \sigma_a$ coordinate the following equation was used:

$$\sigma_a^k \cdot N_f = C \tag{5.7}$$

and this type of regression is called Basquin regression. In matlab® or excel® language:

$$\sigma_a^{SN\_W} \cdot N_f = SN\_C \tag{5.8}$$

As described in [22], linear equations were obtained because some points in the quasi-static and high-cycle regions were excluded. When fatigue tests are carried out in the laboratory a certain statistical dispersion can be observed. If specimens of the same nominal size are tested under the same stress amplitude σ_a, they do not show the same number of cycles to failure N_f, but there is some statistical scatter in the experimental results. Generally, fatigue tests are conducted at different stress levels and it can be observed that, each stress level shown in Fig. 5.15, there is a statistical distribution on the number of cycles to failure. A first hypothesis is that the distribution is Gaussian (or Normal). In practically all applications, the x-axis of the S-N curves, where the number of cycles is presents, is in logarithmic scale in base 10, so, the distribution is of the log-normal type for each stress amplitude. The parameters characterising the Normal distribution are the mean value μ and the standard deviation σ. It is possible to fit the mean values, for each stress level, with a linear curve in log − log scale. This is the curve that for each stress level gives the average value of the number of cycles to failure, the curve at the 50% probability of survival (P.S.50%). Using this curve in machine design is not a prudent cautionary because the risk of failure before it is 50%, which is unacceptable in all engineering applications. At this point, by integrating the probability curves, it is possible to determine points with an higher probability of survival, for example 90% or 97.7% by interpolating them with another line. A second hypothesis that has been made is to force the fit with the same inverse slope as the curve with P.S. 50%, in this way it is assumed that the standard deviation σ is constant for all stress levels. In practice, a widely used curve is the P.S.97.7% curve, which is obtained from the P.S.50% curve by interpolating points with a deviation of 2σ.

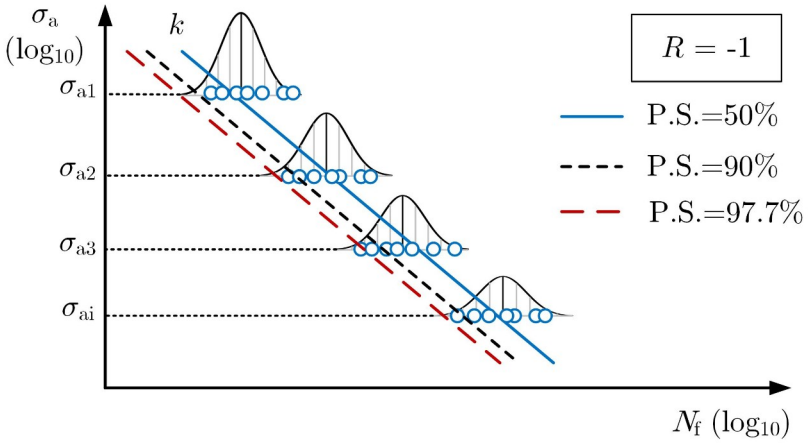

Figure 5.15: *Fatigue curves at different survival probabilities*

Given a certain number of cycles N, it is possible to identify 3 levels of stress that correspond to the 3 different probabilities of survival (Fig. 5.16). The width of the statistical dispersion scatter within which the experimental results fall is indicated by the parameter T_σ which by definition is:

$$T_\sigma = \frac{\sigma_{A,10\%}}{\sigma_{A,90\%}} \tag{5.9}$$

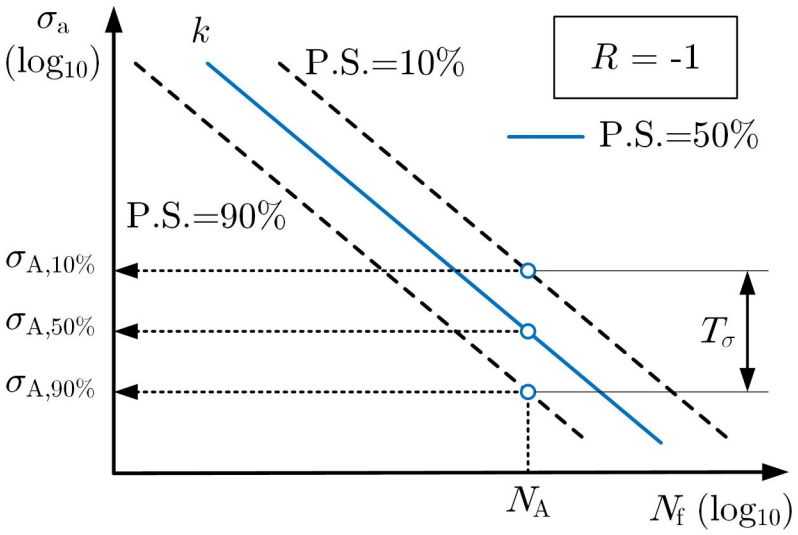

Figure 5.16: *Scatter T_σ*

from the mathematical model described by Eq. 5.5 the standard deviation of logarithms of number of cycles to failure is described by *L1_LOGN* and the standard deviation of stresses is *L1_SLOGS*. From Eq. 5.7 the standard deviation of logarithms is of *SN_SLOGN* and from stress point of view *SN_SLOGS*. Eq. 5.9 is taken as an example, but it is possible to define a similar index considering the stresses for a P.S. of 2.3% and 97.7% respectively.
A non-linear analysis of the data was also carried out. Following [22], the mathematical function was proposed as:

$$\sigma_a = A \cdot \left(C \cdot \frac{N_f + B}{N_f + C} \right)^{\beta} \tag{5.10}$$

which in excel® or matlab® language is written as:

$$\sigma_a = \text{KV\_A} \cdot \left(\text{KV\_C} \cdot \frac{N_f + \text{KV\_B}}{N_f + \text{KV\_C}} \right)^{\text{KV\_BETA}} \tag{5.11}$$

As the curve is defined with a higher number of parameters than linear models, the fitting curve better follows the experimental data even in outward regions. Statistical parameters were also derived here: *KV_SLOGN*, *KV_SLOGS* and *KV_R2*. With regard to the fatigue curve of the smooth specimen FAB014 in 42CrMo4+QT, the graph in Fig. 5.17 was obtained.
Tab. 5.6 shows all the data describing the curves.
Given the standard deviation on the number of cycles to failure it is possible to obtain the statistical range of dispersion for a survival probability of 97.7% and 2.3%. To do this, Basquin type regression from Eq. 5.7 was taken as a reference. The statistical parameters for carrying out the procedure using matlab® can be found in Tab. 5.6. The fatigue limits for a P.S. of 50% have been determined by imposing $N = 2 \cdot 10^7$ cycles. It was obtained Fig. 5.18.
For the smooth specimen, as can be seen in Fig. 5.18, for a number of cycles equal to $N_0 = 2.2012 \cdot 10^7$ cycles, fatigue limit is $\sigma_0 = 573.3$ MPa. Similar information was obtained for the notched specimens as shown in the following Fig. 5.21, 5.22, 5.23, 5.24, 5.19, 5.20 and Tab. 5.8, 5.9, 5.7. The fatigue limits derived all refer to the net nominal section.

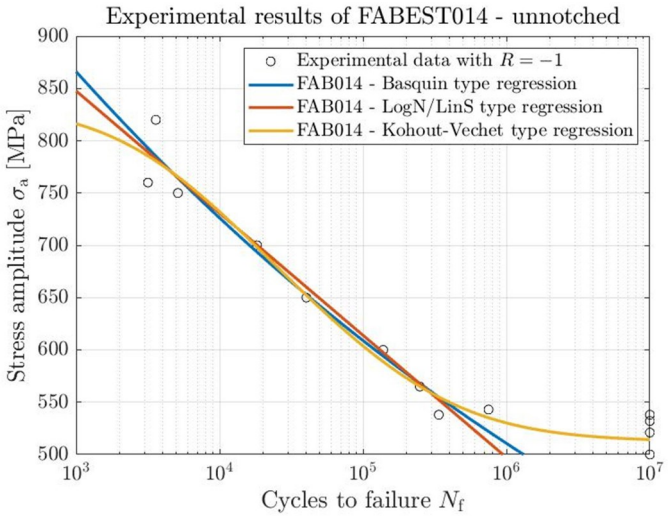

Figure 5.17: *Experimental data of FABEST014 - unnotched specimen - and fit curves from Eq. 5.5, 5.7 and 5.10*

parameters	code	values	description
logN/linS regression			
a	*L1CON*	10.3	y-axis intercept
b	*L1LIN*	-0.009	Slope
$\sigma_{\log_{10}}$	*L1_SLOGN*	0.198	Standard deviation of the logarithm of $_fN$
$\sigma_{\sigma,\log_{10}}$	*L1_SLOGS*	0.015	Standard deviation of the logarithm of stress
R^2	*L1_R2*	0.9584	Coefficient of determination
Basquin regression			
k	*SN_W*	13.076	Slope
C	*SN_C*	$2.57 \cdot 10^{41}$	Constant
$\sigma_{N,\log_{10}}$	*SN_SLOGN*	0.117	Standard deviation of the logarithm of $_fN$
$\sigma_{\sigma,\log_{10}}$	*SN_SLOGS*	0.014	Standard deviation of the logarithm of stress
R^2	*SN_R2*	0.9670	Coefficient of determination
Kohout-Vechet regression			
A	*KV _A*	2014.4	Constant
B	*KV _B*	3874	Constant
C	*KV _C*	388107	Constant
β	*KV _BETA*	-0.106	Constant
$\sigma_{\log_{10}}$	*KV _SLOGN*	0.357	Standard deviation of the logarithm of $_fN$
$\sigma_{\sigma,\log_{10}}$	*KV _SLOGS*	0.014	Standard deviation of the logarithm of stress
R^2	*KV _R2*	0.9662	Coefficient of determination

Table 5.6: *Statistical parameters for the curves of FAB001*

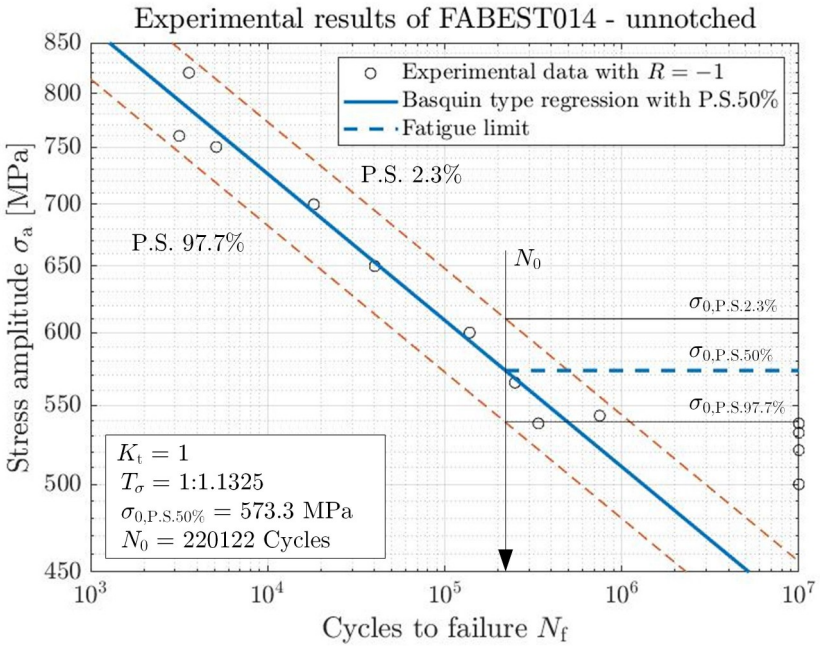

Figure 5.18: *Statistical scatter of smooth specimentFAB014. Kohout-Vechet regression was used to derive the fatigue limit.*

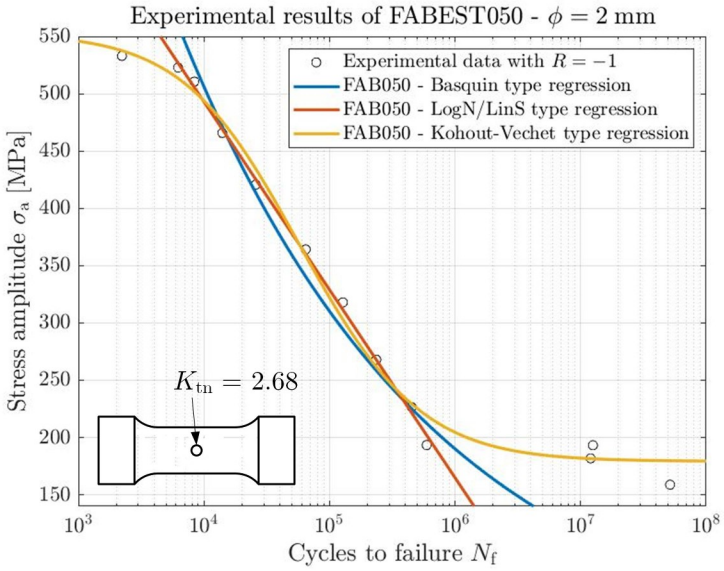

Figure 5.19: *Experimental data of FABEST050 and fit curves from Eq. 5.5, 5.7 and 5.10*

parameters	code	values	description
logN/linS regression			
a	*L1CON*	7.0	y-axis intercept
b	*L1LIN*	-0.006	Slope
$\sigma_{N,\log_{10}}$	*L1_SLOGN*	0.035	Standard deviation of the logarithm of $_fN$
$\sigma_{\sigma,\log_{10}}$	*L1_SLOGS*	0.009	Standard deviation of the logarithm of stress
R^2	*L1_R2*	0.9981	Coefficient of determination
Basquin regression			
k	*SN_W*	4.701	Slope
C	*SN_C*	$5.18 \cdot 10^{16}$	Constant
$\sigma_{N,\log_{10}}$	*SN_SLOGN*	0.125	Standard deviation of the logarithm of $_fN$
$\sigma_{\sigma,\log_{10}}$	*SN_SLOGS*	0.027	Standard deviation of the logarithm of stress
R^2	*SN_R2*	0.9753	Coefficient of determination
Kohout-Vechet regression			
A	*KV _A*	57910	Constant
B	*KV _B*	31306.8	Constant
C	*KV _C*	384558.1	Constant
β	*KV _BETA*	0.449	Constant
$\sigma_{N,\log_{10}}$	*KV _SLOGN*	0.351	Standard deviation of the logarithm of $_fN$
$\sigma_{\sigma,\log_{10}}$	*KV _SLOGS*	0.024	Standard deviation of the logarithm of stress
R^2	*KV _R2*	0.9925	Coefficient of determination

Table 5.7: *Statistical parameters for the curves of FABEST050, with* $\phi = 2$ mm

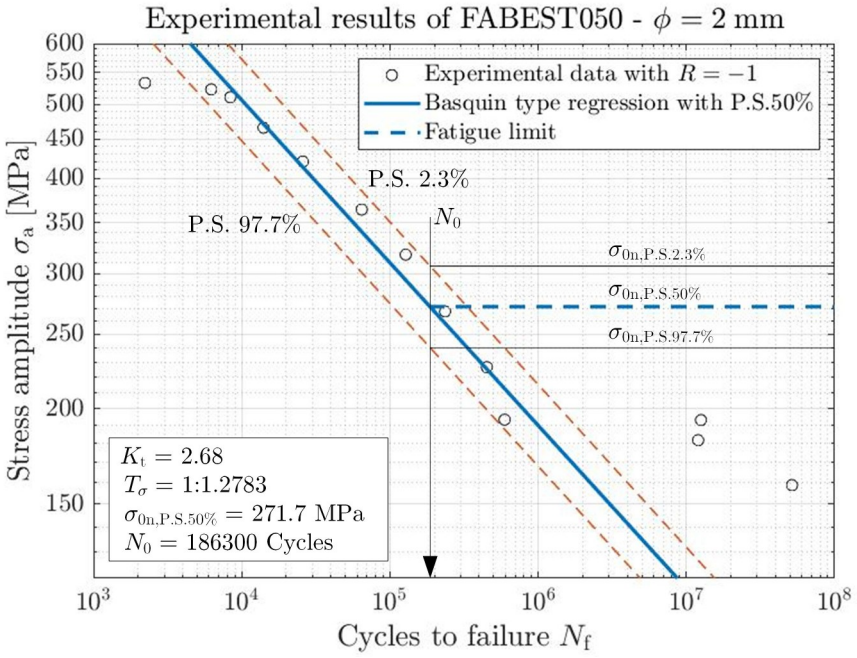

Figure 5.20: *Statistical scatter of FABEST050 with* $\phi = 2$ mm

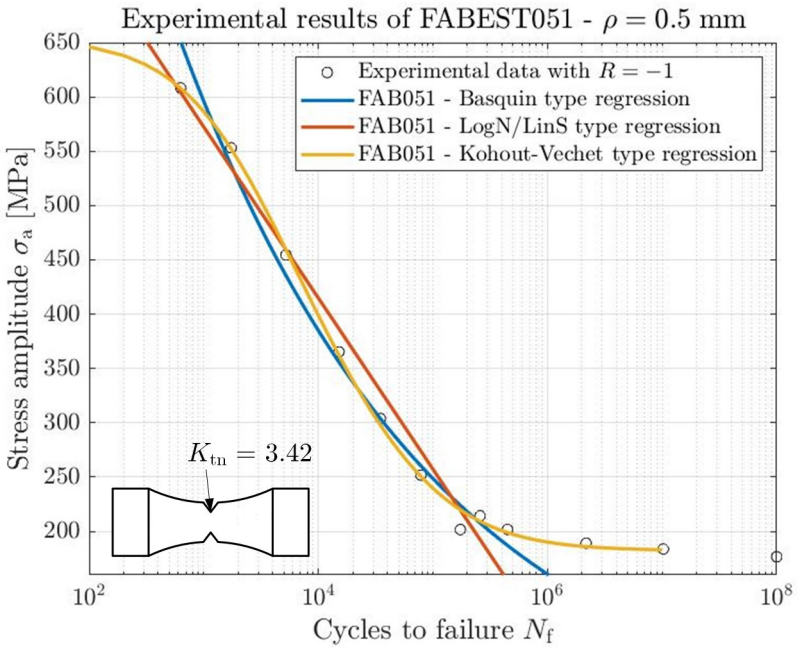

Figure 5.21: *Experimental data of FABEST051 and fit curves from Eq. 5.5, 5.7 and 5.10*

parameters	code	values	description
logN/linS regression			
a	*L1CON*	6.63	y-axis intercept
b	*L1LIN*	-0.006	Slope
$\sigma_{N,\log_{10}}$	*L1_SLOGN*	0.169	Standard deviation of the logarithm of $_fN$
$\sigma_{\sigma,\log_{10}}$	*L1_SLOGS*	0.054	Standard deviation of the logarithm of stress
R^2	*L1_R2*	0.9749	Coefficient of determination
Basquin regression			
k	*SN_W*	5.268	Slope
C	*SN_C*	$4.17 \cdot 10^{17}$	Constant
$\sigma_{\log_{10}}$	*SN_SLOGN*	0.142	Standard deviation of the logarithm of $_fN$
$\sigma_{\sigma,\log_{10}}$	*SN_SLOGS*	0.027	Standard deviation of the logarithm of stress
R^2	*SN_R2*	0.9824	Coefficient of determination
Kohout-Vechet regression			
A	*KV _A*	6740.4	Constant
B	*KV _B*	2232.7	Constant
C	*KV _C*	153153.3	Constant
β	*KV _BETA*	-0.6957	Constant
$\sigma_{\log_{10}}$	*KV _SLOGN*	0.017	Standard deviation of the logarithm of $_fN$
$\sigma_{\sigma,\log_{10}}$	*KV _SLOGS*	0.017	Standard deviation of the logarithm of stress
R^2	*KV _R2*	0.9979	Coefficient of determination

Table 5.8: *Statistical parameters for the curves of FABEST051, with ρ = 0.5 mm*

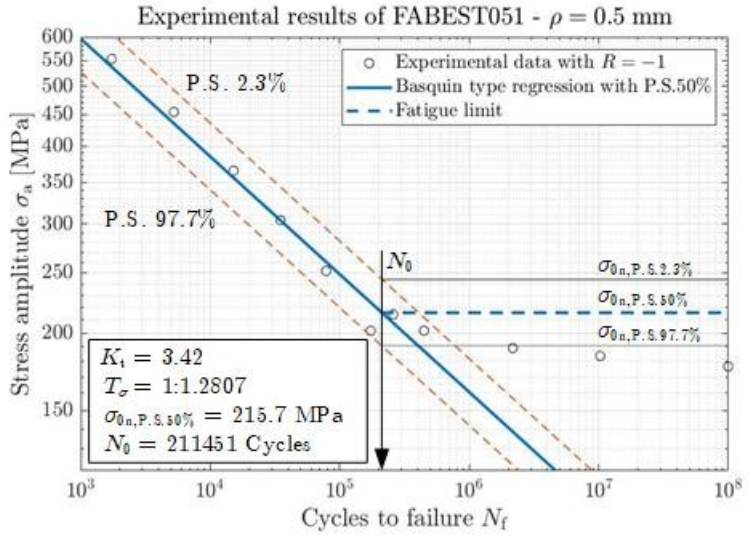

Figure 5.22: *Statistical scatter of FABEST051 with* $\rho = 0.5$ mm

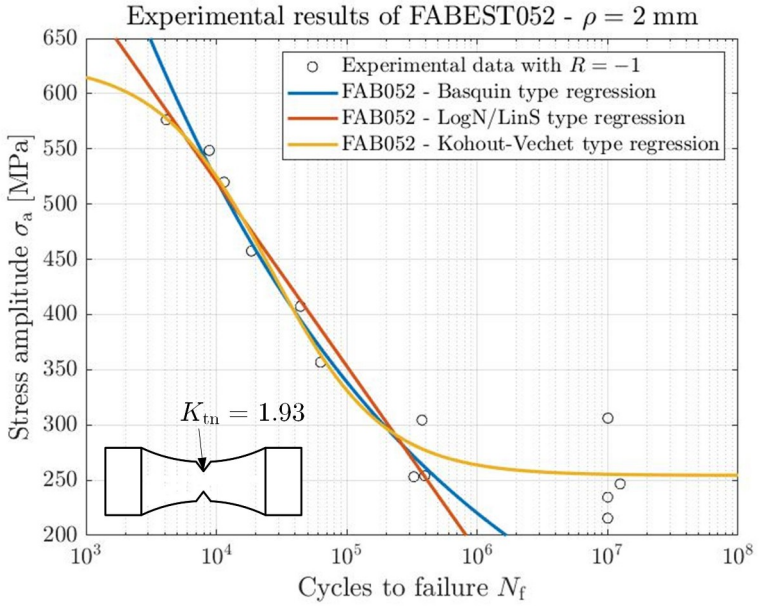

Figure 5.23: *Experimental data of FABEST052 and fit curves from Eq. 5.5, 5.7 and 5.10*

parameters	code	values	description
logN/linS regression			
a	*L1CON*	7.3	y-axis intercept
b	*L1LIN*	-0.007	Slope
$\sigma_{N,\log_{10}}$	*L1_SLOGN*	0.197	Standard deviation of the logarithm of $_fN$
$\sigma_{\sigma,\log_{10}}$	*L1_SLOGS*	0.033	Standard deviation of the logarithm of stress
R^2	*L1_R2*	0.9562	Coefficient of determination
Basquin regression			
k	*SN_W*	5.931	Slope
C	*SN_C*	$9.76 \cdot 10^{19}$	Constant
$\sigma_{N,\log_{10}}$	*SN_SLOGN*	0.248	Standard deviation of the logarithm of $_fN$
$\sigma_{\sigma,\log_{10}}$	*SN_SLOGS*	0.042	Standard deviation of the logarithm of stress
R^2	*SN_R2*	0.9307	Coefficient of determination
Kohout-Vechet regression			
A	*KV _A*	101125469	Constant
B	*KV _B*	27757	Constant
C	*KV _C*	60072.2	Constant
β	*KV _BETA*	-1.172	Constant
$\sigma_{N,\log_{10}}$	*KV _SLOGN*	0.614	Standard deviation of the logarithm of $_fN$
$\sigma_{\sigma,\log_{10}}$	*KV _SLOGS*	0.039	Standard deviation of the logarithm of stress
R^2	*KV _R2*	0.9740	Coefficient of determination

Table 5.9: *Statistical parameters for the curves of FABEST052, with ρ = 2 mm*

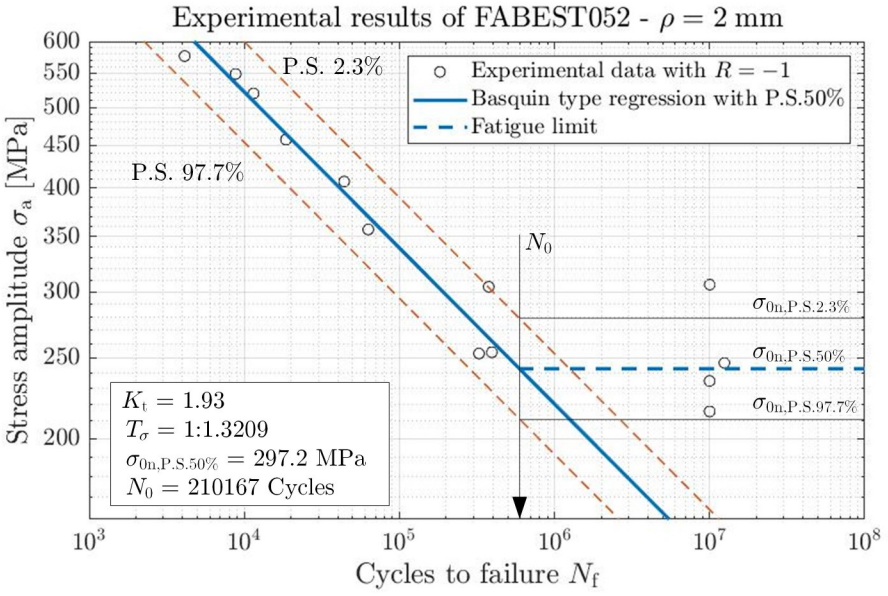

Figure 5.24: *Statistical scatter of FABEST052 with ρ = 2 mm*

5.3 Fatigue tests from literature [39] [44]

With regard to specimens extracted from the literature they were tested at frequencies up to 15 Hz with servohydraulic testing machines and at a frequency of 30 Hz with mechanical resonance testing machine for S275 structural steel and AlMgSi1 alloy [39]. With regard to the data from the Santus, Taylor and Benedetti article [44], was found that the test frequency was 150 Hz. In both articles the stress ratio set was $R = -1$.

5.3.1 Fatigue data from literature [39]

With regard to the fatigue tests performed in [39], the following fit curves were obtained. In Fig. 5.25 and 5.26 and 5.27 the fatigue curves of test specimen F, shown in Fig. **??**, in S275 material are represented. The fit curves were obtained with a programming code similar to that seen in the previous section for FAB001

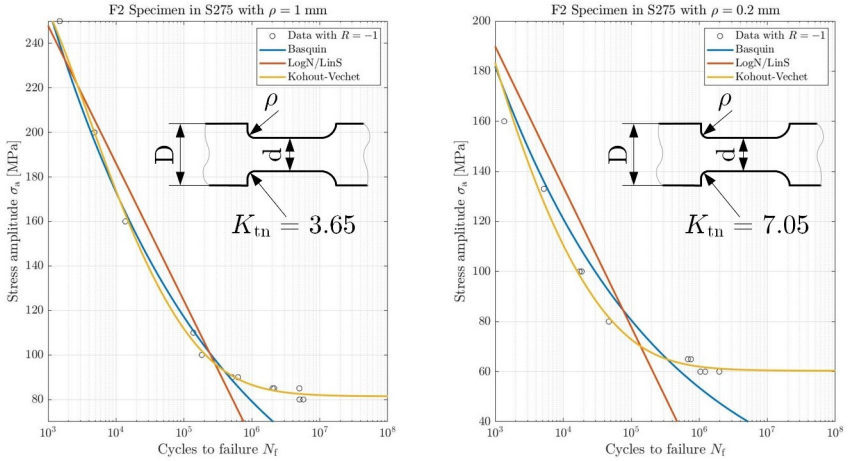

Figure 5.25: *Experimental data found in [39] and fit curves from Eq. 5.5, 5.7 and 5.10*

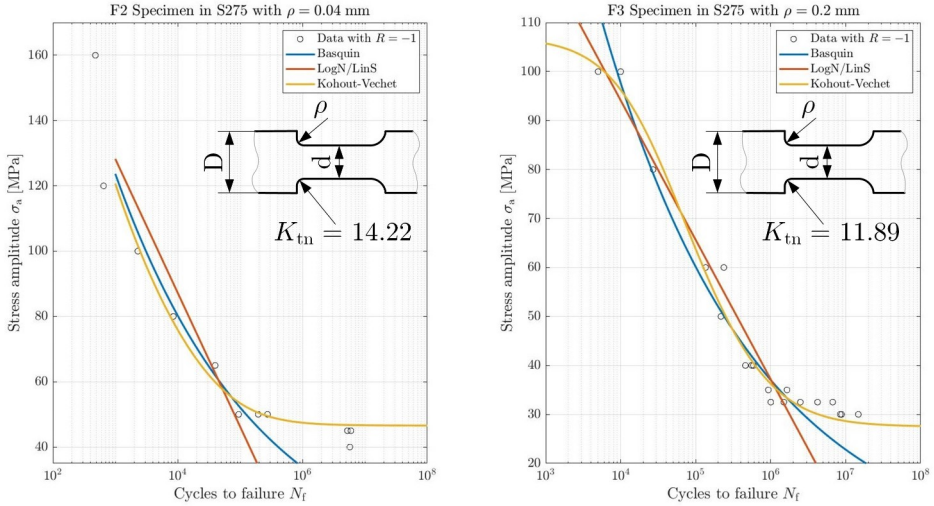

Figure 5.26: *Experimental data found in [39] and fit curves from Eq. 5.5, 5.7 and 5.10*

In Fig. 5.28, 5.29 and 5.30 the fatigue curves of test specimen F, shown in Fig. **??**, in AlMgSi1 material are represented.
As with the previous samples, the statistical scatter was determined using Basquin's equation (Eq. 5.7), in Fig. 5.31, 5.32, 5.33, 5.34 and 5.35 for S275 material.
For AlMgSi1 material the curves in Fig. 5.36, 5.37, 5.38, 5.39 and 5.40 were obtained.

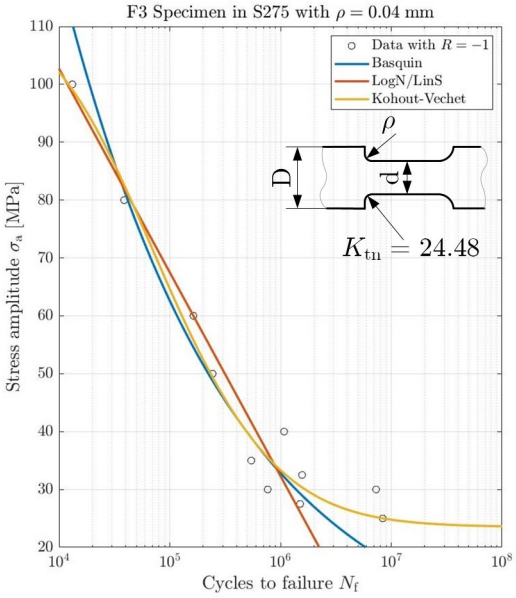

Figure 5.27: *Experimental data found in [39] and fit curves from Eq. 5.5, 5.7 and 5.10*

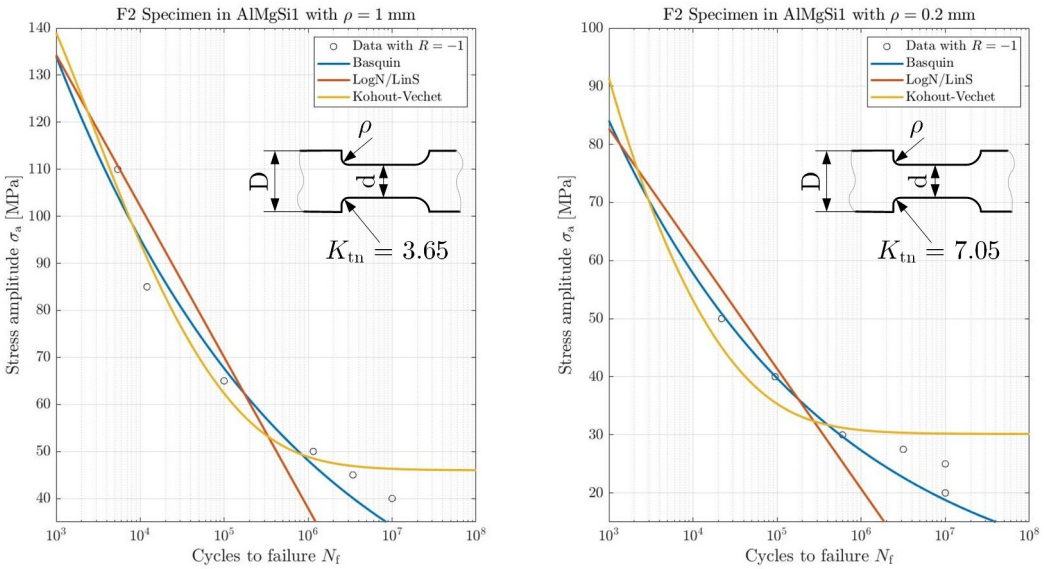

Figure 5.28: *Experimental data found in [39] and fit curves from Eq. 5.5, 5.7 and 5.10*

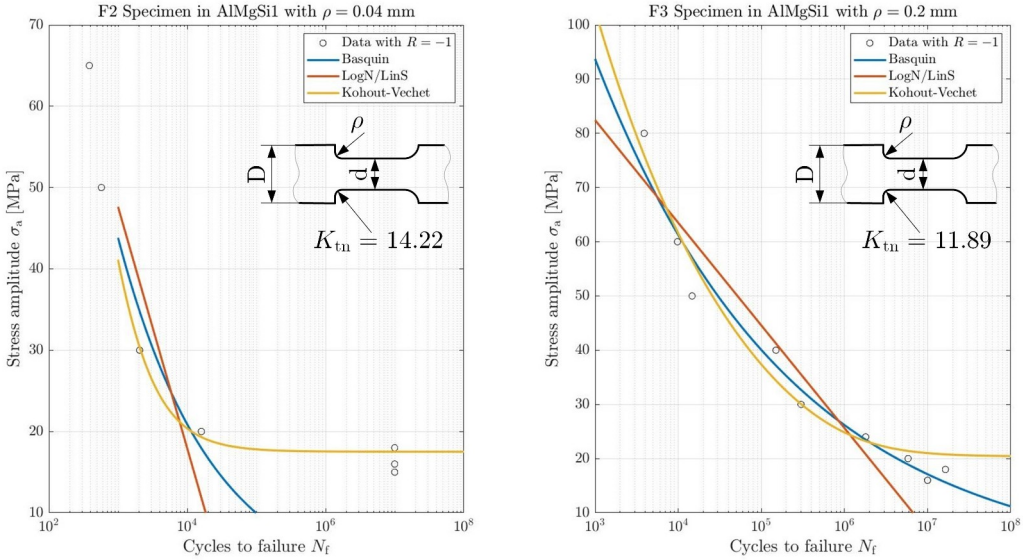

Figure 5.29: *Experimental data found in [39] and fit curves from Eq. 5.5, 5.7 and 5.10*

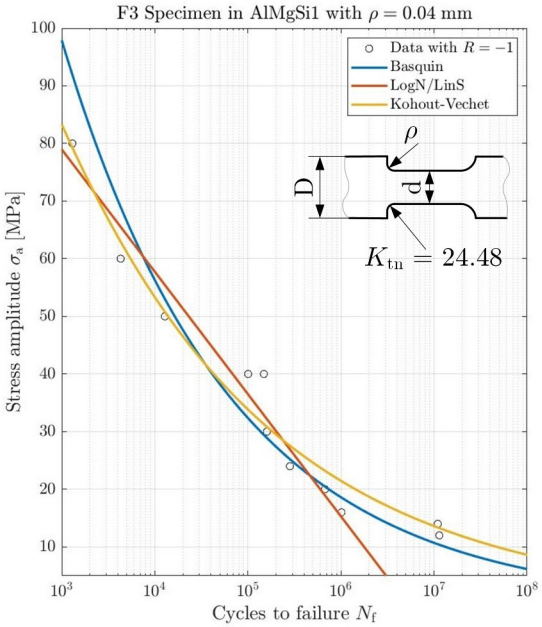

Figure 5.30: *Experimental data found in [39] and fit curves from Eq. 5.5, 5.7 and 5.10*

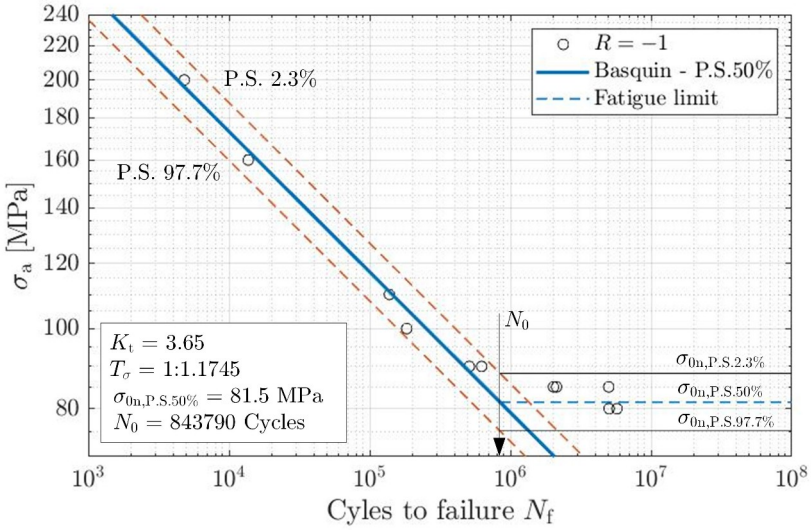

Figure 5.31: *Statistical scatter of F2-specimen in S275 with* $\rho = 1$ mm*, stress related to net section*

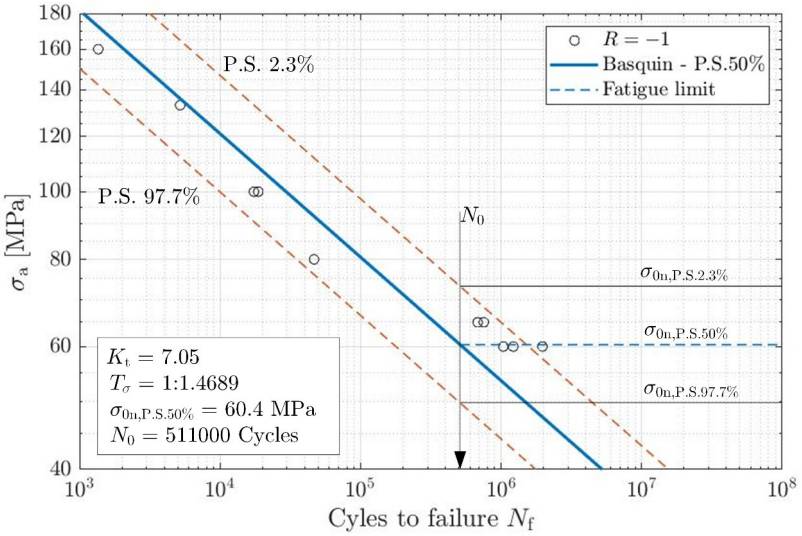

Figure 5.32: *Statistical scatter of F2-specimen in S275 with* $\rho = 0.2$ mm*, stress related to net section*

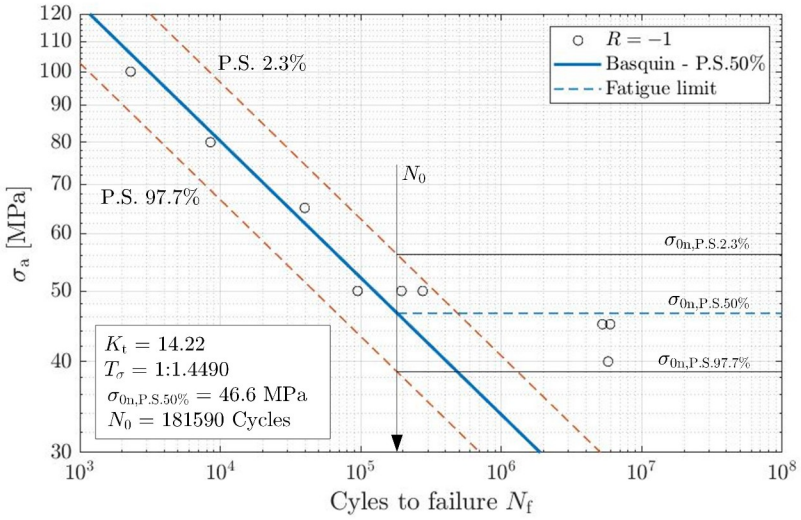

Figure 5.33: *Statistical scatter of F2-specimen in S275 with* $\rho = 0.04$ mm*, stress related to net section*

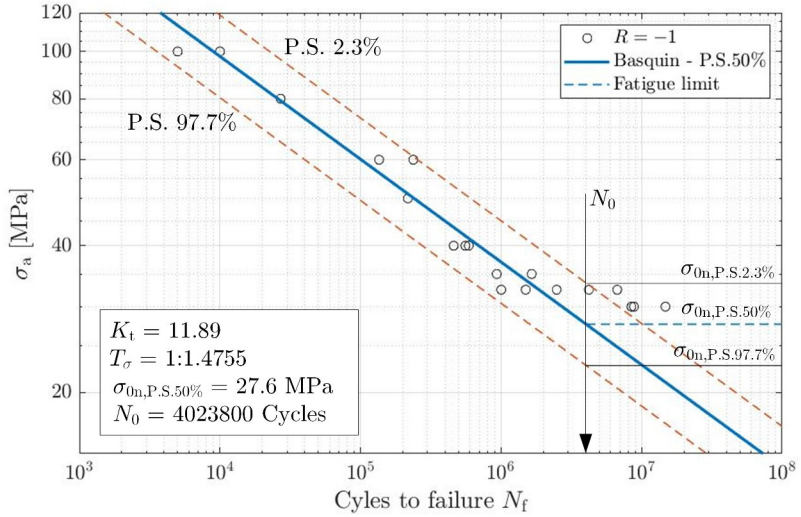

Figure 5.34: *Statistical scatter of F3-specimen in S275 with* $\rho = 0.2$ mm*, stress related to net section*

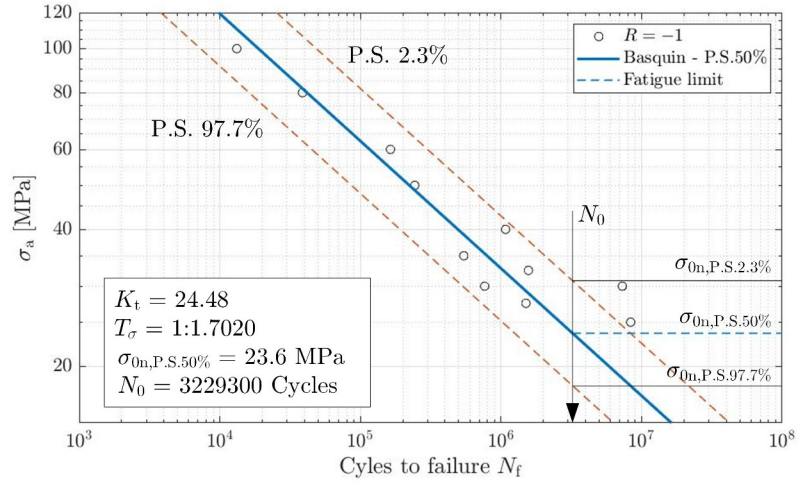

Figure 5.35: *Statistical scatter of F3-specimen in S275 with* $\rho = 0.04$ mm*, stress related to net section*

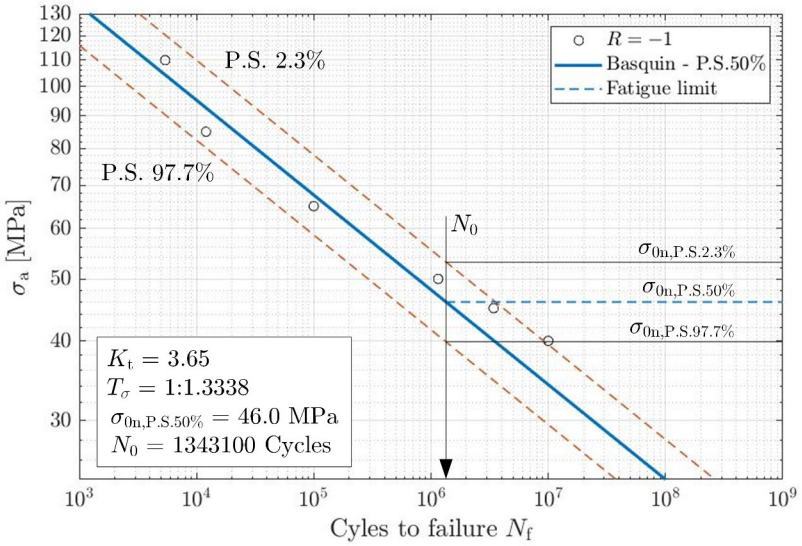

Figure 5.36: *Statistical scatter of F2-specimen in AlMgSi1 with* $\rho = 1$ mm

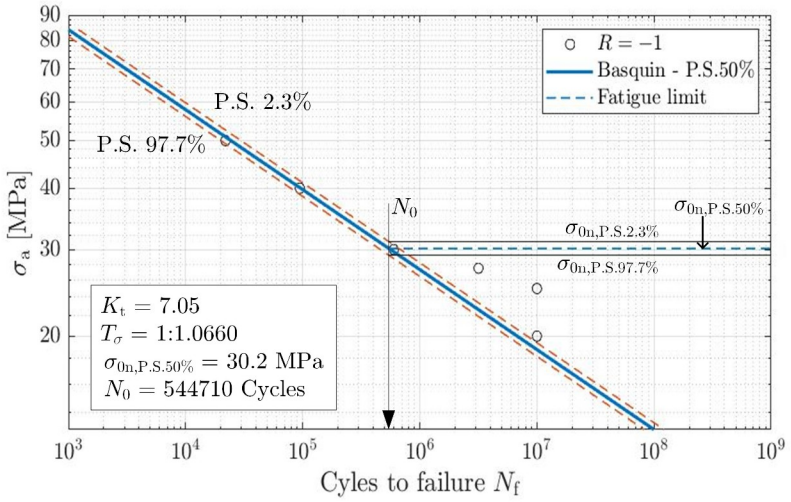

Figure 5.37: *Statistical scatter of F2-specimen in AlMgSi1 with* $\rho = 0.2$ mm

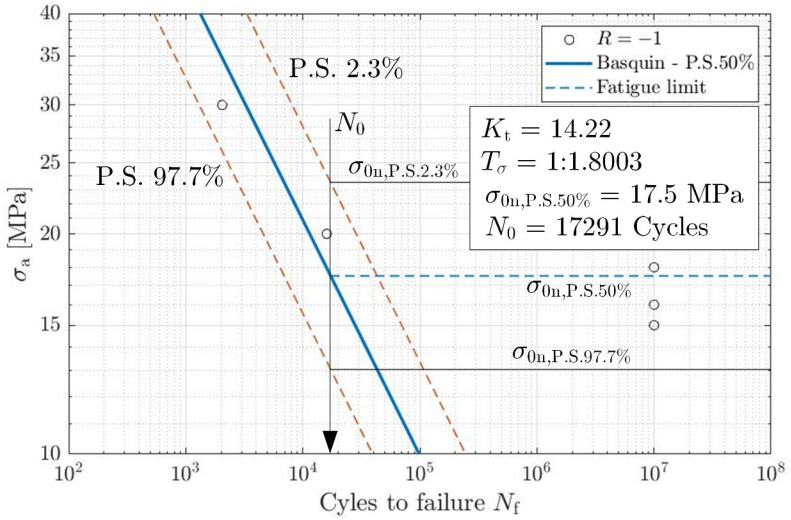

Figure 5.38: *Statistical scatter of F2-specimen in AlMgSi1 with* $\rho = 0.04$ mm

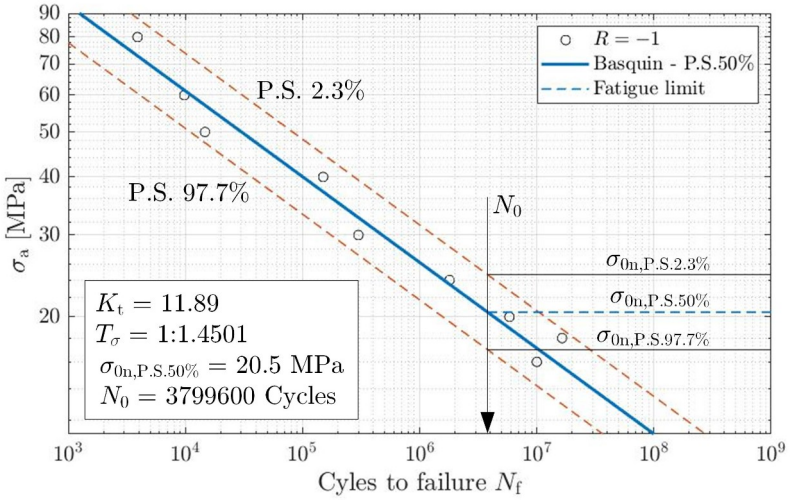

Figure 5.39: *Statistical scatter of F3-specimen in AlMgSi1 with* $\rho = 0.2$ mm

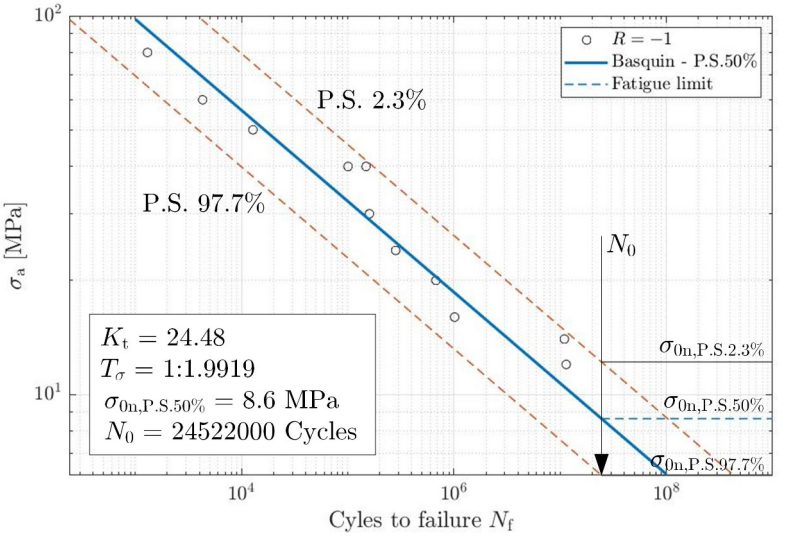

Figure 5.40: *Statistical scatter of F3-specimen in AlMgSi1 with* $\rho = 0.04$ mm

Parameters	Plain	Blunt	Sharp
$P_{50\%}$, MPa	390	163	87.5
$P_{10\%}$, MPa	363	147	83.5
$P_{90\%}$, MPa	417	178	91.3
St.Dev., MPa	20.7	12.1	2.93
k	1163	n/a	2127
b ($\cdot 10^{0}$)	−80.139	n/a	−215.96

Table 5.10: *Data from [44] with stress ratio $R = -1$ for 42CrMo4 + QT*

5.3.2 Fatigue data from literature [44]

In this subsection, data and graphs obtained in [44] are collected. Two specimens with the following characteristics were considered in the cited article:

- Blunt specimen with $\rho = 1$ mm at the tip of the notch
- Sharp specimen with $\rho = 0.2$ mm at the tip of the notch

The corresponding fatigue curves can be viewed in Fig. 5.41.

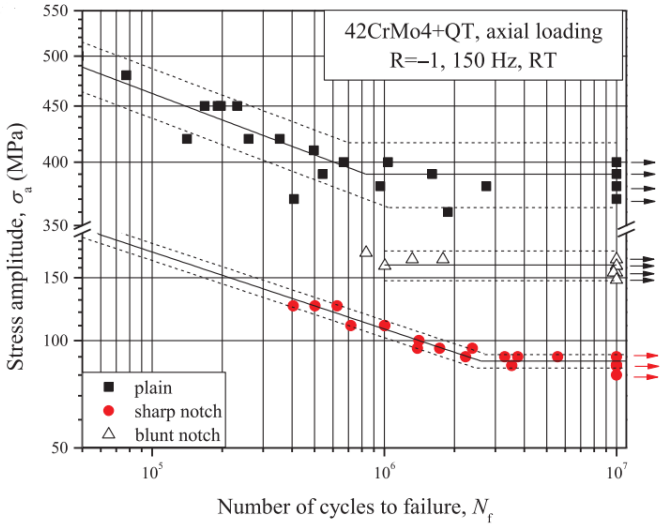

Figure 5.41: *Fatigue curves of specimens found in [44]*

Relevant data from the tests conducted by Santus, Taylor and Benedetti [44] were collected in Tab. 5.10 The equation used here has the following form:

$$\sigma_a = k \cdot N_f^b \tag{5.12}$$

Eq. 5.12 is linked to Eq. 5.7, i.e. the Basquin equation:

$$\begin{aligned} C &= k^w \\ w &= -\frac{1}{b} \end{aligned} \tag{5.13}$$

Chapter 6

DESCRIPTION OF CRACK INITIATION POINT

6.1 Introduction to Dino-Lite microscope

In this chapter the fracture sections of the specimens will be analyzed. The *Dino-Lite* microscope with a 5 MPx camera was used to achieve the goal. It consists of a base where the specimens are placed, support structure and the microscope connected to a PC via USB cable (Fig. 6.1)

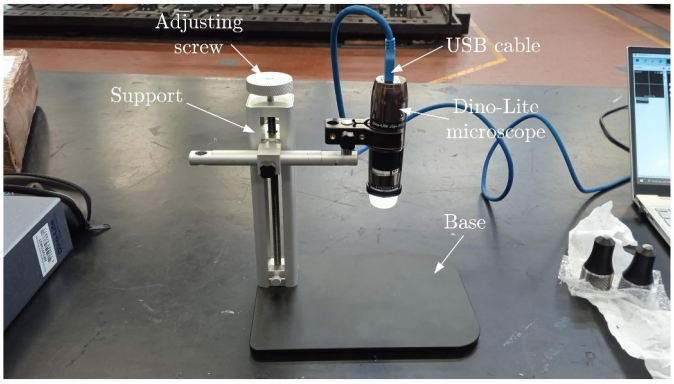

Figure 6.1: *Dino-Lite microscope*

The specimen is placed under the lens as shown in the Fig. 6.2.

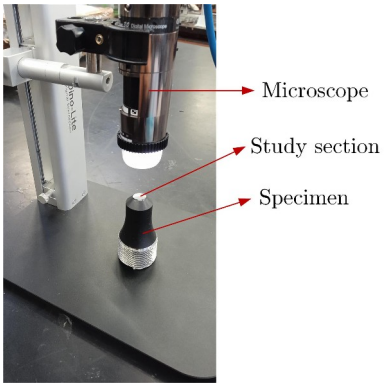

Figure 6.2: *Placement of the specimen under analysis*

Through the *DinoCapture* software it was possible to obtain information on the fracture section, in particular on the fatigue crack initiation point. A typical screenshot of the program can be seen in the Fig. 6.3. With the help of the software it is possible to adjust the parameters of the images, such

as brightness, contrast, etc. and, with the commands placed in the upper menù, add some comments, length measures etc.

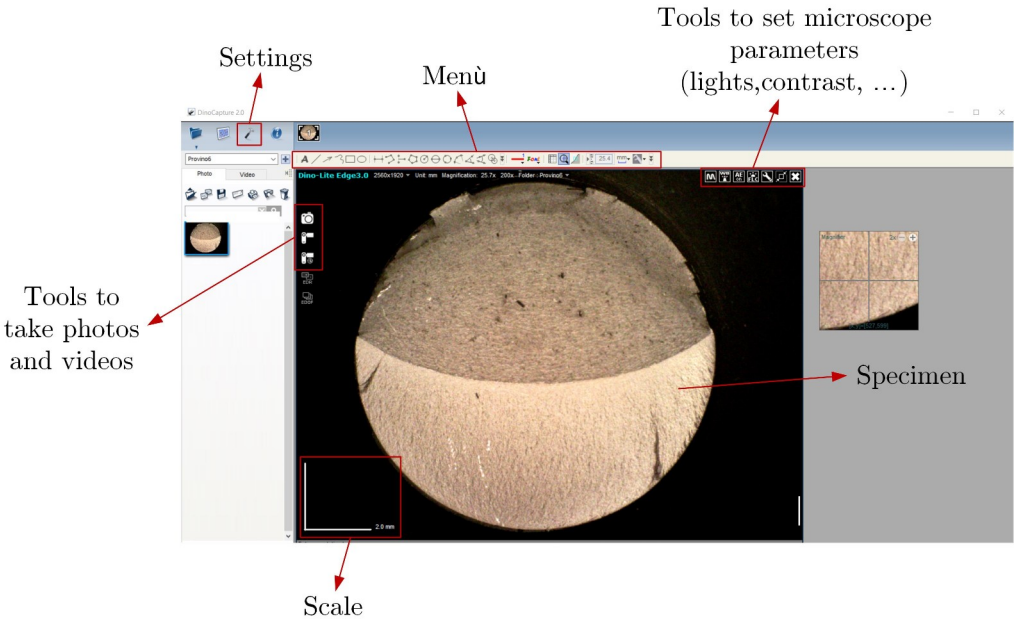

Figure 6.3: *DinoCapture software*

In the following paragraphs, numerous images have been collected describing the fracture section of the specimens. The Amsler testing machine also returned graphs of static force, dynamic force and frequency as functions of time. The sudden decrease in frequency at a certain number of cycles, identifies the initiation of the fatigue crack.

6.2 FABEST_V05 specimen

As mentioned in paragraph 5.2.2 the following experimental data for FAB051 were collected in the current Tab. 6.1: stress ratio R, nominal net stress $\sigma_{a,n}$, number of cycles to fracture N_f, frequency f , start and end of the test.

Specimen	R	$\sigma_{a,n}$ [MPa]	N_f [cycles]	f [Hz]	Start	End
FAB051_2B	-1	608.3	629	184	28/07/21	28/07/21
FAB051_5	-1	553.2	1732	184	20/07/21	20/07/21
FAB051_9B	-1	454.4	5227	184	30/06/2021	30/06/2021
FAB051_10	-1	365.3	15137	184	30/06/2021	30/06/2021
FAB051_8	-1	304.0	34867	184	29/06/21	29/06/21
FAB051_3	-1	251.8	78435	184	28/06/21	28/06/21
FAB051_7	-1	201.7	173482	184	29/06/21	29/06/21
FAB051_4	-1	214.4	258440	184	28/06/21	28/06/21
FAB051_1	-1	201.8	447210	184	20/07/21	20/07/21
FAB051_6	-1	189.2	2169391	184	28/06/21	28/06/21
FAB051_2	-1	183.8	10248826	184	27/07/21	28/07/21
FAB051_9	-1	176.7	100000000	184	30/06/21	07/07/21

Table 6.1: *Parameters of the experimental results of FAB051*

For each specimen, the Amsler test machine returns three graphs: static force, dynamic force and frequency as a function of time. When the frequency drops dramatically, fatigue crack initiation can be observed at that precise instant. An example is shown in Fig. 6.4

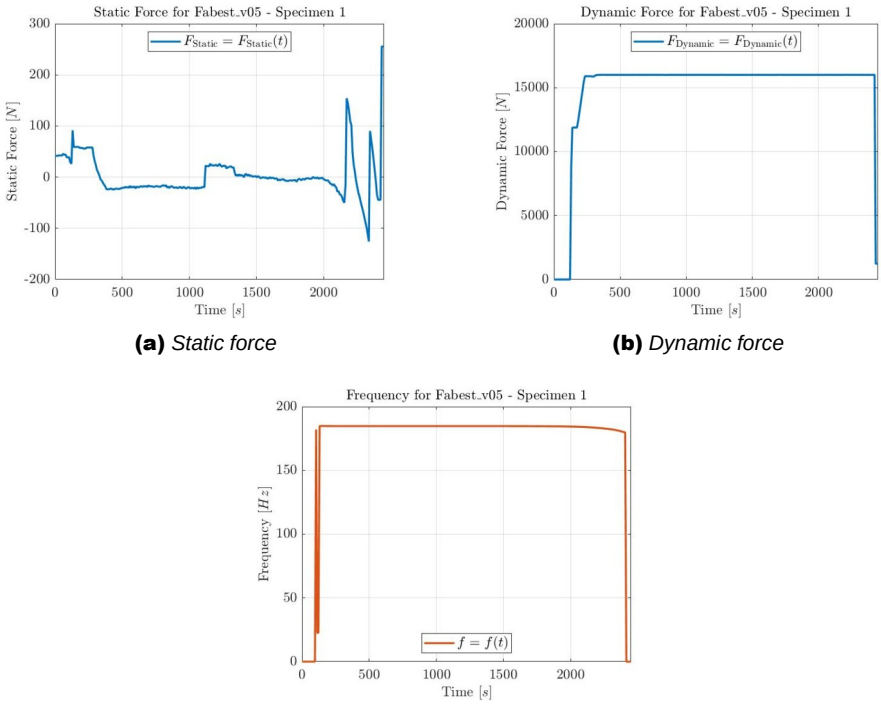

(a) *Static force*

(b) *Dynamic force*

(c) *Frequency*

Figure 6.4: *Forces and frequency as a function of time*

Images in Fig. 6.5, 6.6, 6.7, 6.8, 6.9, 6.10, 6.11, 6.12, 6.13 and 6.14 describing the fracture section of the specimens with the magnification used were collected

(a) *Part of the specimen 1*

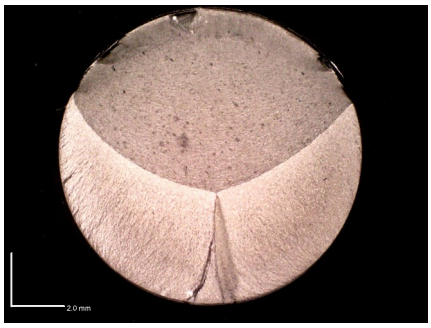

(b) *Fracture section with 24.6x magnification*

(c) *Fatigue lines in part of the fracture section with x magnification*

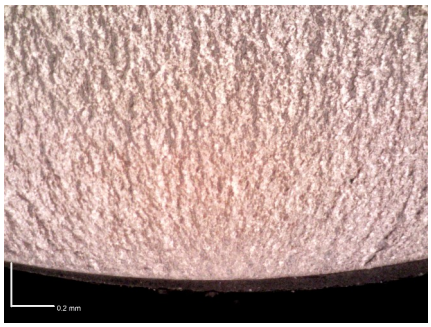

(d) *Crack initiation point with x magnification*

Figure 6.5: *Severalpictures of specimen 1 - FAB051*

(a) *part of the specimen 2*

(b) *Fracture section with 26.3x magnification*

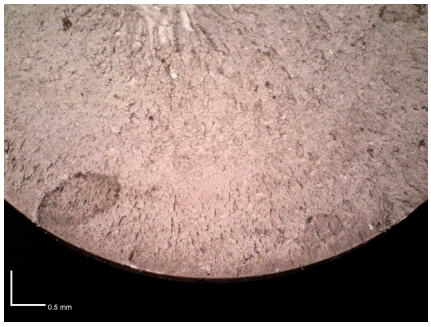

(c) *Fatigue lines in part of the fracture section with 62.6x magnification*

(d) *Part of the fracture section with 199.6x magnification*

Figure 6.6: *Severalpictures of specimen 2 - FAB051*

(a) *part of the specimen 3*

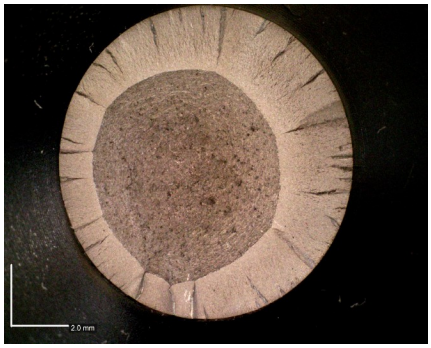

(b) *Fracture section with 26.3x magnification*

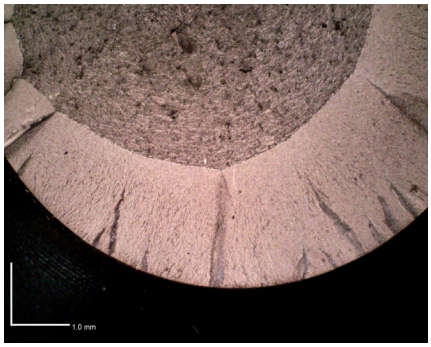

(c) *Part of the fracture section with 53.5x magnification*

(d) *Part of the fracture section with 185.5x magnification*

Figure 6.7: *Severalpictures of specimen 3 - FAB051*

(a) *part of the specimen 4*

(b) *Fracture section with 28.8x magnification*

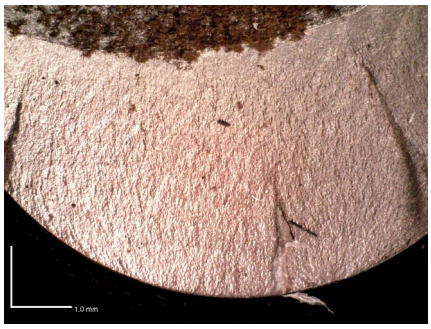

(c) *Fatigue lines in part of the fracture section with 55.7x magnification*

(d) *Crack initiation point with 199.2x magnification*

Figure 6.8: *Severalpictures of specimen 4 - FAB051*

(a) *part of the specimen 5*

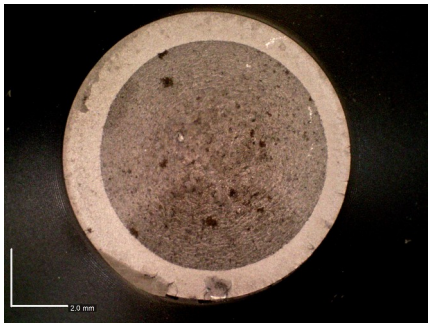

(b) *Fracture section with 26.0x magnification*

(c) *Part of the fracture section with 67.5x magnification*

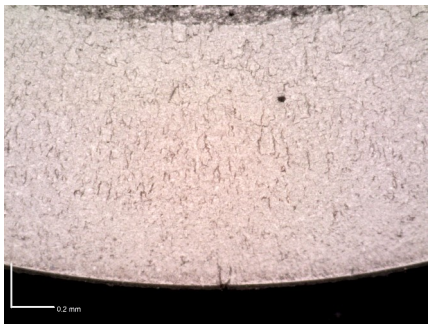

(d) *Part of the fracture section with 200.7x magnification*

Figure 6.9: *Severalpictures of specimen 5 - FAB051*

(a) *part of the specimen 6*

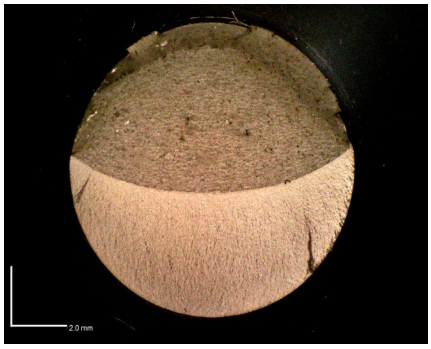

(b) *Fracture section with 28.8x magnification*

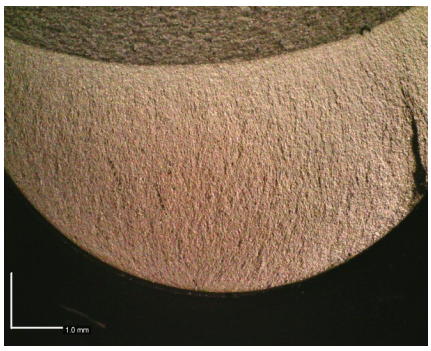

(c) *Fatigue lines in part of the fracture section with 48.3x magnification*

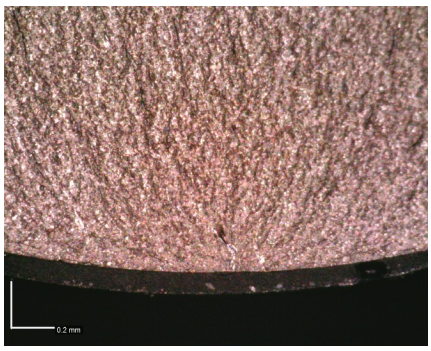

(d) *Crack initiation point with 203.5x magnification*

Figure 6.10: *Severalpictures of specimen 6 - FAB051*

(a) *part of the specimen 7*

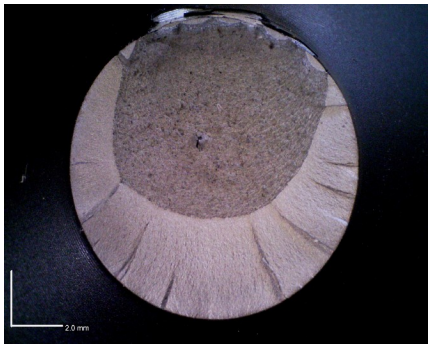

(b) *Fracture section with 23.8x magnification*

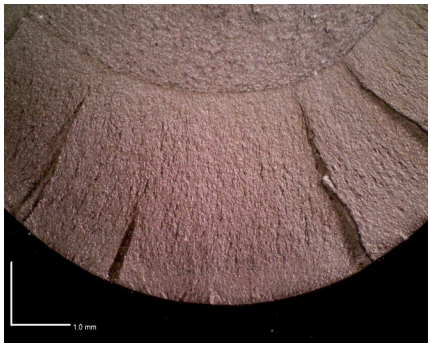

(c) *Fatigue lines in part of the fracture section with 54.3x magnification*

(d) *Crack initiation point with 97.2x magnification*

Figure 6.11: *Severalpictures of specimen 7 - FAB051*

(a) *part of the specimen 8*

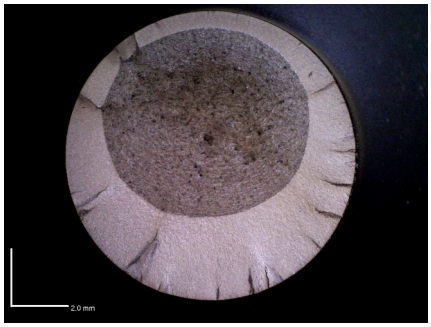

(b) *Fracture section with 26.3x magnification*

(c) *Part of the fracture section with x magnification*

(d) *Part of the fracture section with 99.6x magnification*

Figure 6.12: *Severalpictures of specimen 8 - FAB051*

(a) *part of the specimen 9*

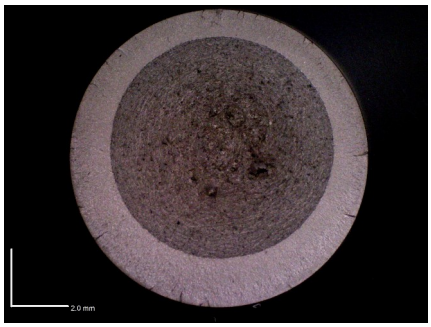

(b) *Fracture section with 26.3x magnification*

(c) *Part of the fracture section with 63.2x magnification*

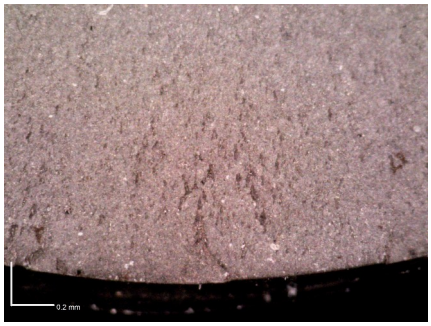

(d) *Part of the fracture section with 97.4x magnification*

Figure 6.13: *Severalpictures of specimen 9 - FAB051*

(a) *part of the specimen 10*

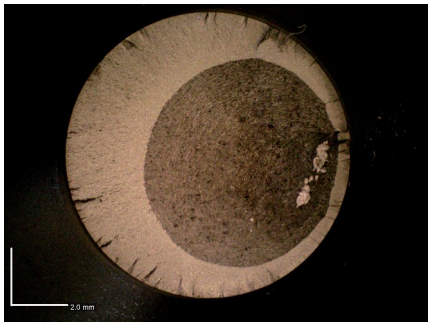

(b) *Fracture section with 26.0x magnification*

(c) *Part of the fracture section with 52.5x magnification*

(d) *Part of the fracture section with 198.9x magnification*

Figure 6.14: *Severalpictures of specimen 10 - FAB051*

Specimen	R	$\sigma_{a,n}$ [MPa]	N_f [cycles]	f [Hz]	Start	End
FAB052_10B	-1	608.7	992	184	20/07/21	20/07/21
FAB052_1B	-1	576.4	4124	184	22/07/21	22/07/21
FAB052_2B	-1	548.6	8806	184	23/07/21	23/07/21
FAB052_8B	-1	519.9	11458	184	08/07/21	08/07/21
FAB052_5	-1	457.5	18571	184	29/06/21	29/06/21
FAB052_3	-1	407.4	44054	184	29/06/21	29/06/21
FAB052_4	-1	356.7	62956	184	29/06/21	29/06/21
FAB052_9	-1	253.1	325894	184	19/07/21	19/07/21
FAB052_6	-1	304.4	376654	184	29/06/21	29/06/21
FAB052_7	-1	254.0	394885	184	29/06/21	29/06/21
FAB052_10	-1	234.6	10000000	184	20/07/21	21/07/21
FAB052_8	-1	215.6	10000000	184	07/07/21	08/07/21
FAB052_2	-1	306.2	10031491	184	22/07/21	23/07/21
FAB052_1	-1	246.6	12453336	184	21/07/21	22/07/21

Table 6.2: *Parameters of the experimental results of FAB052*

6.3 FABEST_V20 specimen

The following experimental data were also collected for test specimen FABEST_V20: stress ratio R, nominal net stress $\sigma_{a,n}$, number of cycles to fracture N_f, frequency f , start and end of the test.
Images in Fig. 6.15, 6.16, 6.17, 6.18, 6.19, 6.20, 6.21, 6.22, 6.23 and 6.24 describing the fracture section of the specimens with the magnification used were collected.

(a) *Part of the specimen 1*

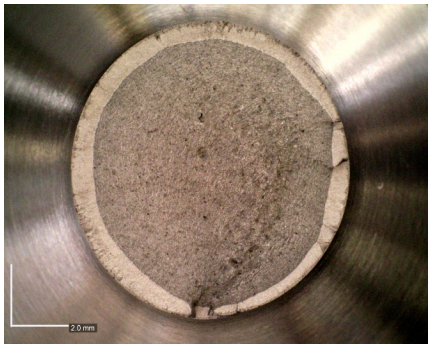

(b) *Fracture section with x magnification*

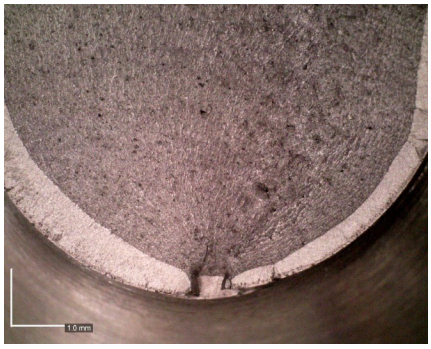

(c) *Part of the fracture section with 49.5x magnification*

(d) *Part of the fracture section with 164.9x magnification*

Figure 6.15: *Severalpictures of specimen 1 - FAB051*

(a) *Part of the specimen 1*

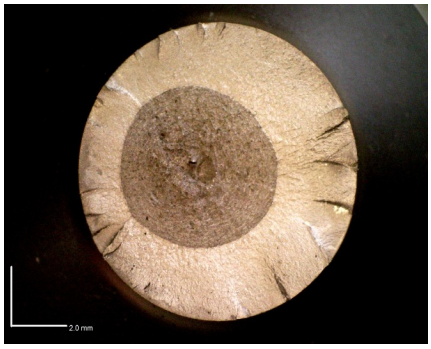

(b) *Fracture section with 25.6x magnification*

(c) *Part of the fracture section with 67.1x magnification*

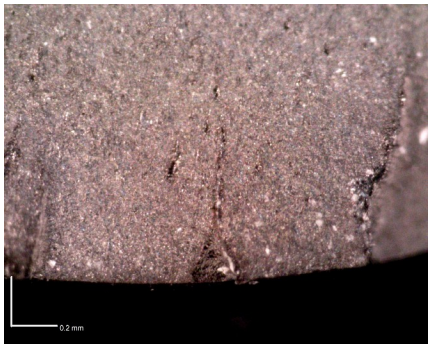

(d) *Part of the fracture section with 211.4x magnification*

Figure 6.16: *Severalpictures of specimen 2 - FAB051*

(a) *Part of the specimen 1*

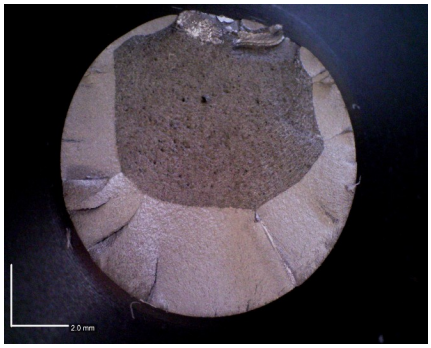

(b) *Fracture section with 26.3x magnification*

(c) *Fatigue lines in part of the fracture section with 67.8x magnification*

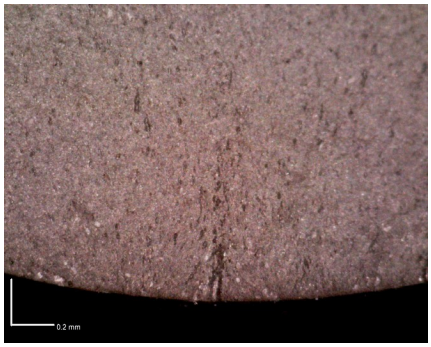

(d) *Crack initiation point with 197.4x magnification*

Figure 6.17: *Severalpictures of specimen 3 - FAB051*

(a) *Part of the specimen 1*

(b) *Fracture section with 28.4x magnification*

(c) *Fatigue lines in part of the fracture section with 63.8x magnification*

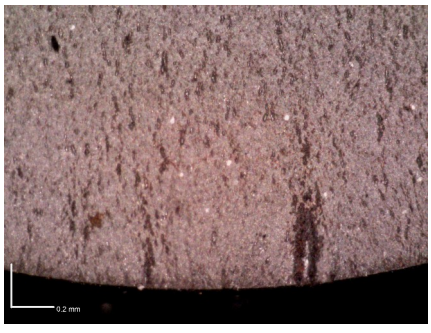

(d) *Crack initiation point with 198.1x magnification*

Figure 6.18: *Severalpictures of specimen 4 - FAB051*

(a) *Part of the specimen 1*

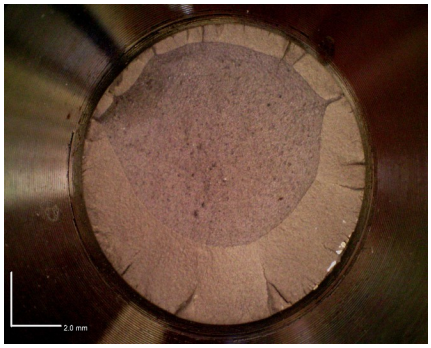

(b) *Fracture section with 23.1x magnification*

(c) *Part of the fracture section with 42.6x magnification*

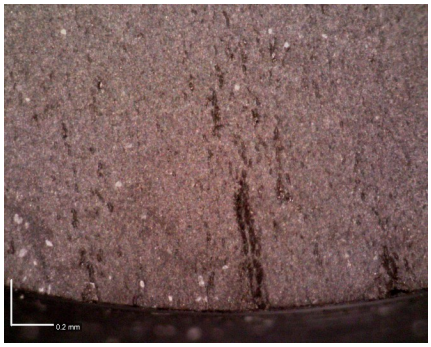

(d) *Part of the fracture section with 195.5x magnification*

Figure 6.19: *Severalpictures of specimen 5 - FAB051*

(a) *Part of the specimen 1*

(b) *Fracture section with 26.3x magnification*

(c) *Fatigue lines in part of the fracture section with 63.1x magnification*

(d) *Crack initiation point with 188.3x magnification*

Figure 6.20: *Severalpictures of specimen 6 - FAB051*

(a) *Part of the specimen 1*

(b) *Fracture section with 25.1x magnification*

(c) *Fatigue lines in part of the fracture section with 57.2x magnification*

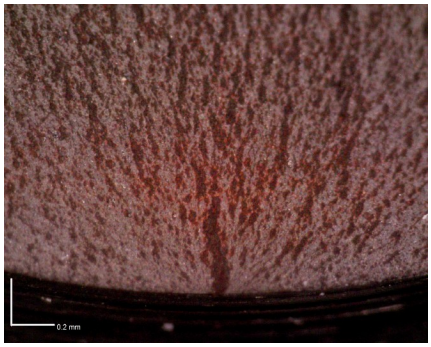

(d) *Crack initiation point with 199.2x magnification*

Figure 6.21: *Severalpictures of specimen 7 - FAB051*

(a) *Part of the specimen 1*

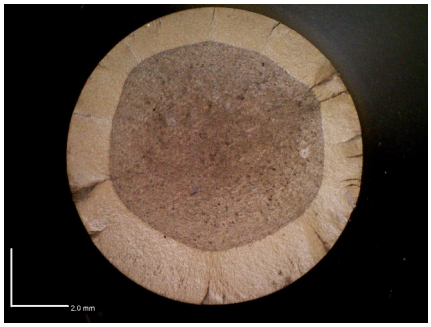

(b) *Fracture section with 26.3x magnification*

(c) *Part of the fracture section with 52.7x magnification*

(d) *Part of the fracture section with 196.2x magnification*

Figure 6.22: *Severalpictures of specimen 8 - FAB051*

(a) *Part of the specimen 1*

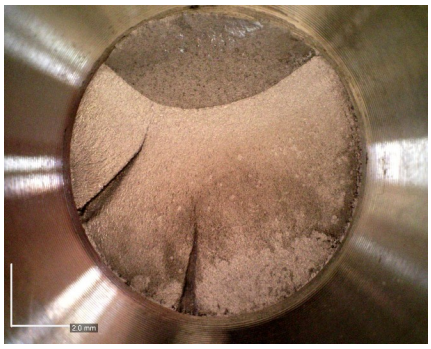

(b) *Fracture section with 26.8x magnification*

(c) *Part of the fracture section with 61.3x magnification*

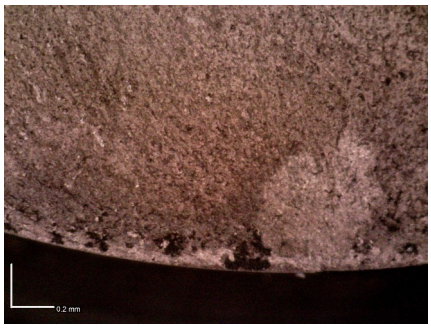

(d) *Part of the fracture section with 197.5x magnification*

Figure 6.23: *Severalpictures of specimen 9 - FAB051*

(a) *Part of the specimen 1*

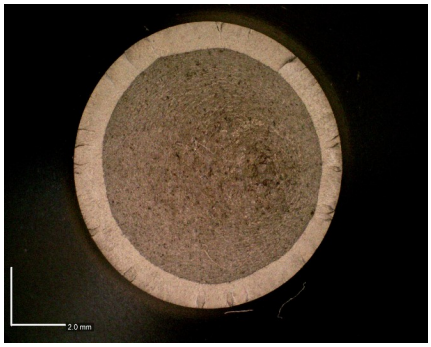

(b) *Fracture section with 24.8x magnification*

(c) *Part of the fracture section with 59.8x magnification*

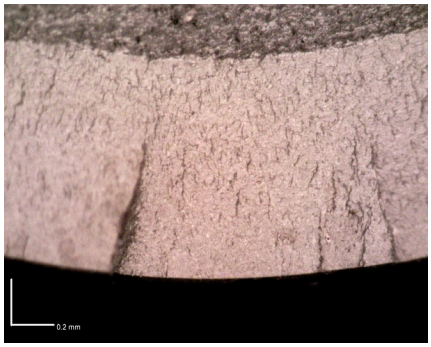

(d) *Part of the fracture section with 197.5x magnification*

Figure 6.24: *Severalpictures of specimen 10 - FAB051*

Chapter 7

FINITE ELEMENT ANALYSIS AND APPLICATION OF THEORETICAL APPROACHES

In this chapter, finite element analyses were carried out on the three specimens with the aim of determin
the physical quantities required to apply the theoretical methods presented in this thesis work (Ch. 2, 3,
FE analyses were performed and the TCD, RSG and SED methods were applied (Figure 7.1).
will then be compared, in the following chapters, with the experimental results coming out of the Amsler
test machine and other findings from literature.

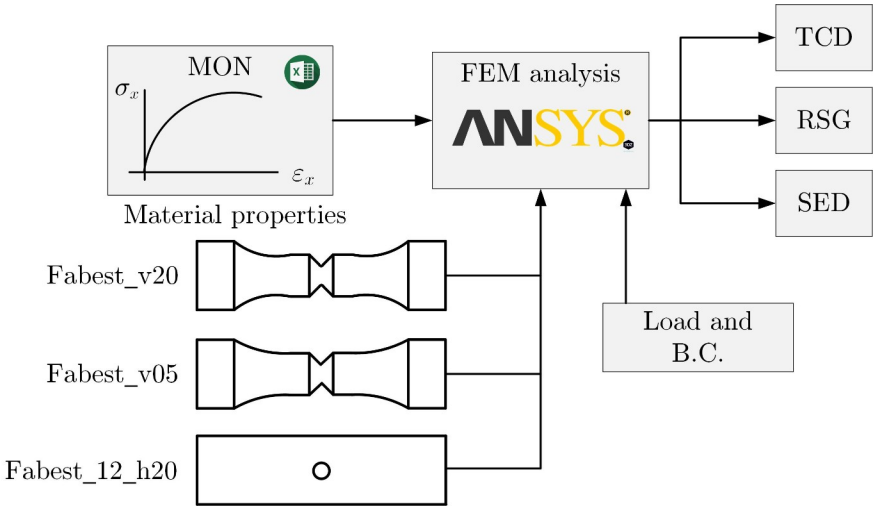

Figure 7.1: *Brief to do list in Chapter 7 for Fabest specimens*

Throughout the chapter, numerical and programming techniques will be used to achieve this aim. The
topics will be addressed in parallel in order to give a practical and immediate impression of what is really
needed to obtain the desired results. It should be noted that Fig. 7.1 shows a synthetic procedure that
will be followed for FABEST specimens, but a similar procedure will be followed for specimens extracted
from the literature [39] [44].

7.1 Finite element analysis of FABEST specimens

In this sub-chapter, finite element analyses will be conducted for the geometries proposed in this thesis work. This part is crucial because the linear elastic stress distribution near the tip of the notch is necessary in order to develop the theoretical approaches (See Ch. 2 and 3). In addition, in order to apply the SED approach, it is also necessary to determine the strain energy density averaged over a certain structural volume (See Ch. 4).
These next sub-chapters are organised as follows. As the TCD and RSG methods need either the maximum principal stress distribution or the Von Mises stress distribution (depending on the case) as an input parameter, and these can be obtained in a single .txt file, the modelling of the specimen is the same. The case for the SED approach is different. For this reason it was decided to divide the analyses, between pre and post processor, into two categories: that which includes the TCD and the RSG and that which includes the SED.

7.1.1 Finite element analysis of specimen FABEST_V05 for TCD and RSG approach

For the numerical modelling of the FABEST_V05 specimen, the starting point is the pre-processor environment. Initially, a FE model was constructed to obtain the necessary data to be able to apply the TCD and RSG methods.

Pre-processor for TCD and RSG approach

The geometry of the test specimen is represented in the 2D technical drawing in Fig. 7.2. A 3D model (useful for understanding how the components work in a FE environment) was created with solidworks ®, shown below.

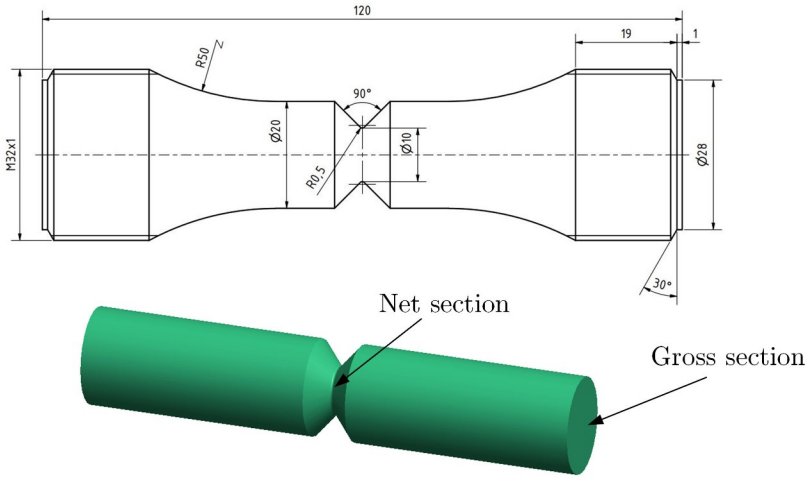

Figure 7.2: *Geometry of FABEST_V05*

Since the test was conducted with cycle-stress ratio $R = -1$ and the specimen is axisymmetric, the symmetry of the problem was exploited (the acting loads are also symmetric). Fig. 7.3 shows how the problem has been simplified to make better use of the computational power of the software.
First of all, the element type to be adopted was defined, namely:

element type → add-edit-delete → solid → quad 4 node 182

through the commands described in Fig. 7.4. In the options, a K1 K-option was set to simple enhanced strain and K3 to axisymmetric to perform a 2D analysis knowing that the specimen is cylindrical in shape.
From Ch. 5 the value of Young's modulus and Poisson's coefficient was entered, as described in Fig. 7.5.

material properties → material models → structural
→ linear → elastic → isotropic

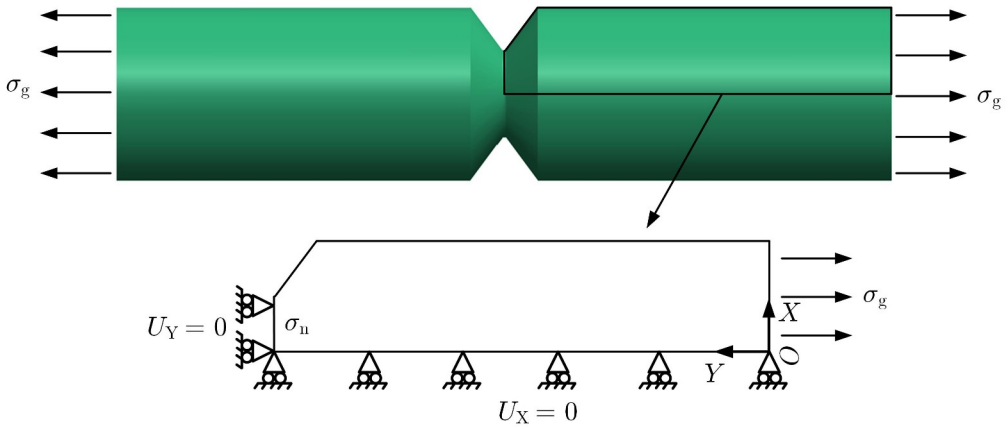

Figure 7.3: *Semplification of the problem and symmetry boundary conditions*

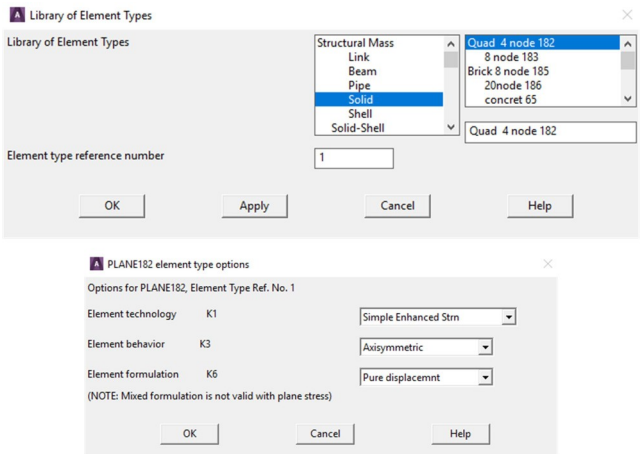

Figure 7.4: *Type of element used for FE analysis and K-options*

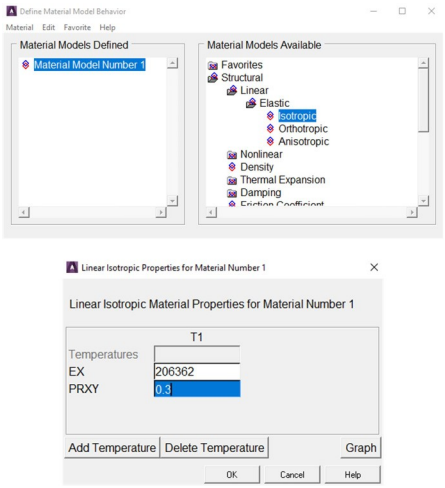

Figure 7.5: *Input of material properties*

As a static and linear elastic structural analysis, only these two values are required. After the type of element (and therefore its structural behaviour) and the material were chosen, the geometry was imported via the .IGES file using the import option. Since the geometric model consists only of lines, it is necessary to create the area entity in order to lay out the mesh. With

modeling → create → structural → areas → arbitrary → by lines

area was created. At this point it was possible to generate the mesh. In order to be able to apply TCD and RSG efficiently, it is necessary to achieve a very fine element size in the vicinity of the notch. Knowing that the diameter of the net section is equal to $\phi_n = 10$ mm (and thus the radius is $r_n = 5$ mm), an element size equal to $\Delta x = 0.005$ mm was chosen to obtain a number of subdivisions along the bisector equal to (Fig. 7.6):

$$n_{sud} = \frac{r_n}{\Delta x} = \frac{5}{0,\,005} = 1000 \tag{7.1}$$

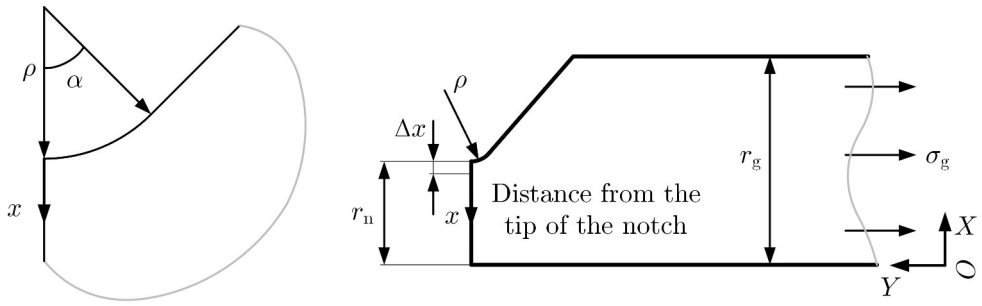

Figure 7.6: *Basic dimensions for calculating the number of subdivisions*

In order to obtain accurate results around the hot zone, it is necessary to construct a mesh that gradually becomes dense from upstream to downstream. To achieve this, it is necessary to derive the number of elements n_ρ to be generated on the fillet. At the notch $\rho = 0.5$ mm and therefore, knowing the angle underlying the arc, which is equal to $\alpha = \pi/4$ rad, it was possible to obtain l (Fig. 7.6):

$$l = \alpha \cdot \rho = \frac{\pi}{4} \cdot 0,\,5 = \frac{\pi}{8} \approx 0,\,393 \text{ mm} \tag{7.2}$$

known l, has been obtained:

$$n_\rho = \frac{l}{\Delta x} = \frac{0,\,393}{0,\,005} \approx 79 \tag{7.3}$$

through the function picked lines a number of subdivisions was set to 79. The mesh creation for the remaining lines is shown in Fig. 7.7 where the number of subdivisions and the spacing ratio have been indicated to obtain a sparse mesh away from the hot zone.

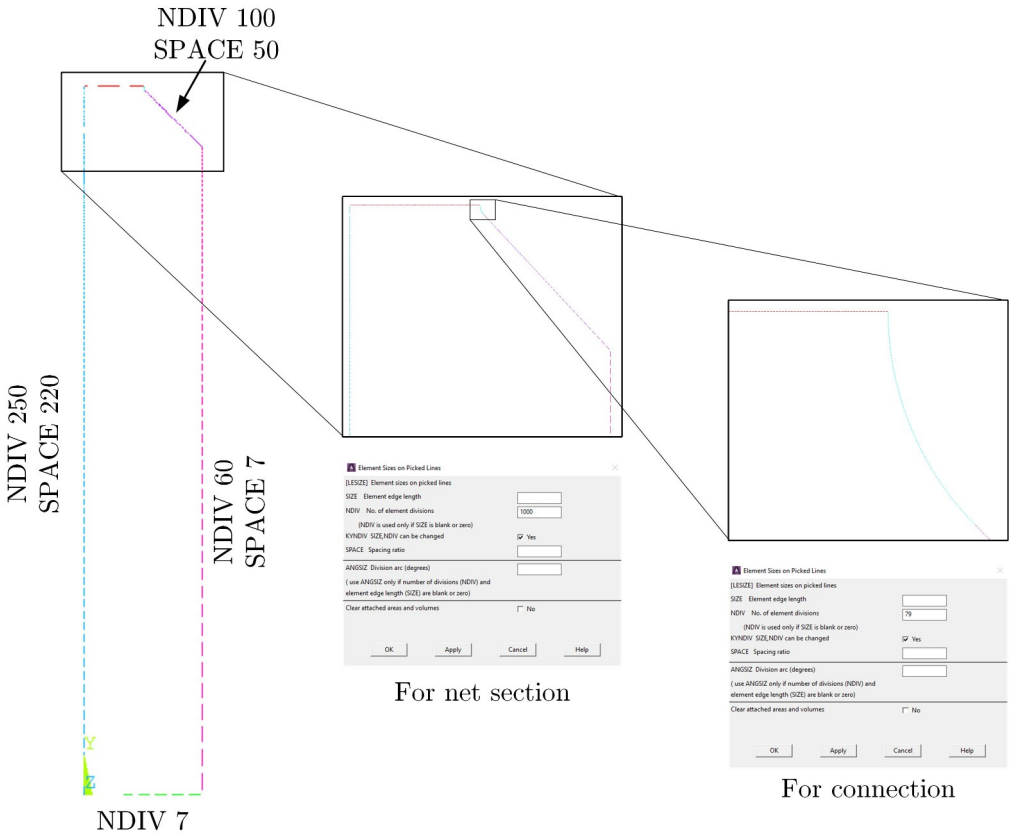

Figure 7.7: *Subdivision and spacing ratio on FABEST_V05*

A free-form mesh was used to mesh the component and the result is shown in Fig. 7.8 with appropriate zooming towards the area of interest.
At this point, symmetry conditions have been applied in the areas highlighted in Fig. 7.3 which impose the following constraint conditions:

$$\text{symmetry B.C.} \begin{cases} U_X = 0 & \text{along axis} \\ U_Y = 0 & \text{along bisector} \end{cases} \tag{7.4}$$

where U_X is the displacement along X and U_Y the displacement along Y and were set as follows:

loads → define loads → apply → structural → displacement → symmetry B.C. → on lines

As the Wöhler curves shown in Ch. 5 relate to the net cross-section, it was decided to set a nominal net stress of $\sigma_n = 1$ MPa. Following the continuity equation:

$$\sigma_n A_n = \sigma_g A_g \tag{7.5}$$

the gross nominal stress to be applied is:

$$\sigma_g = \sigma_n \cdot \frac{A_n}{A_g} = \sigma_n \cdot \frac{\frac{\pi \phi_n^2}{4}}{\frac{\pi \phi_g^2}{4}} = \sigma_n \cdot \frac{\phi_n^2}{\phi_g^2} = \sigma_n \cdot \frac{(2r_n)^2}{(2r_g)^2} = 1 \cdot \frac{10^2}{20^2} = 0.25 \text{ MPa} \tag{7.6}$$

and it was applied with the following commands:

loads → define loads → apply → structural → pressure → on lines

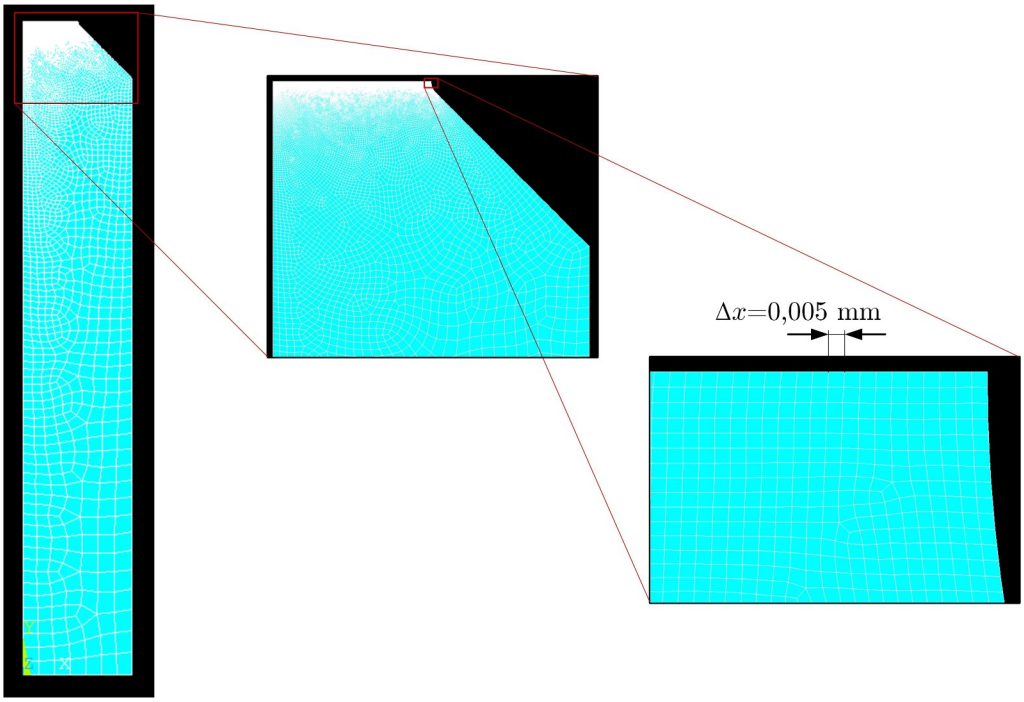

Figure 7.8: *Free mesh on FABEST_V05*

The reason why a nominal unit stress of 1 MPa has been applied is that only one analysis with the computer is required. In this way it is sufficient to scale this unit stress to any stress state to apply the TCD and RSG with the real values. Finally, after the procedures involving the pre-processor environment had been completed, the solution was launched in the solution environment.

Solution

In this environment, the analysis was launched using the following commands:

solve → current LS

through the following screen in Fig. 7.9 it is possible to see some information about the type of analysis carried out.

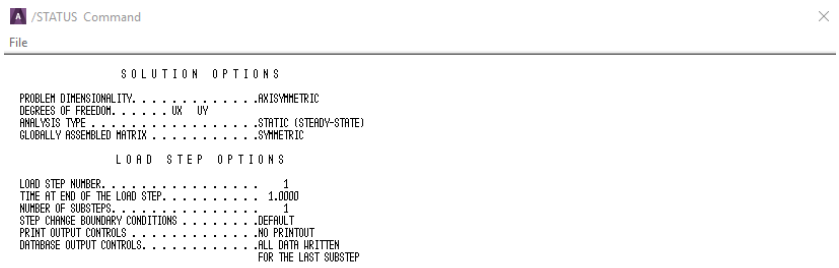

Figure 7.9: *Information on the analysis conducted in the solution environment*

In this specific case it can be seen that the analysis is 2D (For the specimen Fabest_h20 the 3D model will be used, 7.1.3).

Post-processor for TCD and RSG approach

First of all, the deformation plot was obtained to quickly check the correctness of the solution. The result can be seen in Fig. 7.10

plot results → deformed shape

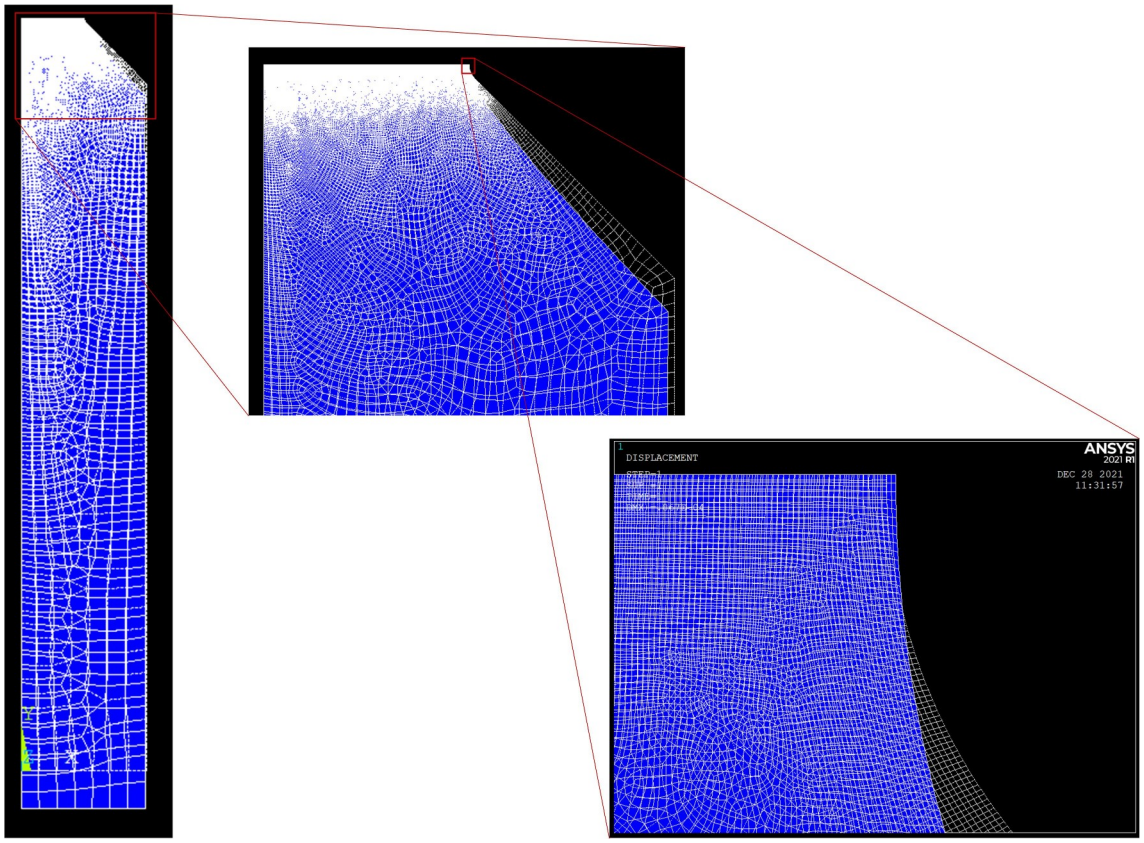

Figure 7.10: *Deformed vs. non-deformed configuration of FABEST_V05*

Using the following options it is possible to plot the maximum principal stress field and the Von Mises stress:

plot results → contour plot → nodal solution
→ stress → 1st principal stress - Von Mises stress

The following commands were used to extract the stress field near the tip of the notch:

select → entities → lines → by num-pick
→ nodes → attached to → lines,all

In this way it was possible to derive the .txt file containing the maximum principal stress values $\sigma_1 = \sigma_1(x)$ and the Von Mises one $\sigma_e = \sigma_e(x)$, as a function of the distance from the notch apex, through the following commands:

list results → nodal solution

Fig. 7.11 clarifies the symbols used in this discussion.
Stress plots are shown in Fig. 7.12.
In Fig. 7.13 it is possible to see the distribution of maximum principal stress and the Von Mises distributio as a function of the distance from the apex x.

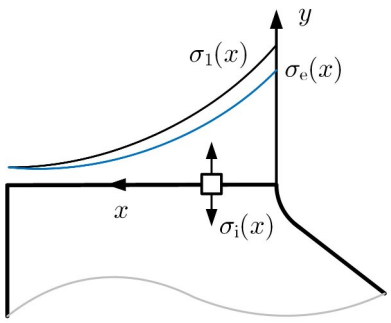

Figure 7.11: *Symbology for the first principal stress and Von Mises stress field*

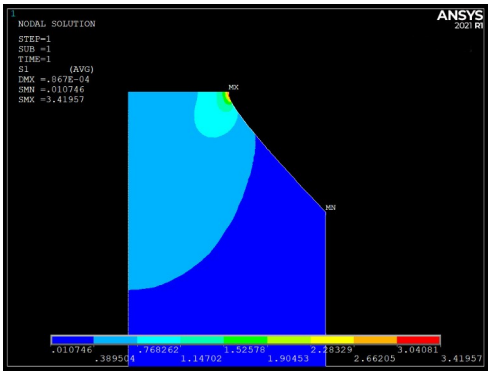

(a) *Plot of first principal stress*

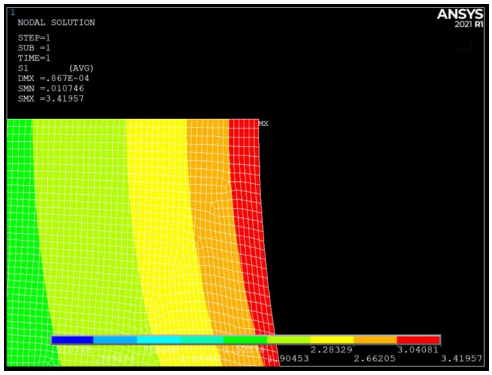

(b) *Zoom* σ_1 *on the hotspot*

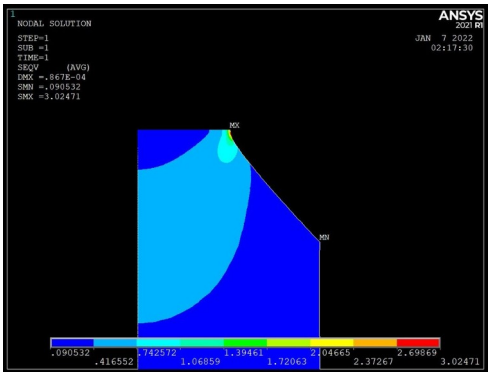

(c) *Plot of Von Mises stress*

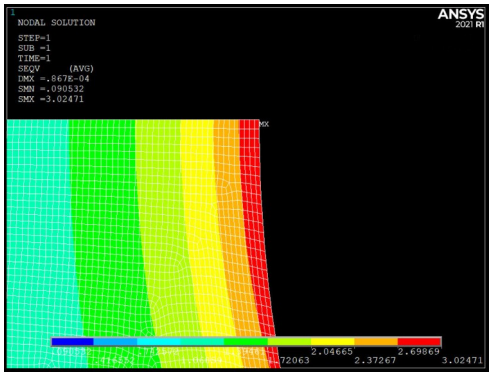

(d) *Zoom* σ_e *on the hotspot*

Figure 7.12: *Contour plot of stress fields*

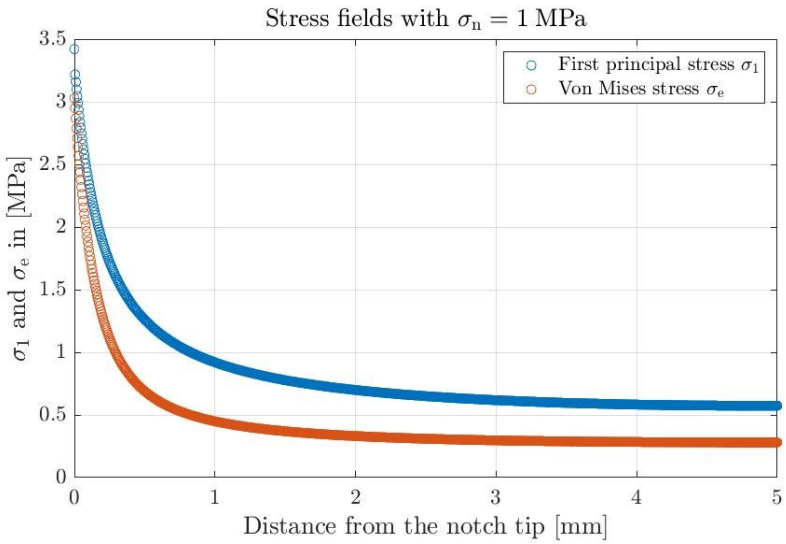

Figure 7.13: *Stress fields: nodal values*

7.1.2 Finite element analysis of specimen FABEST_V20 for TCD and RSG approach

In this subsection, the specimen FABEST_V20, which has a larger fillet radius than FABEST_V05, will be modelled.

Pre-processor for TCD and RSG approach

The geometry of the test specimen is represented in the 2D technical drawing in Fig. 7.14. A 3D model was created with solidworks®, depicted below.

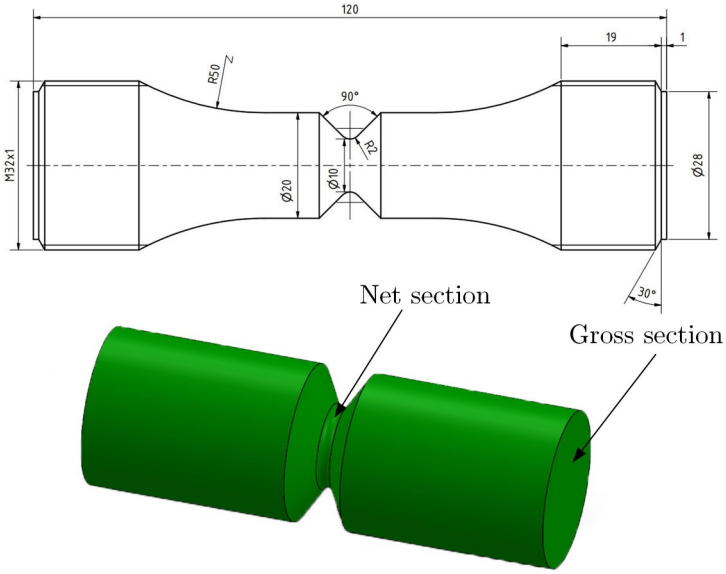

Figure 7.14: *Geometry of FABEST_V20*

Similarly to specimen FABEST_V05, since the test was conducted with cycle ratio $R = -1$ and the specimen is axisymmetric, the symmetry of the problem was exploited as in Fig. 7.3. After these initial considerations, the element type to be adopted was defined in the **pre-processor** environment, quad 4 node 182. Since the shape of this specimen is identical to that of FABEST_V05, the same element k-options have been set.
From Sec. 5.1 the value of Young's modulus and Poisson's coefficient was entered, as described in Fig. 7.
As a static and linear elastic structural analysis, only these two values are required. After the type of

element (and therefore its structural behaviour) and the material were chosen, the geometry was created using autocad® software to speed up the creation of the lines that characterise the contour of the sample. From the 2D mechanical drawing software, the .IGES file was obtained and imported® into ansys. Since the geometric model consists only of lines, it is necessary to create the area entity in order to lay out the mesh. Using the same method as in the previous sample, the area was generated. At this point it was possible to generate the mesh. In order to be able to apply TCD and RSG efficiently, it is necessary to achieve a extremely fine element size in the vicinity of the notch. Knowing that the diameter of the net section is equal to $\phi_n = 10$ mm (and thus the radius is $r = 5$ mm), an element size equal to $\Delta x = 0.005$ mm was chosen to obtain a number of subdivisions along the bisector equal to (Fig. **??**) 1000, as described in Eq. 7.1. In order to obtain accurate results around the hot zone, it is necessary to construct a mesh that gradually becomes dense from upstream to downstream. To achieve this, it is necessary to derive the number of elements to be generated on the fillet. At the notch $\rho = 2$ mm and therefore, knowing the angle underlying the arc, which is equal to $\alpha = \pi/4$ rad, it was possible to obtain l (Fig. **??**):

$$l = \alpha \cdot \rho = \frac{\pi}{4} \cdot 2 = \frac{\pi}{2} \approx 1,571 \text{ mm} \tag{7.7}$$

known l, has been obtained:

$$n_\rho = \frac{l}{\Delta x} = \frac{1,571}{0,005} \approx 314 \tag{7.8}$$

through the function picked lines a number of subdivisions was set to 314. The mesh creation for the remaining lines is shown in Fig. 7.15 where the number of subdivisions and the spacing ratio have been indicated to obtain a sparse mesh away from the hot zone.

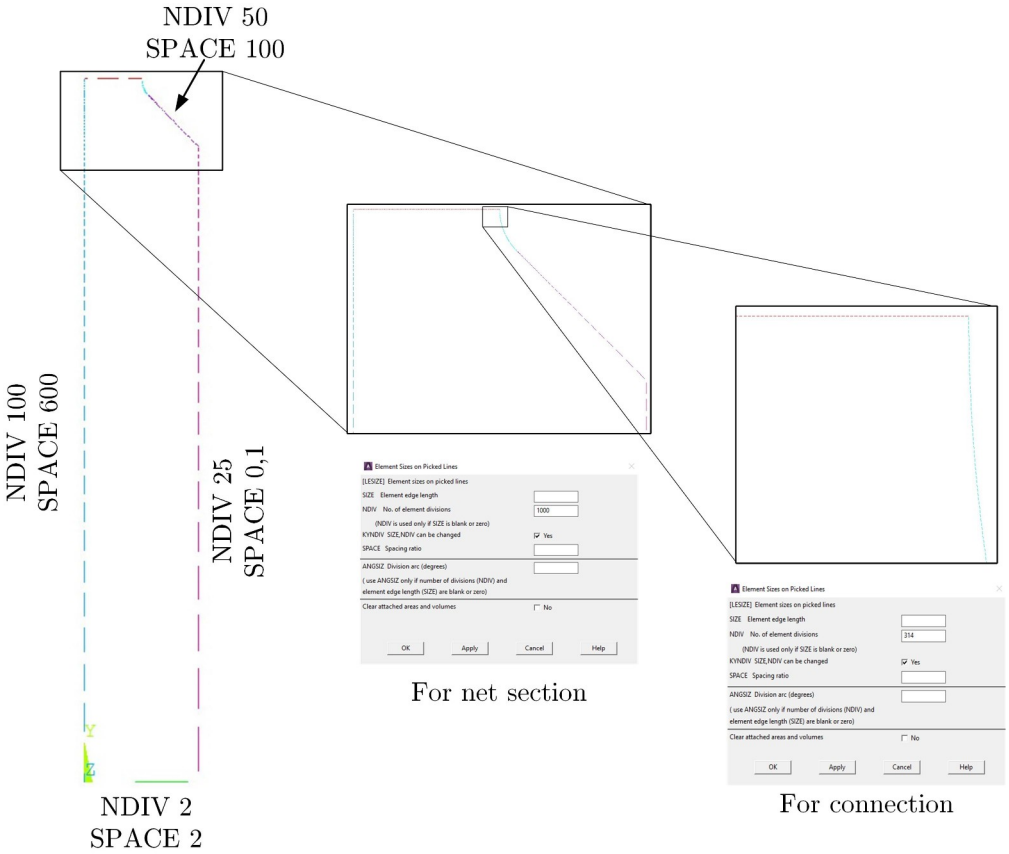

Figure 7.15: *Subdivision and spacing ratio on FABEST_V20*

A free-form mesh was used to mesh the component and the result is shown in Fig. 7.16 with appropriate zooming towards the area of interest.
At this point, symmetry conditions have been applied in the areas highlighted in Fig. 7.3 which impose the same boundary conditions as FABEST_V05. The gross nominal stress to be applied is the same as

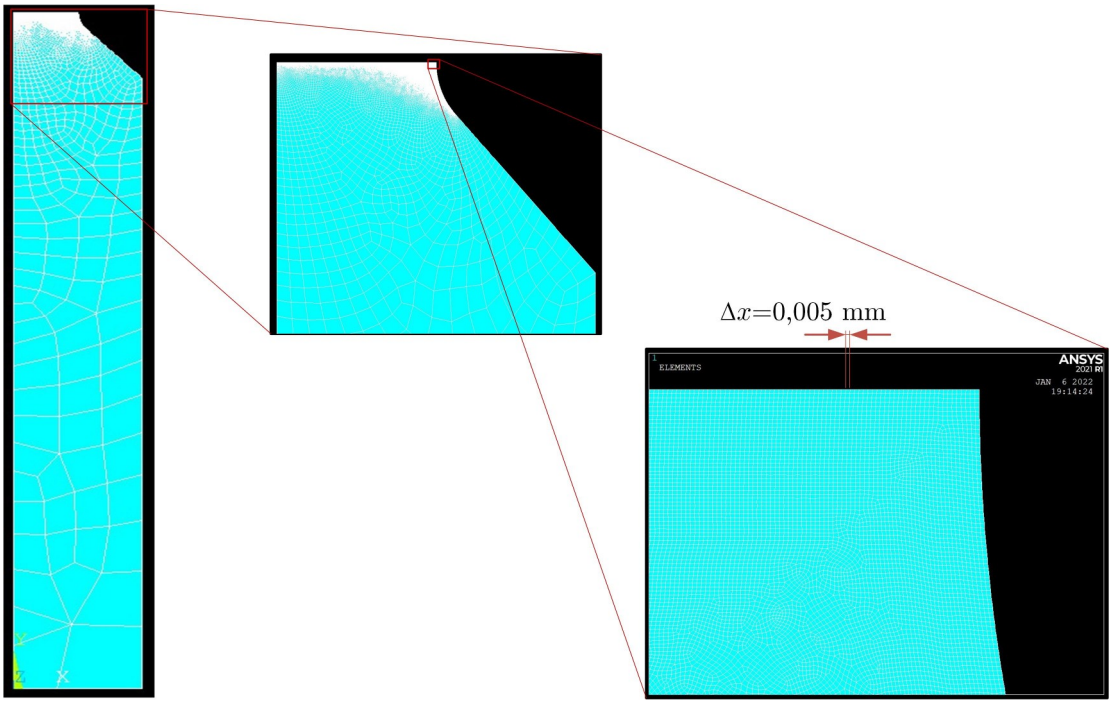

Figure 7.16: *Free mesh on FABEST_V05*

that of FABEST_V05 of the previous Sec. 7.1.1.
Finally, after the procedures involving the pre-processor environment had been completed, the solution was launched in the solution environment.

Post-processor for TCD and RSG approach

First of all, the deformation plot was obtained to quickly check the correctness of the solution. The result can be seen in Fig. 7.17
Using the same options as above (FABEST_V05) it is possible to plot the maximum principal stress field and the Von Mises stress in Fig. 7.18 and extract the .txt file.
In Fig. 7.19 it is possible to see the distribution of maximum principal stress and the Von Mises distributio as a function of the distance from the apex *x*.

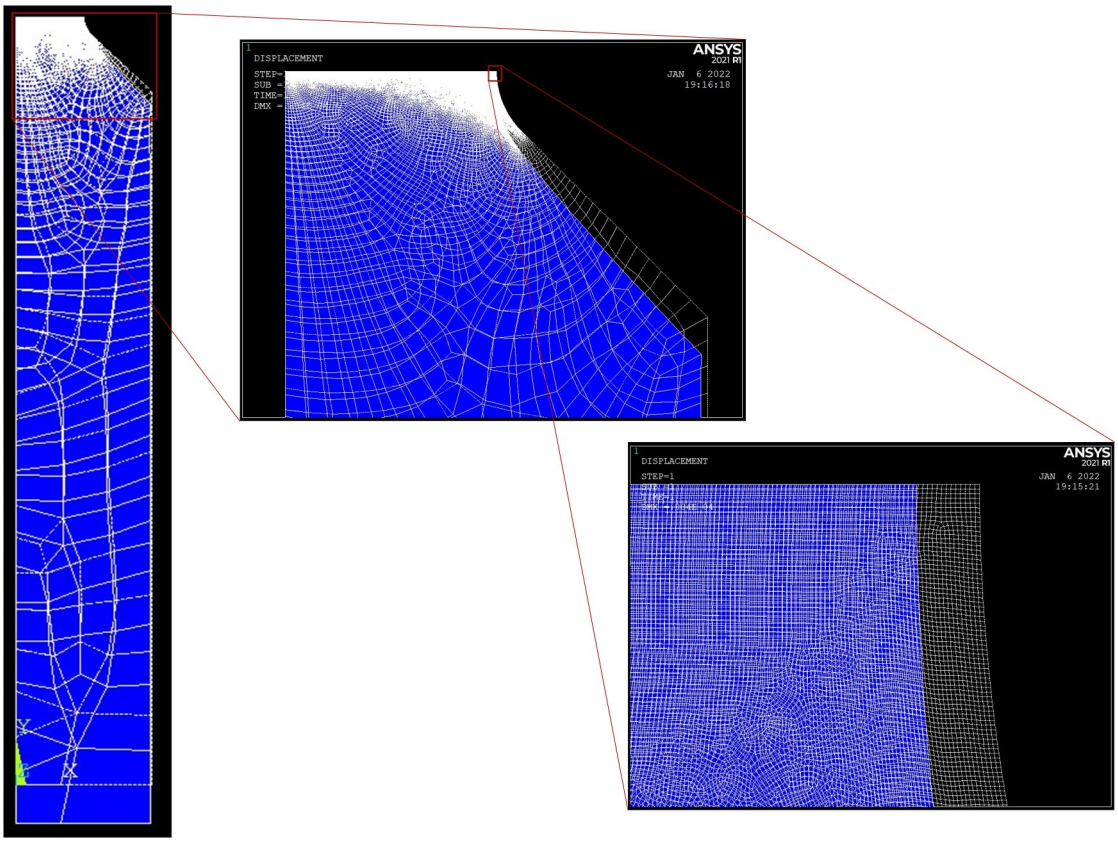

Figure 7.17: *Deformed vs. non-deformed configuration of FABEST_V20*

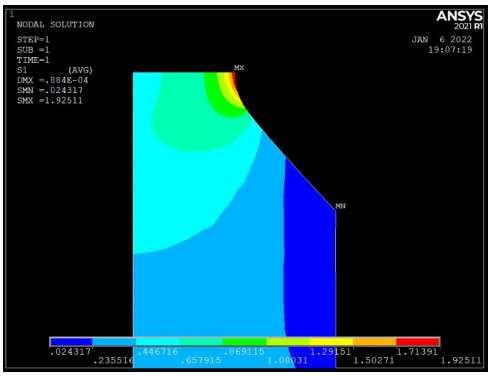

(a) *Plot of first principal stress*

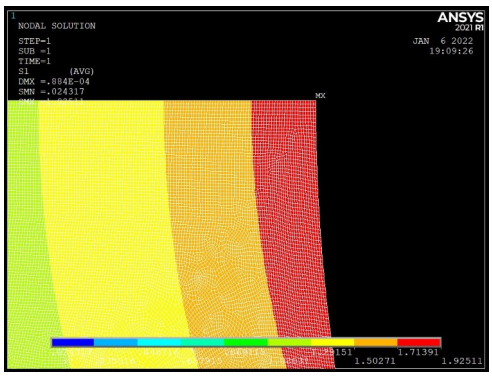

(b) *Zoom* σ_1 *on the hotspot*

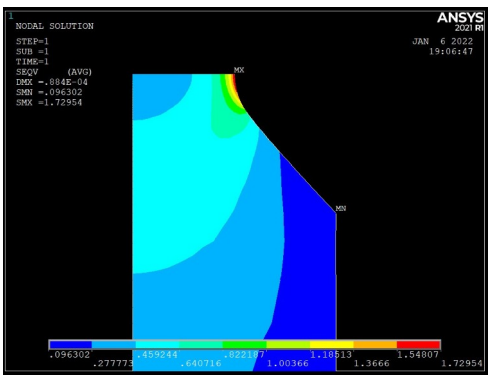

(c) *Plot of Von Mises stress*

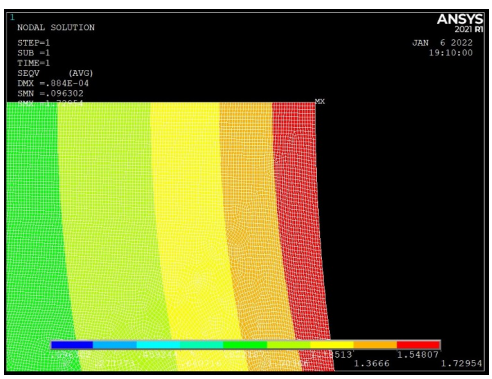

(d) *Zoom* σ_e *on the hotspot*

Figure 7.18: *Contour plot of stress fields*

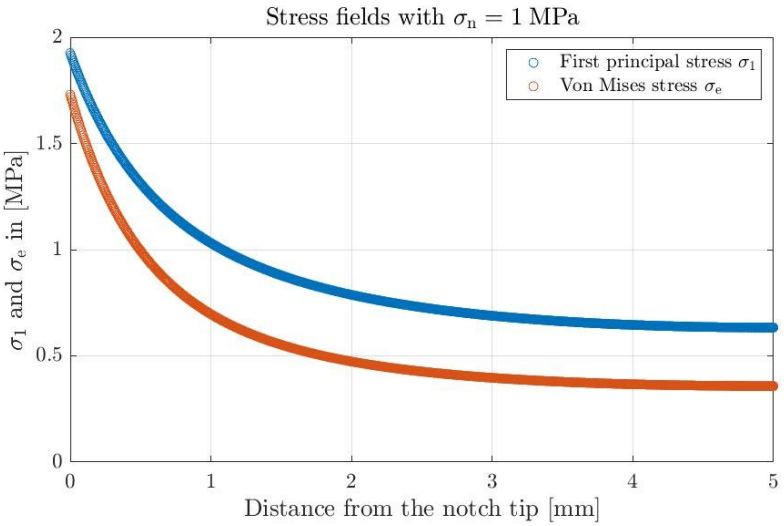

Figure 7.19: *Stress fields: nodal values*

7.1.3 Finite element analysis of specimen FABEST_12_H20 for TCD and RSG approach

Compared to previously studied specimens, FABEST_12_H20 was modelled with 3D tetrahedral elements. A 2D model is insufficient to capture the stress distribution from the surface to the axis of symmetry. As a 3D model requires more computing power, the element size around the hot zone was increased.

Pre-processor for TCD and RSG approach

The geometry of the test specimen is represented in the 2D technical drawing in Fig. 7.20. A 3D model can be seen in Fig. 7.22.

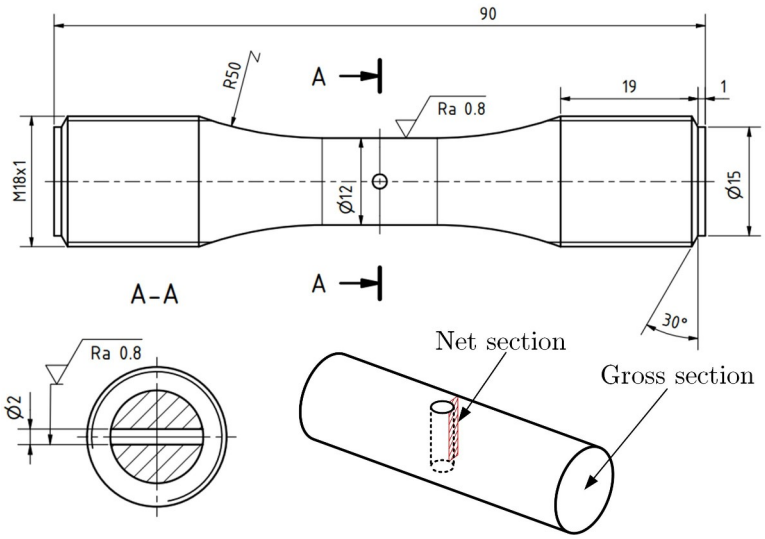

Figure 7.20: *Geometry of FABEST_12_H20*

As described in previous FE analyses, the symmetry of the problem was exploited and therefore only 1/8th of specimen was considered for the analysis (Fig. 7.22 clarifies the type of mesh used). Finite elements of solid the element type (Fig. 7.21) to be adopted was defined, namely:

element type → add-edit-delete → solid → 10 node 187

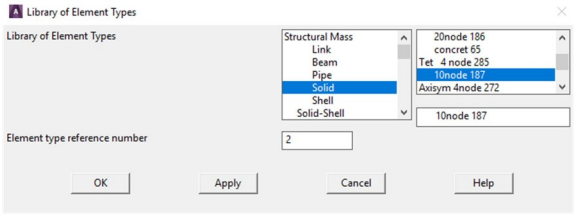

Figure 7.21: *Type of element used for FE analysis*

From Sec. 5.1 the value of Young's modulus and Poisson's coefficient was entered, as described in Fig. 7. A 1/4 circle was modelled in autocad® and then imported into ansys® as described in the V-rounded-notch specimen analysis. Using the commands extrude - areas - by XYZ offset, the circle was extruded by 45 mm. The hole was then created using the booleans - substract - volumes command. At this point, the picked lines tool was used to create subdivisions along all the lines that make up the specimen, Tab. 7.1. Elements with a dimension of $\Delta x \approx 0.01$ mm were obtained along the x-coordinate (Fig. 7.22).

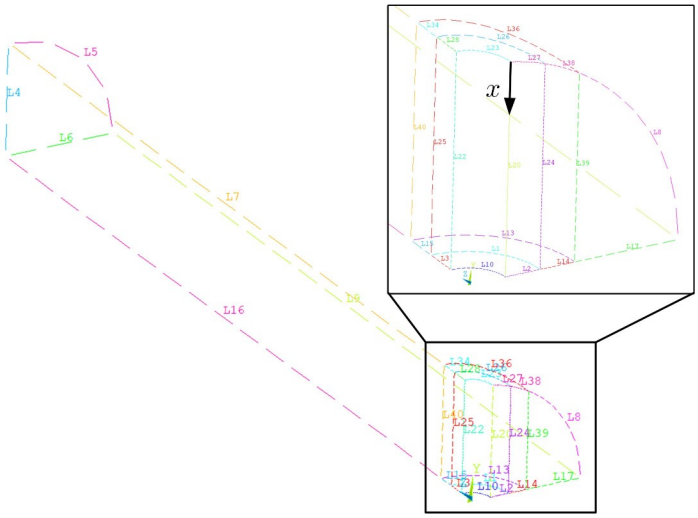

Figure 7.22: *Subdivision and spacing ratio on FABEST_12_h20 and the position of x-coordinate*

After setting the various dimensions of the elements with the appropriate spacing ratios, the component was meshed with a free mesh (Fig. 7.23).
In autocad®, there is an option to measure the area of any geometric figure. In this case it has been used to determine the area of the net section and it is equal to $A_n = 22.3022$ mm^2 (relative to 1/4 of net area). The gross area can be calculated as:

$$A_g = \frac{\pi \phi_n^2}{16} = \frac{\pi \cdot 12^2}{16} = 28.2743 \text{ mm}^2 \tag{7.9}$$

Using Eq. 7.5, the gross stress to be applied for a net stress of 1 MPa was determined, i.e. $\sigma_g = 0.7888$ MPa. Then the solution was launched.

Post-processor for TCD and RSG

First of all, the deformation plot was obtained to quickly check the correctness of the solution. The result can be seen in Fig. 7.24.
By means of the same commands used previously, the stress plots depicted in Fig. 7.25 were obtained. The stress field along the x-coordinate is not decreasing, but there is a point of maximum at a certain depth from the surface (Fig. 7.26). In order to solve the problem, a new reference system will be considered, which originates at the point of maximum stress.

Number	NDIV	Spacing ratio
1	19	0.333
2	14	0.500
3	5	2.000
4	3	1.000
5	4	1.000
6	3	1.000
7	17	1.000
8	10	0.333
9	18	1.000
10	20	0.250
13	15	0.500
14	7	2.000
15	2	2.000
16	17	1.000
17	8	0.500
20	158	1.000
22	40	1.000
23	20	4.000
24	60	1.000
25	15	1.000
26	12	2.000
27	14	2.000
28	5	2.000
34	2	2.000
36	15	0.500
38	7	2.000
39	20	1.000
40	10	1.000

Table 7.1: *Values of SR and number of subdivisons*

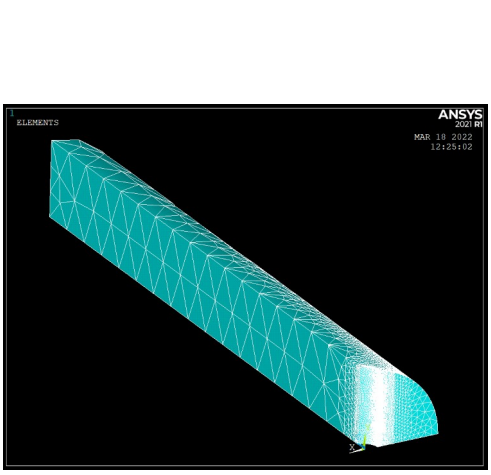

(a) *Mesh in isometric view*

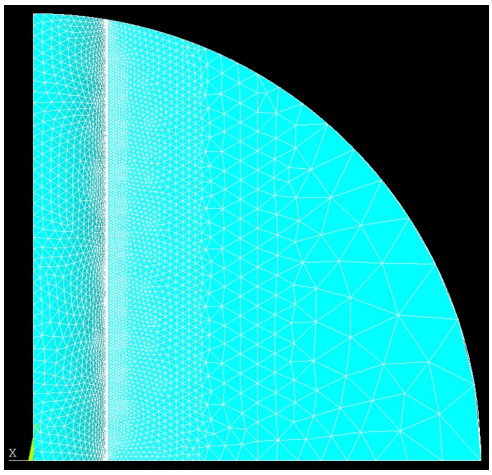

(b) *Mesh in front view*

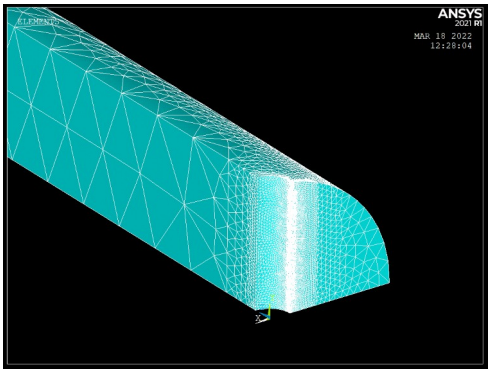

(c) *Mesh in isometric with zoom*

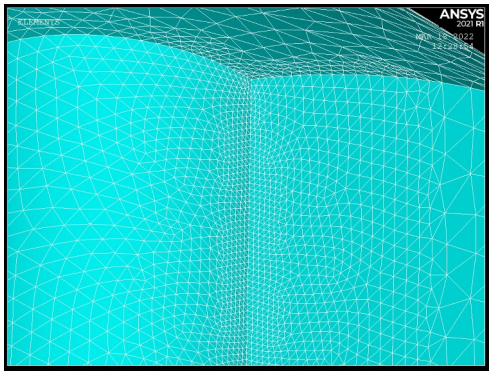

(d) *Hotspot zoom*

Figure 7.23: *Mesh of FABEST_12_h20*

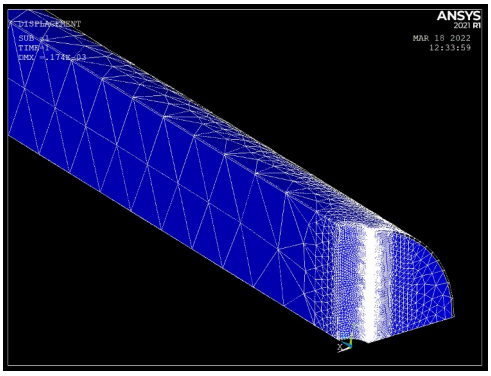

(a)

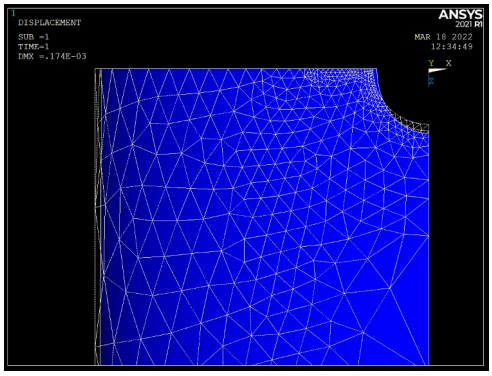

(b)

Figure 7.24: *Deformed vs. non-deformed configuration of FABEST_12_h20*

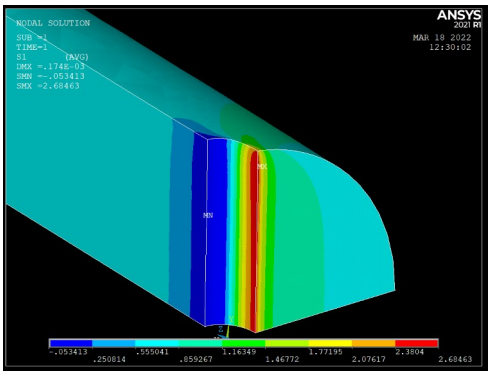

(a) *Plot of first principal stress*

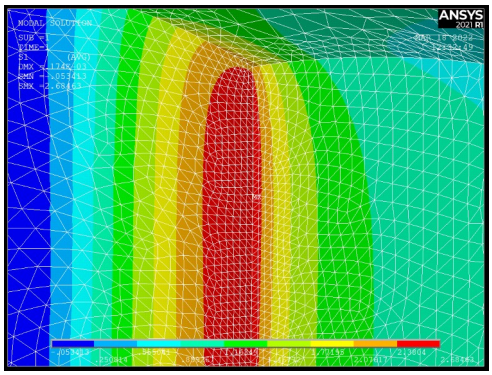

(b) *Zoom* σ_1 *on the hotspot*

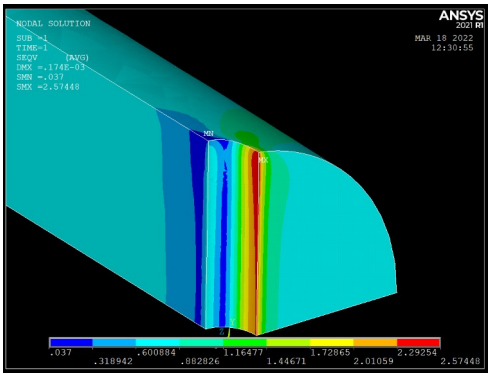

(c) *Plot of Von Mises stress*

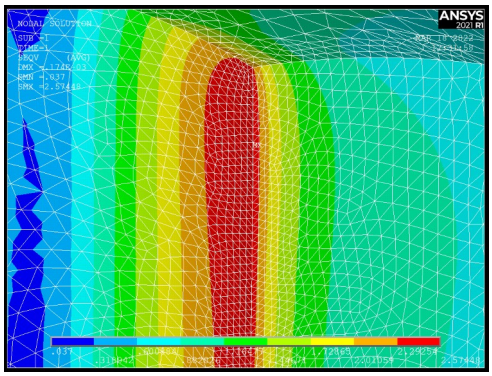

(d) *Zoom* σ_e *on the hotspot*

Figure 7.25: *Contour plot of stress fields*

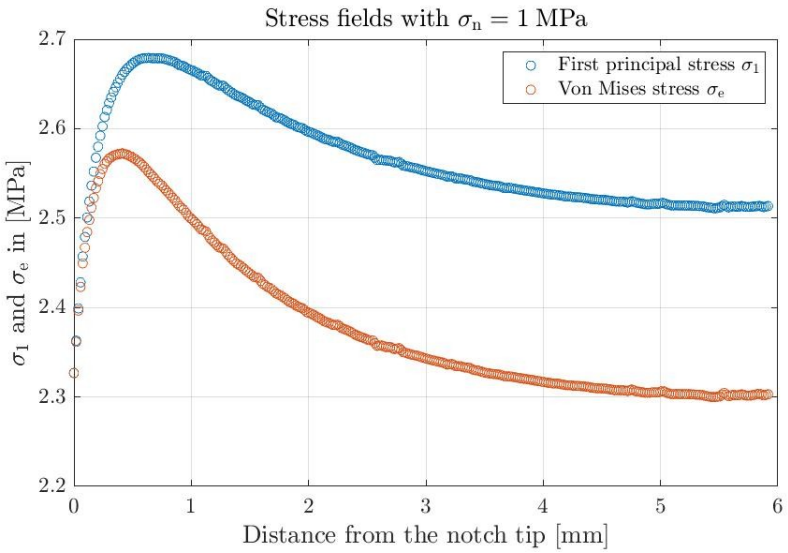

Figure 7.26: *Stress fields: nodal values*

7.2 Finite element analsysis of specimens from literature for TCD and RSG approach

In this sub-section, specimens from the literature were modelled. In particular, specimens were obtained from [44] that have a geometry very similar to FABEST_V05 and _V20, the only difference being the radius of the fillet at the apex of the notch. As far as the specimens from [39] are concerned, different modelling techniques have been adopted due to the completely different geometry.

7.2.1 Blunt and sharp V-notch specimen from [44]

As the specimens considered in ansys® have the same shape as FABEST_V05 or FABEST_V20, the same modelling techniques have been adopted as previously seen.

Pre-processor for TCD and RSG approach

From [44] it can be seen that the net diameter is equal to 14 mm. Modelling only 1/4 specimen due to the symmetry of the problem, the bisector of the notch is 7 mm long. Using the same element size for the Fabest specimens, 1400 elements were obtained (following the procedures for obtaining the mesh and setting the boundary conditions are exactly the same for Fabest specimens). The nominal gross stress to be applied in this case, however, is different:

$$\sigma_g = \sigma_n \cdot \frac{A_n}{A_g} = \sigma_n \cdot \frac{\frac{\pi\phi_n^2}{4}}{\frac{\pi\phi_g^2}{4}} = \sigma_n \cdot \frac{\phi_n^2}{\phi_g^2} = \sigma_n \cdot \frac{(2r_n)^2}{(2r_g)^2} = 1 \cdot \frac{14^2}{20^2} = 0.49 \text{ MPa} \qquad (7.10)$$

Once the operations in this environment were completed, the solution was launched and the results need to develop the theoretical methods were obtained.

Post-processor for TCD and RSG

In the post-processor, the Von Mises stress fields and the maximum principal stress field were obtained (Fig. 7.27 and 7.28).
A single diagram shows the stress fields (first principal stress and Von Mises stress) for the geometric configurations with a net applied nominal stress of 1 MPa (Fig. 7.29, 7.30).

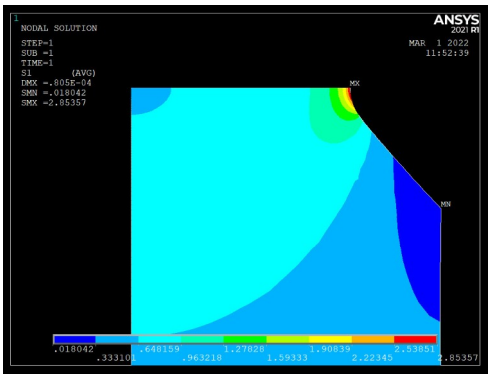

(a) *Plot of first principal stress*

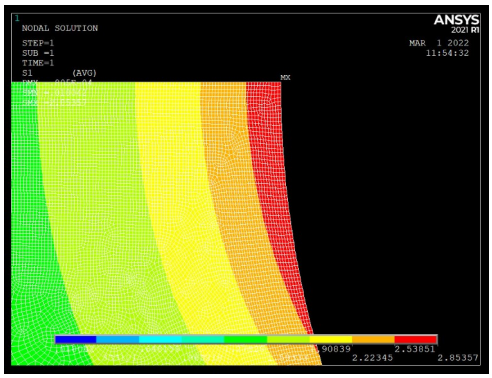

(b) *Zoom σ_1 on the hotspot*

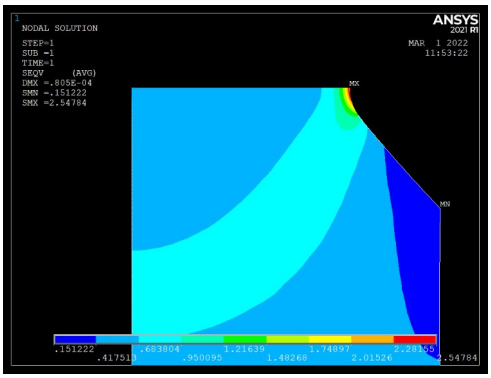

(c) *Plot of Von Mises stress*

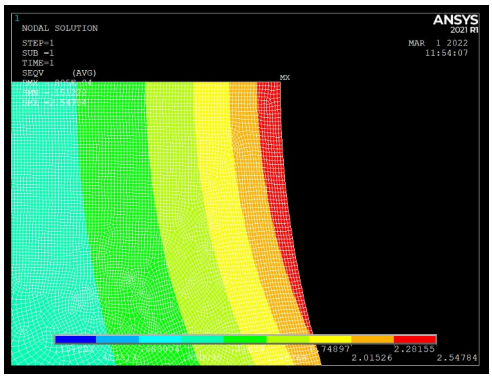

(d) *Zoom σ_e on the hotspot*

Figure 7.27: *Contour plot of stress fields of specimen with $\rho = 1$ mm*

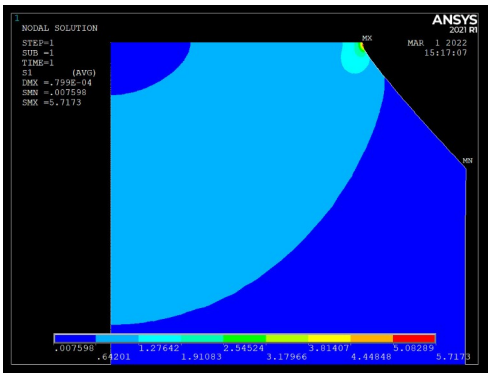

(a) *Plot of first principal stress*

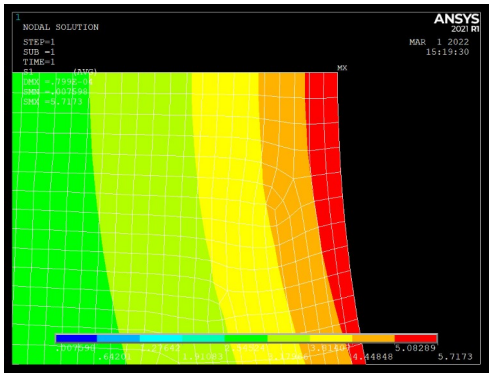

(b) *Zoom σ_1 on the hotspot*

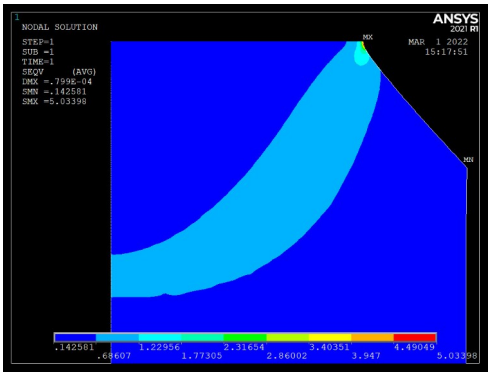

(c) *Plot of Von Mises stress*

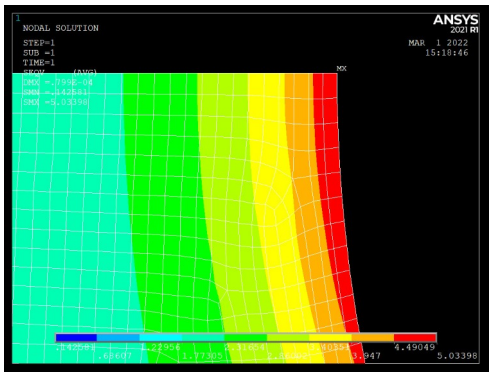

(d) *Zoom σ_e on the hotspot*

Figure 7.28: *Contour plot of stress fields of specimen with $\rho = 0.2$ mm*

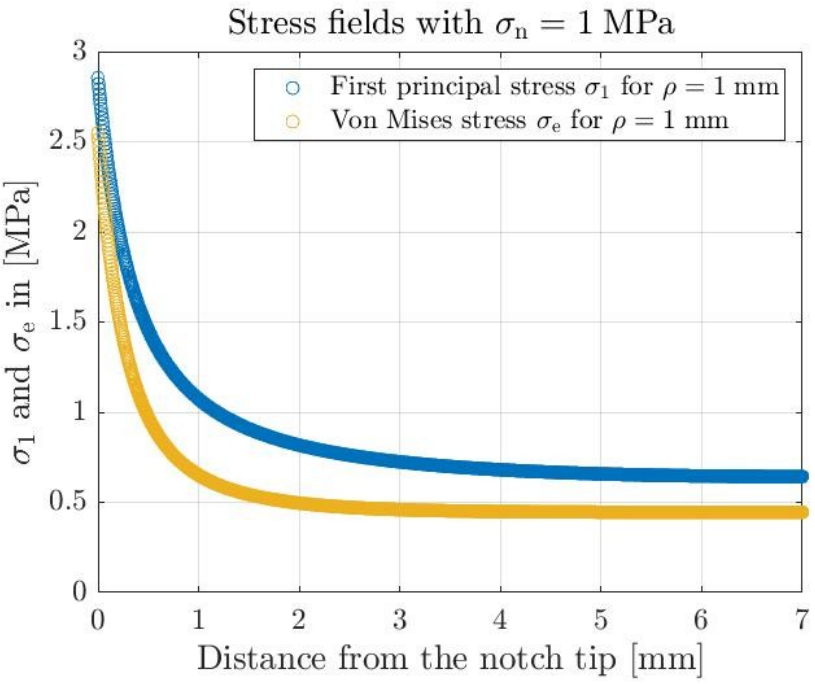

Figure 7.29: *Stress fields: nodal values for* $\rho = 1$ mm *configuration*

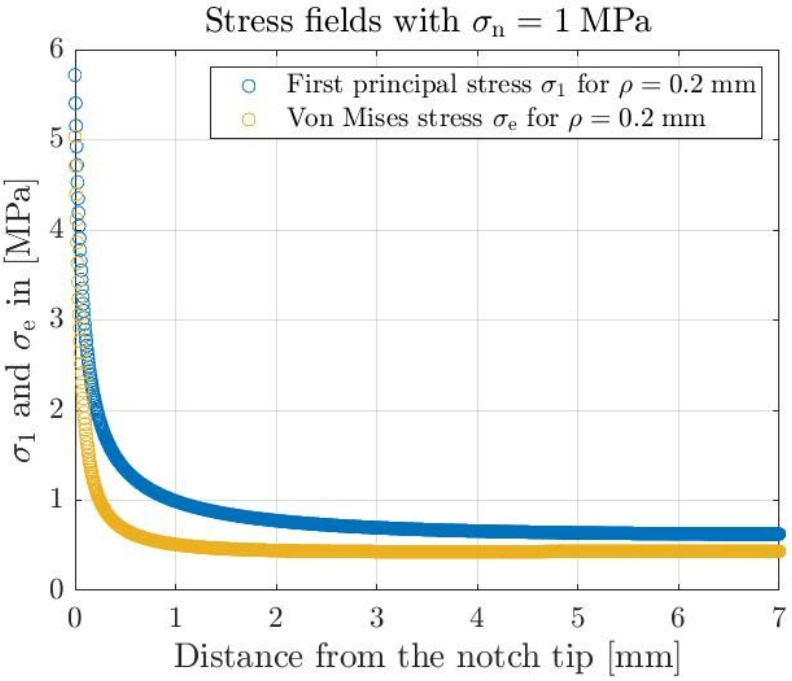

Figure 7.30: *Stress fields: nodal values for* $\rho = 0.2$ mm *configuration*

7.2.2 F2 and F3 specimens from [39]

Pre-processor for TCD and RSG approach

In addition to the V-rounded notch as a geometric notch detail, flat fillet specimens were also considered (Fig. 7.31) in this thesis work.

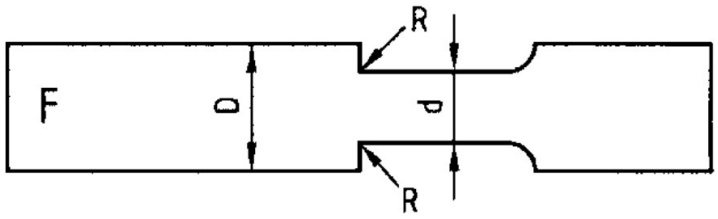

Figure 7.31: *Form of flat specimens with main dimensions [39]*

The dimensions of the F2 and F3 series are collected in Tab. 7.2.

Form	d [mm]	D [mm]	t [mm]	R = 1.00 [mm]	R = 0.20 [mm]	R = 0.04 [mm]
F2	30	54	6	X	X	X
F3	100	180	10	/	X	X

Table 7.2: *Specimen shapes and dimensions*

In order to automate the initial processes, a code was written using the ansys® native programming language (APDL). With this simple script it is possible to define the type of element used, i.e. quad 4 node 182 with K-option plane stress with thickness and simple enhanced strain, the real constant t and the material properties, Young Modulus EX and Poisson's ratio $PRXY$.

```
/PREP7
!ELEMENT TYPE
ET, 1 , PLANE182
!−−−−−−−−−−−−−−−−−−−−−−−−−−−−−−−
!OPTIONS ELEMENT
KEYOPT, 1 , 1 , 3
KEYOPT, 1 , 3 , 3
KEYOPT, 1 , 6 , 0
!−−−−−−−−−−−−−−−−−−−−−−−−−−−−−−−
!THICKNESS
R, 1 , 6 ,
!−−−−−−−−−−−−−−−−−−−−−−−−−−−−−−−
!MATERIAL MODEL
MP,EX, 1 , 2 0 6 0 0 0
MP,PRXY, 1 , 0 . 3
```

The various geometries described in Tab. 7.2 were constructed with autocad® and exported to an .IGES file. Since it is necessary to obtain the stress distribution along the bisector of the notch and it is inclined with respect to the direction of application of the load (Fig. 7.32), a line was generated to take the nodal stress values. The mesh, to output accurate results, needs to be very dense around the hotspot and therefore squares with lines were generated to obtain a gradual mesh up to the edges. Depending on the type of specimen, the dimensions vary, but the concept is highlighted in Fig. 7.32, i.e. the area around the fitting for all type F specimens is very similar. The type of model used in ansys® is also shown here. It can be seen how the boundary conditions (as FEM) and the load in terms of σ_n were applied. In general, the subdivisions on the fillet were obtained using a element size shown in Tab. 7.3.
The notch bisector is 5 mm long. This length was chosen because the most interesting stress values are found near the apex of the notch, and so to extend a greater distance with the line would mean spending more time on FE modelling to obtain information not needed to apply TCD or RSG. Fig. 7.33 shows a mesh for specimen F2 with ρ = 1; mm.
The overall element size is around 0.5 − 1 mm and was chosen so as not to generate huge differences between the contour of the hot zone and the zone of least interest for the application of the approaches. A stress of 1 MPa was applied along the net section.

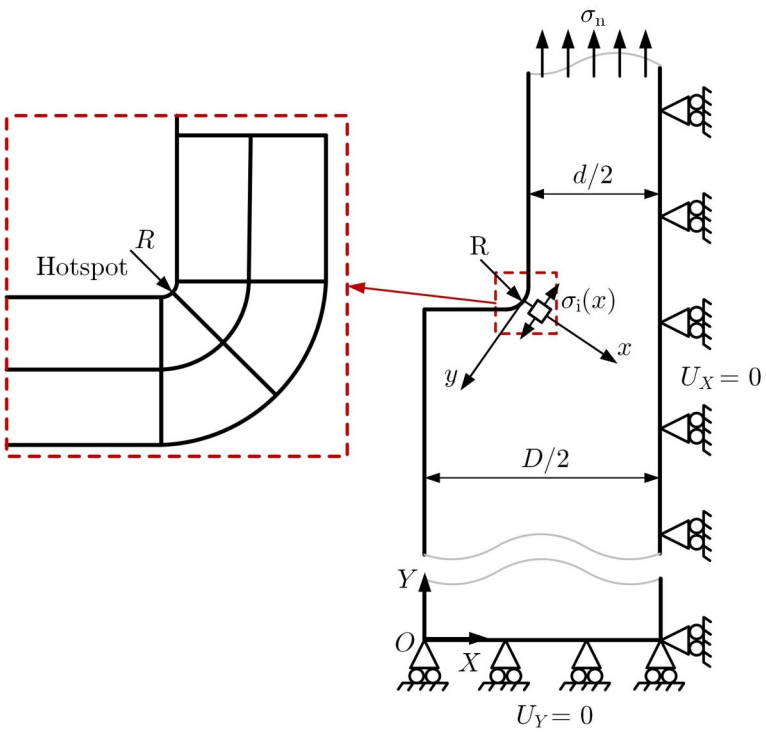

Figure 7.32: *Hotspot area and FE model*

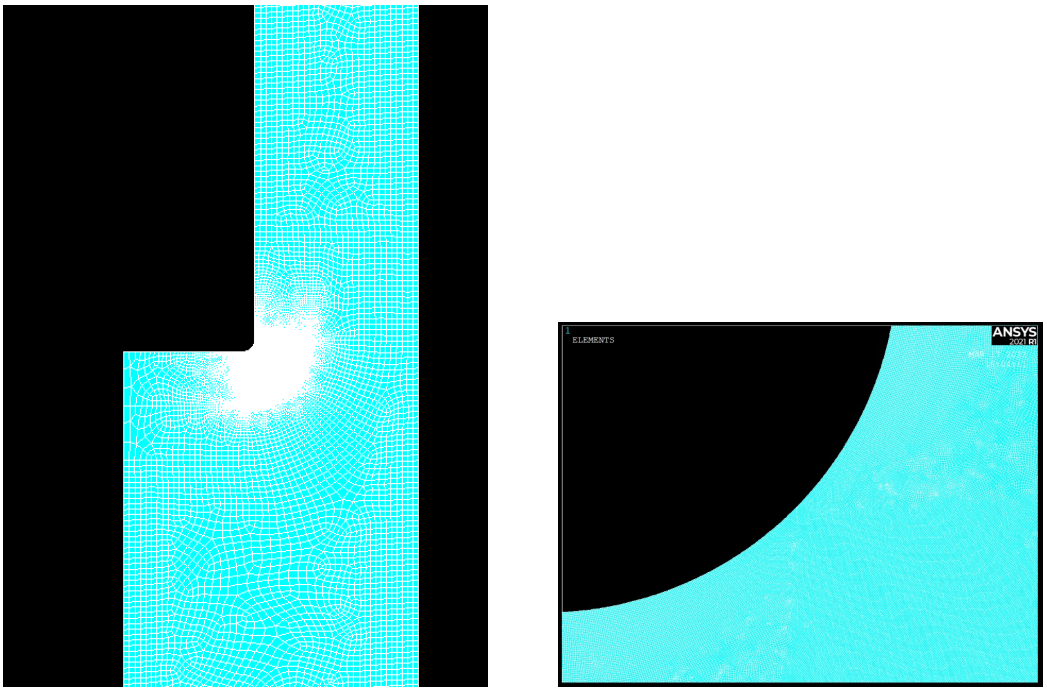

(a) *Mesh around the hot zone* **(b)** *Zoom at the hotspot*

Figure 7.33: *Mesh of specimen with* $\rho = 1$ mm

Specimen	R [mm]	Δx [mm]
F2	1	0.005
F2	0.2	0.005
F2	0.04	0.001
F3	0.2	0.005
F3	0.04	0.002

Table 7.3: *Element dimensions for F specimens*

Post-processor for TCD and RSG

Stress values for each specimen geometry were extrapolated along the notch bisector. In Figure 7.34 it can be see the stress plots for the F2 configuration and $\rho = 1$; mm.

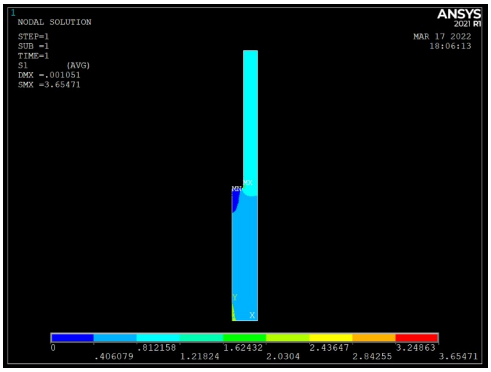

(a) *Plot of first principal stress*

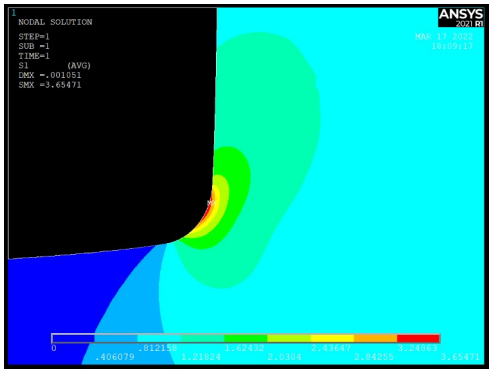

(b) *Zoom σ_1 on the hotspot*

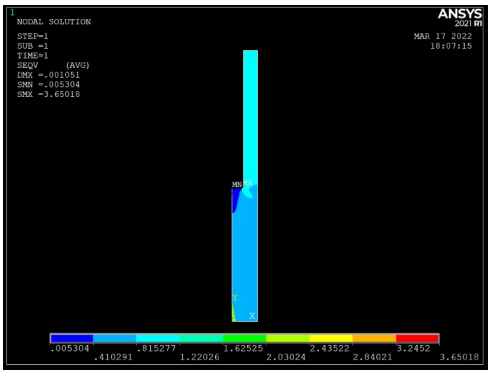

(c) *Plot of Von Mises stress*

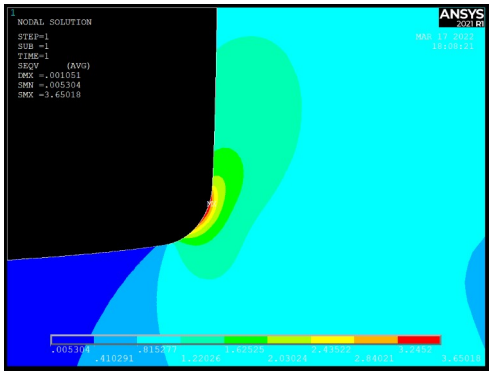

(d) *Zoom σ_e on the hotspot*

Figure 7.34: *Contour plot of stress fields of specimen F2 with $\rho = 1$ mm*

The stress fields of the five geometric configurations with an external unit load applied are shown below, in Fig. 7.35.

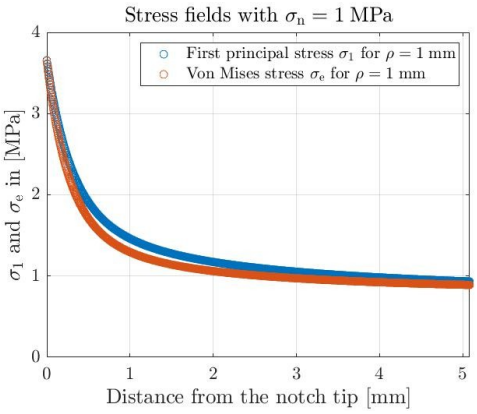

(a) *Stress fields of F2 specimen with* ρ = 1 mm

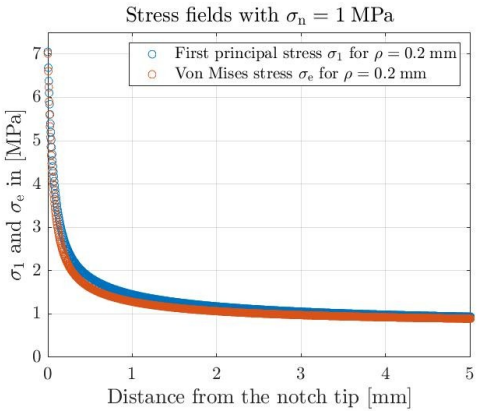

(b) *Stress fields of F2 specimen with* ρ = 0.2 mm

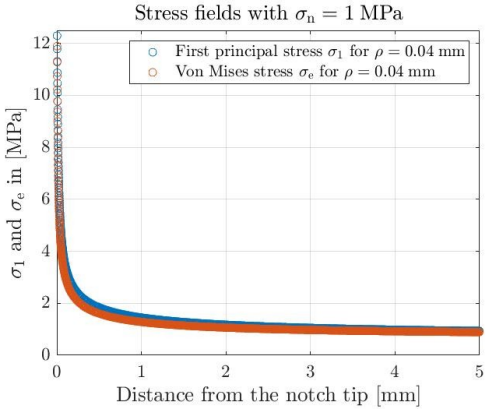

(c) *Stress fields of F2 specimen with* ρ = 0.04 mm

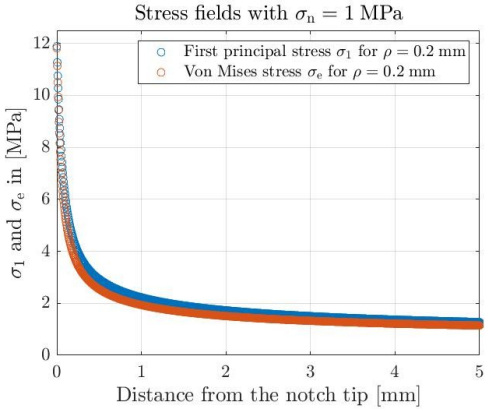

(d) *Stress fields of F3 specimen with* ρ = 0.2 mm

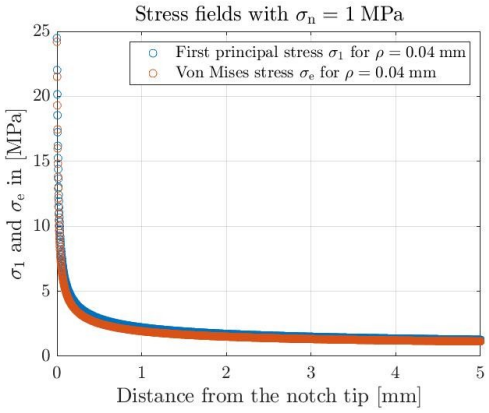

(e) *Stress fields of F3 specimen with* ρ = 0.04 mm

Figure 7.35: *Stress Fields of F specimens*

7.3 Determination of the stress field in the vicinity of the notch

The output of FE analyses should be used to develop the approaches under study. However, for TCD and RSG, it is useful to approximate the nodal data with continuous functions. In the following paragraphs, the goodness of fit, with statistical parameters, will be evaluated. In this sub-section, the case of an infinite plate with a hole is presented from the point of view of the mathematical theory of elasticity. In general, for non-accelerating, isotropic, linear-elastic body subject to small strains, the equations that govern the problem are:

Geometric compatibility

The displacements must match the geometrical boundary conditions and must be continuos functions of position with which the strain components are associated, as follows:

$$\begin{aligned} \varepsilon_x &= \frac{\partial u}{\partial x} \qquad \gamma_{xy} = \frac{\partial v}{\partial x} + \frac{\partial u}{\partial y} \\ \varepsilon_y &= \frac{\partial v}{\partial y} \qquad \gamma_{yz} = \frac{\partial w}{\partial y} + \frac{\partial v}{\partial z} \\ \varepsilon_z &= \frac{\partial w}{\partial z} \qquad \gamma_{zx} = \frac{\partial u}{\partial z} + \frac{\partial w}{\partial x} \end{aligned} \tag{7.11}$$

where u, v and w are the displacement components in the x, y and z directions.

Equilibrium

On the surface the stress components must be in equilibrium with the given external loads, and within the body they must satisfy the following equilibrium differential equations:

$$\begin{aligned} \frac{\partial \sigma_{xx}}{\partial x} + \frac{\partial \tau_{xy}}{\partial y} + \frac{\partial \tau_{xz}}{\partial z} + b_x &= 0 \\ \frac{\partial \tau_{yx}}{\partial x} + \frac{\partial \sigma_{yy}}{\partial y} + \frac{\partial \tau_{yz}}{\partial z} + b_y &= 0 \\ \frac{\partial \tau_{zx}}{\partial x} + \frac{\partial \tau_{zy}}{\partial y} + \frac{\partial \sigma_{zz}}{\partial z} + b_z &= 0 \end{aligned} \tag{7.12}$$

where b_x, b_y and b_z are the body forces.

Stress-strain relations

The relations between stress and strain is:

$$\begin{aligned} \varepsilon_x &= \frac{1}{E}\left[\sigma_x - \upsilon(\sigma_y + \sigma_z)\right] \qquad \gamma_{xy} = \frac{\tau_{xy}}{G} \\ \varepsilon_y &= \frac{1}{E}\left[\sigma_y - \upsilon(\sigma_z + \sigma_x)\right] \qquad \gamma_{yz} = \frac{\tau_{yz}}{G} \\ \varepsilon_z &= \frac{1}{E}\left[\sigma_z - \upsilon(\sigma_x + \sigma_y)\right] \qquad \gamma_{zx} = \frac{\tau_{zx}}{G} \end{aligned} \tag{7.13}$$

Infinite plate with circular hole loaded with uniaxial stress

Eq. 7.11, 7.12 and 7.13 were applied in the following case shown in Fig. 7.36 using cylindrical coordinates. The stresses in the reference system (r, θ), with the appropriate boundary conditions, become:

$$\begin{aligned} \sigma_r(r = R, \theta) &= 0 \\ \sigma_r(r = \infty, \theta) &= \frac{\sigma_g}{2}(1 + 2\cos(2\theta)) \\ \sigma_\theta(r = \infty, \theta) &= \frac{\sigma_g}{2}(1 - 2\cos(2\theta)) \\ \tau_{r\theta}(r, \theta) &= -\frac{\sigma_g}{2}\sin(2\theta) \end{aligned} \tag{7.14}$$

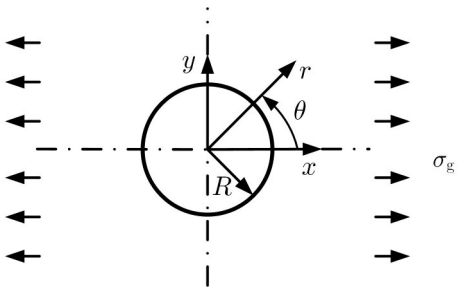

Figure 7.36: *Plate loaded with uniaxial tension*

Using the general solution of the Airy stress function in polar coordinates, which is attributed to the Australian mathematician J.H. Michell, we can arrive at a general solution by selecting appropriate terms. The shape of the chosen stress function is as follows:

$$\Phi(r,\theta) = a_0 + a_1\log(r) + a_2 r^2 + a_3 r^2\log(r) + (a_{21}r^2 + a_{22}r^4 + a_{23}r^{-2} + a_{24})\cos(2\theta) \tag{7.15}$$

stresses then become

$$\begin{aligned}
\sigma_r(r,\theta) &= a_3\left(1 + 2\log(r)\right) + 2a_2 + \frac{a_1}{r^2} - \left(2a_{21} + \frac{6a_{23}}{r^4} + \frac{a_{24}}{r^2}\right)\cos(2\theta)\\
\sigma_\theta(r,\theta) &= a_3\left(3 + 2\log(r)\right) + 2a_2 - \frac{a_1}{r^2} + \left(2a_{21} + \frac{12a_{22}}{r^2} + \frac{6a_{23}}{r^4}\right)\cos(2\theta)\\
\tau_{r\theta}(r,\theta) &= \left(2a_{21} + 6a_{22}r^2 - \frac{6a_{23}}{r^4} - \frac{2a_{24}}{r^2}\right)
\end{aligned} \tag{7.16}$$

From the knowledge of the boundary conditions and stress values, an analytical solution of this problem was obtained. The resulting relationships are as follows:

$$\begin{aligned}
\sigma_r(r,\theta) &= \frac{\sigma_g}{2}\left(1 - \frac{a^2}{r^2}\right) + \frac{\sigma_g}{2}\left(1 + \frac{3a^4}{r^4} - \frac{4a^2}{r^2}\right)\cos(2\theta)\\
\sigma_\theta(r,\theta) &= \frac{\sigma_g}{2}\left(1 + \frac{a^2}{r^2}\right) - \frac{\sigma_g}{2}\left(1 + \frac{3a^4}{r^4}\right)\cos(2\theta)\\
\tau_{r\theta}(r,\theta) &= -\frac{\sigma_g}{2}\left(1 - \frac{3a^4}{r^4} + \frac{2a^2}{r^2}\right)\sin(2\theta)
\end{aligned} \tag{7.17}$$

Stress distributions from the apex notch are required for the application of TCD and for $\theta = \pm\frac{\pi}{2}$, i.e. and $r = [R; \infty)$ (where for $r \to \infty$, $\sigma_\theta(r,\theta) \to \sigma_g$). The following expressions were obtained:

$$\begin{aligned}
\sigma_r\left(r, \theta = \pm\frac{\pi}{2}\right) &= \frac{\sigma_g}{2}\left(\frac{3a^2}{r^2} - \frac{3a^4}{r^4}\right)\\
\sigma_\theta\left(r, \theta = \pm\frac{\pi}{2}\right) &= \frac{\sigma_g}{2}\left(2 + \frac{a^2}{r^2} + \frac{3a^4}{r^4}\right)\\
\tau_{r\theta}\left(r, \theta = \pm\frac{\pi}{2}\right) &= 0
\end{aligned} \tag{7.18}$$

Clearly these equations will be adapted to the case at hand to perform the fit operation.

7.4 Workflow for the application of the TCD method

In this section the theory of critical distances will be addressed both in its classical formulation and in the one proposed by Taylor and Susmel in [49], where a calibration takes place using two curves.

7.4.1 Classic TCD formulation in HCF fatigue

As seen in Ch. 2, in order to be able to apply the theoretical concepts developed, it is essential to know the critical distance L which depends on two material parameters: the fatigue limit range of the smooth specimen $\Delta\sigma_0$ and the range of the threshold value of the stress intensity factor ΔK_{th}. The first value was determined from the experimental curves proposed in Ch. 5 and it is equal to $\Delta\sigma_0 = 1142$ MPa for 42CrMo4 + QT material. By adding the fatigue limits of the other two materials, Tab. 7.4 was obtained.

Material	σ_0 [MPa]	at P.S.50%	Reference
42CrMo4 + QT	573.3		\
42CrM04 + QT	390		[44]
S275	217		[39]
AlMgSi1	113		[39]

Table 7.4: *Fatigue limit of smooth specimens*

The stress intensity factor for 42CrMo4 + QT material was extracted from experimental results according to the ASTM E647 standard using compact tension (CT) specimens. In Fig. 7.37 is depicted the CT specimen type used for the tests, where W is the width and a is the pre-crack length including notch. The stress intensity factor was estimated using the following equation:

$$K = \frac{\Delta F}{B\sqrt{W}} f(\alpha) \tag{7.19}$$

where B is the specimen thickness in mm, $f(\alpha)$ is a function of dimensionless correction factor and ΔF is the force range in N. For description of the fatigue crack growth rate, Klesnil and Lukáš proposed the following relationship [23]:

$$\frac{da}{dN} = C(\Delta K - \Delta K_{th})^m \tag{7.20}$$

The two constants, $C = 2.1 \cdot 10^{-11}\ \frac{m}{cycle}\frac{1}{(MPa\sqrt{m})^{2.59}}$ and $m = 2.59$, were derived from the experimental results and it was then possible to determine the design curve shown in Figure 7.37. In particular, a ΔK_{th} value of 9.1 MPa$\sqrt{m}$ was taken.

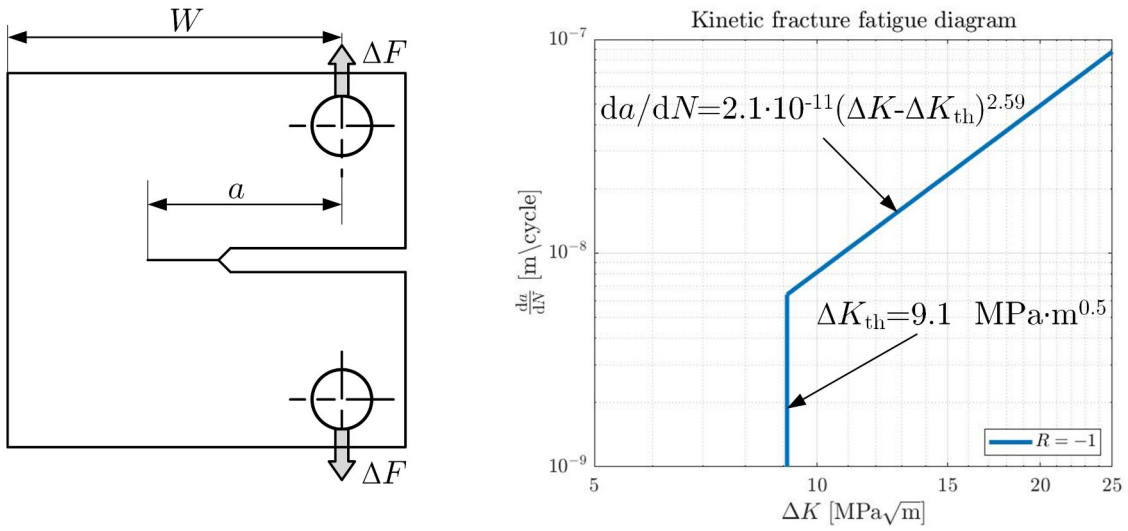

Figure 7.37: *CT specimen and Klesnil and Lukáš fit curve [23] [44]*

ΔK_{th} and $\Delta\sigma_0$ must be determined at the same stress-ratio. The values for the other materials have been collected in the Tab. 7.5.

Material	ΔK_{th} [MPa$\sqrt{m}$]	**Reference**
42CrMo4 + QT	9.10	[44]
S275	5.4	[17]
AlMgSi1	3.68	[7]

Table 7.5: *Threshold value of the stress intensity factor* ΔK_{th}

Since ΔK_{th} values for AlMgSi1 are difficult to find and have been found in the literature with $R = -1$, the following equation has been applied to determine the number in Tab. 7.5:

$$\Delta K_{th}(R) = (1 - R)^{\gamma} \Delta K_{th}(R = 0) \tag{7.21}$$

where γ is a material parameter and $\Delta K_{th}(R = 0)$ is the range of the threshold value of the stress intensity factor with $R = 0$. These two parameters can be derived by imposing a system of two equations in two unknowns, knowing two ΔK_{th} at two different stress cycles R (for the same material). In [7], four ΔK_{th} values were obtained at four different stress ratio. To be more precise, a fit equation was adopted to derive gamma and $\Delta K_{th}(R = 0)$, i.e. $y = (1 - x)^a \cdot b$, where a takes on the meaning of γ and b of $\Delta K_{th}(R = 0)$.
Once the main parameters were determined, it was possible to calculate the critical distance using Eq. 2.

$$\begin{aligned}
L &= \frac{1}{\pi} \cdot \left(\frac{\Delta K_{th}}{\Delta\sigma_0} \right)^2 = \frac{1}{\pi} \cdot \left(\frac{9.1}{2 \cdot 573.3} \right)^2 = 0.020 \text{ mm for 42CrMo4 + QT} \\
L &= \frac{1}{\pi} \cdot \left(\frac{\Delta K_{th}}{\Delta\sigma_0} \right)^2 = \frac{1}{\pi} \cdot \left(\frac{9.1}{2 \cdot 390} \right)^2 = 0.043 \text{ mm for 42CrMo4 + QT} \\
L &= \frac{1}{\pi} \cdot \left(\frac{\Delta K_{th}}{\Delta\sigma_0} \right)^2 = \frac{1}{\pi} \cdot \left(\frac{5.4}{2 \cdot 217} \right)^2 = 0.049 \text{ mm for S275} \\
L &= \frac{1}{\pi} \cdot \left(\frac{\Delta K_{th}}{\Delta\sigma_0} \right)^2 = \frac{1}{\pi} \cdot \left(\frac{3.68}{2 \cdot 113} \right)^2 = 0.084 \text{ mm for AlMgSi1}
\end{aligned} \tag{7.22}$$

After the El-Haddad parameter had been determined, the methods provided by Neuber and Peterson were implemented (Ch. 2).

TCD - Line Method in its classical formulation in HCF

To achieve this goal, a matlab® program was implemented to determine $\Delta\sigma_{eff}$. Fig. 7.38 shows a block diagram.

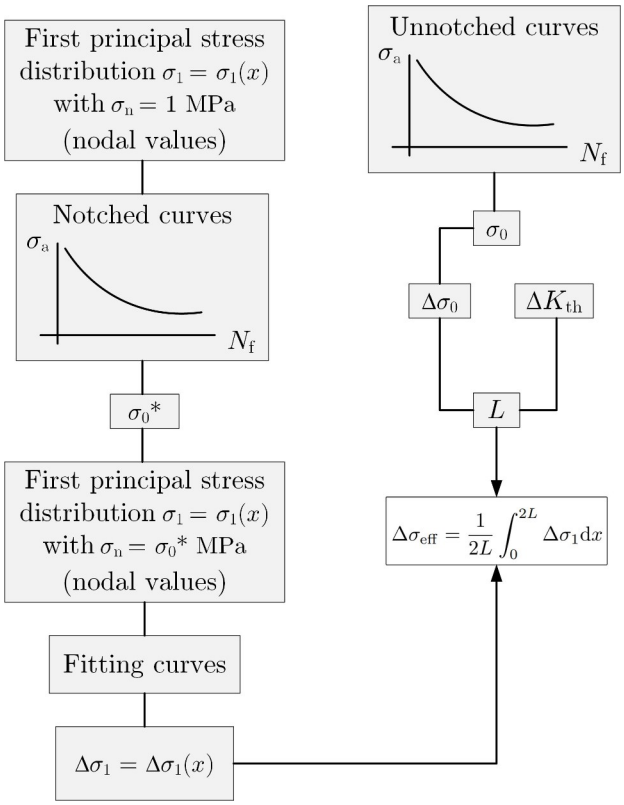

Figure 7.38: *Block diagram of TCD - LM application in its classical formulation in HCF fatigue. In this scheme σ_0^* is the fatigue limit of the notched specimen referred to the net cross-section.*

The text files S1_.txt (A subscript has been inserted after _ to remind the type of geometry), containing the maximum principal stress values for an applied external load, was loaded to perform the analysis. The nodal values were then scaled according to the fatigue limit of notched specimens obtained in Ch. 5 and, the continuum theory developed in Sec. 7.3, was used to derive a continuous function of the stress field, which turns out to be, at the output of ansys® , determined by points (i.e. the mesh nodes). Based on the previous consideration, the following form of the approximation curve was chosen, which is a fourth-order hyperbola containing only even terms. In contrast to the theoretical case, parameters p_2 and p_4 have been added. The reason is that the FE output is evaluated from the root of the notch and not from the centre of the coordinate system, which for the circular hole plate was at the centre of the circle. The following generalised function was obtained:

$$\Delta\sigma_1(x) = p_0 + \frac{p_1}{(q_1 + x)^2} + \frac{p_2}{(q_2 + x)^4} \tag{7.23}$$

where, for the case under consideration, the coefficients have the values described in Tab. 7.6. Tab. 7.6 shows parameters that identify the goodness of fitting the nodal values of the stress fields, i.e. R^2. R-square is the square of the correlation between the nodal values and the predicted values [2]. R^2 can take on any value between 0 and 1, with a value closer to 1 indicating that a greater proportion of variance is accounted for by the model. For example, an R-square value of 0.9976 means that the fit explains 99.76% of the total variation in the data about the average. Applying Eq. 7.23 analytically was obtained:

	Coefficients					
Specimen	p_0	p_1	p_2	q_1	q_2	R^2
Fabest_v05 - 42CrMo4 + QT	189.68	639.10	36.89	1.14	0.51	0.9999
Fabest_v20 - 42CrMo4 + QT	331.91	1434.12	-603.64	1.19	1.31	0.9998
Fabest_h20 - 42CrMo4 + QT	1349.24	688.57	-1384.42	1.64	1.74	0.9991
V-groove ρ = 1 mm - 42CrMo4 + QT	197.41	673.29	138.99	1.19	0.86	1.000
V-groove ρ = 0.2 mm - 42CrMo4 + QT	104.96	261.61	3.19	0.97	0.27	0.9999
F2 with ρ = 1 mm - S275	117.6	3957.6	876.0	5.8	1.2	1.000
F2 with ρ = 0.2 mm - S275	103.5	481.4	3.7	1.6	0.3	0.9998
F2 with ρ = 0.04 mm - S275	86.9	150.5	0.04	0.8	0.08	0.9976
F3 with ρ = 0.2 mm - S275	62.3	435.1	3.5	1.7	0.3	0.9998
F3 with ρ = 0.04 mm - S275	60.2	144.8	0.03	0.8	0.08	0.9972
F2 with ρ = 1 mm - AlMgSi1	66.4	2235.4	494.8	5.8	1.2	1.000
F2 with ρ = 0.2 mm - AlMgSi1	51.7	240.4	1.9	1.6	0.3	0.9998
F2 with ρ = 0.04 mm - AlMgSi1	32.7	56.7	0.01	0.8	0.08	0.9976
F3 with ρ = 0.2 mm - AlMgSi1	46.2	322.4	2.6	1.7	0.3	0.9998
F3 with ρ = 0.04 mm - AlMgSi1	22.0	52.9	0.01	0.8	0.08	0.9972

Table 7.6: *Coefficient of $\Delta\sigma_1 = \Delta\sigma_1(x)$ function at fatigue limit of notched specimens for FABEST and for specimens from [44] and [39]*

$$\begin{aligned}\Delta\sigma_{\text{eff}} &= \frac{1}{2L}\int_0^{2L}\Delta\sigma_1 dx = \frac{1}{2L}\int_0^{2L}\left[p_0 + \frac{p_1}{(q_1+x)^2} + \frac{p_2}{(q_2+x)^4}\right]dx = \\ &= \frac{1}{2L}\left[\int_0^{2L} p_0 dx + \int_0^{2L}\frac{p_1}{(q_1+x)^2}dx + \int_0^{2L}\frac{p_2}{(q_2+x)^4}dx\right] = \\ &= \frac{1}{2L}\left[p_0 x\Big|_0^{2L} - \frac{p_1}{(q_1+x)}\Big|_0^{2L} - \frac{p_2}{3(q_2+x)^3}\Big|_0^{2L}\right] = \\ &= \frac{1}{2L}\left[2Lp_0 - \left(\frac{p_1}{q_1+2L} - \frac{p_1}{q_1}\right) - \left(\frac{p_2}{3(q_2+2L)^3} - \frac{p_2}{3q_2^3}\right)\right]\end{aligned} \tag{7.24}$$

These calculations are performed automatically by matlab®. The results have been collected in Tab. 7.7.

TCD - Point Method in its classical formulation in HCF

With regard to the point method, the function described in Eq. 7.23 was evaluated, following the definitio of Eq. 2.13, for both critical length values derived previously in Eq. 7.22, namely:

$$\Delta\sigma_{\text{eff}} = \Delta\sigma_1\left(x = \frac{L}{2}\right) = p_0 + \left(\frac{p_1}{q_1 + \frac{L}{2}}\right)_2 + \left(\frac{p_2}{q_2 + \frac{L}{2}}\right)_4 \tag{7.25}$$

Again, a simple matlab® program was created to derive the values (Fig. 7.39).
The results have been collected in Tab. 7.8

Specimen	$\Delta\sigma_0$ [MPa]	$2L$ [mm]	$\Delta\sigma_{eff}$ [MPa]	**errors [%]**
Fabest_v05 - 42CrMo4 + QT	1147	0.040	1123.36	-2.03
Fabest_v20 - 42CrMo4 + QT	1147	0.040	1122.14	-2.14
Fabest_h20 - 42CrMo4 + QT	1147	0.040	1454.67	26.86
V-groove ρ = 1 mm - 42CrMo4 + QT	780	0.087	854.5	9.56
V-groove ρ = 0.2 mm - 42CrMo4 + QT	780	0.087	717.1	-8.06
F2 with ρ = 1 mm - S275	434	0.099	544.0	25.4
F2 with ρ = 0.2 mm - S275	434	0.099	594.8	37.0
F2 with ρ = 0.04 mm - S275	434	0.099	529.1	21.9
F3 with ρ = 0.2 mm - S275	434	0.099	458.7	5.7
F3 with ρ = 0.04 mm - S275	434	0.099	456.9	5.2
F2 with ρ = 1 mm - AlMgSi1	226	0.169	290.2	28.39
F2 with ρ = 0.2 mm - AlMgSi1	226	0.169	253.8	12.31
F2 with ρ = 0.04 mm - AlMgSi1	226	0.169	160.2	-29.10
F3 with ρ = 0.2 mm - AlMgSi1	226	0.169	289.8	28.23
F3 with ρ = 0.04 mm - AlMgSi1	226	0.169	133.3	-41.01

Table 7.7: *Output of TCD - LM method in HCF in classical formulation for FABEST and for specimens from [44] and [39]*

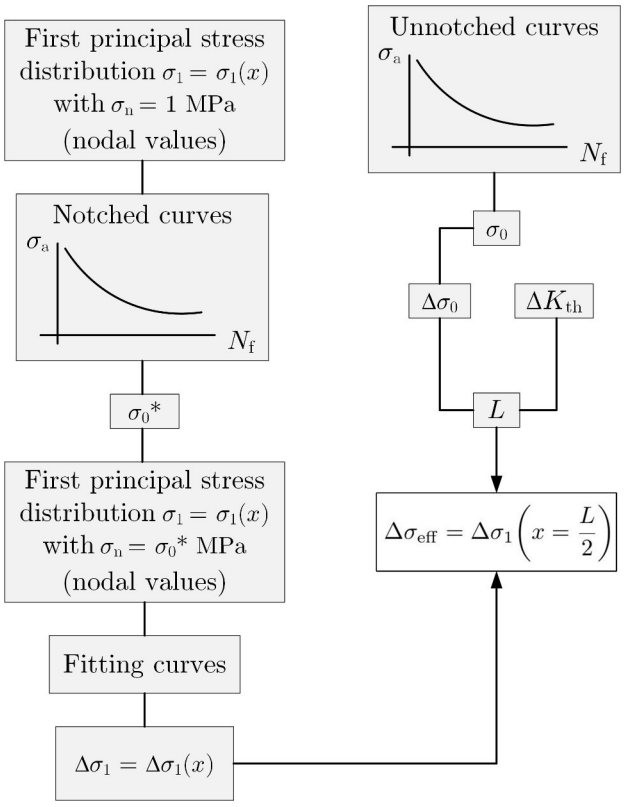

Figure 7.39: *Block diagram of TCD - PM application in its classical formulation in HCF fatigue. In this scheme σ_0^* is the fatigue limit of the notched specimen referred to the net cross-section.*

Specimen	$\Delta\sigma_0$ [MPa]	$L/2$ [mm]	$\Delta\sigma_{eff}$ [MPa]	errors [%]
Fabest_v05 - 42CrMo4 + QT	1147	0.010	1165.29	1.63
Fabest_v20 - 42CrMo4 + QT	1147	0.010	1132.60	-1.22
Fabest_h20 - 42CrMo4 + QT	1147	0.010	1454.42	26.84
V-groove ρ = 1 mm - 42CrMo4 + QT	780	0.022	889.9	14.09
V-groove ρ = 0.2 mm - 42CrMo4 + QT	780	0.022	816.7	4.71
F2 with ρ = 1 mm - S275	434	0.025	568.1	30.9
F2 with ρ = 0.2 mm - S275	434	0.025	681.7	57.0
F2 with ρ = 0.04 mm - S275	434	0.025	630.7	45.3
F3 with ρ = 0.2 mm - S275	434	0.025	526.1	21.2
F3 with ρ = 0.04 mm - S275	434	0.025	548.3	26.3
F2 with ρ = 1 mm - AlMgSi1	226	0.042	310.5	37.37
F2 with ρ = 0.2 mm - AlMgSi1	226	0.042	299.8	32.66
F2 with ρ = 0.04 mm - AlMgSi1	226	0.042	178.1	-21.21
F3 with ρ = 0.2 mm - AlMgSi1	226	0.042	343.6	52.03
F3 with ρ = 0.04 mm - AlMgSi1	226	0.042	149.2	-33.98

Table 7.8: *Output of TCD - PM method in HCF in classical formulation for FABEST and for specimen from [44] and [39]*

7.4.2 Classic TCD formulation in MCF fatigue

TCD - Line Method in its classical formulation in MCF

Susmel and Taylor in [49] extended TCD to the medium cycle regime, i.e., MCF. Here, the classical method has been proposed, which requires knowledge of certain material properties, i.e.:

- σ_{UTS} , ultimate tensile strength;
- σ_0, fatigue limit of the plain specimen,
- ΔK_{th}, range of the threshold value of the stress intensity factor
- $K_{I,c}$, plane strain fracture toughness

From Ch. 5 it is possible to find the value of ultimate tensile strength of 42CrMo + QT equal to σ_{UTS} = 1097 MPa. Due to the enormous difficulty in finding data for other materials, this method was only developed for 42CrMo4 + QT steel, which has $K_{I,c}$ = 82.85 MPa $\sqrt{m}$ following [16]. Using a program implemented in matlab®, it was possible to determine the main quantities of interest following the block diagram proposed in Fig. 7.40 the amplitude of the stress breaking the plain material under static loading σ_0 was calculated in the first instance from Eq. 2.19. The parameters describing the Basquin curve of the smooth specimen were imported together with those of the notched specimens under analysis. Following [49] the two critical lengths in HCF and LCF were derived.
The power law relationship between L and N_f was then determined by imposing the system of two equations in two unknowns as described by Eq. 2.20. Knowing the upper and lower limits, a vector was constructed with some arbitrary cycles and the respective critical distance was calculated for each of them. The program now performs a fit of the nodal values of the stress distribution output from the FEM analysis at a given number of cycles, and, for each of them, determines an effective stress amplitude. In more detail:

1. After performing the experimental tests on the smooth specimen, the fatigue curve described by the parameters C and k was determined using the statistical techniques seen in Ch. 5 and in [49] [45]. It is also possible to derive the fatigue limit σ_0 and the number of cycles at knee point N_0. These data are highlighted in yellow because they are input parameters to the programme.
2. Ultimate tensile strength σ_{UTS} was taken from the tensile tests; this is also an input data, as are $K_{I,c}$ and ΔK_{th}.
3. Amplitude of the stress breaking the plain material under static loading σ_0 was calculated with $R = -1$.

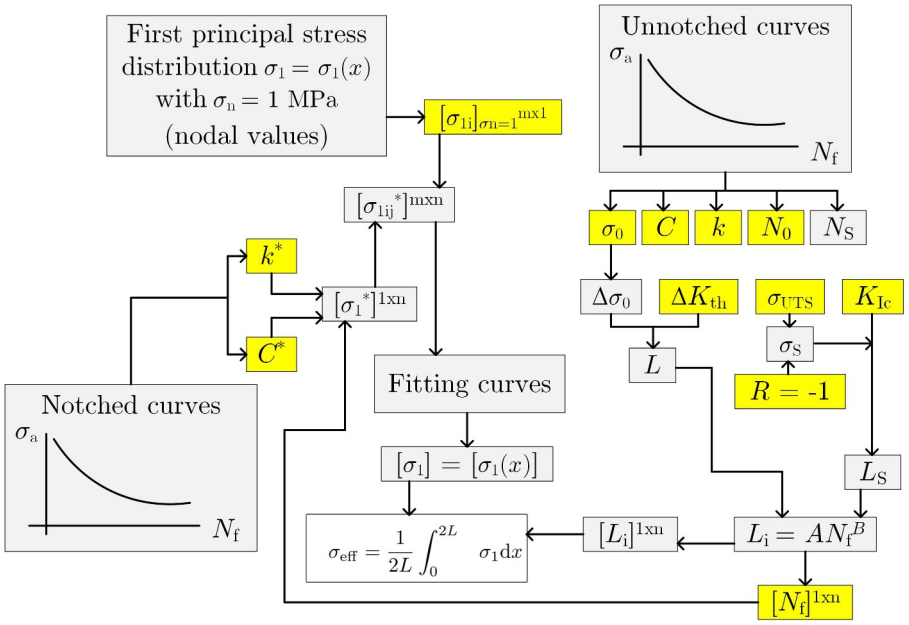

Figure 7.40: *Block diagram of TCD - LM application in its classical formulation in MCF fatigue*

4. The two critical lengths in HCF and LCF were derived respectively.
5. The law $L_i = AN_f^B$ has been derived.
6. A vector of number of cycles $[N_f]^{1xn}$ has been constructed (1 row and *n* columns) and from it a vector of critical lengths was derived.
7. From the FEM analysis, the stress field was obtained with an external load resulting in a nominal net stress of 1 MPa. Here a vector of nodal stresses of dimension mx1 was obtained.
8. Experimental tests were performed on the notched specimens and the parameters k^* and C^* were derived by fitting the data ($*$ refers to the fact that these are parameters for notched specimens).
9. With the previously constructed vector of cycles, a vector of stresses associated with N_f was obtained. The vector has dimension 1xn.
10. Each individual stress value associated with N_f was multiplied by the entire stress field obtained from ansys, and here the advantage of having performed an analysis with a net stress of 1 MPa becomes immediately evident. As can be seen, the entire stress field is scaled according to the stress value determined by the notched specimen curve at a certain number of cycles. This is possible under the assumption of linear elasticity. A mxn matrix has been derived, where the columns represent the stress distributions at a certain N_f.
11. Each individual stress distribution was fitted to obtain a vector of continuous first principal stresses.
12. Each individual function was then imported into the TCD - LM method together with the vector of critical lengths obtained previously. A vector of effective stresses associated with the numbers of cycles defined earlier was obtained.

The results are collected in Tab. 7.9 for FABEST specimens.
with regard to Specimen from [44] it was obtained the Tab. 7.10.

TCD - Point Method in its classical formulation in MCF

For the Point Method, the only substantial difference to the previous case is that the effective stress is calculated at a certain critical distance equal to $L/2$. Fig. 7.41 shows the block diagram which is very similar to Fig. 7.40.
The results are collected in Tab. 7.11.
with regard to Specimen from [44] it was obtained the Tab. 7.12.

N_f [Cycles]	σ_{ref} [MPa]	σ_{eff} [MPa]	**errors [%]**
FABEST_V05			
1000	866.1	999.2	-15.37
2000	821.4	993.8	-21.00
5000	765.8	967.9	-26.39
10^4	726.2	932.3	-28.37
$2 \cdot 10^4$	688.7	883.5	-28.28
$5 \cdot 10^4$	642.1	803.4	-25.12
10^5	609.0	735.8	-20.82
$2 \cdot 10^5$	577.5	666.3	-15.38
FABEST_V20			
1000	866.1	1082.7	-25.01
2000	821.4	1030.0	-25.40
5000	765.8	944.6	-23.35
10^4	726.2	871.7	-20.02
$2 \cdot 10^4$	688.7	796.3	-15.61
$5 \cdot 10^4$	642.1	699.2	-8.88
10^5	609.0	630.2	-3.48
$2 \cdot 10^5$	577.5	565.2	2.14
FABEST_H20			
1000	866.1	2201.9	-154.23
2000	821.4	1904.8	-131.91
5000	765.8	1570.0	-105.02
10^4	726.2	1355.5	-86.64
$2 \cdot 10^4$	688.7	1169.6	-69.81
$5 \cdot 10^4$	642.1	962.5	-49.90
10^5	609.0	830.3	-36.34
$2 \cdot 10^5$	577.5	716.5	-24.06

Table 7.9: *Effective stresses by LM and critical distances for arbitrarily chosen numbers of cycles to failure for FABEST specimens*

N_f [Cycles]	σ_{ref} [MPa]	σ_{eff} [MPa]	**errors [%]**
V-groove ρ = 0.2 mm			
1000	668.6	701.8	-4.97
2000	632.4	680.4	-7.58
5000	587.7	653.1	-11.13
10^4	555.9	632.2	-13.72
$2 \cdot 10^4$	525.9	610.6	-16.10
$5 \cdot 10^4$	488.7	580.1	-18.70
10^5	462.3	554.7	-19.99
$2 \cdot 10^5$	437.3	526.5	-20.41
$5 \cdot 10^5$	406.3	484.5	-19.25

Table 7.10: *Effective stresses by LM and critical distances for arbitrarily chosen numbers of cycles to failure for specimen from [44]*

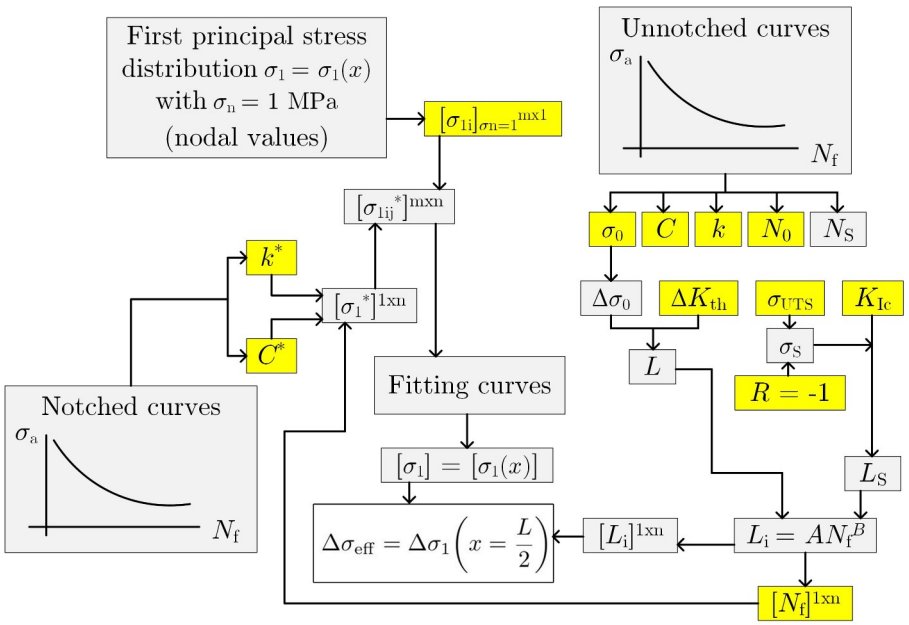

Figure 7.41: *Block diagram of TCD - PM application in its classical formulation in MCF fatigue*

N_f [Cycles]	σ_{ref} [MPa]	σ_{eff} [MPa]	**errors [%]**
FABEST_V05			
1000	866.1	1176.9	-35.88
2000	821.4	1168.4	-42.25
5000	765.8	1117.5	-45.92
10^4	726.2	1053.6	-45.08
$2 \cdot 10^4$	688.7	975.5	-41.63
$5 \cdot 10^4$	642.1	862.0	-34.24
10^5	609.0	775.4	-27.33
$2 \cdot 10^5$	577.5	692.4	-19.89
FABEST_V20			
1000	866.1	1207.2	-39.39
2000	821.4	1121.9	-36.59
5000	765.8	1001.8	-30.83
10^4	726.2	910.0	-25.31
$2 \cdot 10^4$	688.7	821.3	-19.28
$5 \cdot 10^4$	642.1	713.6	-11.13
10^5	609.0	639.1	-4.94
$2 \cdot 10^5$	577.5	570.7	1.18
FABEST_H20			
1000	866.1	2211.7	-154.37
2000	821.4	1909.2	-132.45
5000	765.8	1571.0	-105.15
10^4	726.2	1355.6	-86.66
$2 \cdot 10^4$	688.7	1169.4	-69.78
$5 \cdot 10^4$	642.1	962.3	-49.86
10^5	609.0	830.1	-36.31
$2 \cdot 10^5$	577.5	716.4	-24.04

Table 7.11: *Effective stresses by PM and critical distances for arbitrarily chosen numbers of cycles to failure for FABEST specimens*

V-groove ρ = 0.2 mm			
N_f [Cycles]	σ_{ref} [MPa]	σ_{eff} [MPa]	**errors [%]**
1000	668.6	754.4	-12.84
2000	632.5	744.1	-17.65
5000	587.7	734.7	-25.02
10^4	555.9	728.1	-30.98
$2 \cdot 10^4$	525.9	717.8	-36.49
$5 \cdot 10^4$	488.7	692.3	-41.67
10^5	462.3	661.9	-43.18
$2 \cdot 10^5$	437.3	622.4	-42.34
$5 \cdot 10^5$	406.3	560.9	-37.85

Table 7.12: *Effective stresses by PM and critical distances for arbitrarily chosen numbers of cycles to failure for specimen from [44]*

As can be seen, the lack of precise data regarding material properties (such as K_{fc}) leads to high deviations between actual and reference stress.

7.4.3 TCD in HCF by using two calibration curves

As seen in the previous subsections, the practical application of the TCD, in its classical formulation, requires a prior knowledge of the range of fatigue limit of the smooth specimen $\Delta\sigma_0$ and the range of the threshold value of the stress intensity factor ΔK_{th}. $\Delta\sigma_0$ can be obtained from the curve of the smooth specimen at a high number of cycles (see Chap. 5). Due to the difficulty in finding ΔK_{th} from the literature, the Point Method for determining the characteristic length of the material was also proposed in this thesis work. This approach involves the use of two calibration curves, one smooth and the notched specimen. Since L is a parameter that only depends on the material, it can be seen from Fig. 7.42 that the different stress gradients due to different types of geometries should have no influence if the TCD concept is correct.

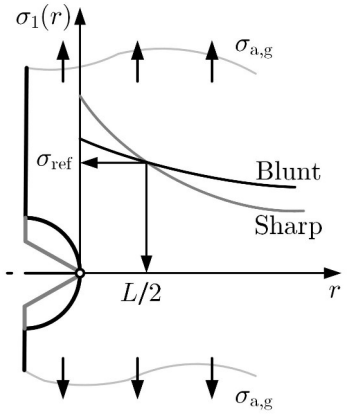

Figure 7.42: *Critical Distance Estimation for sharp and blunt notches*

Two curves can be used to find a value of the inherent strength σ_{ref} that makes the two estimations agree. Ideally, considering a sharp notch and a blunt notch, the critical distance should be unambiguous. In reality, it must be noticed that when a blunt notch is adopted, small errors on stresses bring to large error in critical distance estimation. On the contrary, when sharp notches are studied, small errors on critical distance result in large errors on the reference stress. For this reason, the use of sharp notches has to be preferred for critical distance estimation. For the bar specimens, the one with ρ = 0.2 mm was chosen because it is the specimen with the most pronounced degree of sharpness compared to the other specimens under analysis from [44]. L is a length derived from LEFM, in order to respect the assumptions through which it is derived, a notch, as acute as possible, must be considered. For FABEST campaign the specimen with ρ = 0.5 mm was taken. Therefore, a component subjected to a fatigue

load, it is possible to determine the linear elastic stress field in the vicinity of the stress concentrator and, following the reverse path, this is possible to enter with the reference stress, $\Delta\sigma_{a,ref}$ across the diagram and determine the length $L/2$. Fig. 2.9 clarifies the procedure to be followed to extrapolate the critical length. A matlab ® program has been implemented:

1. Stress fields with a $\Delta\sigma_{a,ref} = 1$ MPa have been imported.
2. The fatigue limit, a material property, was loaded together with the fatigue limits of the notched specimens from the experimental tests.
3. As done previously, the fit function was derived for first principal stress
4. Using Newton's method for solving non-linear equations, the critical distance was calculated by imposing the equality $\Delta\sigma_0 = \Delta\sigma_1(x)$
5. When the critical distance was known, the PM were applied.

The results were collected in Tab. 7.13.

Point Method				
Specimen	$\Delta\sigma_0$ [MPa]	$L/2$ [mm]	$\Delta\sigma_{eff}$ [MPa]	**errors [%]**
FABEST_V05 - 42CrMo4 + QT	1147	0.014	1147	0
FABEST_V20 - 42CrMo4 + QT	1147	0.014	1128.2	-1.61
FABEST_H20 - 42CrMo4 + QT	1147	0.014	1454.5	26.85
V-groove ρ = 1 mm - 42CrMo4 + QT	780	0.027	879.6	12.76
V-groove ρ = 0.2 mm - 42CrMo4 + QT	780	0.027	780	0

Table 7.13: *Output of TCD - using reverse Point Method for 42CrM04 + QT for FABEST and specimens from [44]*

The following were used for the flat specimens with ρ = 0.04 mm. A programme has been written for each type of material. The results for the S275 steel specimen have been compiled in Tab. 7.14.

Point Method				
Specimen	$\Delta\sigma_0$ [MPa]	$L/2$ [mm]	$\Delta\sigma_{eff}$ [MPa]	**errors [%]**
Niessner F2 ρ = 1 mm	434	0.038	554.0	27.65
Niessner F2 ρ = 0.2 mm	434	0.038	618.0	42.40
Niessner F2 ρ = 0.04 mm	434	0.038	501.9	15.64
Niessner F3 ρ = 0.2 mm	434	0.038	477.4	9.99
Niessner F3 ρ = 0.04 mm	434	0.038	434	0

Table 7.14: *Output of TCD - using reverse Point Method for S275 with F3, ρ = 0.04 mm, reference specimen [39]*

The same strategy has been adopted for aluminium alloy test pieces. The results were collected in Tab. 7.15.

Point Method				
Specimen	$\Delta\sigma_0$ [MPa]	$L/2$ [mm]	$\Delta\sigma_{eff}$ [MPa]	**errors [%]**
Niessner F2 ρ = 1 mm	226	0.019	324.3	43.49
Niessner F2 ρ = 0.2 mm	226	0.019	355.7	57.39
Niessner F2 ρ = 0.04 mm	226	0.019	267.3	18.27
Niessner F3 ρ = 0.2 mm	226	0.019	407.0	80.08
Niessner F3 ρ = 0.04 mm	226	0.019	226	0

Table 7.15: *Output of TCD - using reverse Point Method for AlMgSi1 with F3,* ρ = 0.04 mm, *reference specimen [39]*

7.4.4 TCD in MCF by using two calibration curves

For the MCF fatigue region, the same criterion was adopted as in HCF. The only difference is that now it is necessary to determine a critical distance at two different numbers of cycles to failure in order to derive a function as in Eq. 2.18. In order to determine the functional relationship between the critical distance and the number of cycles, 10^4 and $5 \cdot 10^5$ cycles with the respective stresses were taken for both the smooth and the notched specimen curves for FABEST campaign. A matlab® program was implemented which derived the critical distances and then saved these in a .mat file. The fit function found for FABEST_V05 is:

$$L = 70.12 \cdot N_f^{0.53} \tag{7.26}$$

In subsequent programs, those critical distances were adopted for the PM method. The following effective stresses were obtained in Tab. 7.16.
For the specimens from [44], the one with ρ = 0.2 mm was taken as the reference specimen. The function is:

$$L = 18.58 \cdot N_f^{0.36} \tag{7.27}$$

The results in Tab. 7.17 were obtained.
With regard to the flat specimens from Niessner's article [39], with ρ = 0.04 mm were taken as reference. In this case, 10^4 and 10^6 cycles with the respective stresses were taken. The tables for steel and aluminium alloy were obtained, Tabs. 7.18, 7.19. The function for steel is:

$$L = 382,29 \cdot N_f^{0.56} \tag{7.28}$$

For aluminium the function is:

$$L = 22.04 \cdot N_f^{0.35} \tag{7.29}$$

N_f [Cycles]	σ_{ref} [MPa]	σ_{eff} [MPa] - PM	**errors [%]**
FABEST_V05			
10^4	726.2	634.6	12.6
$2 \cdot 10^4$	688.7	644.8	6.4
$5 \cdot 10^4$	642.1	639.1	0.5
10^5	609.0	618.6	-1.6
$2 \cdot 10^5$	577.5	586.1	-1.5
$5 \cdot 10^5$	538.5	530.3	1.5
FABEST_V20			
10^4	726.2	756.8	-4.2
$2 \cdot 10^4$	688.7	718.5	-4.3
$5 \cdot 10^4$	642.1	653.2	-1.7
10^5	609.0	600.9	1.3
$2 \cdot 10^5$	577.5	546.7	5.3
$5 \cdot 10^5$	538.5	477.8	11.3
FABEST_H20			
10^4	726.2	1353.1	-86.3
$2 \cdot 10^4$	688.7	1169.2	-69.8
$5 \cdot 10^4$	642.1	962.8	-49.9
10^5	609.0	830.7	-36.4
$2 \cdot 10^5$	577.5	716.8	-24.1
$5 \cdot 10^5$	538.5	589.8	-9.5

Table 7.16: *Effective stresses by PM using reverse path for FABEST specimens*

V-groove ρ = 0.2 mm			
N_f [Cycles]	σ_{ref} [MPa]	σ_{eff} [MPa] - PM	**errors [%]**
10^4	555.9	466.0	15.5
$2 \cdot 10^4$	525.9	455.4	13.4
$5 \cdot 10^4$	488.7	438.8	10.2
10^5	462.3	427.0	7.6
$2 \cdot 10^5$	437.3	414.3	5.3
$5 \cdot 10^5$	406.3	393.9	3.1

Table 7.17: *Effective stresses by PM using reverse path for specimens from [44]*

N_f [Cycles]	σ_{ref} [MPa]	σ_{eff} [MPa] - PM	**errors [%]**
	F2 ρ = 1 mm		
10^4	365.8	250.5	31.5
$2 \cdot 10^4$	338.2	258.6	23.5
$5 \cdot 10^4$	304.8	271.7	10.9
10^5	281.8	277.9	1.4
$2 \cdot 10^5$	260.6	277.6	-6.6
$5 \cdot 10^5$	234.7	266.5	-13.5
10^6	217.0	251.7	-16.0
	F2 ρ = 0.2 mm		
10^4	365.8	175.2	52.1
$2 \cdot 10^4$	338.2	177.0	47.7
$5 \cdot 10^4$	304.8	180.0	40.9
10^5	281.8	185.1	34.3
$2 \cdot 10^5$	260.6	194.0	25.5
$5 \cdot 10^5$	234.7	209.2	10.9
10^6	217.0	218.8	-0.8
	F2 ρ = 0.04 mm		
10^4	365.8	113.8	68.9
$2 \cdot 10^4$	338.2	117.1	65.4
$5 \cdot 10^4$	304.8	121.4	60.2
10^5	281.8	122.9	56.4
$2 \cdot 10^5$	260.6	122.8	52.8
$5 \cdot 10^5$	234.7	123.4	47.4
10^6	217.0	127.7	41.1
	F3 ρ = 0.2 mm		
10^4	365.8	217.3	40.6
$2 \cdot 10^4$	338.2	219.0	35.2
$5 \cdot 10^4$	304.8	221.3	27.2
10^5	281.8	226.0	19.8
$2 \cdot 10^5$	260.6	234.7	9.9
$5 \cdot 10^5$	234.7	248.5	-5.8
10^6	217.0	254.9	-17.5

Table 7.18: *Effective stresses by PM using reverse path for specimens from [39] for S275*

N_f [Cycles]	σ_{ref} [MPa]	σ_{eff} [MPa] - PM	**errors [%]**
	F2 ρ = 1 mm		
10^4	223.8	188.9	15.6
$2 \cdot 10^4$	201.9	186.6	7.6
$5 \cdot 10^4$	176.3	181.6	-3.0
10^5	159.0	176.0	-10.7
$2 \cdot 10^5$	143.5	169.0	-17.8
$5 \cdot 10^5$	125.2	157.8	-26.0
10^6	113.0	148.4	-31.3
	F2 ρ = 0.2 mm		
10^4	223.8	110.3	50.7
$2 \cdot 10^4$	201.9	107.4	46.8
$5 \cdot 10^4$	176.3	104.9	40.5
10^5	159.0	103.8	34.7
$2 \cdot 10^5$	143.5	103.3	28.0
$5 \cdot 10^5$	125.2	102.9	17.8
10^6	113.0	102.2	9.5
	F2 ρ = 0.04 mm		
10^4	223.8	41.1	81.6
$2 \cdot 10^4$	201.9	36.0	82.2
$5 \cdot 10^4$	176.3	30.0	83.0
10^5	159.0	26.4	83.4
$2 \cdot 10^5$	143.5	22.4	84.4
$5 \cdot 10^5$	125.2	18.5	85.2
10^6	113.0	16.4	85.5
	F3 ρ = 0.2 mm		
10^4	223.8	187.2	16.3
$2 \cdot 10^4$	201.9	181.6	10.1
$5 \cdot 10^4$	176.3	175.9	0.2
10^5	159.0	173.1	-8.8
$2 \cdot 10^5$	143.5	171.0	-19.2
$5 \cdot 10^5$	125.2	168.1	-34.2
10^6	113.0	165.0	-46.0

Table 7.19: *Effective stresses by PM using reverse path for specimens from [39] for AlMgSi1*

7.5 Workflow for the application of RSG method

In this subsection, the stress gradient method will be applied according to the FEMFAT and FKM approaches.

7.5.1 FEMFAT approach

In the previous paragraphs, the stress field for each geometric configuration was determined. With the .txt files it is also possible to derive the Von Mises stress as a function of the distance from the tip of the notch, following [13]. Following the FEMFAT approach it is possible to determine the derivative of the stress field with respect to the x-coordinate (See Eq. 3.5). In this formulation, the S-N curve is only determined at the most critical point, i.e. the point with the highest equivalent stress. The stress gradient values are collected in Tab. 7.20.

Specimen	χ $\left[\frac{\text{MPa}}{\text{mm}}\right]$	χ' $[\text{mm}^{-1}]$
Fabest_v05	2515.6	5.1717
Fabest_v20	475.5	1.2489
V-groove ρ = 1 mm	1134.5	2.7318
V-groove ρ = 0.2 mm	5708.5	12.9599
F2 with ρ = 1 mm	773.4	2.3081
F2 with ρ = 0.2 mm	4723.3	11.5356
F2 with ρ = 0.04 mm	29304.0	57.5753
F3 with ρ = 0.2 mm	5054.2	11.5616
F3 with ρ = 0.04 mm	43985.0	55.4247

Table 7.20: *Stress gradient at the tip of the notch and relative stress gradient*

With reference to specimen Fabest_h20, an anomaly was found. The tangent to the point of maximum stress (which should represent the stress gradient, see Fig. 7.26) is practically flat, and for this reason the output was not convincing to continue with the RSG approach. Three methods have been developed in FEMFAT to take into account the effect of the relative stress gradient, but only two of these will be developed in this thesis work (see [3], Sec. 3.1). The Stieler equation depends on the yield stress of the material and therefore parametric curves can be derived as in Fig. 7.43. According to the IABG method, the curve in Fig. 7.43 was obtained for steel.

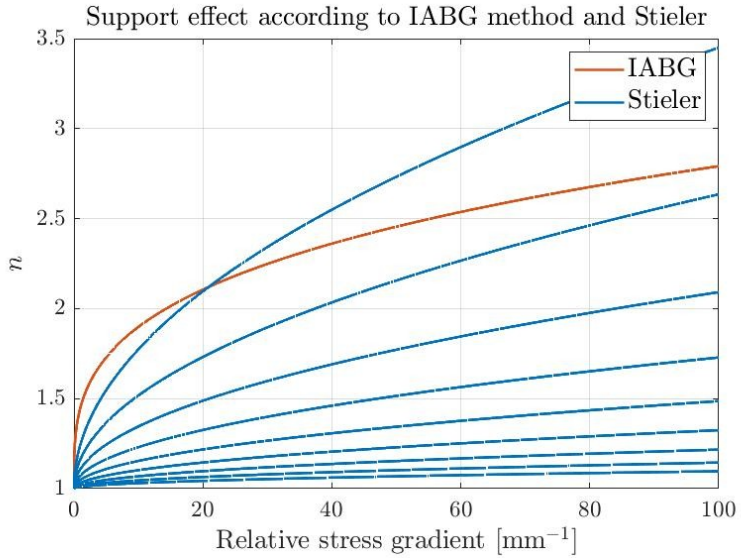

Figure 7.43: *Support effect as a function of relative stress gradient according to Stieler and IABG method*

n	Stieler			IABG	
Specimen	**42CrMo4+QT**	**S275**	**AlMgSi1**	**42CrMo4+QT**	**S275**
Fabest_v05	1.0417	x	x	1.7367	x
Fabest_v20	1.0205	x	x	1.4810	x
V-groove ρ = 1 mm	1.0736	x	x	1.6083	x
V-groove ρ = 0.2 mm	1.1604	x	x	1.9705	x
F2 with ρ = 1 mm	x	1.2366	1.2676	x	1.5784
F2 with ρ = 0.2 mm	x	1.529	1.5982	x	1.9372
F2 with ρ = 0.04 mm	x	2.1819	2.3365	x	2.518
F3 with ρ = 0.2 mm	x	1.5296	1.5593	x	1.9378
F3 with ρ = 0.04 mm	x	2.1596	2.4559	x	2.5008

Table 7.21: *Support factors for different materials and geometries*

Local fatigue limit $\sigma_{af,C}$	Stieler			IABG	
Specimen	**42CrMo4+QT**	**S275**	**AlMgSi1**	**42CrMo4+QT**	**S275**
Fabest_v05	597.2	x	x	995.7	x
Fabest_v20	585.1	x	x	849.1	x
V-groove ρ = 1 mm	418.7	x	x	627.2	x
V-groove ρ = 0.2 mm	452.6	x	x	768.5	x
F2 with ρ = 1 mm	x	268.4	143.2	x	342.5
F2 with ρ = 0.2 mm	x	331.8	180.6	x	420.3
F2 with ρ = 0.04 mm	x	473.5	264.0	x	546.4
F3 with ρ = 0.2 mm	x	331.9	176.2	x	420.5
F3 with ρ = 0.04 mm	x	468.6	277.5	x	542.7

Table 7.22: *Local fatigue limit $\sigma_{af,C}$ for different materials and geometries*

A matlab ® program was implemented to determine the support factors for the two methods. The results were collected in Tab. 7.21.
The programme returns the graph of the support factor following Stieler's definition and IABG definition, as a function of the relative stress gradient in Fig. 7.44. In addition to the curve, there are also points relating to the specific notch geometry. It can be seen that the higher the degree of acuity, the more the support factor tends to increase.
With regard to the geometries from literature [39], the diagrams in Fig. 7.45 were obtained.
Next, the fatigue limits of the local S-N curves were determined using Eq.3.12. The following values were obtained for Stieler method, Tab. 7.22:
The relative stress gradient also influences the slope of the curve. For each material, the values in Tab. 7.23
Fatigue limits of 10^6 cycles and failure stresses of up to 10^3 cycles were used to determine the slope of the smooth material curve for S275 and AlMgSi1. Given these two points in the S-N plane, the slope of the curve was derived using the following equation:

$$k_M = \frac{\log_{10}\left(\frac{10^6}{10^3}\right)}{\log_{10}\left(\frac{\sigma_{UTS}}{\sigma_0}\right)} \tag{7.30}$$

The graphs in Fig. 7.47 were obtained for FABEST specimen and for specimen from [44].
The same curves were also obtained for specimens from [39] in Fig. 7.48
The cycles at the respective local fatigue limits were then determined (Tab. 7.24).
Graphs of the factor $f_{GR,cf}$ against the relative stress gradient can be determined for both Stieler and IABG methods (Fig. 7.50 7.51 7.52).
Once the 3 parameters characterising the local Wohler curve have been determined, the material fatigue curve can be plotted to observe the main differences. In general, compared to the curve of the smooth specimen, there is an increase in fatigue strength, the local fatigue limit moves towards higher values. Conversely, the knee point moves to the left, towards lower numbers of cycles to failure. The slope

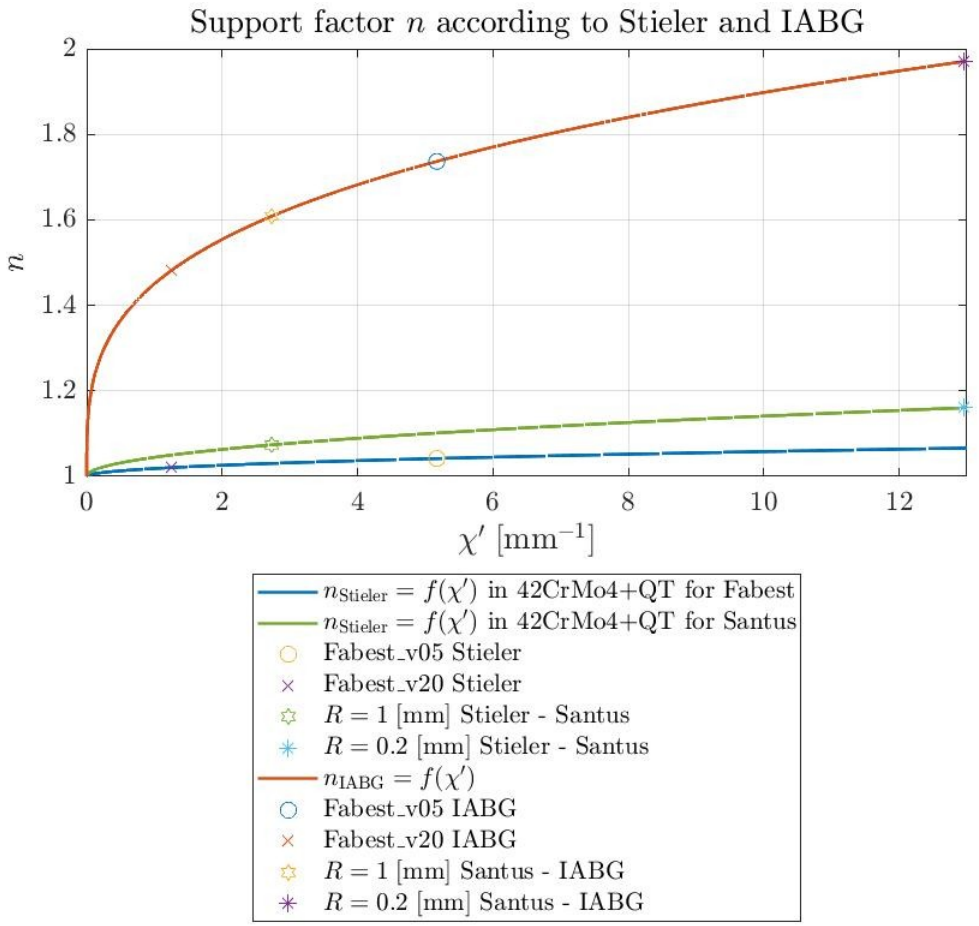

Figure 7.44: *Points of the support factor for each geometry in 42CrMo4+QT - Stieler and IABG method. Diagrams of support factor versus relative stress gradient in accordance with Stieler's and IABG approach [13] for FABEST experimental campaign and from [44]*

k_C	Stieler			IABG	
Specimen	**42CrMo4+QT**	**S275**	**AlMgSi1**	**42CrMo4+QT**	**S275**
Fabest_v05	3.056	x	x	3.1413	x
Fabest_v20	3.9235	x	x	4.5056	x
V-groove [] ρ = 1 mm	3.2176	x	x	3.4222	x
V-groove [] ρ = 0.2 mm	3.0079	x	x	3.022	x
F2 with ρ = 1 mm	x	3.2354	3.1573	x	3.3441
F2 with ρ = 0.2 mm	x	3.0109	3.0076	x	3.017
F2 with ρ = 0.04 mm	x	3.0005	3.0004	x	3.0007
F3 with ρ = 0.2 mm	x	3.0108	3.0100	x	3.017
F3 with ρ = 0.04 mm	x	3.0005	3.0003	x	3.0007

Table 7.23: *Slope of the S-N localcurves*

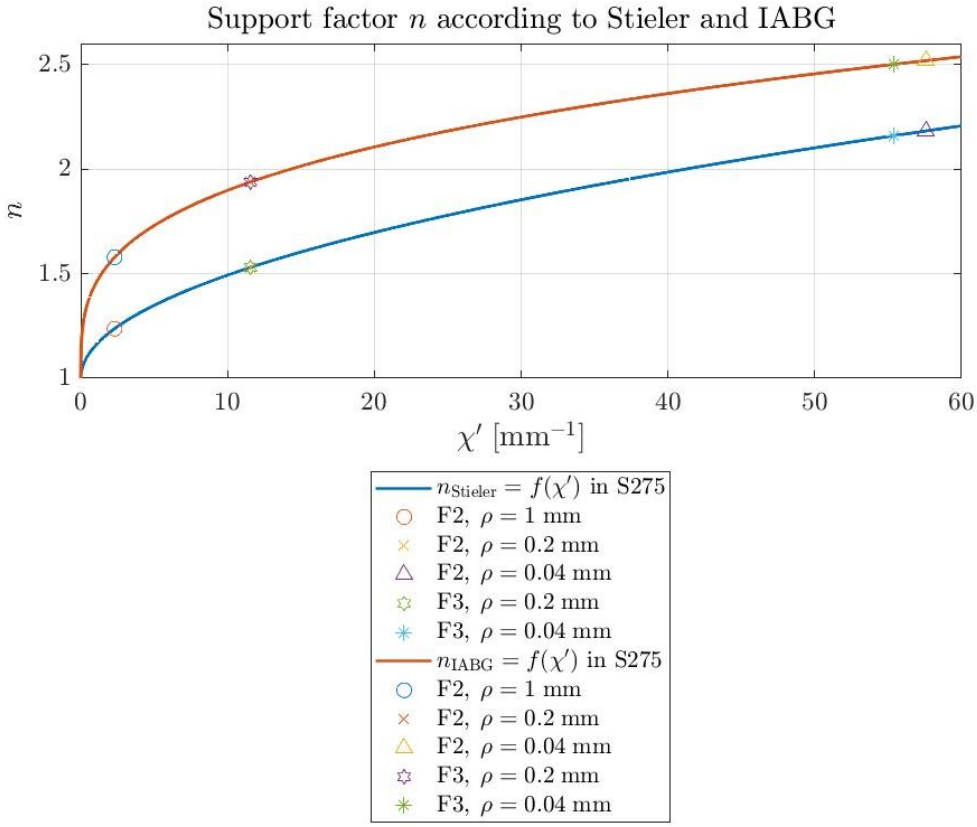

Figure 7.45: *Points of the support factor for each geometry in S275 - Stieler and IABG method. Diagrams of support factor versus relative stress gradient in accordance with Stieler's and IABG approach [13] for article [39]*

$N_{cf,C}$	Stieler			IABG	
Specimen	**42CrMo4+QT**	**S275**	**AlMgSi1**	**42CrMo4+QT**	**S275**
Fabest_v05	27541	x	x	29645	x
Fabest_v20	50170	x	x	65915	x
V-groove ρ = 1 mm	123259	x	x	143784	x
V-groove ρ = 0.2 mm	102996	x	x	104324	x
F2 with ρ = 1 mm	x	197508	247784	x	214666
F2 with ρ = 0.2 mm	x	163158	217425	x	164080
F2 with ρ = 0.04 mm	x	161615	215986	x	161639
F3 with ρ = 0.2 mm	x	163151	219517	x	164069
F3 with ρ = 0.04 mm	x	161620	218644	x	161647

Table 7.24: *Endurance limit of the S-N local curves*

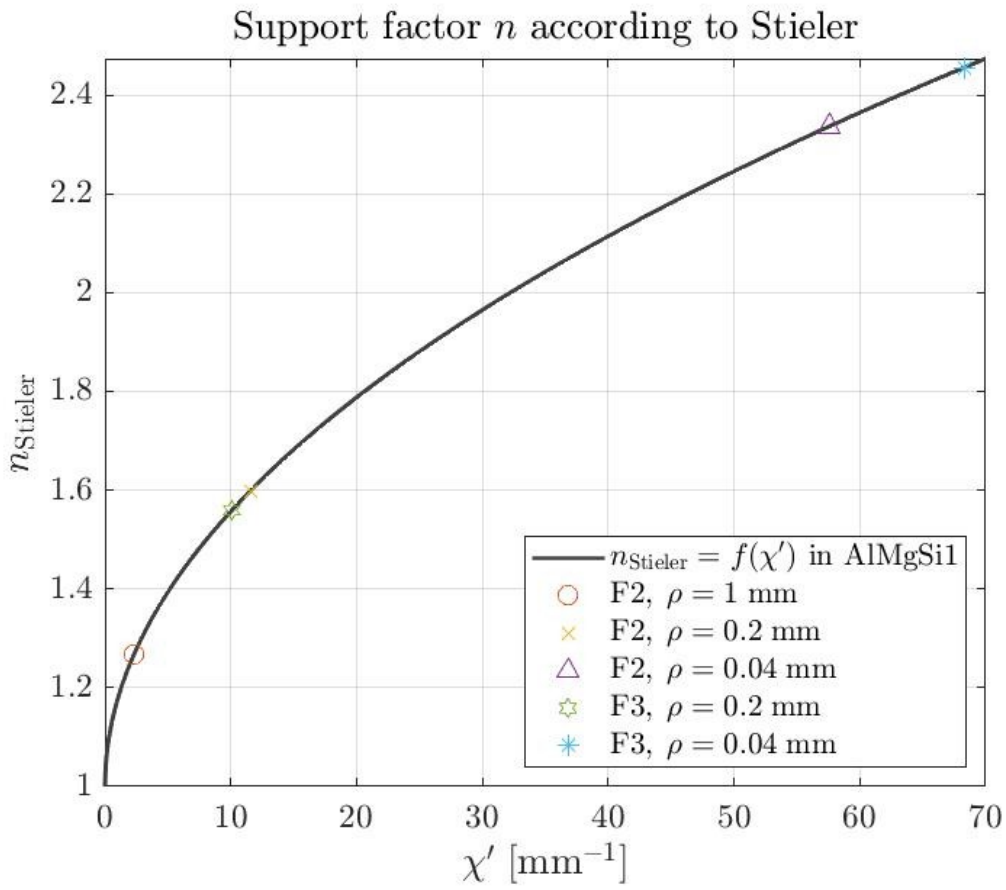

Figure 7.46: *Points of the support factor for each geometry in AlMgSi1 - Stieler method. Diagrams of support factor versus relative stress gradient in accordance with Stieler's approach [13] for article [39]*

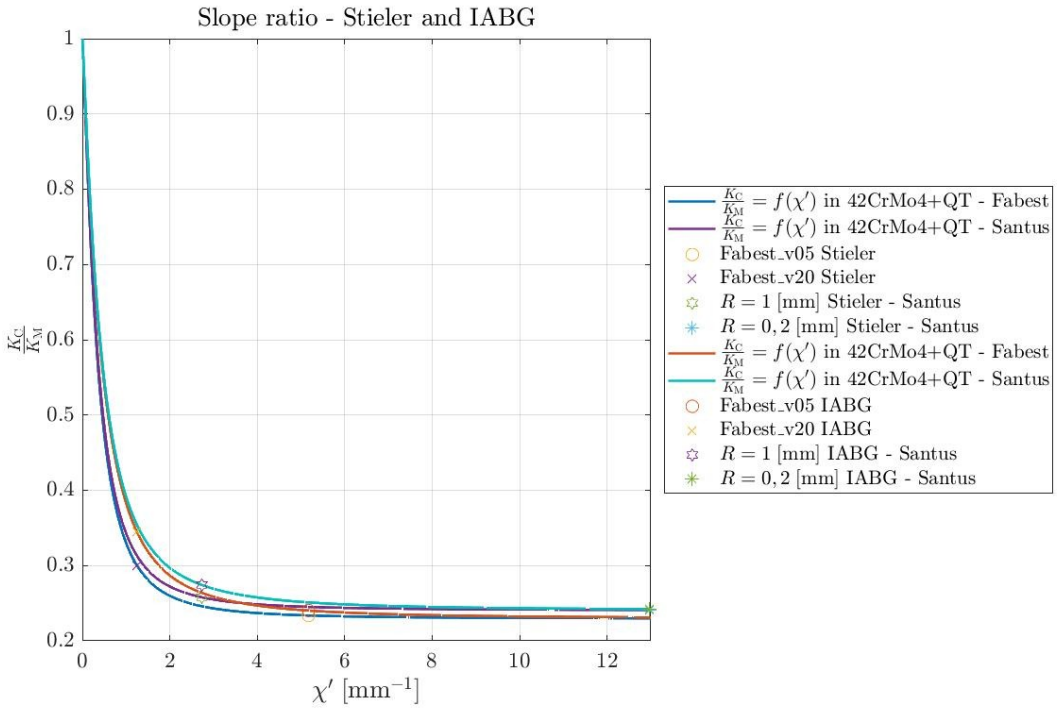

Figure 7.47: *Points of the slope ratio for each geometry in 42CrMo4+QT - Stieler and IABG method. Diagrams of slop ratio versus relative stress gradient in accordance with Stieler's and IABG approach [13] for FABEST experimental campaign and from [44]*

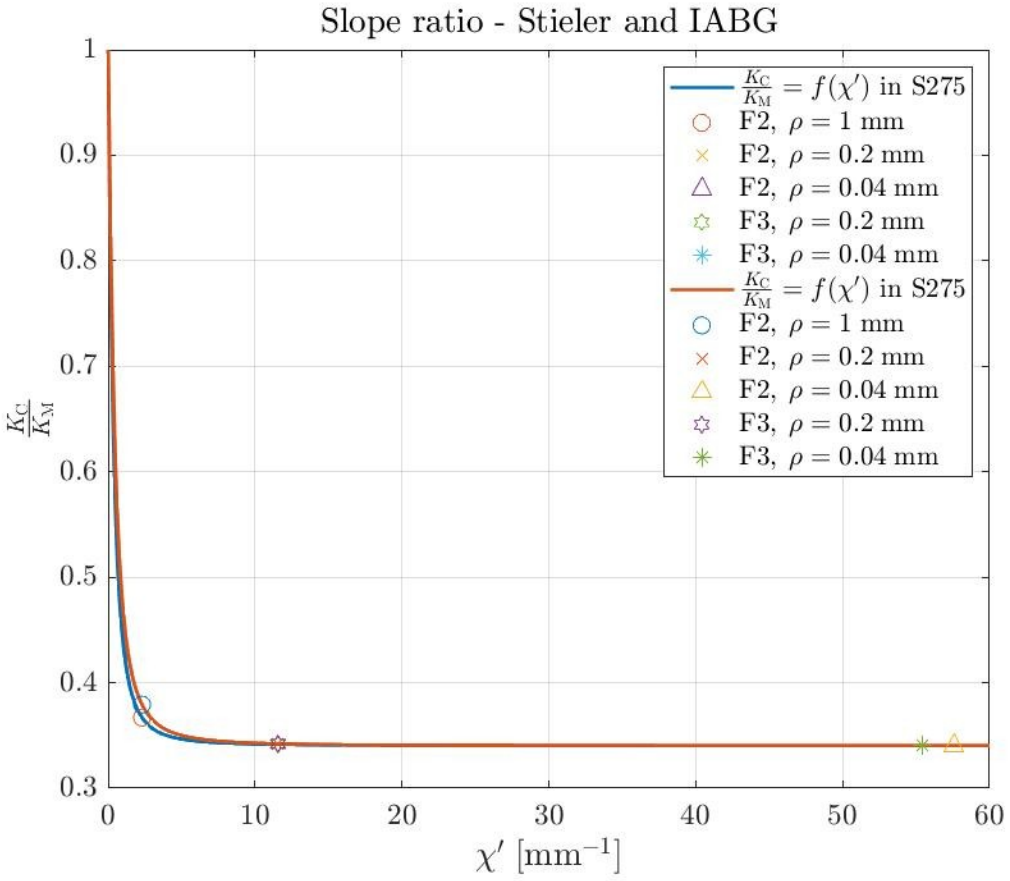

Figure 7.48: *Points of the slope ratio for each geometry in S275 - Stieler and IABG method Diagrams of slop ratio versus relative stress gradient in accordance with Stieler's and IABG approach [13] for Niessner experimental campaign and from [39]*

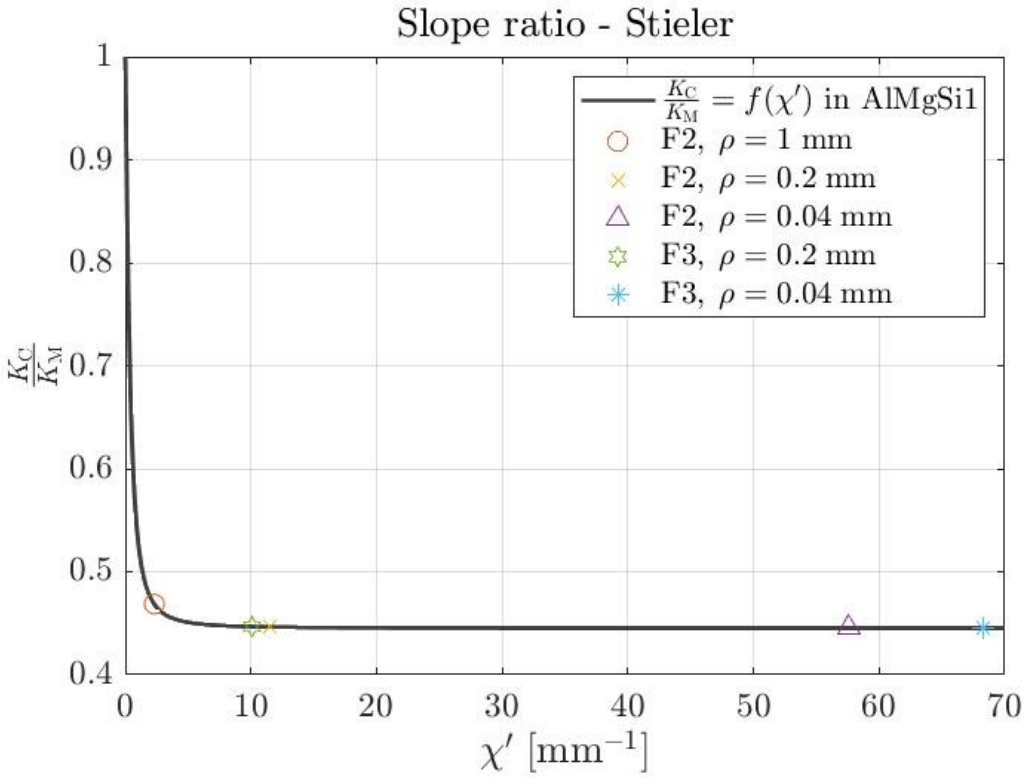

Figure 7.49: *Points of the slope ratio for each geometry in AlMgSi1 - Stieler method. Diagrams of slop ratio versus relative stress gradient in accordance with Stieler's approach [13] for Niessner experimental campaign and from [39]*

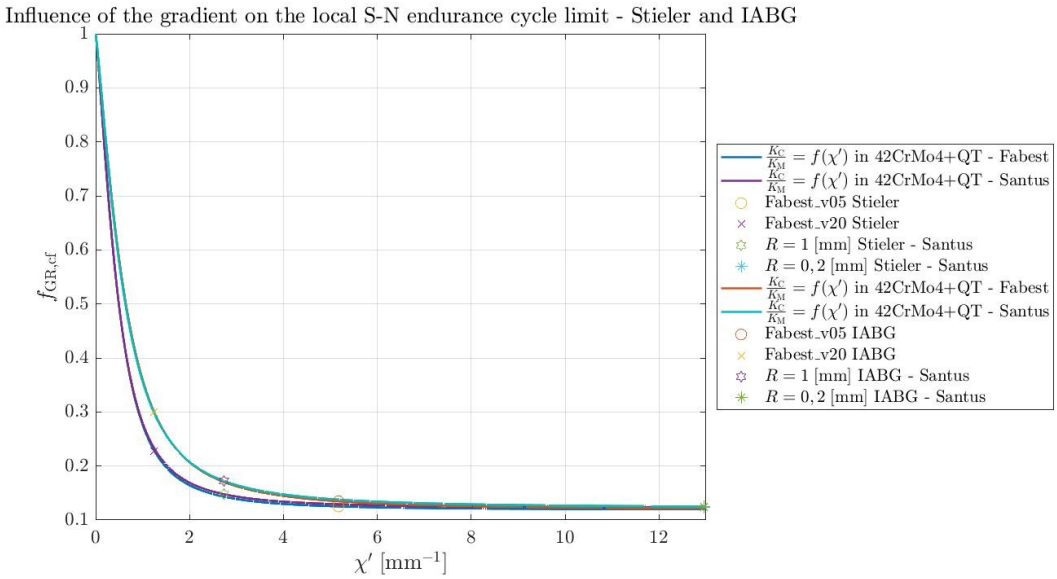

Figure 7.50: *Points of $f_{GR,cf}$ for each geometry in 42CrMo4+QT - Stieler and IABG method. Diagrams of $f_{GR,cf}$ versus relative stress gradient in accordance with Stieler's and IABG approach [13] for FABEST experimental campaign and from [44]*

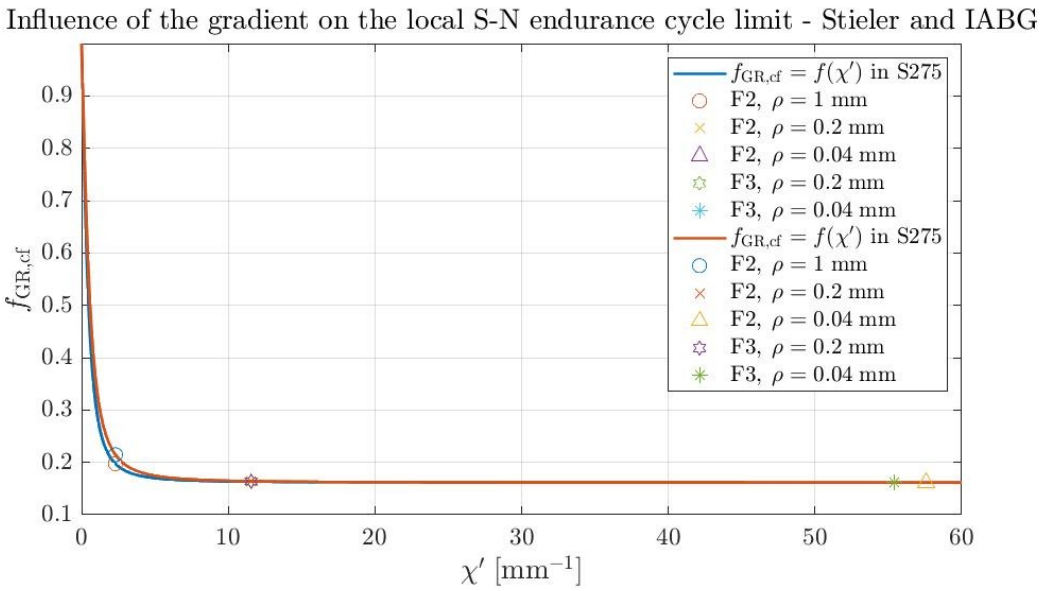

Figure 7.51: *Points of $f_{GR,cf}$ for each geometry in S275 - Stieler and IABG method. Diagrams of $f_{GR,cf}$ versus relative stress gradient in accordance with Stieler's and IABG approach [13] for Niessner experimental campaign and from [39]*

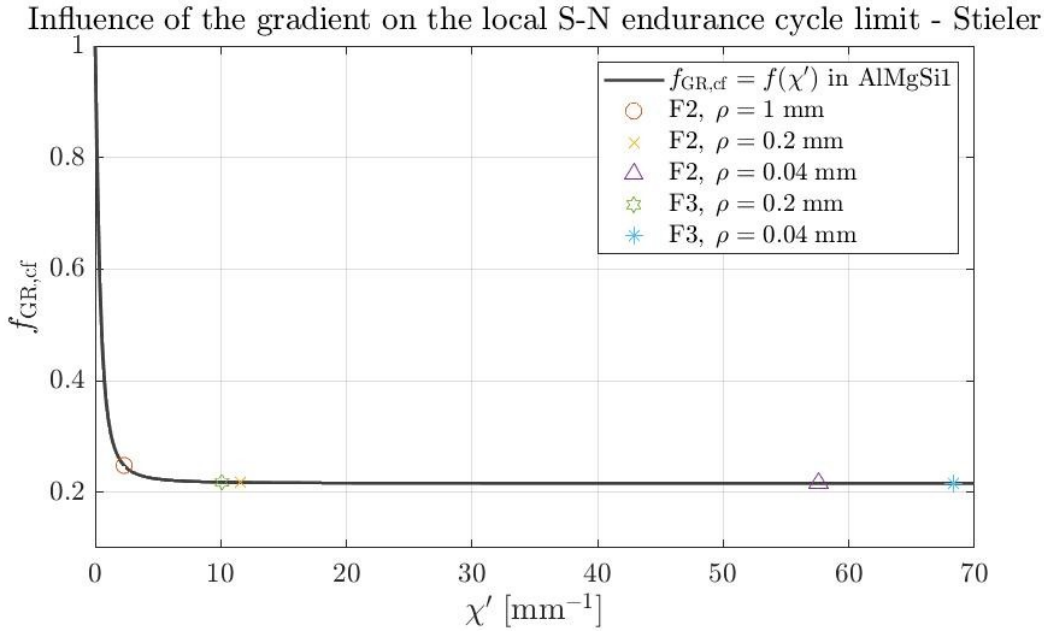

Figure 7.52: *Points of $f_{GR,cf}$ for each geometry in AlMgSi1 - Stieler method. Diagrams of $f_{GR,cf}$ versus relative stress gradient in accordance with Stieler's approach [13] for Niessner experimental campaign and from [39]*

of the local curve decreases. Comparative graphs are shown in Fig. 7.53 where the support factor was calculated in accordance with Stieler.

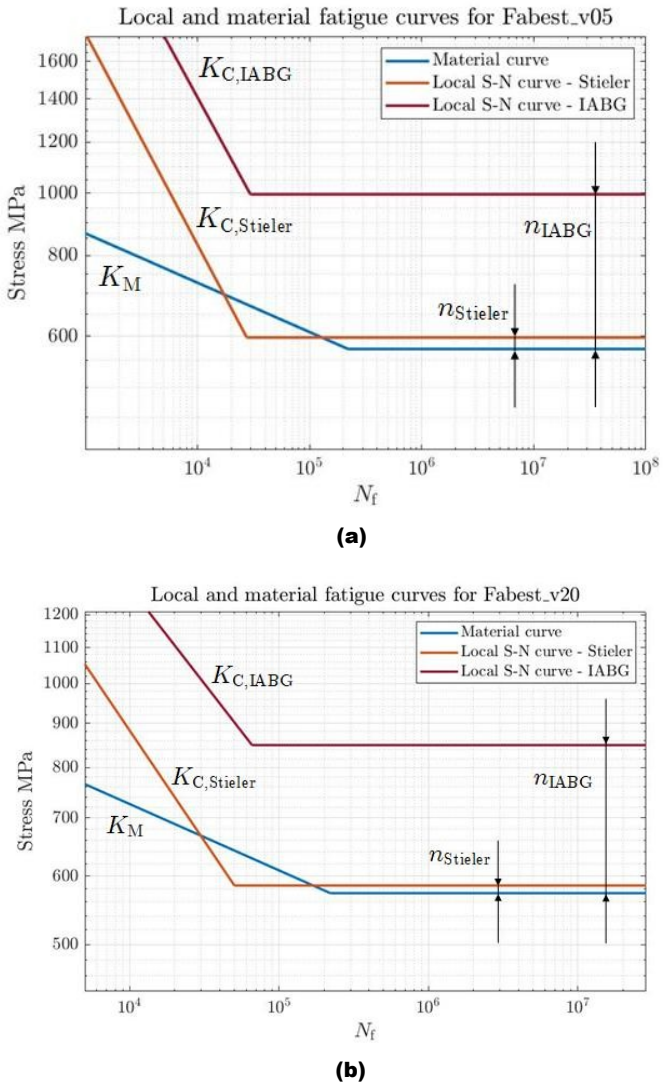

Figure 7.53: *Comparison of local and material fatigue curves for FABEST campaign specimens*

7.5.2 FKM guidelines

The approach followed by the FKM guidelines is to calculate the relative stress gradient using the first principal stress. The results were compiled in Tab. 7.25 in a similar way as for FEMFAT.

Specimen	χ $\left[\frac{MPa}{mm}\right]$	χ' $[mm^{-1}]$
Fabest_v05	6520.4	11.8679
Fabest_v20	444.6	1.0493
V-groove ρ = 1 mm	1085.6	2.3339
V-groove ρ = 0.2 mm	5475.7	10.9457
F2 with ρ = 1 mm	699.3	2.0845
F2 with ρ = 0.2 mm	4283.8	10.4035
F2 with ρ = 0.04 mm	26460.0	51.6878
F3 with ρ = 0.2 mm	4588.0	10.4324
F3 with ρ = 0.04 mm	40295.0	50.1859

Table 7.25: *Stress gradient at the tip of the notch and relative stress gradient according to FKM*

Following Eq. 3.17 the calculation of the support factor is strictly dependent on the relative stress gradien and some material parameters. Depending on the value of χ' different formulations have been proposed for the calculation of n. A matlab® program has been implemented which, depending on the value of χ' obtained, returns the correct support factor (App. ??). For each geometric configuration and for each material, the results were tabulated (Tab. 7.26).

n	FKM		
Specimen	**42CrMo4+QT**	**S275**	**AlMgSi1**
Fabest_v05	1.2498	x	x
Fabest_v20	1.1362	x	x
V-groove ρ = 1 mm	1.1853	x	x
V-groove ρ = 0.2 mm	1.2727	x	x
F2 with ρ = 1 mm	x	1.2534	1.4562
F2 with ρ = 0.2 mm	x	1.3788	1.6819
F2 with ρ = 0.04 mm	x	1.5655	2.018
F3 with ρ = 0.2 mm	x	1.3790	1.6824
F3 with ρ = 0.04 mm	x	1.5613	2.0105

Table 7.26: *Support factors for different materials and geometries*

The guide now sets constant values for the number of cycles at knee point and the slope (See Ch. Sec.3.2). it is possible to observe the graph in Fig.5 which makes a comparison between the local S-N curves and the material curve.
The local fatigue limits become, Tab. 7.27:

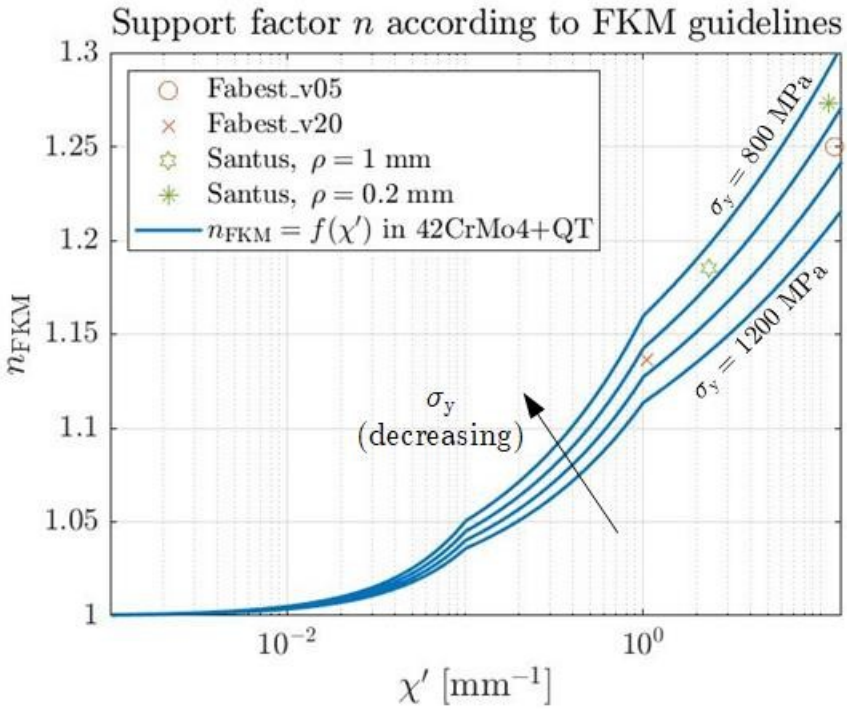

Figure 7.54: *Support effect as a function of relative stress gradient according to FKM*

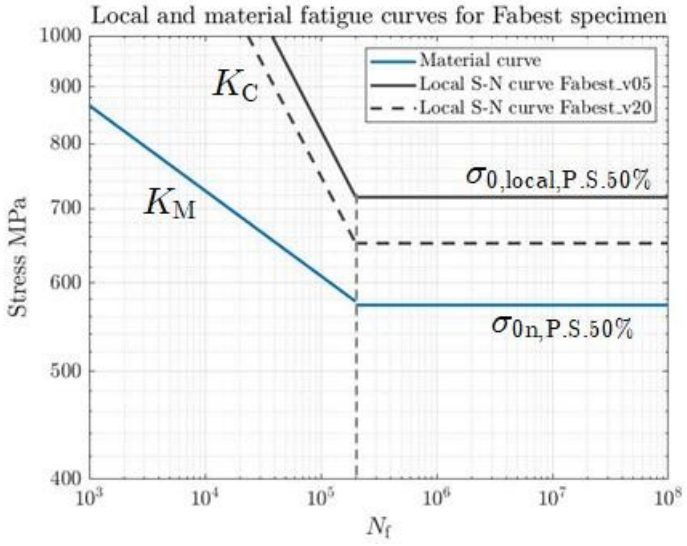

Figure 7.55

Specimen	Local fatigue limits
Fabest_v05 in 42CrM04+QT	716.6
Fabest_v20 in 42CrM04+QT	651.4
V-groove ρ = 1 mm in 42CrM04+QT	462.3
V-groove ρ = 0.2 mm in 42CrM04+QT	496.4
F2 with ρ = 1 mm in S275	272.0
F2 with ρ = 0.2 mm in S275	299.2
F2 with ρ = 0.04 mm in S275	339.7
F3 with ρ = 0.2 mm in S275	299.2
F3 with ρ = 0.04 mm in S275	338.8
F2 with ρ = 1 mm in AlMgSi1	164.6
F2 with ρ = 0.2 mm in AlMgSi1	190.1
F2 with ρ = 0.04 mm in AlMgSi1	228.0
F3 with ρ = 0.2 mm in AlMgSi1	190.1
F3 with ρ = 0.04 mm in AlMgSi1	227.2

Table 7.27: *Local fatigue limits according to FKM guidelines*

7.6 Workflow for the application of SED method

The finite element analysis for calculating the averaged SED involves steps in both the pre-processor and post-processor that are different from those seen for the TCD and the SCF. The quantity to be taken is a strain energy density present within a certain structural volume of radius R_c [28]. It is therefore not necessary to extrapolate the maximum principal stress field or the Von Mises stress field as seen in Ch. 4 it is necessary to determine the control radius in order to obtain the variable of interest.

7.6.1 Finite element analysis of FABEST specimens for SED approach

To determine the critical radius, following Eq. 4.23, it is necessary to impose equality between the strain energy density of the smooth specimen and the strain energy density of the notched specimen, at a fixed number of cycles to failure. For the smooth specimen, under uniaxial loading conditions, the following strain energy density was obtained for $N_f = 10^5$ cycles to failure:

$$\Delta \overline{W}_D^{\text{unnotched}} = \frac{\Delta \sigma_D^2}{2E} = \frac{1147^2}{2 \cdot 206362} = 3.19 \frac{\text{MJ}}{\text{m}^3} \tag{7.31}$$

The only unknown in the strain energy density for the notched specimen is the range of the SIF $\Delta K_{1,D}^V$. The problem, however, is that no data is available for this parameter in this thesis work and it is therefore mandatory to find it. In addition, the specimens under analysis do not show a V-notch. The initial idea is to perform an FE analysis on a specimen with a V-notch subject to the fatigue load of the most notched specimen (i.e. FABEST_V05) and derive a first attempt control radius. In order to do this, it is necessary to obtain an extremely dense mesh around the tip of the notch and this may cause some problems from a computational point of view. Recently, a method called *Peak Stress Method* (PSM) has been proposed which allows finite element analysis using coarse meshes [34][33]. K_1^V was connected with the peak stress σ_{peak} calculated at the tip of the notch and the analytical relation is:

$$K_1^V = K_{FE}^* \cdot \sigma_{peak} \cdot d^{1-\lambda_1} \tag{7.32}$$

Where d is the medium size of the elements and K_{FE}^* is a constant that depends on the software, type of element and the mesh pattern [35]. The advantages of this method can be summarised as follows:

- Coarse mesh that reduces calculation time.
- Only the peak stress evaluated at the tip of the notch is used and not a stress distribution which would have to be worked out later.

To carry out the analysis of the V-notch specimen, it is necessary to know some basic settings. From Fig. 7.56 it is possible to exploit the symmetry of the problem, as done previously in Fig. 7.3.

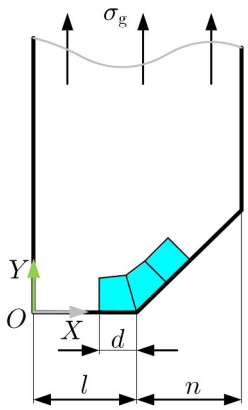

Figure 7.56: *Definition of the parameters for Peak Stress Method*

Starting with the K_{FE} parameter, from [35] it can be seen that for a 2D plane-4 element type, 1.38 ± 3% was obtained for opening angles of $2\alpha = 90°$. It is important to note that K-option 1 must be the third in ansys®. To obtain plausible values, the mesh must be free and the following condition must be met:

$$\frac{a}{d} \geq 3 \tag{7.33}$$

where $a = \min(n, l)$ and d is the minimum element dimension (Fig. 7.56). In this case $l = n = 5$ mm and therefore the minimum d to be respected is equal to ≈ 1.67 mm. The peak stress can be taken once the analysis is complete by assimilating it into the first principal stress. λ_1, from Tab. 4.1, is equal to 0.5445. Using common mechanical drawing software, it is possible to draw the geometry with V-notch and export an .IGES file. The material was set as in the FE analyses for TCD and RSG. a global element size of 1.67 mm was set and the free mesh technique was applied. The result can be seen in Fig. 7.57.

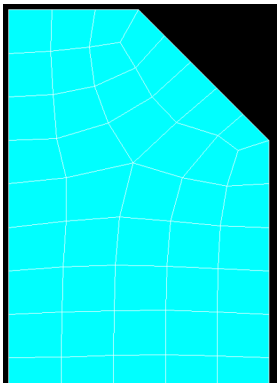

Figure 7.57: *Free mesh for peak stress determination. Plane-4 node 182 was used with K1 option set to enhanced strain and K3 set to axisymmetric.*

The same boundary conditions as seen in Fig. 7.3 were set and a unit tensile stress was applied along the gross section. The solution was then launched and a peak stress of 4.68 MPa was taken. Since this is a linear elastic analysis, it is possible to scale the value obtained for a unit stress to a real one:

$$\sigma_{\text{peak}}^{1\text{ MPa}} : K_1^{1\text{ MPa}} = \sigma_{\text{peak}}^{\text{any load}} : K_1^{\text{any load}} \tag{7.34}$$

The fatigue limit derived in Ch. 5 refers to the net nominal section. it is necessary to use Eq. 7.5 to obtain the corresponding gross load. The fatigue limit related to net section is $\sigma_{0,n} = 215.7$ MPa and:

$$\sigma_{0,g} = \frac{A_n \sigma_{0,n}}{A_g} = 53.9 \text{ MPa} \tag{7.35}$$

A value of $K_{1,\sigma_g=1}^{V} = 8.2 \text{ MPa} \cdot \text{mm}^{0.4555}$ was obtained for $\sigma_g = 1$ MPa. To find the correct value under the fatigue load of Eq. 7.35 it was obtained:

$$K_1^V = K_{1,\sigma_g=1}^V \cdot \sigma_{0,g} = 8.2 \cdot 53.9 = 440.0 \text{ MPa} \cdot \text{mm}^{0.4555} \tag{7.36}$$

From the Eq. 7.37 the first attempt control radius was obtained:

$$R_c^{(1)} = \left(\sqrt{2e_1} \cdot \frac{\Delta K_1^V}{\Delta\sigma_0} \right)^{\frac{1}{1-\Lambda_1}} = \left(\sqrt{2 \cdot 0.146} \frac{2 \cdot 440.0}{2 \cdot 573.3} \right)^{\frac{1}{1-0.5445}} = 0.1448 \text{ mm} \tag{7.37}$$

At this point it is possible to use this value to shape the control volume at the apex of the notch (Fig. 7.58

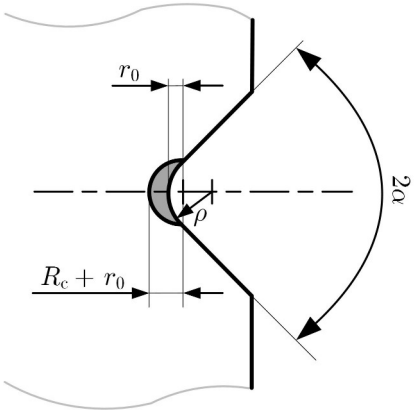

Figure 7.58: *Definition of control volume [26]*

$q = 1.5$ for $2\alpha = 90°$ and therefore $r_0 = 0.1667$ mm (Eq. 4.30 and Eq. 4.31). the sum of R_c and r_0 is needed to define the control volume:

$$R_2 = R_c + r_0 = 0.1448 + 0.1667 = 0.3115 \text{ mm} \tag{7.38}$$

An 8-node plane element, i.e. quad 8 plane 183, was adopted for the FE analysis with the second K-option set to axisymmetry. Following Fig. 7.5 the material was used. Using an .IGES file, the geometry with the control volume created in autocad® was imported. The area for the model and the control volume has been generated. After meshing the component and imposing the load and constraints, control volume was isolated to extract the SED with the option select - entities (Fig. 7.59).
An element table consisting of the entity *SENE* and *VOLU* has been defined:

element table → define table → add → energy → SENE

and

element table → define table → add → geometry → VOLU

The sum of each item function was used to find the total *SENE* and total *VOLU*. The ratio constitutes the SED:

$$SED = \frac{SENE}{VOLU} = \frac{0.374026 \cdot 10^{-3}}{1.46355} = 2.5556 \cdot 10^{4} \frac{\text{MJ}}{\text{m}^3} \tag{7.39}$$

To find the SED at a given load, it is necessary to use a proportion taking into account the fact that stresses have a quadratic trend. It has been achieved:

$$SED_{\sigma_{0,g}} = SED_{\text{unit load}} \cdot \Delta\sigma_{0,g}^2 = 2.5556 \cdot 10^{4} \cdot (2 \cdot 53.9)^2 = 2.9737 \frac{\text{MJ}}{\text{m}^3} \tag{7.40}$$

The first attempt value of R_c is not correct because the SED does not equal $\Delta\overline{W}_D^{\text{unnotched}}$. At this point it is necessary to proceed by trial until the strain energy density of the smooth specimen equals that of the notch one. Tab. 7.28 has been constructed which collects some notable points of R_c.
Using these points from FE analysis, the following fit function was adopted:

$$\Delta\overline{W}_D^{\text{notched}} = a \cdot e^{b \cdot R_c} \tag{7.41}$$

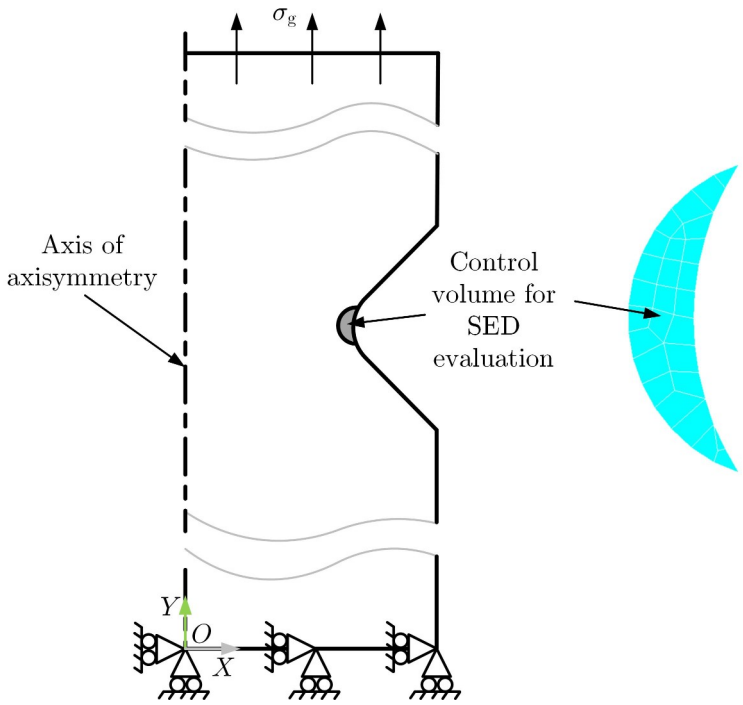

Figure 7.59: *FE model for bar specimens*

$R_c^{(i)}$	$R_2^{(i)}$	$\Delta\overline{W}_D^{notched,i}$	$\Delta\overline{W}_D^{unnotched}$
0.0448	0.2115	4.4990	3.1856
0.0948	0.2615	3.6409	3.1856
0.1198	0.2865	3.2972	3.1856
0.1323	0.2990	3.1353	3.1856
0.0698	0.2365	4.0370	3.1856
0.0823	0.2490	3.8304	3.1856
0.1448	0.3115	2.9737	3.1856

Table 7.28: *Averaged SED values for discrete points of R_c. Iterations based on a given critical radius value*

where $a = 5.397$ and $b = -4.127$ with $R^2 = 0.9995$. Through the Newton-Raphson method an estimate of the control radius $R_c = 0.1277$ mm has been derived on the intersection of the function and the averaged SED of the smooth specimen, as can be seen in Fig. 7.60.

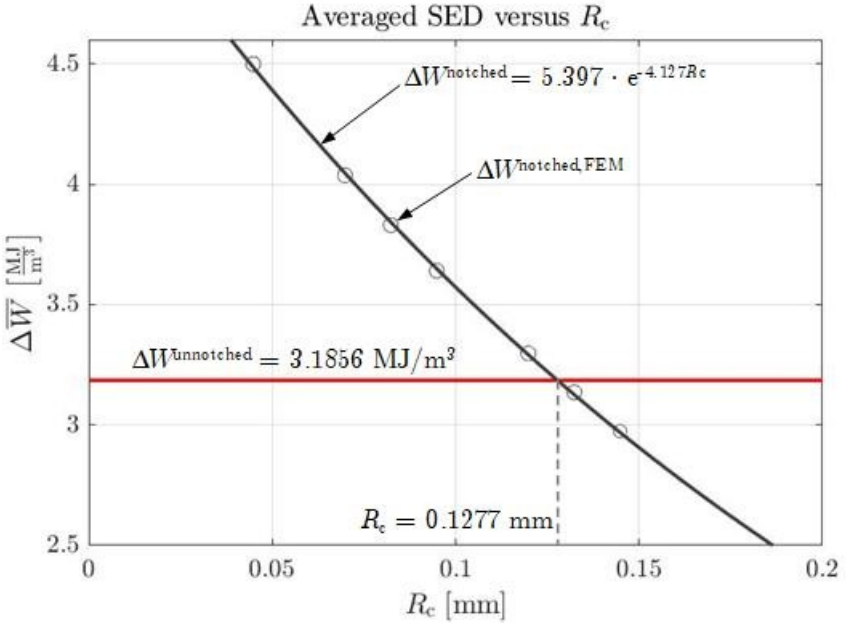

Figure 7.60: *Strain Energy Density versus control radius R_c.*

Once the value of R_c is known, the energy method can be applied to FABEST_V2.0. In this case: $\rho = 2$ mm, $r_0 = 0.6667$ mm, $R_2 = 0.7944$ mm, $\sigma_{0,n} = 297.1$ MPa, $\sigma_{0,g} = 74.2$ MPa and $SED_{\text{unit load}} = 1.2487 \cdot 10^{-4} \frac{\text{MJ}}{\text{m}^3}$. Applying Eq. 7.40 a value of $SED_{\sigma_{0,g}} = 2.7565 \frac{\text{MJ}}{\text{m}^3}$ was obtained. Comparing this value with $\Delta \overline{W}_D^{unnotched}$ the following error has been made:

$$\text{Error}(\%) = \frac{SED_{\sigma_{0,g}} - \Delta \overline{W}_D^{unnotched}}{\Delta \overline{W}_D^{unnotched}} \cdot 100 = \frac{2.7565 - 3.1856}{3.1856} \cdot 100 = -13.5\% \qquad (7.42)$$

7.6.2 Finite element analysis of V-groove specimen from [44] for SED approach

Following the same procedures as for the FABEST specimens, the strain energy density of the smooth specimen is:

$$\Delta \overline{W}_D^{unnotched} = \frac{\Delta \sigma_D^2}{2E} = \frac{780^2}{2 \cdot 206000} = 1.4767 \frac{\text{MJ}}{\text{m}^3} \qquad (7.43)$$

An FE analysis was performed to determine an estimate of the NSIF per model unit load. In this case the parameters for determining K_1^V are the same except for the element size, in fact $a = \min(n, l) = 3$ mm and then $d = 1$ mm. The mesh can be seen in Fig. **??**
Once the peak stress value has been found, ΔK_1^V can be calculated using Eq. 7.35, Eq. 7.34 and Eq. 7.36 with $\sigma_n = 87.5$ MPa. The control radius is:

$$R_c^{(1)} = \left(\sqrt{2e_1} \cdot \frac{\Delta K_1^V}{\Delta \sigma_0} \right)^{\frac{1}{1 - \Lambda_1}} = \left(\sqrt{2 \cdot 0.146} \cdot \frac{2 \cdot 202.3647}{2 \cdot 390} \right)^{\frac{1}{1 - 0.5445}} = 0.0613 \text{ mm} \qquad (7.44)$$

$q = 1.5$ for $2\alpha = 90°$ and therefore $r_0 = 0.0667$ mm (Eq. 4.30 and Eq. 4.31). The sum of R_c and r_0 is needed to define the control volume:

$$R_2 = R_c + r_0 = 0.0613 + 0.0667 = 0.1280 \text{ mm} \qquad (7.45)$$

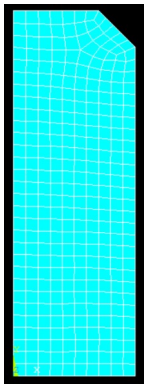

Figure 7.61: *V-notch specimen mesh*

After determining some points by FE analysis, as done previously, an interpolation function was derived and Newton's method was applied to find the value of the control radius. In this case it is R_c = 0.037962 mm. In Fig. 7.62 it is possible to see the graph of the strain energy density against the control radius, with its interpolation function.

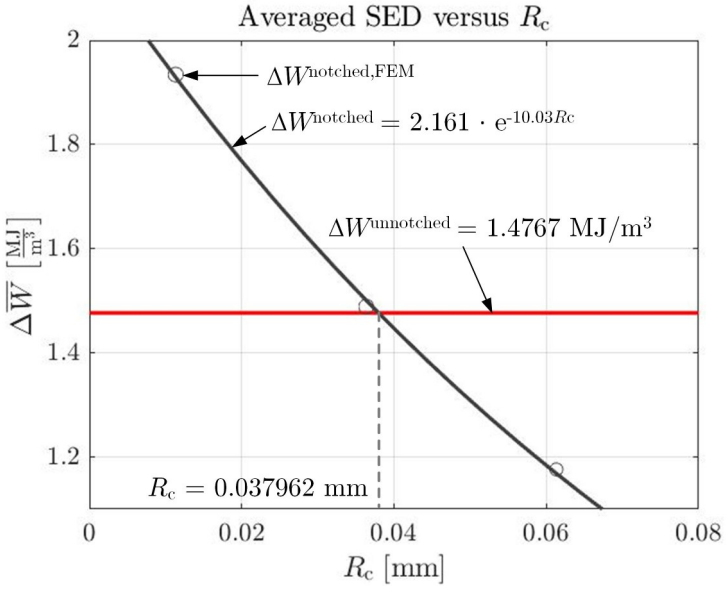

Figure 7.62: *Strain Energy Density versus control radius R_c.*

Once the radius R_c was known, all other geometric parameters were determined for the specimen with ρ = 1 mm and a strain energy density was derived equal to $SED_{\sigma_{0,g}} = 1.7454 \frac{MJ}{m^3}$. The committed error is:

$$\text{Error}(\%) = \frac{SED_{\sigma_{0,g}} - \Delta\overline{W}_D^{unnotched}}{\Delta\overline{W}_D^{unnotched}} \cdot 100 = \frac{1.7454 - 1.4767}{1.4767} \cdot 100 = 18.2\% \qquad (7.46)$$

7.6.3 Finite element analysis of Flat specimen from [39] for SED approach

Initially, the strain energy density of the smooth specimens were calculated. For S275 steel:

$$\Delta\overline{W}_D^{unnotched} = \frac{\Delta\sigma_D^2}{2E} = \frac{434^2}{2 \cdot 206000} = 0.4572 \frac{MJ}{m^3} \qquad (7.47)$$

and for Aluminium alloy AlMgSi1:

$$\Delta\overline{W}_D^{unnotched} = \frac{\Delta\sigma_D^2}{2E} = \frac{226^2}{2 \cdot 70000} = 0.3648 \frac{MJ}{m^3} \qquad (7.48)$$

Starting with steel specimens, the control radius for the F2 specimens was determined, using Eq. **??** and it is equal to $R_c^{(1)} = 0.1089$ mm. The value of K_1^V was determined by imposing the following values for the FE calculation and analysis:

- $d = 4$ mm
- K_{FE}^* , Λ_1 same as previosly analyses
- $\sigma_{peak} = 1.21$ MPa with external load equal to 1 MPa.

The values were then updated to the real net area. Using autocad® , the first attempt control volume was constructed and through iterations similar to those made in the previous paragraphs, the curves of the strain energy density as a function of the control radius was obtained. Since the specimens are flat and not axisymmetric, the same type of element was adopted with K-option set to plane stress. This is the only substantial difference between the two geometries. As unit load was applied along the net section and the boundary conditions can be seen in Fig. 7.62. The Tab. 7.29 collects the main output parameters from the FE analysis and the SED approach.

$R_c^{(i)}$	$R_2^{(i)}$	$\Delta\overline{W}_D^{notched,i}$	$\Delta\overline{W}_D^{unnotched}$
0.0989	0.1122	0.6887	0.4572
0.0889	0.1022	0.8249	0.4572
0.1089	0.1222	0.5925	0.4572
0.1189	0.1322	0.4041	0.4572

Table 7.29: *Main values for SED approach for F2 specimens in S275 steel*

A fit function, Eq. 7.41, was adopted to determine the corresponding values of R_c crossing the SED line of the smooth specimen:

$$\Delta\overline{W}_D^{notched} = 5.52 \cdot e^{-21.19 \cdot R_c} \tag{7.49}$$

The following Fig. 7.63 was obtained

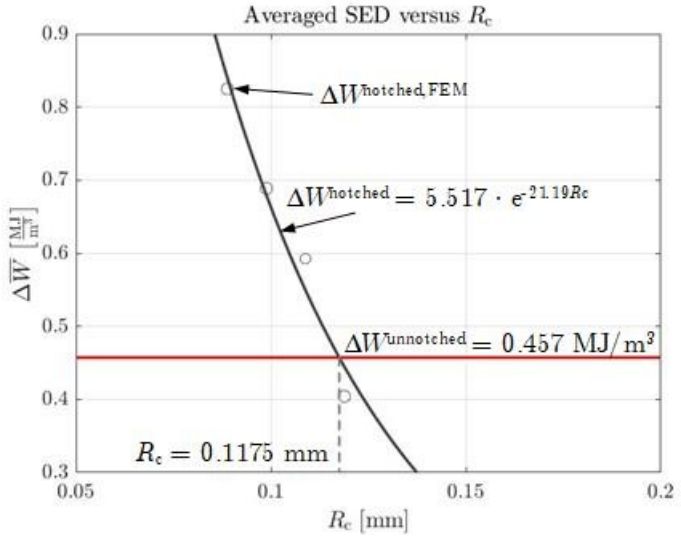

Figure 7.63: *Strain Energy Density versus control radius R_c.*

The value obtained was used to find the SED of the other two F2 specimens. The percentage errors committed are:

$$\text{Error}(\%) = \frac{SED_{\sigma_{0,n}} - \Delta\overline{W}_D^{unnotched}}{\Delta\overline{W}_D^{unnotched}} \cdot 100 = \frac{0.9111 - 0.4572}{0.4572} \cdot 100 = 99.3\% \tag{7.50}$$

for specimen with ρ = 0.2 mm and

$$\text{Error}(\%) = \frac{SED_{\sigma_{0,n}} - \Delta\overline{W}_D^{\text{unnotched}}}{\Delta\overline{W}_D^{\text{unnotched}}} \cdot 100 = \frac{0.5354 - 0.4572}{0.4572} \cdot 100 = 17.1\% \tag{7.51}$$

for specimen with ρ = 1 mm. At this point, an $R_c^{(1)}$ = 0.0849 mm was obtained for specimen AF3. with specimen F2, averaged SED values were calculated to determine a fit function. The main results are collected in Tab. 7.30.

$R_c^{(i)}$	$R_2^{(i)}$	$\Delta\overline{W}_D^{\text{notched,i}}$	$\Delta\overline{W}_D^{\text{unnotched}}$
0.025	0.0383	0.9566	0.4572
0.0849	0.0982	0.1837	0.4572
0.1849	0.1982	0.1718	0.4572

Table 7.30: *Main values for SED approach for F3 specimens in S275 steel*

the fit function obtained is:

$$\Delta\overline{W}_D^{\text{notched}} = 3.19 \cdot 10^{6} \cdot R_c^{-3.365} + 0.1709 \tag{7.52}$$

the value of the control radius, applying Newton's method, is R_c = 0.034 mm. The value of SED for specimen F3 with ρ = 0.2 mm was calculated using the control radius just determined. The error committed is:

$$\text{Error}(\%) = \frac{SED_{\sigma_{0,n}} - \Delta\overline{W}_D^{\text{unnotched}}}{\Delta\overline{W}_D^{\text{unnotched}}} \cdot 100 = \frac{0.3102 - 0.4572}{0.4572} \cdot 100 = -32.1\% \tag{7.53}$$

Regarding aluminium alloy, the first-attempt value of the control radius, for F2 specimen type, is $R_c^{(1)}$ = 0.0533 mm. Again, the attempts were collected in a summary Tab. 7.31.

$R_c^{(i)}$	$R_2^{(i)}$	$\Delta\overline{W}_D^{\text{notched,i}}$	$\Delta\overline{W}_D^{\text{unnotched}}$
0.02	0.0333	0.5990	0.3648
0.0533	0.0666	0.3193	0.3648

Table 7.31: *Main values for SED approach for F2 specimens in AlMgSi1 alloy*

Fit function is:

$$\Delta\overline{W}_D^{\text{notched}} = -8.409 \cdot R_c + 0.7672 \tag{7.54}$$

and, via Newton's method, the corresponding control radius is R_c = 0.048 mm. The percentage errors made on the other two F2 specimens are:

$$\text{Error}(\%) = \frac{SED_{\sigma_{0,n}} - \Delta\overline{W}_D^{\text{unnotched}}}{\Delta\overline{W}_D^{\text{unnotched}}} \cdot 100 = \frac{0.6381 - 0.3648}{0.3648} \cdot 100 = 74.9\% \tag{7.55}$$

$$\text{Error}(\%) = \frac{SED_{\sigma_{0,n}} - \Delta\overline{W}_D^{\text{unnotched}}}{\Delta\overline{W}_D^{\text{unnotched}}} \cdot 100 = \frac{0.4861 - 0.3648}{0.3648} \cdot 100 = 33.2\% \tag{7.56}$$

At the first iteration, the control radius for the aluminium alloy F3 specimen is $R_c^{(1)}$ = 0.0389 mm. In this case the fit function is $\Delta\overline{W}_D^{\text{notched}} = -9.589 \cdot R_c + 0.6235$ and the corresponding control radius is R_c = 0.027 mm. The percentage errors made on the F3 specimen with ρ = 0.2 mm is:

$$\text{Error}(\%) = \frac{SED_{\sigma_{0,n}} - \Delta\overline{W}_D^{\text{unnotched}}}{\Delta\overline{W}_D^{\text{unnotched}}} \cdot 100 = \frac{0.1071 - 0.3648}{0.3648} \cdot 100 = -70.6\% \tag{7.57}$$

Chapter 8

COMPARISON BETWEEN TCD, RSG AND SED WITH EXPERIMENTAL RESULTS AND CONCLUSIONS

8.1 Theory of critical distances

8.1.1 TCD in HCF in its classical formulation

For the classical method in HCF the percentage deviations between the range of the effective stress $\Delta\sigma_{eff}$ and the range of the reference stress, i.e. the fatigue limit of the smooth specimen, $\Delta\sigma_0$, were obtained. For each specimen, relative stress gradients were determined in Sect. 7.5.1. It is possible to plot the percentage error committed in the evaluation of the actual stress, versus χ', Figs. 8.1.

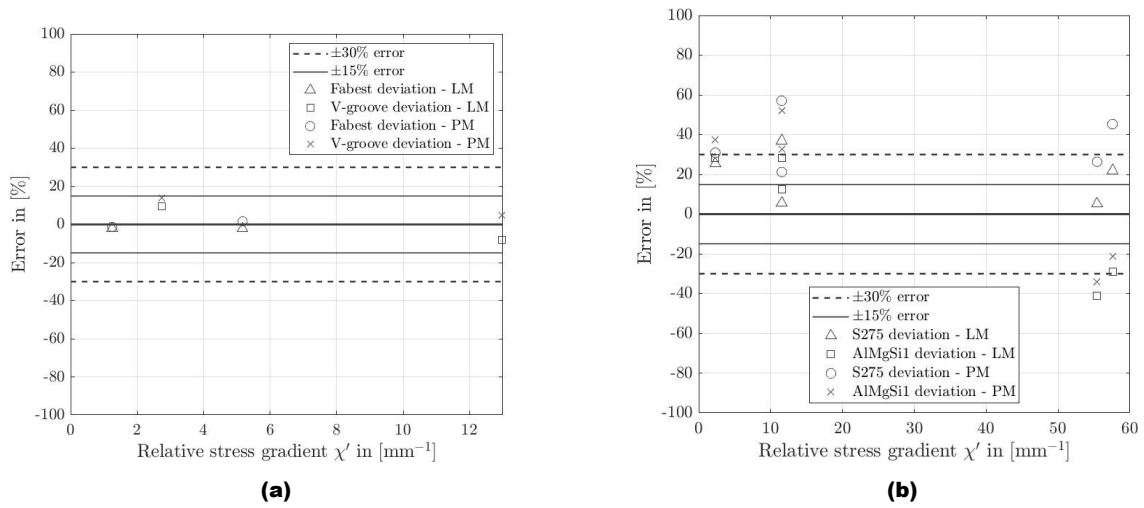

Figure 8.1: *% error committed versus relative stress gradient calculated according to Eq. 3.6 - TCD in its classical formulation*

The percentage error was determined using the following equation:

$$\text{Error}(\%) = \frac{\Delta\sigma_{\text{eff}} - \Delta\sigma_{\text{ref}}}{\Delta\sigma_{\text{ref}}} \cdot 100 \qquad (8.1)$$

where for problems in HCF, $\Delta\sigma_{ref} = \Delta\sigma_0$. As far as V-rounded specimens are concerned, the percentage errors remain within a band of ±15%. Both the line method and the point method estimate the effective

stress in a very similar way. Although the specimens in the FABEST campaign and those in the article [44] nominally have the same material, data on σ_u, ΔK_{th} or other material parameters, could induce these deviations which are not exaggeratedly pronounced. The lack of reliable data on steel and aluminium alloy, on the other hand, leads to huge errors. In the best case, errors fall within the ±15% band, but in the worst case the actual stress deviates from the relative reference stress by values even higher than 40%, which is not acceptable from an engineering point of view.

8.1.2 TCD in MCF in its classical formulation

The concepts seen for HCF were also extended in MCF. Stresses were determined according to classical TCD at arbitrarily chosen cycles and were compared with stresses derived from the Basquin curve at the same number of cycles. For the LM method, the diagram in Fig. 8.2 was obtained, while for the PM method, the diagram in Fig. 8.3 was obtained.

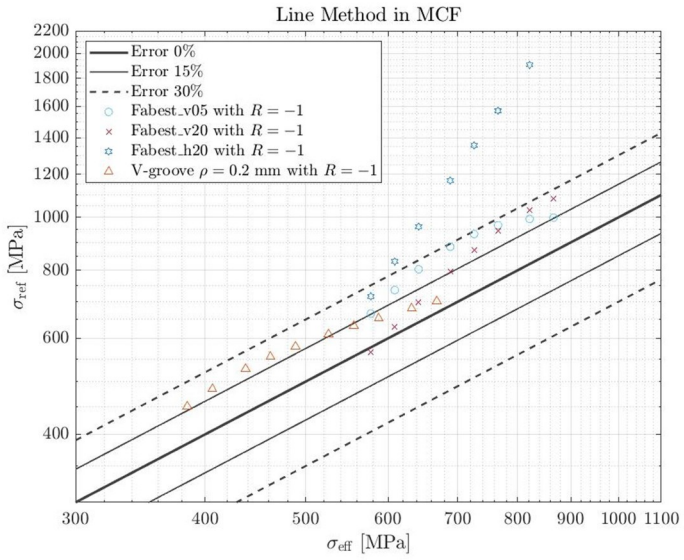

Figure 8.2: *Effective stress versus reference material strength for 42CrMo4+QT, Line Method*

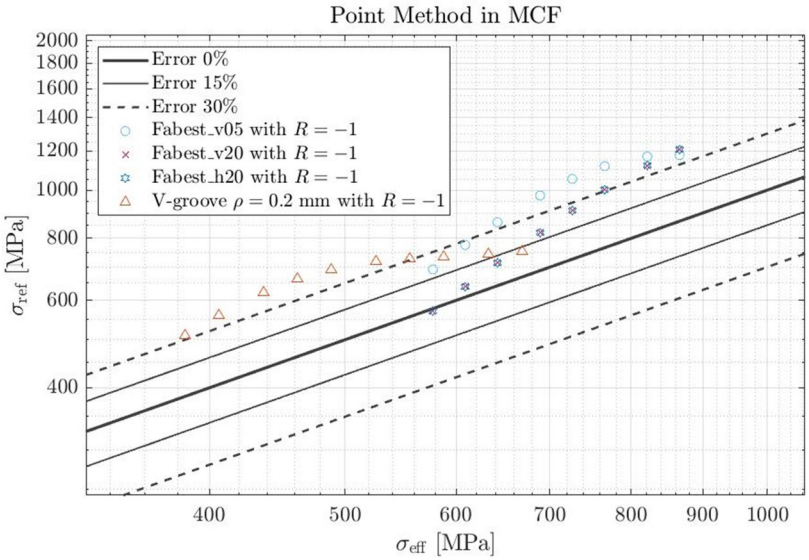

Figure 8.3: *Effective stress versus reference material strength for 42CrMo4+QT, Point Method*

With regard to the Line Method, it is interesting to note that the blunt V-notch specimens lie within an error interval of about ±30%. The only exception is the specimen Fabest_h20, which estimate in MCF

is highly wrong. However, the situation improves with the PM method, where even for Fabest_h20, the percentage error is close to 30%.

8.1.3 TCD in HCF by using two calibration curve

In this paragraph, error graphs were determined according to reverse Point Method in Fig. 8.4.

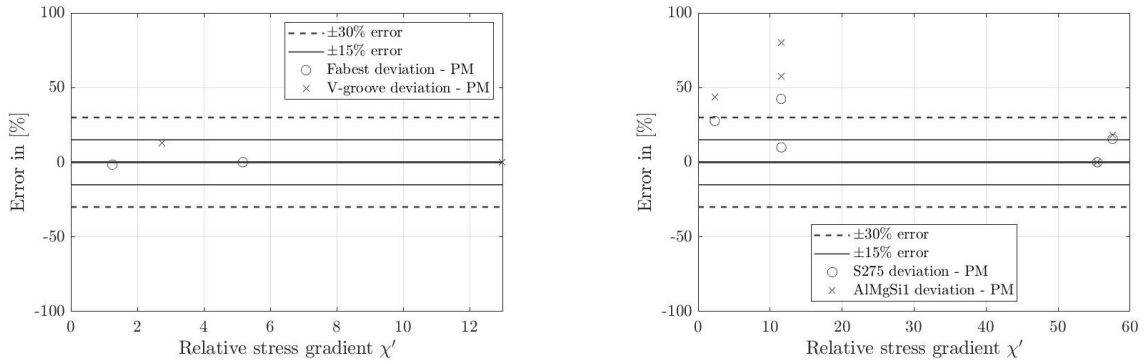

Figure 8.4: *% error committed versus relative stress gradient calculated according to Eq. 3.6*

As seen in Par. 7.5, the relative stress gradient of the Fabest_h20 specimen was not determined. The error made with respect to the reference stress was collected in Table 7.13. For the 42CrMo4+QT specimens, the errors are contained within a range of ±15%, while for S275 the interval error increases to 30%. For aluminium alloy, this deviation is out of the range ±30% for specimens with a low relative stress gradient.

8.1.4 TCD in MCF by using two calibration curve

The reverse Point Method was also extended in the medium cycle zone. For a certain number of cycles, the reference stress obtained from the Basquin curve was compared to the stress obtained by the PM method. The deviations were represented in the graphs in Fig. 8.5.

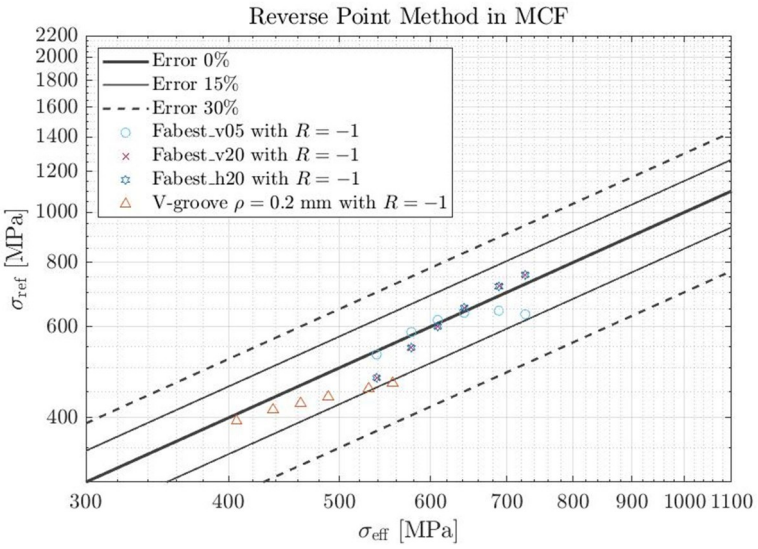

Figure 8.5: *Effective stress versus reference material strength for 42CrMo4+QT, Reverse Point Method*

Compared to the classical approach for the material 42CrMo4+QT, the % error is smaller and more centred, i.e. the data falls within the error range of 15%.

8.1.5 Executive summary

At the fatigue limit points of the experimentally fatigue life and the TCD predicted fatigue life have been depicted in Fig. 8.6.

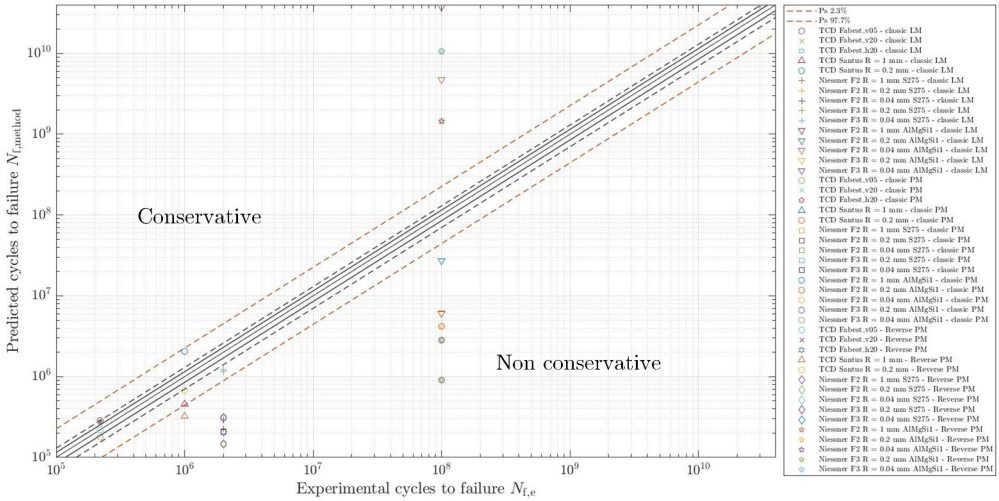

Figure 8.6: *Fatigue Data of TCD method*

The black dashed strip corresponds to an error band of 30%, while the solid strip corresponds to an error 15%. As can be observed, for the fabest campaign samples, the error band is contained within 30%. With the steel specimens from the Santus and Niessner campaign, non-conservative results were obtained, wh for the aluminium alloy, depending on the type of geometry, conservative and non-conservative values were obtained.

8.2 Relative stress gradient approach

In this section, it is interesting to compare the percentage deviation that is present between the experimentally calculated support factor and that determined by the method of Stieler, IABG and FKM. n_{exp} is calculated as follows:

$$n_{exp} = \frac{K_{t,n} \cdot \sigma_{D(\chi=0)}}{\sigma_{D(\chi=0)}} \tag{8.2}$$

where, using the same nomenclature as in Ch. 3, $\sigma_{D(\chi=0)}$ is the experimental value of the fatigue limit of the notched specimen related to the net section and $\sigma_{D(\chi=0)}$ is the experimental value of the fatigue limit of a smooth (unnotched) specimen. The stress concentration factors can be found from the graphs in Ch. 5, as well as the fatigue limits. Tab. 8.1 shows the support factors calculated according to the experimental method and according to the 3 approaches seen.

Specimen	n_{exp}	$n_{Stieler}$	n_{IABG}	n_{FKM}
42CrMo4 + QT				
Fabest_v05	1.2870	1.0417	1.7367	1.2498
Fabest_v20	1.0003	1.0205	1.4810	1.1362
V-groove ρ = 1 mm	1.1912	1.0736	1.6083	1.1853
V-groove ρ = 0.2 mm	1.2833	1.1604	1.9705	1.2727
S275				
F2 with ρ = 1 mm	1.3703	1.2366	1.5784	1.2534
F2 with ρ = 0.2 mm	1.9614	1.5290	1.9372	1.3788
F2 with ρ = 0.04 mm	3.0531	2.1819	2.5180	1.5655
F3 with ρ = 0.2 mm	1.5136	1.5296	1.9378	1.3790
F3 with ρ = 0.04 mm	2.6660	2.1596	2.5008	1.5613
AlMgSi1				
F2 with ρ = 1 mm	1.4863	1.2676	x	1.4562
F2 with ρ = 0.2 mm	1.8814	1.5982	x	1.6819
F2 with ρ = 0.04 mm	2.2046	2.3365	x	2.018
F3 with ρ = 0.2 mm	2.1539	1.5593	x	1.6824
F3 with ρ = 0.04 mm	1.8688	2.4559	x	2.0105

Table 8.1: *Experimental and numerical data*

The percentage deviations were collected in Tab. 8.2. The following formula was used to determine the errors:

$$\text{Error}(\%) = \frac{n_{exp} - n_{method}}{n_{exp}} \cdot 100 \tag{8.3}$$

where with n_{exp} denotes the experimentally calculated fatigue factor following Eq. 3.4 and n_{method} represents the fatigue factor calculated using the methods seen in this thesis work.
From the point of view of stresses, graphs of the percentage deviations as a function of the relative stress gradient were obtained in Fig. 8.7, 8.8 and 8.9.

8.2.1 Executive summary

At the fatigue limit, points of the experimentally fatigue life and the RSG predicted fatigue life have been depicted in Fig. 8.10.
For the RSG approach, both from Stieler's and IABG's point of view, non-conservative values were obtained.

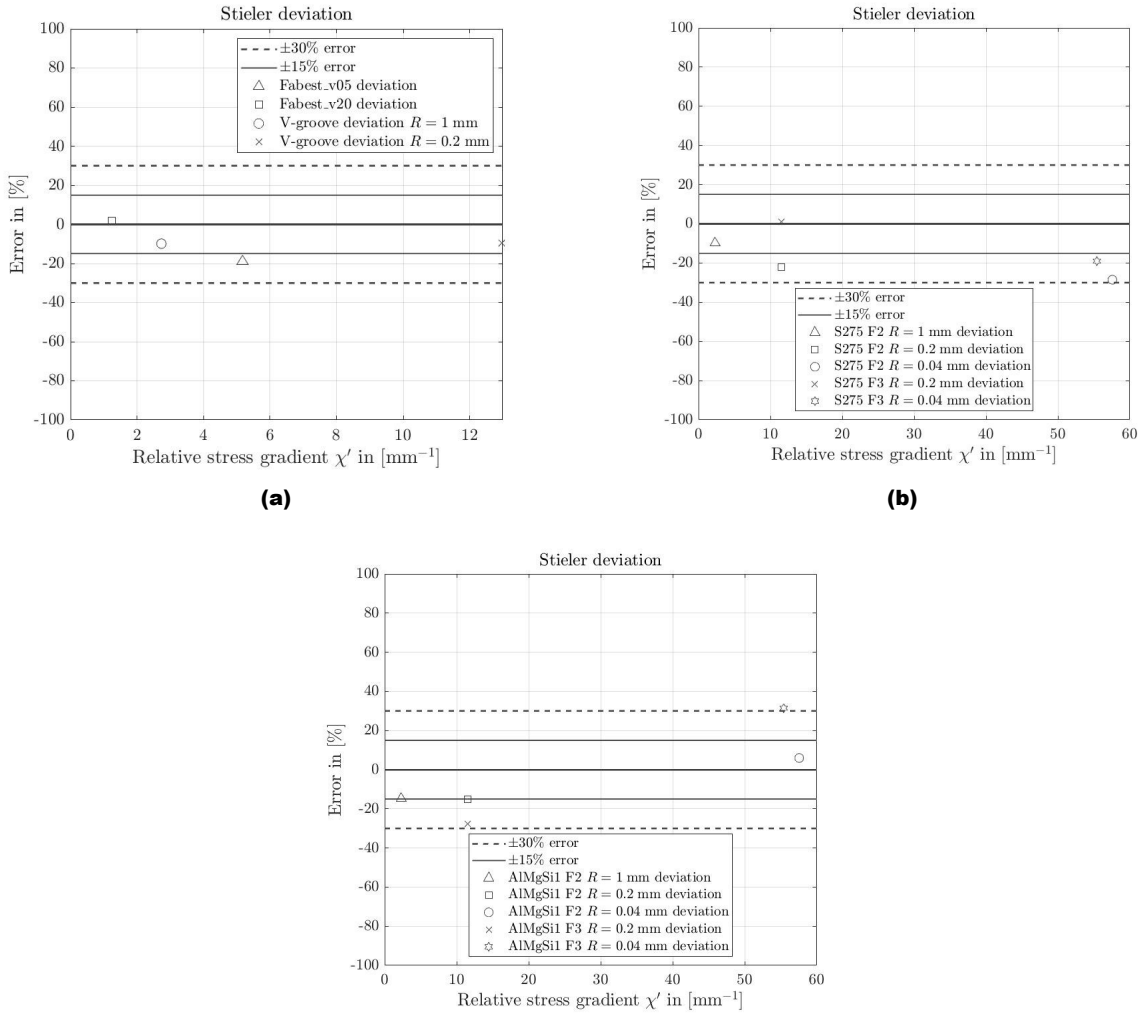

Figure 8.7: *% error committed versus relative stress gradient calculated according to Eq. 3.6 - Stieler method.*

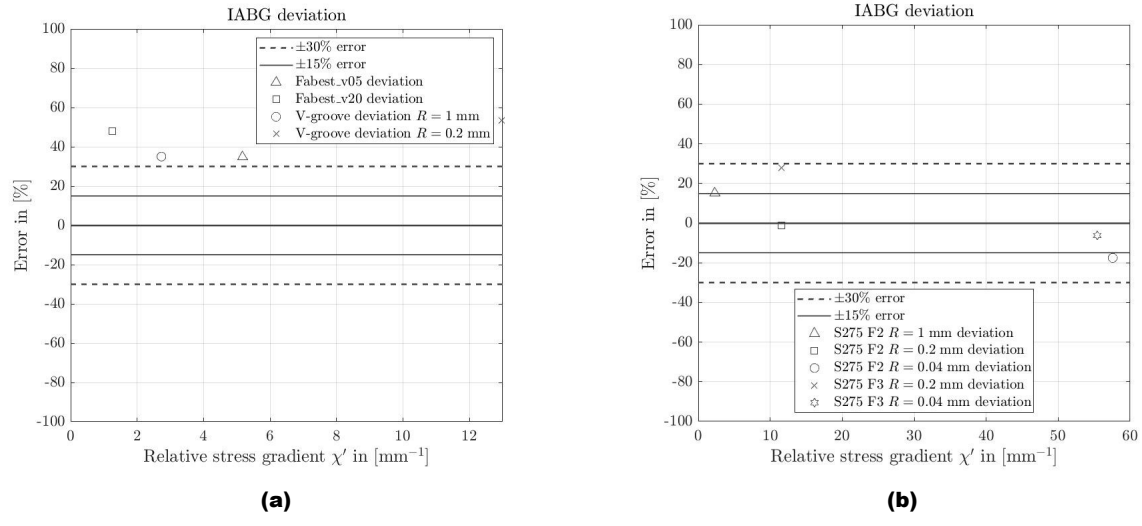

Figure 8.8: *% error committed versus relative stress gradient calculated according to Eq. 3.6 - IABG method.*

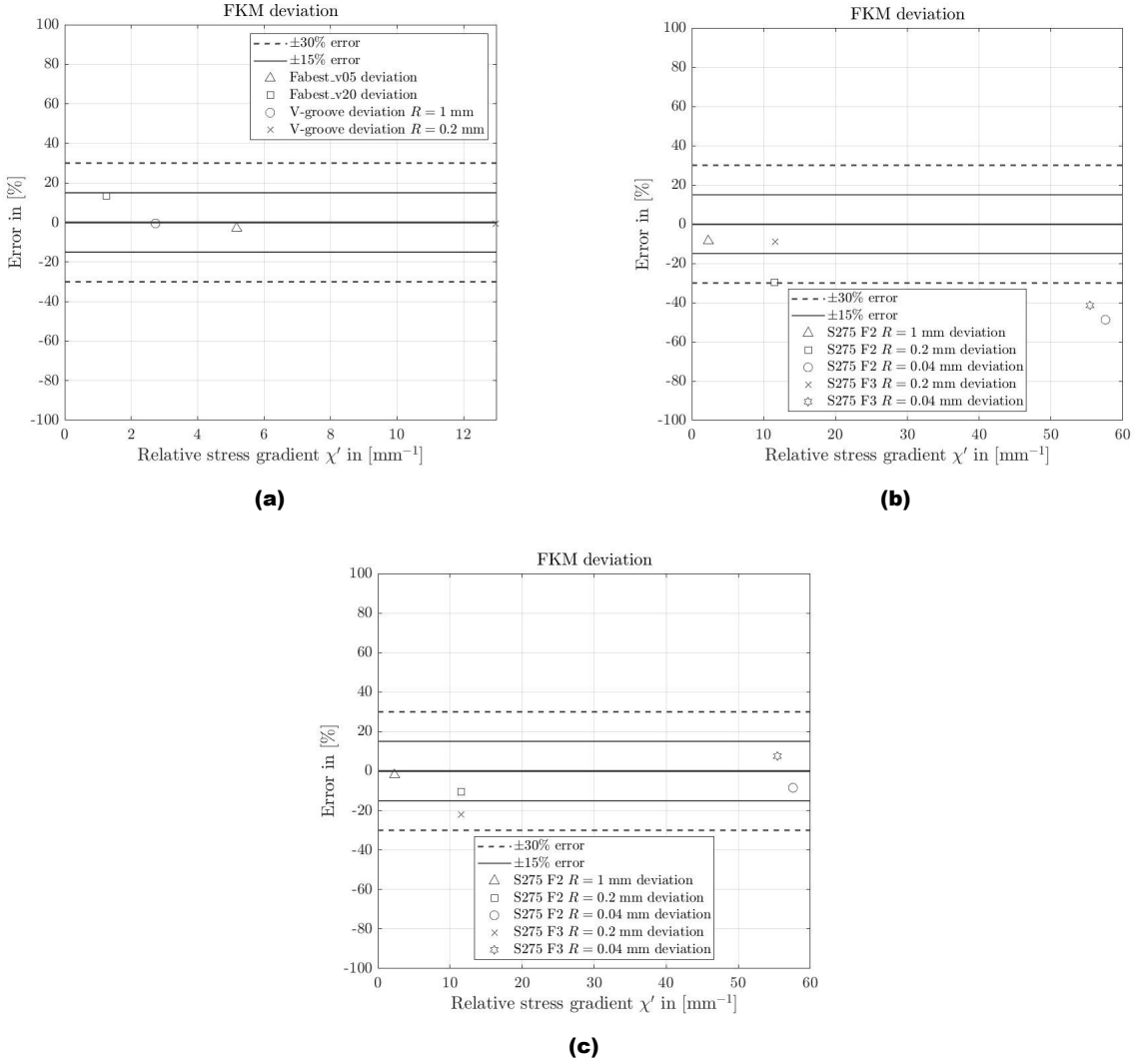

Figure 8.9: *% error committed versus relative stress gradient calculated according to Eq. 3.6 - FKM method.*

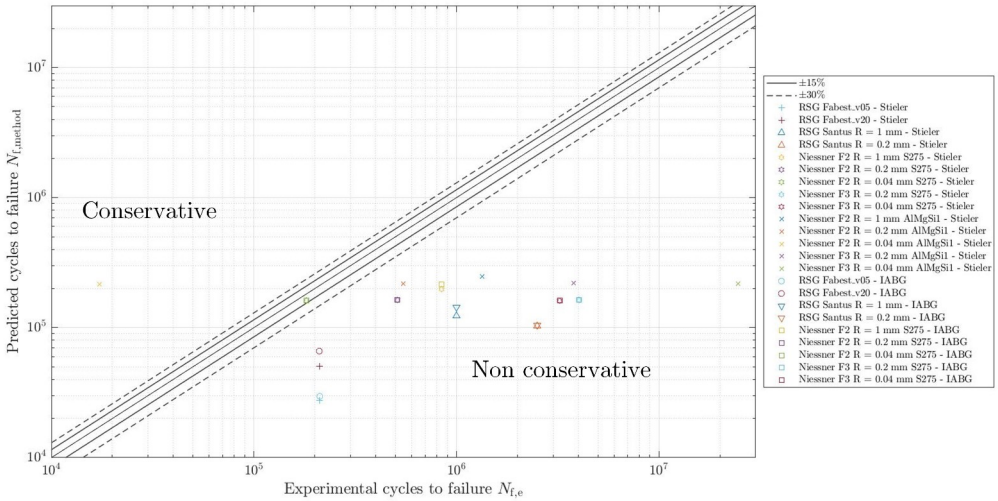

Figure 8.10: *Fatigue Data of RSG method*

Specimen	n_{exp}	Errors $n_{Stieler}$	Errors n_{IABG}	Errors n_{FKM}
42CrMo4 + QT				
Fabest_v05	1.2870	19.1	-34.9	2.9
Fabest_v20	1.0003	-2.0	-48.1	-13.6
V-groove ρ = 1 mm	1.1912	9.9	-35.0	0.5
V-groove ρ = 0.2 mm	1.2833	9.6	-53.5	0.8
S275				
F2 with ρ = 1 mm	1.3703	9.8	-15.2	8.5
F2 with ρ = 0.2 mm	1.9614	22.0	1.2	29.7
F2 with ρ = 0.04 mm	3.0531	28.5	17.5	48.7
F3 with ρ = 0.2 mm	1.5136	-1.0	-28.0	8.9
F3 with ρ = 0.04 mm	2.6660	19.0	6.2	41.4
AlMgSi1				
F2 with ρ = 1 mm	1.4863	14.7	x	2.0
F2 with ρ = 0.2 mm	1.8814	15.1	x	10.6
F2 with ρ = 0.04 mm	2.2046	-6.0	x	8.5
F3 with ρ = 0.2 mm	2.1539	27.6	x	21.9
F3 with ρ = 0.04 mm	1.8688	-31.4	x	-7.6

Table 8.2: *Percentage deviations between experimental and numerical data*

8.3 Strain energy density approach

For the SED approach, as well as the TCD, the percentage deviations were represented as a function of the relative stress gradient in Fig. 8.11, 8.12 and 8.13.

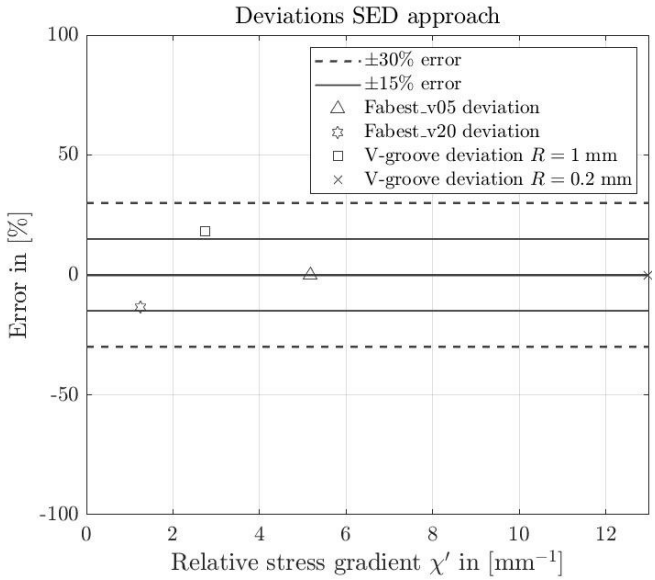

Figure 8.11: *% error committed versus relative stress gradient calculated according to Eq. 3.6*

As can be seen from the graphs, for the 42CrMo4+QT steel, the SED approach exhibits deviations within ±15% error, while for the S275 steel and aluminium alloy, the estimates fall outside the ±30% range and in some cases reach errors that are too high.

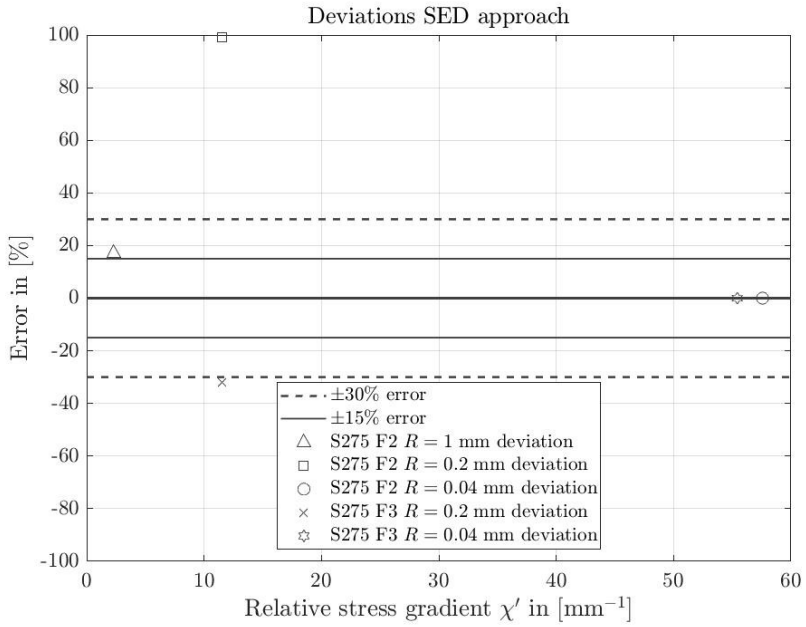

Figure 8.12: *% error committed versus relative stress gradient calculated according to Eq. 3.6*

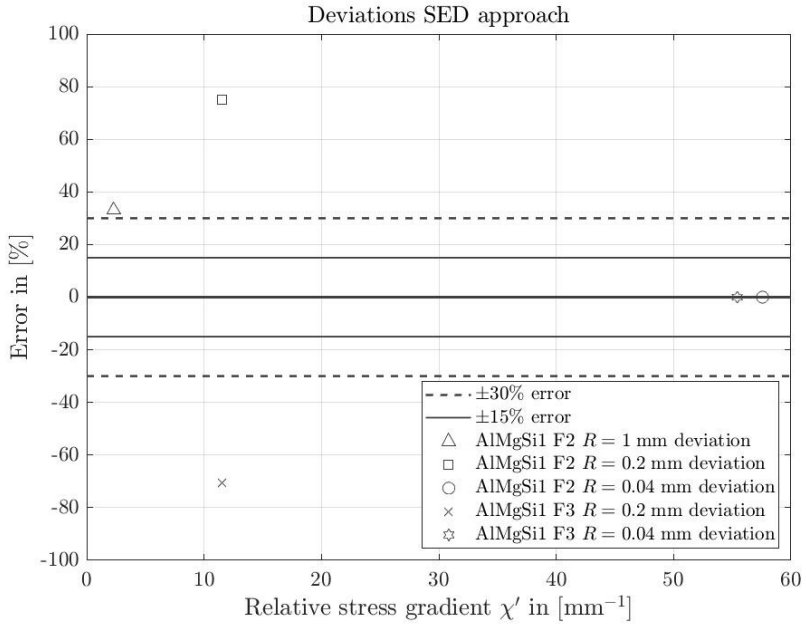

Figure 8.13: *% error committed versus relative stress gradient calculated according to Eq. 3.6*

8.3.1 Executive summary

At the fatigue limit, points of the experimentally fatigue life and the SED predicted fatigue life have been depicted in Fig. 8.14.

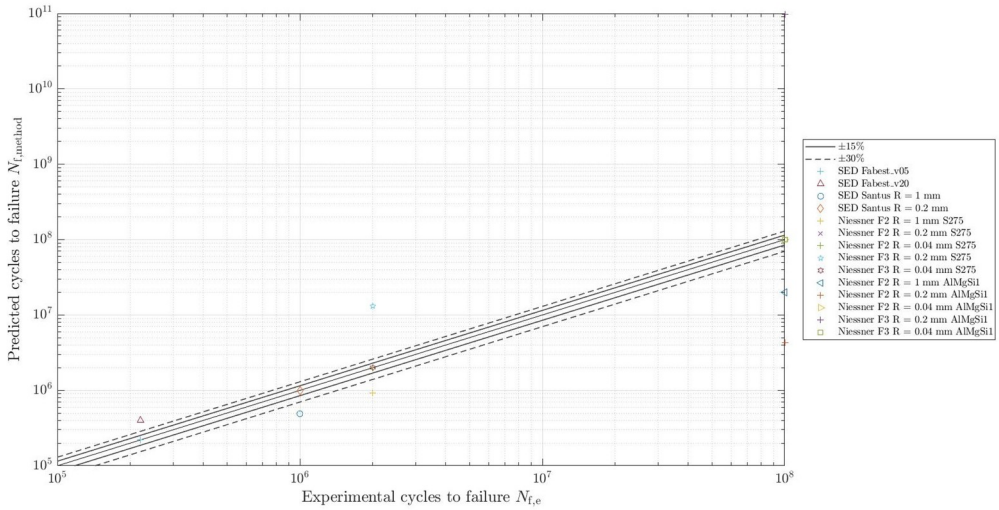

Figure 8.14: *Fatigue Data of SED method*

With the SED approach, the data converges more on the zero-error line than with the TCD and RSG approaches. The situation for aluminium alloy, however, remains highly variable.

8.4 Conclusions

In this thesis work, three approaches were proposed for the prediction of the fatigue life of different specimens with different geometries: Critical Distance Theory, Relative Stress Gradient and Strain Energy Density. The first method was applied in HCF and a small attempt was also proposed in MCF, with the available data. The second method was presented following 3 different schools of thought: Siebel, ABG and FKM. The third method was applied in HCF. The TCD also found application with the special shape specimen Fabest_h20, however reporting high errors, as demonstrated in the previous chapters. The RSG failed in the determination of the 3 main parameters of the fatigue curve, while the SED was not applied given the previous results. In conclusion, the approaches studied on the Fabest campaign prove to fall within an error band of at least 30%. In the best of cases, percentage deviations even approached 1%, while in the worst of cases errors of 30% were reached for TCD, RSG and SED. As far as the data from the literature is concerned, slightly higher errors were obtained for the Santus article's campaign, while for Niessner's campaign, perhaps also due to the lack of more precise data, highly percentage errors were obtained. In the worst case, values close to 100 per cent were reached.

Appendix A

DETERMINATION OF STATIC PROPERTIES OF MATERIAL

In addition to Ch. 5, this appendix contains data from static tensile tests carried out at at UTP Bydgoszcz in Poland.The data were analysed in excel.
Tab. A.1 shows the slopes of the $\sigma_x = \sigma_x(\varepsilon_x)$ and $\sigma_x = \sigma_x(\varepsilon_y)$ curves.The first column correspond to the elastic moduli, the second are necessary to calculate the Poisson's coefficient according to Eq. 5.4.

Specimen	E [MPa]	p_1 **slope on** $(\sigma_x, \varepsilon_y)$ **plane**	υ
MON01	205782	756167	0.272
MON02	206031	641709	0.321
MON03	207255	645032	0.321
MON04	260380	767506	0.269
mean value	206362		0.296
St.Dev.	644		0.029

Table A.1: *Values of E and υ*

The following are the fit diagrams from which the values described in Tab. A.1 were derived.

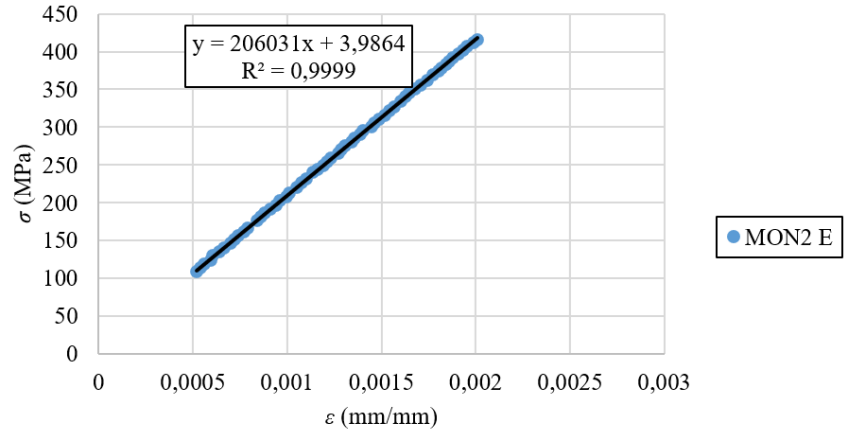

(a)

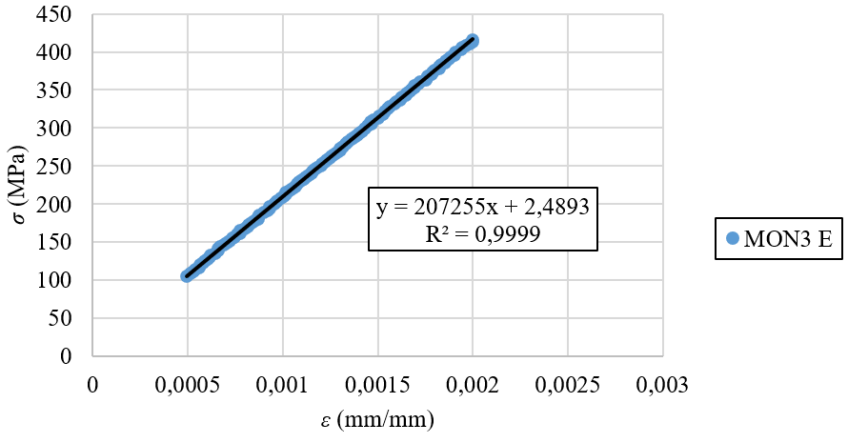

(b)

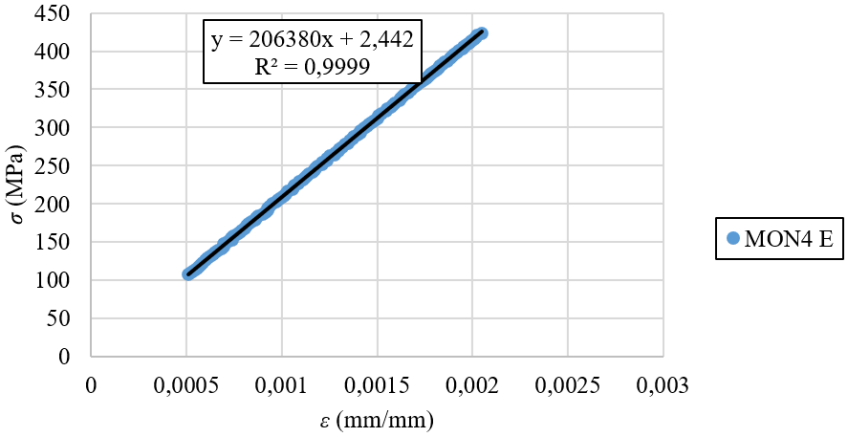

(c)

Figure A.1: *Curves for determining the modulus of elasticity*

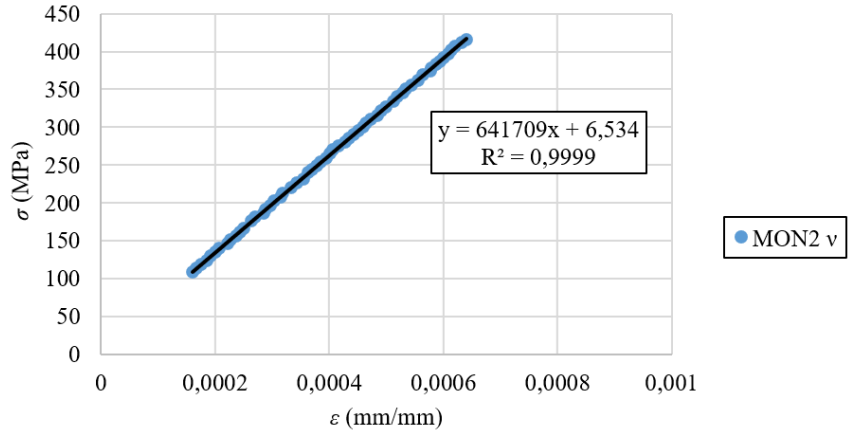

(a)

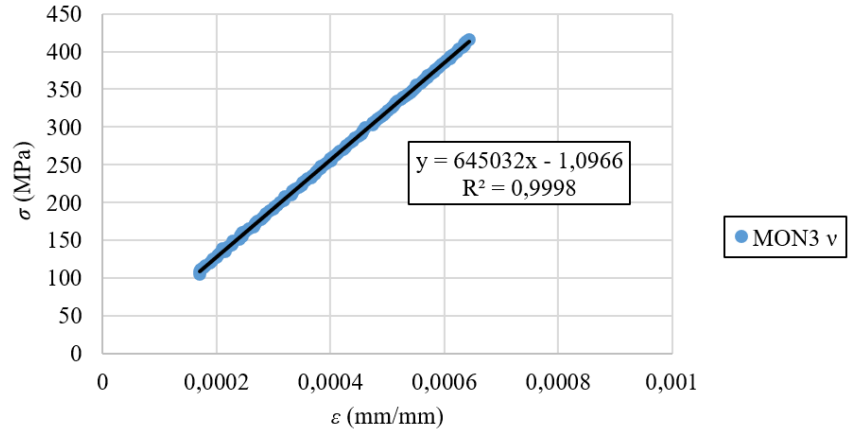

(b)

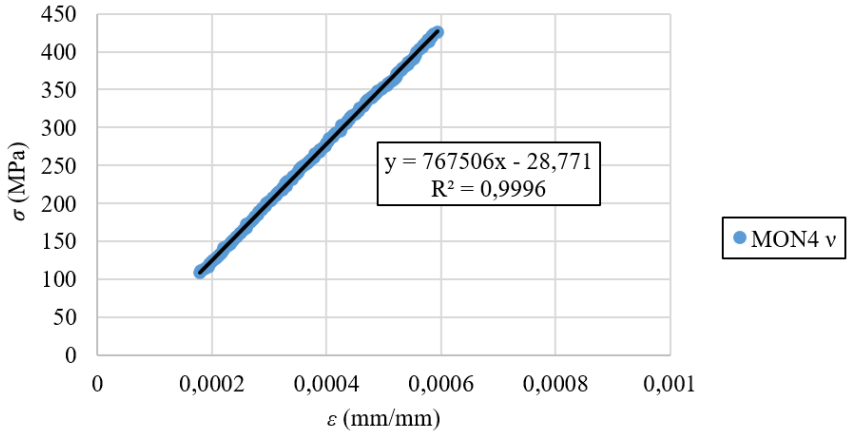

(c)

Figure A.2: *Curves for determining slope on (σ_x, ε_y) plane*

Bibliography

[1] Introduction to metal fatigue.

[2] Matlab website.

[3] H Askes, P Livieri, L Susmel, D Taylor, and R Tovo. Intrinsic material length, theory of critical distances and gradient mechanics: analogies and differences in processing linear-elastic crack tip stress fields. *Fatigue & Fracture of Engineering Materials & Structures*, 36(1):39–55, 2013.

[4] Bruno Atzori. *Appunti di costruzione di macchine: anno accademico 2000/2001*. Libreria Cortina, 2000.

[5] Matteo Benedetti and Ciro Santus. Mean stress and plasticity effect prediction on notch fatigue and crack growth threshold combining the theory of critical distances and multiaxial fatigue criteria. *Fatigue & Fracture of Engineering Materials & Structures*, 42(6):1228–1246, 2019.

[6] E. Bernardo. Lezioni di materiali non metallici.

[7] LP Borrego, JM Ferreira, and JM Costa. Fatigue crack growth and crack closure in an almgsi alloy. *Fatigue & Fracture of Engineering Materials & Structures*, 24(4):255–265, 2001.

[8] Moritz Braun, André Mischa Müller, Aleksandar-Saša Milaković, Wolfgang Fricke, and Sören Ehlers. Requirements for stress gradient-based fatigue assessment of notched structures according to theor of critical distance. *Fatigue & Fracture of Engineering Materials & Structures*, 43(7):1541–1554, 2020.

[9] Luigi Caligaris, Stefano Fava, and Carlo Tomasello. *Manuale di meccanica: matematica, informatica, fisica tecnica, chimica, disegno tecnico, tecnologia dei materiali, tecnologia meccanica, meccanica, costruzioni di macchine, meccanica dell'auto, elettrotecnica ed elettronica, sistemi automatici, controllo e regolazione automatica, sensori e trasduttori, robotica industriale, termotecnica, macchine e fluido, organizzazione industriale, antinfortunistica*. Hoepli, 2007.

[10] Ruslizam Daud, Ahmad Kamal Ariffin, Shahrum Abdullah, and Al Emran Ismail. Fatigue failure analysis using the theory of critical distance. *Key Engineering Materials*, 462-463:663–667, 01 2011.

[11] Wilfried Eichlseder. Fatigue analysis by local stress concept based on finite element results. *Computers & Structures*, 80(27-30):2109–2113, 2002.

[12] MH El Haddad, TH Topper, and KN Smith. Prediction of non propagating cracks. *Engineering fracture mechanics*, 11(3):573–584, 1979.

[13] Magnasteyr Engineering. *Femfat 4.4 basic theory manual*.

[14] S Filippi, Paolo Lazzarin, and Roberto Tovo. Developments of some explicit formulas useful to describe elastic stress fields ahead of notches in plates. *International Journal of Solids and Structures*, 39(17):4543–4565, 2002.

[15] FKM. *Analytical stregth assessment, 5th edition*.

[16] Srečko Glodež, Matjaž Šraml, and Janez Kramberger. A computational model for determination of service life of gears. *International Journal of Fatigue*, 24(10):1013–1020, 2002.

[17] A. F. Hobbacher. Recommendations for fatigue design of welded joints and components.

[18] Zheng Hu, Filippo Berto, Youshi Hong, and Luca Susmel. Comparison of tcd and sed methods in fatigue lifetime assessment. *International Journal of Fatigue*, 123:105–134, 2019.

[19] Charles Edward Inglis. Stresses in a plate due to the presence of cracks and sharp corners. *Trans Inst Naval Archit*, 55:219–241, 1913.

[20] George R Irwin. Analysis of stresses and strains near the end of a crack traversing a plate. 1957.

[21] Maxim Lutovinov Jan Papuga. Help for finliv.vba excel database. *FADOFF, Fatigue analysis documentation Office*.

[22] Miguel Vargas Aleš Hodr Aleksander Karolczuk Martin Fusek Radim Halama Dagmar Říčková Jan Papuga, František Fojtík. Summary of experiments on 2124-t851. *FADOFF, Fatigue analysis documentation Office*.

[23] M. Klesnil and P. Lukáš. Influence of strength and stress history on growth and stabilisation of fatigue cracks. *Engineering Fracture Mechanics*, 4(1):77–92, 1972.

[24] P Lazzarin and S Filippi. A generalized stress intensity factor to be applied to rounded v-shaped notches. *International journal of solids and structures*, 43(9):2461–2478, 2006.

[25] P Lazzarin and R Tovo. A notch intensity factor approach to the stress analysis of welds. *Fatigue & fracture of engineering materials & structures*, 21(9):1089–1103, 1998.

[26] Paolo Lazzarin and F Berto. Some expressions for the strain energy in a finite volume surrounding the root of blunt v-notches. *International Journal of fracture*, 135(1):161–185, 2005.

[27] Paolo Lazzarin, Filippo Berto, and Michele Zappalorto. Rapid calculations of notch stress intensity factors based on averaged strain energy density from coarse meshes: Theoretical bases and applications. *International Journal of Fatigue*, 32(10):1559–1567, 2010.

[28] Paolo Lazzarin and R Zambardi. A finite-volume-energy based approach to predict the static and fatigue behavior of components with sharp v-shaped notches. *International journal of fracture*, 112(3):275–298, 2001.

[29] Ding Liao, Shun-Peng Zhu, José AFO Correia, Abílio MP De Jesus, and Filippo Berto. Recent advances on notch effects in metal fatigue: A review. *Fatigue & Fracture of Engineering Materials & Structures*, 43(4):637–659, 2020.

[30] P Livieri and P Lazzarin. Fatigue strength of steel and aluminium welded joints based on generalised stress intensity factors and local strain energy values. *International Journal of Fracture*, 133(3):247–276, 2005.

[31] R Louks, H Askes, and L Susmel. A generalised approach to rapid finite element design of notched materials against static loading using the theory of critical distances. *Materials & Design*, 108:769–779, 2016.

[32] G. Meneghetti. Progettazione a fatica di componenti meccanici indeboliti da intaglia v a spigolo vivo - applicazione ai giunti saldati.

[33] G Meneghetti. The peak stress method applied to fatigue assessments of steel and aluminium fillet-welded joints subjected to mode i loading. *Fatigue & Fracture of Engineering Materials & Structures*, 31(5):346–369, 2008.

[34] G Meneghetti. Utilizzo della tensione di picco per la verifica a fatica dei giunti saldati d'angolo con il metodo degli elementi finiti. *Frattura ed Integrità Strutturale*, 3(9):85–94, 2009.

[35] Giovanni Meneghetti and Alberto Campagnolo. State-of-the-art review of peak stress method for fatigue strength assessment of welded joints. *International Journal of Fatigue*, 139:105705, 2020.

[36] Igor Milošević, Gerhard Winter, Florian Grün, and Martin Kober. Influence of size effect and stress gradient on the high-cycle fatigue strength of a 1.4542 steel. *Procedia Engineering*, 160:61–68, 2016.

[37] Igor Miloševic, Gerhard Winter, Florian Grün, and Martin Kober. Influence of the stress gradient on the fatigue life calculation of a martensitic high strength steel. *Frattura ed Integrità Strutturale*, 11(42):1–8, 2017.

[38] Heinz Neuber. *Kerbspannungslehre: Theorie der Spannungskonzentration Genaue Berechnung der Festigkeit*. Springer-Verlag, 2013.

[39] M Niessner, T Seeger, J Hohe, and D Siegele. Festigkeitsberechnung schwach gekerbter bauteile. *Materialwissenschaft und Werkstofftechnik: Entwicklung, Fertigung, Prüfung, Eigenschaften und Anwendungen technischer Werkstoffe*, 34(9):797–811, 2003.

[40] Stipica Novoselac, Dražan Kozak, Todor Ergić, and Ivan Šimić. Influence of stress gradients on bolted joint fatigue behaviour under different preloads and cyclic loads ratio uticaj gradijenata napona na zamor vijčane veze pod dejstvom različitih predopterećenja i odnosa cikličnih opterećenja.

[41] Walter D Pilkey, Deborah F Pilkey, and Zhuming Bi. *Peterson's stress concentration factors*. John Wiley & Sons, 2020.

[42] Barbara Reggiani and Alessandro Freddi. Effetto supporto, tensione locale e gradiente relativo di tensione nella predizione della vita a fatica. *Frattura ed Integrità Strutturale*, 2(4):2–11, 2008.

[43] Alfredo Ribeiro, José Correia, António Silva, and Abilio De Jesus. Evolution of fatigue history 01 2011.

[44] C Santus, D Taylor, and M Benedetti. Experimental determination and sensitivity analysis of the fatigue critical distance obtained with rounded v-notched specimens. *International Journal of Fatigue*, 113:113–125, 2018.

[45] CRA Schneider and SJ Maddox. Best practice guide on statistical analysis of fatigue data. *Weld Inst Stat Rep*, 2003.

[46] Walter Schütz. A history of fatigue. *Engineering Fracture Mechanics*, 54(2):263–300, 1996.

[47] L Susmel. The theory of critical distances: Applications in fatigue. In *Fracture of Nano and Engineering Materials and Structures*, pages 1101–1102. Springer, 2006.

[48] Luca Susmel. The theory of critical distances: a review of its applications in fatigue. *Engineering Fracture Mechanics*, 75(7):1706–1724, 2008.

[49] Luca Susmel and David Taylor. A novel formulation of the theory of critical distances to estimate life-time of notched components in the medium-cycle fatigue regime. *Fatigue & Fracture of Engineering Materials & Structures*, 30(7):567–581, 2007.

[50] David Taylor. Chapter 1 - introduction. Materials under stress. In David Taylor, editor, *The Theory of Critical Distances*, pages 1–19. Elsevier Science Ltd, Oxford, 2007.

[51] David Taylor. The theory of critical distances. *Engineering Fracture Mechanics*, 75(7):1696–1705, 2008.

[52] L Tóth and S Ya Yarema. Formation of the science of fatigue of metals. part 1. 1825–1870. *Materials Science*, 42(5):673–680, 2006.